Synthesis, Structure and Properties of Mixed Metal Oxides: From Pyrochlores to Fluorites

PAYNE, JULIA,LOUISE

Abstract

"Synthesis, Structure and Properties of Mixed Metal Oxides: From Pyrochlores to Fluorites"

PhD Thesis Julia L. Payne December 2010

Introduction and Literature Review: Different families of oxide ion conductors and their applications are discussed.

Experimental and Characterisation Methods: The synthetic methods and characterisation techniques used throughout this thesis are described.

Synthesis, Structure and Transport Properties of $Bi_2Zr_{2-x}Ti_xO_7$ Phases: The characterisation of $Bi_2Zr_{2-x}Ti_xO_7$ compounds is reported for the first time. An increase in conductivity of 3 orders of magnitude is found for the Zr- rich end member. $Bi_2Ti_2O_7$, which adopts centrosymmetric space group $Fd\bar{3}m$ has been found to be SHG active.

Structure Solution of β-$Bi_2Sn_2O_7$ and Properties of $Bi_2Sn_2O_7$ Based Materials: Analysis of synchrotron powder X-ray and powder neutron diffraction data has shown for the first time that β-$Bi_2Sn_2O_7$ is not cubic and has a monoclinic structure, most likely in space group *Pc*. The effect of doping in both $Bi_2Sn_2O_7$ and Bi_2ScNbO_7 on their respective conductivities has been explored.

Synthesis and Characterisation of $Nd_2Zr_2O_7$: A range of average and local structural techniques have been used to demonstrate that $Nd_2Zr_2O_7$ prepared by wet-chemistry routes adopts the fluorite-type structure, as opposed to the pyrochlore structure adopted by samples synthesised by solid state methods.

Synthesis, Characterisation, Simulations and Properties of Bi_6WO_{12} and Related Oxide Ion Conductors: We report for the first time details of DFT molecular dynamics simulations to probe the oxide ion conduction pathways in the oxide ion conductor Bi_6WO_{12}. Appropriate doping has led to enhancements in oxide ion conductivity.

Simulations, Characterisation and Properties of New Bismuth Vanadate Oxide Ion Conductors: DFT molecular dynamics simulations carried out on $Bi_{19}V_2O_{33.5}$ have revealed the O^{2-} migration pathways in this material with exceptional ionic conductivity. The synthesis and characterisation of new doped bismuth vanadates with formula $Bi_{19-x}M_x V_2O_{33.5-x/2}$ (M = Ca^{2+} or Sr^{2+}), also excellent oxide ion conductors, is reported.

Overall Conclusions and Suggestions for Future Work: This briefly reviews the conclusions and makes suggestions for further work.

Synthesis, Structure and Properties of Mixed Metal Oxides: From Pyrochlores to Fluorites

Julia L. Payne MChem(hons)

Durham University

Supervisor: Dr. Ivana Radosavljević Evans

A thesis submitted in partial fulfilment of the requirements for the degree of

Doctor of Philosophy

Department of Chemistry

Durham University

2010

Acknowledgements

Ivana for being an excellent supervisor and for encouraging me to be more positive!

Thanks are also due to all of those people who have helped with the science: Matt Tucker for assistance with collection of GEM data and help with RMC simulations; Mark Johnson for allowing me to spend one month in Grenoble to do MD simulations; Budhika Mendis for electron diffraction data; Andy Beeby for Raman spectra; David Apperley for ^{91}Zr NMR spectra. Beamline scientists at ISIS and Diamond for help with data collection: Aziz Daoud-Aladine, Stephen Thompson, Julia Parker, Chiu Tang. Leon Bowen for SEM training and help with EDX data collection. Doug Carswell for TGA and Judith Magee for ICP analysis. John Evans for help with I11 data collection and interest in my research in group meetings.

To the past and current members of CG031: Xiaojun for useful impedance spectroscopy discussions, Jenny for early morning conversation, Lars for help at the very beginning of my PhD and Anne for company at conferences. Sarah for being able to answer all my random questions and Emma for her enthusiasm! Dave for his computer skills and being in the same year group as me, hence being able to answer or discuss all relevant admin-type questions. Sam for answering random LAMP questions and her knowledge of Grenoble, Rebecca for random stories, Andrew for trying to fix the printer and Gary for doing his best to keep the diffractometers working. Thanks to all the fourth years: Alex, Oliver, Yuandi, Francesca, Erin, Zoe, Victoria, Tom, Adam, Andrew, Ian, Vicky and Alistair.

To Sara, Suzanne, Sarah, Dave, Nick, David and Jason for our many hours of chemistry discussions over the years. Friends from Howlands Choir, DUOS, DUPO, TSO, UWSO and string orchestra, for many hours of music making.

I would especially like to thank all my family, especially Dad and my sisters Sarah and Rita, to thank you properly would require an extra chapter! Thanks for 'Dad's taxi service' and cooking and conversations ranging from nursing to theology to name a few! Thanks to Scott, soon to be brother-in-law for looking after Sarah and keeping Dad company!

Finally, I would like to thank my Mam, who fought a year long battle with ovarian cancer during the course of my PhD, but lost her battle with the illness in December 2009. Without 25 years of her love, support and encouragement I would not be where I am today.

Declaration

The work described in this thesis is entirely my own, except where I have acknowledged help from a named person or given a reference to a published source of a thesis.

The research presented was performed in the Department of Chemistry, Durham University between October 2007 and November 2010, the results of which have not been submitted for a degree in this or any other university. This thesis conforms to the work limit set out in the Degree Regulations of the university.

List of Abbreviations

BIMEVOX	$Bi_2V_{1-x}M_xO_{5.5-\delta}$ (where M = metal) family of oxide ion conductors
BVS	Bond Valence Sum
DFT	Density Functional Theory
EDX	Energy Dispersive X-ray (analysis)
GEM	General Materials diffractometer (at ISIS)
HRPD	High Resolution Powder Diffractometer (at ISIS)
FT-IR	Fourier Transform Infra-red spectroscopy
ICP	Inductively Coupled Plasma
LAMOX	$La_2Mo_2O_9$
LAMP	Large Array Manipulation Program
MD	Molecular Dynamics
ND	Neutron Diffraction
NMR	Nuclear Magnetic Resonance
PND	Powder Neutron Diffraction
PXRD	Powder X-ray Diffraction
QCPMG	Quadrupolar Carr-Purcell-Meiboom-Gill
RMC	Reverse Monte-Carlo
SEM	Scanning Electron Microscopy
SHG	Second Harmonic Generation
SOFC	Solid Oxide Fuel Cell
TEM	Transmission Electron Microscopy
TGA	Thermogravimetric Analysis
VASP	Vienna *ab-initio* Simulation Package
VT	Variable Temperature
VT-PXRD	Variable Temperature Powder X-ray Diffraction
WURST	Wide band Uniform-Rate Smooth Truncation
XRD	X-ray Diffraction

Table of Contents

1 Introduction and Literature Review

The mineral pyrochlore, $(Ca,Na)_2Nb_2O_6(OH,F)$, has the general formula $A_2B_2X_7$, whilst the mineral fluorite (CaF_2) has the general formula MX_2. In a pyrochlore typically, the A cation is in an oxidation state of +2 or +3 and the B cation is in an oxidation state of +5 or +4; pyrochlores with $(A^{1+})_2(B^{6+})_2O_7$ and defect pyrochlores are also known. The formation of the pyrochlore structure over the fluorite structure is generally governed by the radius ratios of the cations, r_A/r_B, with pyrochlore forming between 1.46 and 1.78.[1] Research in pyrochlores has been partly driven by potential applications in solid oxide fuel cells and oxygen sensors and as host materials for nuclear waste due to their ability to accommodate a range of cations in their crystal structure. [2, 3 4, 5] This project focuses on pyrochlores and fluorites as potential oxide ion conductors.

1.1 Description of the fluorite and pyrochlore crystal structures

The fluorite and pyrochlore (Figure 1.1) crystal structures are closely related. The fluorite structure adopts the space group *Fm*$\bar{3}$ *m* and can be described as a face centred cubic array of cations, with the anions occupying the tetrahedral interstices. There are only two unique crystallographic sites in fluorite. Cations occupy the 4a site and are coordinated by eight oxygens in a cubic geometry. Oxygen occupies the 8c site at the centre of a tetrahedron of cations.

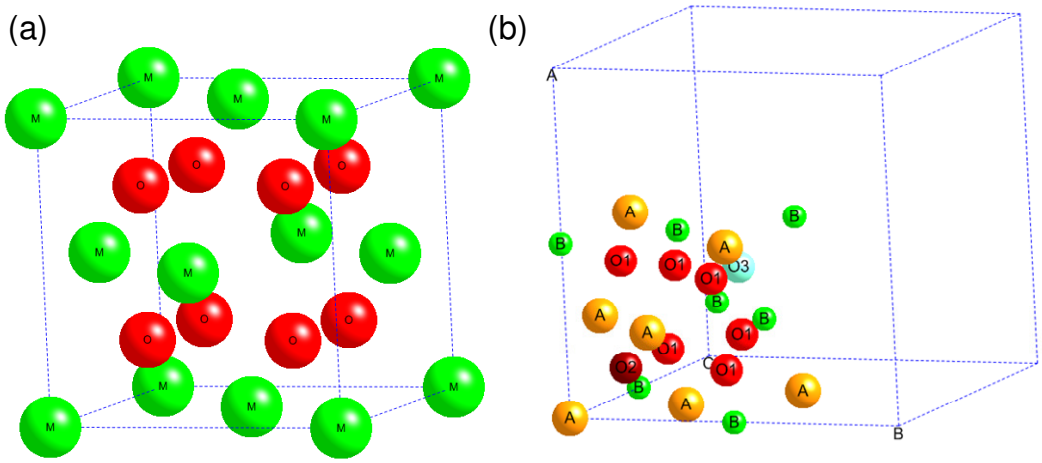

Figure 1.1: (a) Unit cell of MO_2, a typical fluorite. Green spheres are metal atoms and red spheres are oxygen atoms. (b) One-eighth of the pyrochlore $A_2B_2O_7$ unit cell. Orange spheres are A cations, green spheres are B cations, red spheres 48f oxygen, dark red spheres are 8a oxygen and the light blue sphere is the vacancy (8b).

Pyrochlore (Figure 1.1b) consists of an ordered face centred array of cations and crystallises in the space group $Fd\bar{3}m$. The presence of aliovalent A and B cations in $A_2B_2O_7$ requires vacancies in 12.5% of the anion sites, relative to the fluorite type M_4O_8 formula, in order to maintain electroneutrality. Cations are ordered in the [110] planes, which results in a doubling of the unit cell parameters relative to a fluorite and therefore eight $A_2B_2O_7$ formula units are present in the unit cell. [1] It should be noted that compounds with empirical formula $A_2B_2O_7$ may also possess the fluorite structure. Whether the fluorite structure is adopted or not depends on the radius ratio, r_A/r_B, of the A and B cations.

Table 1.1: Crystallographic sites in the pyrochlore structure. Note: The structural description of pyrochlore in this table and throughout this document is given in origin choice number 2 of space group $Fd\bar{3}m$.

Site	Wyckoff site	Site symmetry	Fractional coordinates	Coordination number
A	16c	$\bar{3}m$	(0, 0, 0)	8
B	16d	$\bar{3}m$	(0.5, 0.5, 0.5)	6
O	48f	mm	(x, 0.125, 0.125)	4
O'	8a	$\bar{4}3m$	(0.125, 0.125, 0.125)	4
Vacancy	8b	$\bar{4}3m$	(0.375, 0.375, 0.375)	4

The ideal pyrochlore has four occupied unique crystallographic sites and one vacant site (see Table 1.1). The pyrochlore formula is sometimes written as $A_2B_2O_6O'$ to distinguish between the two occupied oxygen sites. All crystallographic sites in a pyrochlore structure occupy a special crystallographic position, with only the 48f x parameter being refineable. [1]

The A cation, on site 16c, has a coordination number of 8 and is surrounded by 8 oxygens (six 48f oxygens and two 8a oxygens). The geometry adopted depends on the x parameter of the 48f oxygen and varies from cubic (x = 0.375, Figure 1.2a), to a puckered hexagon with two 'axial' sites occupied by the two special (8a) oxygen positions (x = 0.4375, Figure 1.2b). The puckered hexagon is sometimes described as a 6+2 coordination. The B cation, on site 16d, is surrounded by six 48f oxygens and the geometry varies from a trigonal antiprism (Figure 1.2c) to an ideal octahedron (Figure 1.2d). The 8a (Figure 1.2e) oxygen position is surrounded by a tetrahedron of four A cations and the 48f oxygen sites are surrounded by two A cations and two B cations (Figure 1.2f). The vacancy (8b) is surrounded by a tetrahedron of B cations.

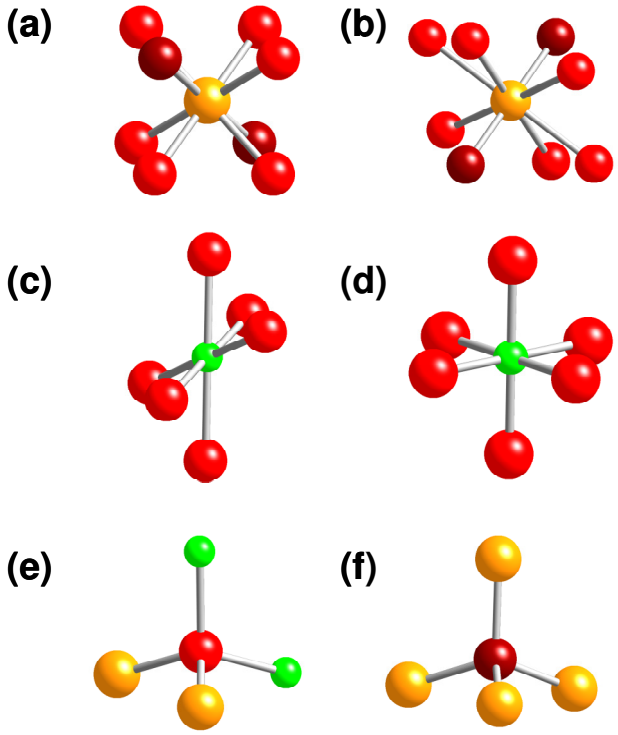

Figure 1.2: Coordination environments of atoms in the fluorite and pyrochlore crystal structures. (a-d) show the A cation (orange) and B cation (green) coordination in the pyrochlore structure. O(1) is bright red and O(2) is dark red. (a) shows the coordination around the A cation in a fluorite or pyrochlore when the 48f x = 0.375, (b) shows the coordination around the A cation when 48f x = 0.4375, (c) shows the coordination around the B cation when x = 0.375 and (d) shows the coordination around the B cation when 48f x = 0.4375. (e) and (f) show the 48f and 8a oxygens respectively.

The pyrochlore structure may also be described as being formed by two interpenetrating networks. It consists of A_2O' chains, formed by corner sharing O' centred A_4O' tetrahedra and B_2O_6 networks, formed by corner sharing BO_6 octahedra (Figure 1.3). This description of the structure is particularly useful as it reflects the compositional flexibility of the pyrochlore structure, as both cation and anion deficiency can be accommodated in the A_2O' network, without disrupting the pyrochlore structure. There are several examples of this in the literature, such as $Sn^{2+}_{2-x}(M_{2-y}Sn^{4+}_{y})O_{7-x-y/2}$ where M = Ta^{5+} or Nb^{5+} and $Bi_{1.74}Ti_2O_{6.62}$.[6, 7]

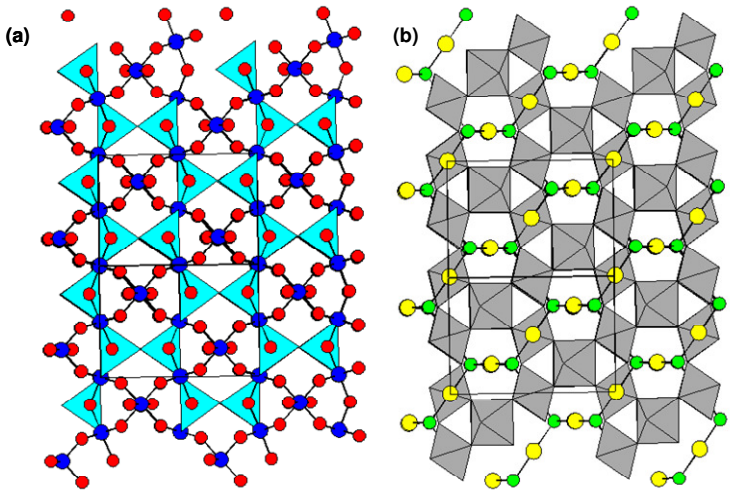

Figure 1.3: View of the two interpenetrating networks of the pyrochlore structure. (a) shows the A_2O' network of corner sharing, $O'A_4$, tetrahedra (blue). Blue spheres are B cations and red spheres are 48f oxygens respectively. (b) shows the B_2O_6 network of corner sharing BO_6 octahedra (grey). Yellow spheres are A cations and green spheres are O'.

Elements with a lone pair such as Bi^{3+}or Sn^{2+} cannot readily be accommodated on the usual A crystallographic site on the three-fold axis, hence they usually occupy a site of lower symmetry which is slightly displaced from that of the ideal pyrochlore A site. This was first reported by Sleight and Birchall in the $Sn^{2+}_{2-x}(M_{2-y}Sn_y^{4+})O_{7-x-y/2}$ system, where M = Ta and Nb.[6] Since then it has also been reported in both stoichiometric and non-stoichiometric $Bi_2Ti_2O_7$, γ–$Bi_2Sn_2O_7$ and $Bi_{2-x}M_xRu_2O_{7-\delta}$ (where M = Co or Cu).[7-10] In the case of $Bi_2Ti_2O_7$, this resulted in bismuth being placed on a 96h or 96g site, due to the stereochemically active lone pair, which corresponds to a displacement of 0.38 Å from the A cation site, in directions perpendicular to the cubic three-fold axis. [7, 8] The presence of the lone pair and its stereochemical activity are thought to be one explanation as to why the radius ratio rules are not obeyed in some cases. Table 1.2 summarises the r_A/r_B values for some examples of bismuth containing pyrochlores. All values lie outside the upper pyrochlore boundary of 1.78, apart from $Bi_2Sn_2O_7$ which is just inside the pyrochlore stability region.

Table 1.2: Radius ratios of selected bismuth pyrochlores.

Pyrochlore	Radius ratio
$Bi_2Ru_2O_7$	1.89
$Bi_2Rh_2O_7$	1.95
$Bi_2Ir_2O_7$	1.87
$Bi_2Sn_2O_7$	1.70
$Bi_2Ti_2O_7$	1.93
$Bi_2Pt_2O_7$	1.87

1.2 Oxide ion conductivity

Oxide ion conductivity is the movement of oxide ions (O^{2-}) through a crystal lattice and it can be described by Equation (1.1), where σ is the oxide ion conductivity, n is the number of charge carriers (*i.e.* species that are conducted), e the charge on the ion and μ is the mobility.

$$\sigma = ne\mu \tag{1.1}$$

Oxide ion conductivity (σ) has a simple temperature dependence. This can be summarised by Equation (1.2). σ_0 is the pre-exponential factor, which includes several factors such as the number of mobile ions and vacancies. [11] In Equation (1.2), E_a is the activation energy, R is the gas constant and T is the temperature.

$$\sigma = \sigma_0 e^{\left(\frac{-E_a}{RT}\right)} \tag{1.2}$$

The total conductivity (σ_t) displayed by a solid electrolyte is the sum of both electronic (σ_e) and ionic conductivity (σ_i), as described by Equation (1.3) below. Ionic conductors which also exhibit electronic conductivity are classified as 'mixed conductors' and they can also have important applications in devices such as fuel cell cathodes.

$$\sigma_t = \sigma_e + \sigma_i \tag{1.3}$$

Several criteria have been outlined in order for ionic conductivity to be achieved. Although it is not necessary for a material to possess all characteristics, it must have as many as possible of the following:[12]

- There must be a low activation energy for the migration of the ion.
- The crystal structure must possess an open framework or channels for the movement of ions.

- The anion framework should be polarisable.
- There should be a high number of vacancies.
- There must be a high number of charge carriers that are able to move.
- Anion sites should have high symmetry and therefore be energetically equivalent.[12]

In general, oxide ion conductivity may be increased by three methods: aliovalent doping, isovalent doping, and oxygen intercalation. Depending on the valence of the cation used, aliovalent doping may bring about oxygen excess or deficiency, whilst oxygen intercalation introduces oxygen excess. Although isovalent doping does not alter the oxygen stoichiometry, it may induce structural disorder due to the size mismatch between the host and dopant species.

Oxide vacancies may be classified as extrinsic or intrinsic, with both types contributing to oxide ion conductivity. Extrinsic vacancies are created as a result of doping with a cation of lower valency, as in stabilised zirconias, whereas intrinsic vacancies are present in the crystal structure without the need for doping (for example in δ-Bi_2O_3). In some cases the conductivity may be reduced by the formation of dopant-vacancy clusters.[13]

There are several classes of mechanisms for oxide ion conductivity.[14] The most common is the vacancy mechanism, where ions move from their usual crystallographic site to another identical site that is vacant, which is common for fluorite and perovskite oxide ion conductors.[12, 14] The interstitial mechanism has been demonstrated in apatite ceramics.[15] Ions are promoted into interstitial sites and migration proceeds via these sites.[14] Recently, the interstitial oxide ions have been attributed to the increase oxide ion conductivity in the melilite structure.[16] A cooperative mechanism is also possible, where the movement of one ion causes the movement of another.[14] Molecular dynamics simulations in $La_{1-x}Ba_{1+x}GaO_{4-x/2}$ have demonstrated a cooperative mechanism which involves the making and breaking of Ga_2O_7 units.[17] Studies on the $La_2Mo_2O_9$ oxide ion conductor have found that molybdenum exhibits coordination numbers of four, five and six, therefore the mechanism of oxide ion conductivity is facilitated by the ability of molybdenum to display a variable coordination number.[18]

Catlow and Wilde proposed that the oxide ion conductivity mechanism in pyrochlores occurs via thermal excitation of a 48f oxygen atom into the vacant 8b

oxygen site, followed by movement of 48f oxygen atoms through the other 48f sites, as only the 48f site forms a continuous network.[19] They also calculated that creating a defect on the 48f site is more energetically favourable than creating a defect on an occupied 8a site.

1.3 Structural families of oxide ion conductors

Many different classes of oxides display high oxide ion conductivities. They include $La_2Mo_2O_9$ (LAMOX) based materials, Aurivillius doped $Bi_2VO_{5.5}$ phases (BIMEVOX), apatites, fluorites, pyrochlores and perovskites. Figure 1.4 shows the temperature dependence of oxide ion conductivity for some selected families of oxide ion conductors. Changes in the gradient are caused by phase transitions. The blue curve represents $Bi_2V_{0.9}Cu_{0.1}O_{5.35}$ and represents the highest conductivity at low temperatures. The green curve represents yttria stabilized zirconia which is used in commercial applications.

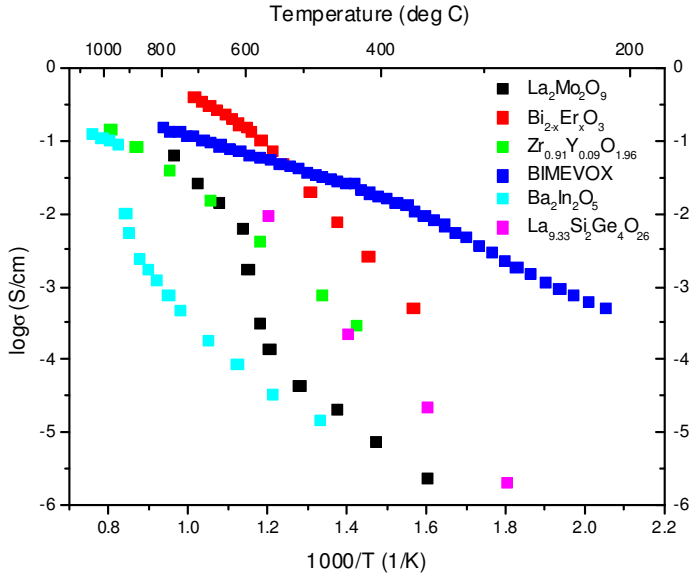

Figure 1.4: Oxide ion conductivity of some selected compounds. $Ba_2In_2O_5$ is a brownmillerite phase, BIMEVOX is the $Bi_2V_{0.9}Cu_{0.1}O_{5.35}$ Aurivillius phase, $Y_{0.09}Zr_{0.91}O_{1.96}$ has the fluorite structure, as does $Bi_{2-x}Er_xO_3$, whilst $La_2Mo_2O_9$ is the parent member of the LAMOX family. $La_{9.33}Si_2Ge_4O_{26}$ is an example of an apatite oxide ion conductor. [20-23]

1.3.1 $A_2B_2O_7$ pyrochlore and fluorite oxide ion conductors

The degree of conductivity displayed by fluorites and pyrochlores depends on the ordering of the oxygen sublattice. In an ideal pyrochlore, oxygens and vacancies are ordered, which results in a low conductivity. When an oxide has the pyrochlore stoichiometry, $A_2B_2O_7$, but possesses the fluorite structure, oxide ions and vacancies are disordered. Therefore by probing the boundary between the fluorite and pyrochlore crystal structures as a function of chemical composition, the conductivity may be

maximised. With appropriate isovalent or aliovalent doping on either A or B cation sites conductivity may be increased, through creation of vacancies or cation and anion sublattice disorder.

There have been many studies of aliovalent and isovalent doping of pyrochlores and the effect this has on the ionic conductivity. Aliovalent doping introduces oxygen vacancies if the chosen cation has a lower valency. The current best pyrochlore oxide ion conductors are those which have a degree of aliovalent substitution on the A cation site, with the highest conductivity (0.2 S cm^{-1} at 1000 ℃) being achieved for $Yb_{1.8}Ca_{0.2}Ti_2O_{6.9}$, which shows an increase of one order of magnitude over the parent pyrochlore $Yb_2Ti_2O_7$.[24] Neutron diffraction studies of $Yb_{1.8}Ca_{0.2}Ti_2O_{6.9}$ have shown that the oxygen sublattice is disordered and that the normally vacant 8b site is partially occupied with oxygen from the 48f site.[25] Ca^{2+} doping also increased the conductivity of $Gd_2Ti_2O_7$, with a value of 5×10^{-2} S cm^{-1} at 1000 ℃ being achieved for $Gd_{1.8}Ca_{0.2}Ti_2O_{6.9}$.[26] The increase in conductivity observed for $Gd_{1.8}Ca_{0.2}Ti_2O_{6.9}$ was approximately 2.5 orders of magnitude with respect to the parent $Gd_2Ti_2O_7$, which is a greater increase than that observed in the $Yb_{2-x}Ca_xTi_2O_{7-x/2}$ system.[26] Tuller *et al.* compared the conductivity of $M_{2-x}Ca_xTi_2O_{7-x/2}$ systems (where M = Gd^{3+}, Y^{3+} and Sm^{3+}) and found that the highest conductivity was observed for the gadolinium compounds, followed by the yttrium and samarium analogues.[27] In the $Sm_{1.8}M_{0.2}Ti_2O_{6.9}$ system where M = Ca^{2+}, Sr^{2+} and Mg^{2+}, the highest conductivity was once again observed for the calcium doped analogue.[27] This was attributed to Ca^{2+} matching the ionic radius of Sm^{3+} most closely. The conductivity of some $M_{2-x}Ca_xTi_2O_{7-x/2}$ compositions are shown in Table 1.3. Doping $Gd_2Sn_2O_7$ with calcium also increased the ionic conductivity for $Gd_{1.9}Ca_{0.1}Sn_2O_{6.95}$.[28]

Table 1.3: Conductivity of some pyrochlore titanates compared to the conductivity of their calcium doped analogues at 1000 ℃

$M_2Ti_2O_7$	Conductivity at 1000 °C (S cm^{-1})	$M_{2-x}Ca_xTi_2O_{7-x/2}$	Conductivity at 1000 °C (S cm^{-1})
$Gd_2Ti_2O_7$[26]	1×10^{-4}	$Gd_{1.8}Ca_{0.2}Ti_2O_{6.9}$	5×10^{-2}
$Yb_2Ti_2O_7$[24]	1×10^{-2}	$Yb_{1.8}Ca_{0.2}Ti_2O_{6.9}$	2×10^{-1}
$Y_2Ti_2O_7$[27, 29]	8×10^{-4}	$Y_{1.8}Ca_{0.2}Ti_2O_{6.9}$	1×10^{-2}

Apart from calcium, other divalent cations have been used as aliovalent A site substitutients.[30, 31] Strontium doping has also increased the conductivity in the $Gd_{2-x}Sr_xZr_2O_{7-x/2}$ and $Nd_{2-x}Sr_xZr_2O_{7-x/2}$ systems. $Gd_{1.9}Sr_{0.1}Zr_2O_{6.95}$ and $Gd_{1.8}Sr_{0.2}Zr_2O_{6.90}$

showed higher ionic conductivity than the parent $Gd_2Zr_2O_7$ at high temperatures.[30] At all temperatures, $Nd_{1.9}Sr_{0.1}Zr_2O_{6.95}$ has a higher conductivity than the parent $Nd_2Zr_2O_7$, but further increases of Sr^{2+} results in formation of $SrZrO_3$ impurities. [30]

Shlylakhtina *et al*. have looked at the influence of Ca^{2+}, Mg^{2+} and Zn^{2+} doping in $Yb_2Ti_2O_7$, $Dy_2Ti_2O_7$ and $Ho_2Ti_2O_7$.[31] As discussed earlier, the highest conductivity was observed for $Yb_{1.8}Ca_{0.2}Ti_2O_{6.9}$, but the next best conductivity was obtained for $Yb_{1.8}Mg_{0.2}Ti_2O_{6.9}$ (9×10^{-3} S cm^{-1} at 750 °C), with $Dy_{1.8}Ca_{0.2}Ti_2O_{6.9}$ and $Ho_{1.8}Ca_{0.2}Ti_2O_{6.9}$ showing comparable conductivities.[31] However, with respect to the parent titantates, the increase in the conductivity is only 0.5 to 1 order of magnitude, which is much lower than the 2.5 orders of magnitude increase seen in $Gd_{1.8}Ca_{0.2}Ti_2O_{6.9}$.[26, 31]

Fewer studies on aliovalent doping of the B cation site have been carried out. Al^{3+} substitution of Ti^{4+} (on the B pyrochlore cation site) has increased the conductivity of $Gd_2Ti_2O_7$ by approximately 1.5 orders of magnitude, however, the conductivity was lower than $Gd_{2-x}Ca_xTi_2O_{7-x/2}$ phases. [26] Doping Nb^{5+} onto the Zr^{4+} site in $Gd_2Zr_2O_7$ has recently been found to increase the conductivity in $Gd_2Zr_{1.8}Nb_{0.2}O_{7.1}$, but these materials exhibit a degree of proton conductivity.[32]

The effect of isovalent substitution, particularly on the B cation site has also been explored with respect to oxide ion conductivity in pyrochlores. In particular, there have been several studies on the $M_2Ti_{2-x}Zr_xO_7$ system (where M = Gd, Y).[33, 34] For $Y_2(Ti_{1-x}Zr_x)_2O_7$ compounds, increasing the zirconium content increases the ionic conductivity.[33] Rietveld refinement (using neutron diffraction data) has shown that when x = 0.3, the normally vacant O3 site becomes occupied, indicating the onset of anion disorder.[33] This coincides with a large increase in conductivity, of approximately 1-2 orders of magnitude with respect to the parent $Y_2Ti_2O_7$ compound.[33] At approximately x = 0.6, the cation sublattice begins to disorder, with full cation disorder (*i.e.* defect fluorite formation) not occurring until x = 0.9.[33] The zirconium end member, $Y_2Zr_2O_7$ has the highest conductivity in this series.[33] However, it should be noted that in the Rietveld study of this system, compounds in the x = 0.3 to x = 0.6 region were reported to be a mixture of pyrochlore and fluorite, with the fluorite having a cell parameter only slightly different from the pyrochlore $a/2$ cell parameter.[33] Nevertheless, this study has important implications for the design of fluorite and pyrochlore oxide ion conductors as it appears that the anion disorder can be tuned by controlling the chemical composition.

Although no neutron diffraction studies have been carried out, $Dy_2Ti_{2-x}Zr_xO_7$ compounds show similar behaviour to the $Y_2Ti_{2-x}Zr_xO_7$ systems.[34] Pyrochlore compounds were stable in the region $Dy_2Ti_2O_7$ –$Dy_2Ti_{0.6}Zr_{1.4}O_7$ and the conductivity of $Dy_2Ti_{1.2}Zr_{0.8}O_7$ showed an increase of 1.5 orders of magnitude over the parent $Dy_2Ti_2O_7$, whilst the highest conductivity was displayed for $Dy_2Zr_2O_7$ which had a conductivity two orders of magnitude greater than $Dy_2Ti_2O_7$.[34]

The $Gd_2Ti_{2-x}Zr_xO_7$ system has been studied by Tuller *et al.*.[35] Again, the titanate end member has the lowest conductivity. Increasing the amount of zirconium in the $Gd_2(Ti_{1-x}Zr_x)_2O_7$ system has been shown to increase the ionic conductivity. For $x = 0.4$ or greater, the ionic conductivity reaches 10^{-2} S cm^{-1} at 1000 °C.[26, 28] Takamura and Tuller have investigated the $Gd_2(GaSb)_{1-x}Zr_{2x}O_7$ system, as Ga^{3+} (0.62 Å) and Sb^{5+} (0.60 Å) have an average radius very close to the ionic radius of Ti^{4+}(0.605 Å), thereby allowing comparison with the well studied $Gd_2Ti_{2-x}Zr_xO_7$ system.[36] They found that conductivity increased with increasing zirconium content, with $Gd_2(GaSb)_{0.2}Zr_{1.6}O_7$ having the lowest activation energy and highest conductivity (2.14×10^{-3} S cm^{-1} at 1000 °C). [36] The conductivity of this system was compared to $Gd_2Ti_{2-x}Zr_xO_7$ (which have the same radius ratios) and the conductivity of $Gd_2(GaSb)_{0.6}Zr_{0.8}O_7$ was approximately three orders of magnitude lower than that of $Gd_2Ti_{1.2}Zr_{0.8}O_7$, with the difference being attributed to the differing chemical nature of Ti and (GaSb).[36]

As the radius of Sn^{4+} is intermediate to Zr^{4+} and Ti^{4+}, Wuensch *et al.* have carried out detailed structural studies on the $Y_2Sn_{2-x}Ti_xO_7$ and $Gd_2Sn_{2-x}Ti_xO_7$ systems.[29] Little disordering of the anion sublattice was observed in the $Y_2Sn_{2-x}Ti_xO_7$ compounds, with the occupation of the O(1) site remaining fully occupied.[29] Although no neutron diffraction data were collected on the $Gd_2Sn_{2-x}Ti_xO_7$ system (due to the absorbing nature of gadolinium), the O(3) site was reported to be partially occupied for $Gd_2Sn_{1.2}Ti_{0.4}O_7$.[29] Unlike the $Y_2Ti_{2-x}Zr_xO_7$ system, the highest conductivities were found for $Gd_2Sn_{0.8}Ti_{1.2}O_7$ and $Y_2Sn_{0.8}Ti_{1.2}O_7$, *i.e.* for compounds with intermediate compositions rather than an end member.[29] Additionally, the magnitude of increase in conductivity for the $M_2Sn_{2-x}Ti_xO_7$ systems was only one order of magnitude, less than that observed in $Y_2Ti_{2-x}Zr_xO_7$.[29] Weunsch *et al.* have attributed this to the retention of structural ordering and also the higher covalency of the Sn-O bond, rather than the influence of average B site radius.[29]

Although the conductivity of $Y_2Sn_{2-x}Zr_xO_7$ was not measured by Weunsch, the variation of the 48f x parameter was similar to that observed for $Y_2Ti_{2-x}Zr_xO_7$, hence

this system also was attributed to have a degree of structural disorder.[29] The occupation of the O(3) site increased with Zr^{4+} content.[29] However, in this system, there was a region of pyrochlore and fluorite phase coexistence, like in the $Y_2Zr_{2-x}Ti_xO_7$ system.[29] In the chemically similar $Gd_2Sn_{2-x}Zr_xO_7$ phases, increasing the zirconium content increased the ionic conductivity by just over one order of magnitude, although no details of any structural disordering were given in this case.[28]

Although most studies have focused on aliovalent doping on the A cation site or isovalent doping on the B cation site, there are also some examples of isovalent doping on the A cation site. Eberman *et al.* have carried out neutron diffraction studies on the $Yb_{2-x}Sc_xTi_2O_7$ systems, as a function of both composition and temperature, paying particular attention to the 48f x parameter.[37] As Sc^{3+} is smaller than Yb^{3+}, this doping would reduce the cation radius ratio. As the Sc^{3+} content increased, the value of the 48f x parameter distorted from the parent value towards (but not reaching) the value expected for a fluorite.[37] Certain features of the variation of the 48f parameter were attributed to the occupation of the O(3) site and cation disordering, but no details of the occupation or disordering of these sites were reported.[37] Shlyakhtina *et al.* have since measured the conductivity for several compositions in the $Yb_{2-x}Sc_xTi_2O_7$ system and claimed that the highest conductivity was observed for the $Yb_{1.82}Sc_{0.18}Ti_2O_7$ composition; however on closer inspection, it appears that this conductivity is virtually identical to that of the parent compound.[38] $Yb_{1.4}Sc_{0.6}Ti_2O_7$ has a lower conductivity than the parent compound.[38]

Another example of isovalent substitution on the A cation site is in $Gd_{2-x}La_xZr_2O_7$.[39] When x = 0.0 and 0.2, compounds have the fluorite structure, whilst when $x \geq 0.4$, the pyrochlore structure is present.[39] The maximum conductivity in this series was observed for x = 0.4 which is the first composition in this series with the pyrochlore structure.[39] It appears that this work may be comparable to the work by Yamamura who found the maximum conductivity in a range of zirconates to be close to the fluorite-pyrochlore phase boundary.[40]

In the $(Sm_{1-x}Yb_x)_2Zr_2O_7$ system, when x = 0-0.1 the pyrochlore structure was adopted, but when x = 0.3-1.0 the fluorite structure was favoured. [41] Interestingly, the compounds with the fluorite structure had the lowest conductivities, (and highest activation energies) whilst the pyrochlores had the highest conductivity. [41] The highest conductivity was found for $Sm_{1.8}Yb_{0.2}Zr_2O_7$, which was only fractionally higher than that of $Sm_2Zr_2O_7$ at high temperatures. Across the series there was approximately a

difference of four orders of magnitude at low temperature, but at high temperature this difference was reduced to approximately 1.5 orders of magnitude.[41] A further study has recently been carried out using three cations on the A site in $SmYb_{1-x}Gd_xZr_2O_7$, with x = 0-0.5 having the fluorite structure and x = 0.7-1.0 having the pyrochlore structure. The highest conductivity was found for the $SmGdZr_2O_7$ end member.[42]

Another example of isovalent subsititution on the A cation site is in the $Gd_{2-x}Eu_xZr_2O_7$ system.[43] When x = 0.2 or more a pyrochlore structure is favoured, whilst in this case $Gd_2Zr_2O_7$ was said to adopt a fluorite structure.[43] $Gd_2Zr_2O_7$ had the lowest conductivity whilst $Eu_2Zr_2O_7$ had the highest conductivity.[43] If $Gd_2Zr_2O_7$ does have a fluorite structure, this offers an example of a fluorite having a lower conductivity than a pyrochlore.

A study on the electrical conductivity for a range of zirconate fluorites and pyrochlores with varying radius ratios has shown that the conductivity reaches a maximum around the fluorite - pyrochlore phase boundary. [40] Of all the compounds studied, only $La_2Zr_2O_7$ showed electronic conductivity and oxide ion conductivity was displayed by all other compounds. $Eu_2Zr_2O_7$, which is closest to the fluorite – pyrochlore phase boundary, displayed the highest conductivity (8.3×10^{-3} S cm^{-1} at 800 °C). [40] The conductivity increased with increasing radius ratio when oxides possessed a fluorite structure, but for pyrochlore compounds, conductivity decreased with increasing radius ratio. [40]

Tuller *et al.* have also explored the affect of aliovalent doping on both the A and B cation sites in the $Gd_2Zr_{0.6}Ti_{1.4}O_7$ pyrochlore, which already has cation disorder on the B cation site. $Gd_{1.96}Ca_{0.04}Zr_{0.6}Ti_{1.4}O_{6.98}$ exhibited a conductivity 1.5 orders of magnitude higher than $Gd_2Zr_{0.6}Ti_{1.4}O_7$, whilst Ta^{5+} doping on the Ti^{4+} site reduced the conductivity by approximately 0.5 orders of magnitude.[35]

Yashumura *et al.* have studied isovalent doping in the $(Y_{1-x}La_x)_2(Ce_{1-x}Zr_x)_2O_7$ system.[44] When x = 0.1-0.5, the system adopts a fluorite structure, but then transforms to a pyrochlore structure when x = 0.6. Oxide ion conductivity measurements have also shown that the conductivity was greatest when the cation r_A/r_B ratio was low, with the highest value (4.351×10^{-3} S cm^{-1}) obtained when x = 0.1 at 800 °C, where the fluorite structure is present.[44] When x = 0.1 or more the conductivity gradually decreases.[44] Where the pyrochlore structure was stable, decreasing conductivities were attributed to

increased oxygen ordering, as shown by the increased occupancy of the 48f O(1) site from Rietveld refinements using neutron diffraction data.[44]

Shlyakhtina *et al.* have investigated the total conductivity of various zirconates and hafnates and the effect of non-stoichiometry on the cation sites. [45] The highest total conductivities were found for the stoichiometric pyrochlore compounds, with $Sm_2Zr_2O_7$, $Eu_2Zr_2O_7$ and $Gd_2Zr_2O_7$ displaying values of 5.0×10^{-3} S cm^{-1}, 6×10^{-3} S cm^{-1} and 8.0×10^{-3} S cm^{-1} at 780 °C respectively. [45, 46] A similar situation was observed in $Er_2Ti_2O_7$.[46]

Pyrochlores may also operate as mixed conductors, where both electronic and oxide ion conductivity is exhibited. One example is the $Gd_2(Ti_{1-x}Mo_x)_2O_7$ system, where electronic conductivity increases with molybdenum content, which is thought to be due to the exhibition of variable oxidation states by molybdenum.[47] This may also result in oxygen non-stoichiometry, thus increasing oxide ion conductivity. The Gd_2TiMoO_7 series member is a good mixed conductor (with an ionic conductivity of 1×10^{-2} S cm^{-1} at 900 °C) and therefore may be a potential anode material for solid oxide fuel cells.[47] Some pyrochlores also display proton conductivity, as demonstrated recently by Knee *et al.* in some calcium doped stannate pyrochlores.[48, 49]

In summary, pyrochlores can display both pure ionic conductivity and mixed ionic-electronic conductivity, although the magnitude of the oxide ion conductivity is lower than that observed by the leading oxide ion conductors. However, the possibility of creating a monolithic fuel cell is one of the driving factors in pyrochlore oxide ion conductor research.[50] In a monolithic fuel cell, cathode, anode and electrolyte are all based on the same material, with the cathode and anode both being suitably doped in order to display electronic conductivity.[50] The advantages of monolithic fuel cells include chemical, mechanical and thermal compatibility of all components, which overcomes some of the problems faced in solid oxide fuel cell development.

1.3.2 Fluorite oxide ion conductors

Substituted ZrO_2, δ-Bi_2O_3 and CeO_2 are the most widely studied fluorite type oxide ion conductors. Although other oxides such as HfO_2 and ThO_2 also have the fluorite structure, lower oxide ion conductivities, poor thermal stability and in the case of ThO_2 radioactivity, have limited their applications as oxide ion conductors.[51]

Above 2370 °C, the cubic ZrO_2 polymorph, with a fluorite structure, is stable. Cubic zirconia may be stabilised to room temperature with small amounts of metals. In particular, high conductivities may be achieved when stabilised with small amounts of trivalent cations such as Yb^{3+}, Sc^{3+} and Y^{3+} (Table 1.4), which creates oxygen deficiency.[51] Although $Zr_{0.90}Sc_{0.10}O_{1.95}$ has a higher conductivity than $Zr_{0.90}Y_{0.10}O_{1.95}$, the high cost of Sc_2O_3 prevents use in solid oxide fuel cells.

Table 1.4: Oxide ion conductivity of some stabilised zirconias. [51]

Composition	Conductivity at 800 °C (S cm^{-1})
$Zr_{0.90}Y_{0.10}O_{1.95}$	4.2×10^{-2}
$Zr_{0.90}Sc_{0.10}O_{1.95}$	8.9×10^{-2}
$Zr_{0.90}Yb_{0.10}O_{1.95}$	7.9×10^{-2}

Ternary ZrO_2 based phases also exist, with the conductivity typically lying between the conductivity of the two binary ZrO_2 systems.[51] Examples include the Y_2O_3 – Sc_2O_3 – ZrO_2 and Yb_2O_3-Y_2O_3-ZrO_2 compounds, with high conductivity found in the system containing 3 mol% Sc_2O_3 and 3-7mol% Y_2O_3.[51] However, it was noted that ternary phases could only be formed when both members can stabilise cubic ZrO_2. [51] Mixed conductors have also been created when stabilised ZrO_2 is doped with various transition metals such as titanium and manganese.[51]

δ-Bi_2O_3 possesses the fluorite structure, but contains 25% oxygen vacancies, which are statistically distributed, which results in δ-Bi_2O_3 displaying one of the highest oxide ion conductivities known to date (2.3 S cm^{-1} at 800 °C).[11] However, δ-Bi_2O_3 is only stable in the region between 739 °C – 804 °C (where it melts), but has been successfully stabilised to room temperature through small additions of Er^{3+} and Y^{3+}.[52] In comparison to yttria stabilised zirconia, which has an ionic conductivity of 5×10^{-4} S cm^{-1} at 500 °C, $(Bi_2O_3)_{0.75}(Y_2O_3)_{0.25}$ has a conductivity of 1.3×10^{-2} S cm^{-1} at 500 °C, *i.e.* two orders of magnitude greater than yttria stabilised zirconia (YSZ).[53,54] $Bi_{0.8}Er_{0.2}O_{1.5}$ also exhibits a similar high ionic conductivity of 2.1×10^{-2} at 500 °C.[55] Greaves *et al.* have found enhanced ionic conductivities (and also low activation energies) when Bi_2O_3 is co-doped with rare earths (RE = La, Nd, Eu, and Er) and rhenium in the ratio 12.5 Bi_2O_3: 1.5 RE_2O_3 : 1 NH_4ReO_4.[54] The highest conductivity, of 1.1×10^{-3} S cm^{-1} at 300 °C was achieved for the composition $Bi_{12.5}La_{1.5}ReO_{24.5}$, which retained a fluorite structure at room temperature.[54] The ease of reduction of Bi^{3+} to Bi^0 is problematic and may result in the development of electronic conductivity.

Bismuth oxides substituted with a wide variety of cations such as Mo^{6+}, Nb^{5+}, Ta^{5+}, W^{6+} and V^{5+}, typically form fluorite related superstructures, which are crystallographically complex, but also retain high oxide ion conductivities.[55-60] At lower levels of substitution, a large increase in ionic conductivity often coincides with a phase transformation to a δ-Bi_2O_3 analogue, but this is not observed with higher levels of substitution. For example, $Bi_7WO_{13.5}$ has a fluorite related structure at ambient conditions and no phase transition occurs at higher temperature, therefore a linear increase in conductivity with temperature was observed, with the magnitude of conductivity being higher than YSZ.[56] Bismuth rhenium oxides also show good oxide ion conductivities at low temperature.[57] Bi_9ReO_{17} undergoes an order-disorder transformation to the fluorite structure at 1000 °C and this form could be quenched to room temperature and the quenched form had a conductivity approximately one order of magnitude higher than the ordered monoclinic phase at 400 °C (9.1×10^{-4} S cm^{-1} compared to 2.9×10^{-5} S cm^{-1}).[57]

Although CeO_2 also possesses the fluorite structure, oxide vacancies are not present, which results in a low conductivity. However, doping CeO_2 with aliovalent cations increases oxide ion conductivity, by the introduction of oxide vacancies. Gadolinia stabilised ceria has a high oxide ion conductivity (0.01 S cm^{-1} at 500 °C for $Ce_{0.9}Gd_{0.1}O_{1.95}$) and is a potential candidate for SOFC electrolytes.[58] Samaria stabilised ceria also displays a high oxide ion conductivity. Both Sm^{3+} and Gd^{3+} have an ionic radius close to that of Ce^{4+}, hence are suitable dopants for CeO_2 as the mismatch in size between these ions is low. It has been proposed that in order to maintain a high conductivity, there is a critical dopant radius, which prevents vacancy-dopant associations. Calculations have shown that radioactive Pm^{3+} has the ideal ionic radius for CeO_2. To overcome this problem, a 1:1 ratio of Sm^{3+} and Nd^{3+} is used, as the average radius of these ions is close to that of Pm^{3+}.[59] This resulted in the composition $Sm_{0.075}Nd_{0.075}Ce_{0.85}O_{2-x}$ having a conductivity of 0.014 S cm^{-1} at 550 °C, which is higher than $Ce_{0.9}Gd_{0.1}O_{1.95}$ at 550 °C.[59]

The ease of reduction of Ce^{4+} to Ce^{3+} has resulted in cerium containing compounds having many catalytic applications, but this same feature results in an increase in the electronic conductivity at the expense of oxide ion conductivity and may also be accompanied by undesirable changes in structure types. However, the presence of electronic conductivity may offer the potential for the development of mixed conductors.

1.3.3 Pyrochlore-fluorite order-disorder transformations

Five methods have been used to induce pyrochlore-fluorite transformations. These transformations can be described as 'order-disorder' transitions, due to the disordering of both cation and anion sublattices.

This structural distortion in pyrochlores is particularly relevant to the design of oxide ion conductors as several studies have shown that the cation and anion sublattices disorder independently, with the oxygen sites disordering first. The onset of cation disordering is not seen until significant disordering of the anion sublattice has taken place.[37] Oxygen disorder in pyrochlores occurs when occupancy of the vacant site (8b) occurs, which is often accompanied by the decrease in occupancy of the 48f oxygen site. Cation disorder is usually caused by the formation of anti-site defects, *i.e.* the occupation of the A cation site by the B cation and *vice versa*.

1.3.3.1 Chemical doping

The effect of chemical doping in pyrochlores has already been discussed in section 1.3.1. However, some order-disorder studies have been carried out and no conductivity data has been reported. Sometimes only a partial order-disorder transformation, *i.e.* pyrochlore to 'defect pyrochlore' is observed, whereby the cation sites have partial anti-site disorder and the O(3) site is partially occupied.[60, 61]

1.3.3.2 High temperature transitions

$Gd_2Zr_2O_7$, $Sm_2Zr_2O_7$ and $Nd_2Zr_2O_7$ pyrochlores undergo a transition to the fluorite structure at high temperatures at 1530 °C, 2000 °C and 2300 °C respectively.[62] $Gd_2Hf_2O_7$ also transforms from a pyrochlore to fluorite at 2400 °C.[63] However, the high transition temperature prevents the fluorite derivatives having applications as oxide ion conductors.

1.3.3.3 Mechanochemical milling

Mechanochemical milling is primarily a synthetic technique. Whilst enabling intimate mixing of reagents, thereby enhancing diffusion, grinding in a ball mill has the effect of increasing pressure, possibly to as high as 6 GPa, whilst temperatures may also reach 100 °C.[34] Often the grinding causes the crystal structure of the constituent oxides to break down and become amorphous. Mechanochemical milling has recently been used in the synthesis of several pyrochlore systems by Fuentes *et al.,* namely: $A_2Ti_2O_7$, (where A = Y^{3+}, Gd^{3+} and Dy^{3+}), $Gd_2(Ti_{1-y}Zr_y)_2O_7$, $Gd_2(Sn_{1-y}Zr_y)_2O_7$ and

$Dy_2(Ti_{1-y}Zr_y)_2O_7$.[34, 64-66] It appears that in several cases the 'as milled' samples possess the fluorite structure.[69, 71] However, structural characterisation of these phases only used X-ray diffraction and no local structure probes, therefore whether the samples are pyrochlores or fluorites is still unclear. Thermal treatment is required to produce more crystalline samples and in some cases a transformation from fluorite to pyrochlore is observed, whilst in other cases the fluorite or pyrochore structure is retained but with improved crystallinity.[35, 69, 70] For example, $Gd_2(Ti_{0.1}Zr_{0.9})_2O_7$ remains a fluorite even after firing at 1200 °C.[67] As the titanium content is increased, the transformation from fluorite to pyrochlore occurs at lower temperatures.[67] $Gd_2(Ti_{0.35}Zr_{0.65})_2O_7$ transforms to a pyrochlore after firing at 1200 °C, whilst $Gd_2(Ti_{0.65}Zr_{0.35})_2O_7$ adopts the pyrochlore structure at 1000 °C.[67] $Dy_2Zr_{2-x}Ti_xO_7$ compounds were synthesised by a combination of mechanochemical milling and thermal treatment and their conductivity was discussed in section 1.3.1. [34]

1.3.3.4 High pressure

Relatively little research has been carried out on the high pressure transformations of pyrochlores. In several cases the pyrochlore – fluorite transition does not occur, but rather pyrochlore transforms to an alternative crystal structure or to an amorphous material. However, Zhang *et al.* have shown a pyrochlore-fluorite transition in $Y_2Ti_2O_7$ but this required a high pressure of 60 GPa. [68] XRD showed that the fluorite structure was retained after returning to ambient conditions. The transformation in $Gd_2Ti_2O_7$ was also explored by Zhang. [68] At 51 GPa, a distorted pyrochlore is present, along with an amorphous phase, with no evidence of a fluorite phase. [68] Another pyrochlore which displays an order-disorder transition to a fluorite at high pressure is $Cd_2Nb_2O_7$. [69] The pyrochlore-fluorite transition is reported to occur around 12-15 GPa and on applying further pressure, a high pressure phase is obtained at 27.7 GPa, which is thought to possess a monoclinic or orthorhombic structure. Cheetham *et al.* have studied the high pressure transformations of $Tb_2Ti_2O_7$, Tb_2TiSnO_7 and $Tb_2Sn_2O_7$, but no transformation to fluorite was observed.[70] Instead, a high pressure phase, which is thought to be monoclinic, was observed above pressures of 40 GPa, 44 GPa and 51 GPa, for $Tb_2Sn_2O_7$, Tb_2TiSnO_7 and $Tb_2Ti_2O_7$ respectively. $Sm_2Zr_2O_7$ has also been shown to undergo a pressure induced transition, but to a monoclinic structure, rather than the fluorite structure.[71]

1.3.3.5 Ion irradiation

Particular attention has been paid to the affects of ion irradiation of pyrochlores, due to their potential application as host materials for nuclear waste. Of all the pyrochlores, the zirconates have been shown to be radiation resistant.[72] Ion irradiation involves bombarding samples with high energy ions such as Ar^+, Xe^+, and Ne^+. This creates defects in the sample under investigation. Ewing used electron diffraction to show the pyrochlore to fluorite transition. [72] In the $Gd_2Zr_{2-x}Ti_xO_7$ system, different behaviour under ion irradiation was observed for the zirconium rich and titanium rich phases. The zirconium rich phase forms a fluorite structure which is stable to high levels of irradiation damage, which is thought to be due to the similar size of the Gd^{3+} and Zr^{4+}. The titanium rich compounds also form a fluorite phase but this transforms to an amorphous state at high irradiation levels. [72] The disappearance of certain reflections, in the electron diffraction patterns, which are mainly due to the degree of anion ordering, has been attributed to formation of a disordered pyrochlore. [72]

Ewing has carried out a study of the ion-irradiation of $A_2Ti_2O_7$ (A = Sm, Lu and Y) and $Gd_2Ti_2O_7$ pyrochlores.[73] A pyrochlore – fluorite – amorphous transition is also observed for $Lu_2Ti_2O_7$ and $Er_2Ti_2O_7$.[73] $Cd_2Nb_2O_7$ shows a transition to fluorite when irradiated with Xe^{2+} and Ne^+ ions. [74] In the case of Ne^+ ions, the transformation to fluorite occurs before amorphisation. [74]

1.4 Other structural families of oxide ion conductors

1.4.1 $La_2Mo_2O_9$ ('LAMOX') related

The LAMOX family of oxide ion conductors is based on the parent compound $La_2Mo_2O_9$, which is structurally related to β-$SnWO_4$. The room temperature (α-$La_2Mo_2O_9$) polymorph undergoes a transition at 580 °C, to a high temperature polymorph (β-$La_2Mo_2O_9$) which exhibits a greater ionic conductivity (4.6×10^{-5} S cm^{-1} for α-$La_2Mo_2O_9$ at 500 °C and 8.0×10^{-2} S cm^{-1} for β-$La_2Mo_2O_9$ at 800 °C), of the same magnitude as YSZ.[75] Lacorre *et al.* have determined the crystal structure of β-$La_2Mo_2O_9$ by powder neutron diffraction. Of the three oxygen sites present, two are partially occupied and all have large atomic displacement parameters, both of which are suggestive of oxide ion conductivity. [76] In α–$La_2Mo_2O_9$, molybdenum is present with oxygen coordination numbers of four, five and six.[18] This allows the possibility of molybdenum changing coordination number and they may be viewed as 'virtual' oxide

vacancies, which offer a pathway for oxide ion migration.[18] Analysis of the local structure of both the α– and β-$La_2Mo_2O_9$ phases by pair distribution function (PDF) method has shown that the local structure of both polymorphs are identical, which confirmed the relationship between the α- and β-$La_2Mo_2O_9$ polymorphs outlined by Evans *et al*..[18,77]

The effect of doping the cation sites with different metals has been explored, and has been successful with cations such as Bi^{3+}, V^{5+} and W^{6+}. Up to 15% Bi^{3+} may be incorporated onto the lanthanum site and this shows a high oxide ion conductivity (1.33×10^{-4} S cm^{-1} at 500 °C). [78] Doping the lanthanum site with barium or gadolinium also increases ionic conductivity. [79]

It has been proposed that in $Sn_2W_2O_8$ (*i.e.* $2 \times SnWO_4$), two lone pairs (one from each Sn^{2+}) take up two sites occupied by oxygen in $La_2Mo_2O_9$. Therefore in the $La_2Mo_2O_9$ structure, one lone pair site is occupied by oxygen, whilst the other is vacant, due to La^{3+} having no lone pairs. Hence this allows oxide ion conduction to take place. It is likely that new anionic conductors may be created by replacing a lone pair cation with one of the same size but higher oxidation state, but without a lone pair. [75] This lone pair design hypothesis was first published in 2000, but we are still lacking evidence that it does work in predicting new ionic conductors.

1.4.2 Perovskites and Brownmillerites

Perovskites have a general formula ABO_3, however oxide ion vacancies are not inherent to their structure. The B cation is surrounded by six oxygen atoms in octahedral coordination. The octahedra are corner sharing and eight octahedra surround the A cation, with the A cation being coordinated to 12 oxygens. Appropriate aliovalent doping of the A and B cation sites introduces oxygen vacancies into the perovskite structure. For example, $La_{0.9}Sr_{0.1}Ga_{0.8}Mg_{0.2}O_{2.65}$ has a high conductivity of 0.1 S cm^{-1} at 700 °C.[53] Another example is the relatively low conductivity displayed by $NdAlO_3$ (1×10^{-5} S cm^{-1}at 700 °C), but doping both cation sites causes a increase in conductivity of four orders of magnitude in $Nd_{0.9}Ca_{0.1}Al_{0.9}Cu_{0.1}O_{2.9}$, which displays a conductivity of 0.1 S cm^{-1} at 700 °C.[53] Substitution of Ti^{4+} by Ca^{2+} in $BaTi_{1-x}Ca_xO_{3-x}$ has also shown a higher ionic conductivity for the calcium doped compounds than the parent compound at moderate temperatures.[80]

Brownmillerite phases are closely related to the perovskite structure, but are oxygen deficient and have the general formula $A_2B'B''O_5$. Relative to perovskite, one sixth

(16.7%) of the oxygen sites are vacant. At high temperatures $Ba_2In_2O_5$ shows a sharp increase in conductivity around 870-960 °C and displays a high conductivity of 0.1 S cm^{-1} at 950 °C.[53] The increase in conductivity at approximately 900 °C is attributed to an order-disorder transition on the oxygen sublattice. $BaZr_{0.5}In_{0.5}O_{2.75}$ has a conductivity of 1×10^{-2} S cm^{-1} at 700 °C, which is higher than that of $Ba_2In_2O_5$ at lower temperatures.[53]

1.4.3 Aurivillius phases

One of the original Aurivillius phases is Bi_2MoO_6, which consists of octahedral corner sharing $[MoO_4]^{2-}$ perovskite layers sandwiched between square based pyramidal $[Bi_2O_2]^{2+}$ sheets. By substituting Mo^{6+} with aliovalent cations, the ionic conductivity may be increased. [81]

$Bi_2VO_{5.5}$ is an intrinsic ion conductor and is the parent BIMEVOX structure.[82] It is the tetragonal polymorph (γ) of $Bi_2VO_{5.5}$ which exhibits high (0.1 S cm^{-1} at 600 °C) oxide conductivities. However this is only stable at temperatures above 580 °C. [82] The oxide vacancies are accommodated in the perovskite layer and the ability of V^{5+} to be coordinated by different numbers of oxygens is one of they key factors influencing oxide ion conductivity.[81] The oxygen vacancies are distributed statistically and the perovskite-type layer can be viewed as an array of both octahedral and tetrahedral moieties.

Substitution of vanadium with other metals such as copper and zinc stabilises the phase down to room temperature; however, like several other oxide conductors, the materials are prone to reduction (which can cause electronic conductivity) and phase segregation. Due to the layered structure of $Bi_2VO_{5.5}$, the conductivity measured in single crystals depends on the direction measured (high conductivities are obtained parallel to the bismuth plane, but conductivities are several orders of magnitude lower when measured perpendicular to the bismuth plane).[82] High conductivities of 5×10^{-2} S cm^{-1} and 7×10^{-2} S cm^{-1} at 500 °C are exhibited by $Bi_2V_{0.9}Cu_{0.1}O_{5.35}$ and $Bi_2V_{0.9}Co_{0.1}O_{5.35}$ respectively.[82] γ–$Bi_2V_{0.85}Ti_{0.15}O_{5.425}$ also has a high conductivity of 4×10^{-4} S cm^{-1} at 500 °C. [11]

1.4.4 Apatite type phases

Apatites have the general formula $A_{10}(MO_4)_6O_{2+x}$, where A is a trivalent cation and M is a tetravalent cation.[83] The structure may be described as isolated MO_4 tetrahedra,

with channels of cations and oxide ions parallel to the *c* direction.[83] Early studies found that the structure adopted depends on the size of the trivalent cation in the case of M = Ge.[84] Smaller rare earths form triclinic structures but with appropriate doping the hexagonal structure may be adopted.[85] Apatites with hexagonal symmetry have the highest oxide ion conductivity, with the highest conductivities being found in those apatites with oxygen excess, for example, $La_{9.67}(SiO_4)_6O_{2.5}$ has a conductivity of 1.3×10^{-3} S cm^{-1} at 500 °C.[83]

1.5 Applications of oxide ion conductors

Solid oxide fuel cells (SOFCs), oxygen sensors and oxygen pumps are the three main applications of oxide ion conductors. Research into oxide ion conductors has been largely driven by environmental factors, such as the search for alternative energy sources, higher fuel efficiency, higher power outputs and lower exhaust emissions.

Fuel cells were first discovered by William Grove in 1839.[2] In 1899 Nernst discovered 15% yttria stabilised zirconia and patented it to be used as a filament for a lamp.[2] Today, yttria stabilised zirconia is the electrolyte of choice in SOFCs, although with a lower yttrium content than that used by Nernst. There are five main types of fuel cell: solid oxide, polymer electrolyte membrane, phosphoric acid, alkaline and molten carbonate. Of these, the solid oxide fuel cell utilises various ceramic oxide ion conductors and provides a wide range of operating temperatures (500-1000 °C) depending on the electrolyte to be used and the application of the fuel cell.

1.5.1 Solid oxide fuel cells

A SOFC consists of a cathode, electrolyte and anode. 8 mol% yttria stabilised zirconia (YSZ) is the main electrolyte material currently used in SOFCs, although gadolinium doped ceria is also used.[86] The cathodes and anodes must typically be porous, electronically conducting, have similar thermal expansion to the electrolyte and finally, be stable in an oxidising atmosphere (cathode) or reducing atmosphere (anode).[2] Perovskite materials $LaMnO_3$ and $LaCoO_3$ are some of the oxides used in cathode materials and their electrical conductivities may be improved by doping the lanthanum site with strontium.[2] However, above 1200 °C, a reaction between the cathode material and electrolyte may occur, forming layers of impurities such as $La_2Zr_2O_7$ if the electrolyte is ZrO_2 based.[2] This is detrimental to the operation of the fuel cell as certain impurities (*e.g.* $La_2Zr_2O_7$) are insulating. $Bi_{2-x}M_xRu_2O_{7-d}$ pyrochlores (with M = Pb^{2+} or

Sr^{2+}) have been investigated as potential cathode materials, due to the ability of ruthenium to reduce oxygen.[87]

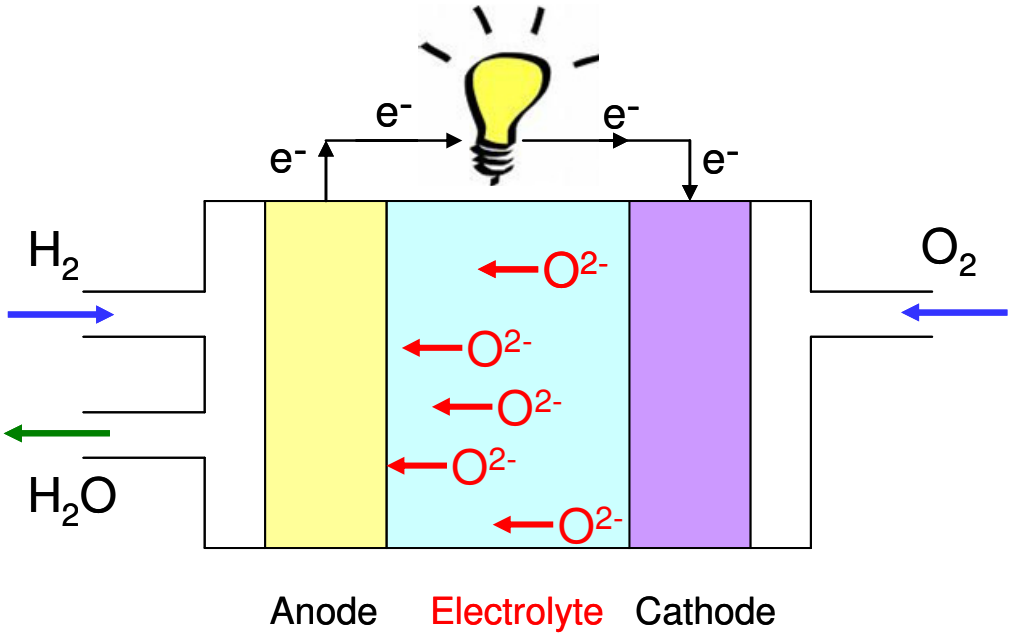

Figure 1.5: Diagram of a typical solid oxide fuel cell.

Nickel - YSZ composites are commonly used as anodes, but present problems, as the deposition of carbon and sulfur poisons the anodes.[2] Nickel is used in the anode as it is an electronic conductor, whilst YSZ is used for its anionic conducting properties. Mixing the nickel with YSZ allows the electrode to maintain its porosity. Metals such as copper and iridium have been explored as alternative anodes.[88]

SOFCs operate by a series of simple oxidation and reduction processes (Figure 1.5). Oxide ions, created in reduction reactions at the cathode, are then transported through the solid oxide electrolyte, to the anode, where they oxidise hydrogen (or other suitable hydrocarbon fuel). The electrons, generated at the anode, are transported to the cathode (through an electrical circuit), where they provide the required number of electrons to reduce oxygen gas.

The reaction at the anode is described by Equation 1.4:

$$H_{2\,(g)} + O^{2-} \rightarrow H_2O_{\,(g)} + 2e^- \qquad (1.4)$$

The reaction at the cathode may be described by Equation 1.5:

$$0.5\,O_{2\,(g)} + 2e^- \rightarrow O^{2-} \qquad (1.5)$$

Therefore the overall reaction is described in Equation 1.6:

$$H_{2(g)} + 0.5O_{2(g)} \rightarrow H_2O_{(g)} \quad (1.6)$$

Alternatively, fuels other than hydrogen, such as methane, propane, butane and even methanol may be used, which are stored more easily than hydrogen. However, these fuels must be reformed into synthesis gas (a mixture of H_2 and CO) and this may occur externally or be catalysed by the anode. Park *et al.* have shown that higher hydrocarbons may be oxidised in solid oxide fuel cells and gas chromatography has shown that the hydrocarbons studied are fully oxidised to H_2O and CO_2.[88] They used copper in the anode, which appears to be more favourable than nickel, as unlike nickel, no graphite formation or carbon deposition is observed.[88]

Heat is also generated in this oxidation process, and it is possible that this may be used to drive an external turbine, thus allowing more electricity to be generated. [2]

1.5.2 Oxygen sensors

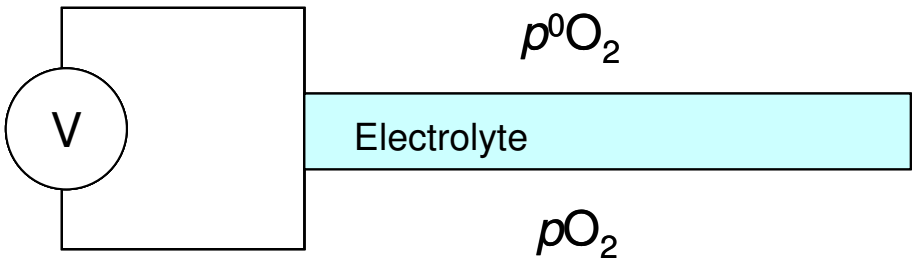

Figure 1.6: Diagram of a typical oxygen sensor. [20]

Figure 1.6 shows a simple diagram of an oxygen sensor. Solid oxide oxygen sensors are important in automobile exhaust systems, where they are used to determine the air to fuel ratio.[3] The difference in partial pressures of oxygen of the standard (p^0O_2) and an unknown (pO_2) cause a voltage to be generated, which is proportional to the difference in oxygen free energies.[20] The concentration of oxygen in the system is proportional to the peak current of the device.[3] However for certain applications, lower operating temperatures are required which prevents the use of oxides such as YSZ, therefore other oxygen sensors are required.[3]

1.5.3 Oxygen pumps

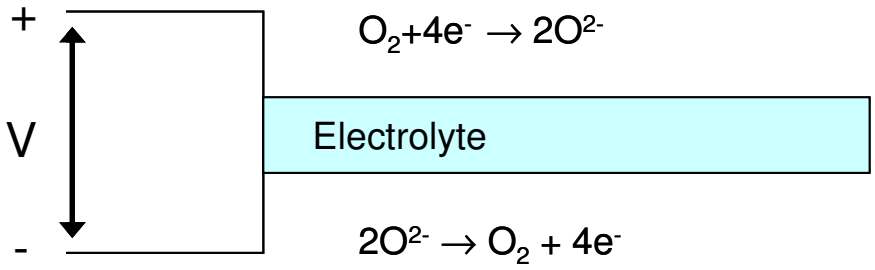

Figure 1.7: Diagram of an oxygen pump. [20]

Figure 1.7 shows a simple diagram of an oxygen pump. In an ionic transport membrane or an oxygen pump, high purity and high pressure oxygen is separated from air (a low pressure oxygen source), through the use of an electrolyte containing both an ionic component and an electronically conducting component.[89] Ceria based electrolytes are commonly used with a perovskite based electronic conductor.[89] By applying a voltage, oxygen is driven across the oxide ion conducting membrane as oxide ions.[20]

1.6 References

1. M. A. Subramanian, G. Aravamundan and G. V. S. Rao, *Prog. Solid St. Chem*, 1983, **15**, 55-143.
2. R. M. Ormerod, *Chem. Soc. Rev.*, 2003, **32**, 17-28.
3. R. Ramamoorthy, P. K. Dutta and S. A. Akbar, *J. Mater. Sci.*, 2003, **38**, 4271 - 4282.
4. K. E. Sickafus, R. W. Grimes, J. A. Valdez, A. Cleave, M. Tang, M. Ishimaru, S. M. Corish, C. R. Stanek and B. P. Uberuaga, *Nature Materials*, 2007, **6**, 217-223.
5. K. E. Sickafus, L. Minervini, R. W. Grimes, J. A. Valdez, M. Ishimaru, F. Li, K. J. McClellan and T. Hartmann, *Science*, 2000, **289**, 748-751.
6. T. Birchall and A. W. Sleight, *J. Solid State Chem.*, 1975, **13**, 118-130.
7. I. Radosavljevic, J.S.O. Evans and A. W. Sleight, *J. Solid State Chem.*, 1998, **136**, 63-66.
8. A. L. Hector and S. B. Wiggin, *J. Solid State Chem.*, 2004, **177**, 139-145.
9. R. H. Jones and K. S. Knight, *J. Chem. Soc., Dalton Trans.*, 1997, 2551-2555.
10. M. Avdeev, M. K. Haas, J. D. Jorgenson and R. J. Cava, *J. Solid State Chem.*, 2002, **169**, 24-34.
11. J. B. Goodenough, *Annu. Rev. Mater. Res.*, 2003, **33**, 91-128.
12. M. Mogensen, D. Lybye, N. Bonanos, R. Hendriksen and F. W. Poulsen, *Solid State Ionics*, 2004, **174**, 279-286.

13. J. A. Kilner, *Solid State Ionics*, 2000, **129**, 13-23.
14. *Solid State Electrochemistry*, Cambridge University Press, Cambridge, 1995.
15. E. Kendrick, M. S. Islam and P. R. Slater, *Chem. Commun.*, 2008, 715-717.
16. X. Kuang, M. A. Green, H. Niu, P. Zajdel, C. Dickinson, J. B. Claridge, L. Jantsky and M. J. Rosseinsky, *Nat. Mater.*, 2008, **7**, 498-504.
17. E. Kendrick, J. Kendrick, K. S. Knight, M. S. Islam and P. R. Slater, *Nat. Mater.*, 2007, **6**, 871-875.
18. I. R. Evans, J. S. O. Evans and J. A. K. Howard, *Chem. Mater.*, 2005, **17**, 4074 - 4077.
19. P. J. Wilde and C. R. A. Catlow, *Solid State Ionics*, 1998, **112**, 173-183.
20. J. B. Goodenough, *Solid State Ionics*, 1997, **94**, 17-25.
21. J. C. Boivin and G. Mairesse, *Chem. Mater.*, 1998, **10**, 2870-2888.
22. V. V. Kharton, F. M. B. Marques and A. Atkinson, *Solid State Ionics*, 2004, **174**, 135-149.
23. J. E. H. Sansom and P. R. Slater, *Solid State Ionics*, 2004, **167**, 23-27.
24. A. V. Shlyakhtina, P. Fedtke, A. Busch, I. V. Kolbanev, T. Barfels, M. Wienecke, A. E. Sokolov, V. A. Ulianov, V. A. Trounov and L. G. Shcherbakova, *Solid State Ionics*, 2008, **179**, 1004-1008.
25. A. V. Shlyakhtina, A. E. Sokolov, V. A. Ul'yanov, V. A. Trunov, M. V. Boguslavskii, A. V. Levchenko and L. G. Shcherbakova, *Crystallography Reports*, 2009, **54**, 25-30.
26. S. A. Kramers and H. L. Tuller, *Solid State Ionics*, 1995, **82**, 15-23.
27. S. Kramer, M. Spears and H. L. Tuller, *Solid State Ionics*, 1994, **72**, 59-66.
28. T. H. Yu and H. L. Tuller, *Solid State Ionics*, 1996, **86-8**, 177-182.
29. B. J. Wuensch, K. W. Eberman, C. Heremans, E. M. Ku, P. Onnerud, E. M. E. Yeo, S. M. Haile, J. K. Stalick and J. D. Jorgensen, *Solid State Ionics*, 2000, **129**, 111-133.
30. K. V. G. Kutty, C. K. Matthews, T. N. Rao and U. V. Varadaraju, *Solid State Ionics*, 1995, **80**, 99 - 110.
31. D. A. Belov, A. V. Shlyakhtina, S. Y. Stefanovich, I. V. Kolbanev, Y. A. Belousov, O. K. Karyagina and L. G. Shcherbakova, *Mater. Res. Bul.*, 2009, **44**, 1613-1620.
32. X. L. Xia, S. A. Gao, Z. G. Liu and J. H. Ouyang, *Electrochimica Acta*, 2010, **55**, 5301-5306.
33. C. Heremans, B. J. Wuensch, J. K. Stalick and E. Prince, *J. Solid State Chem.*, 1995, **117**, 108-121.
34. K. J. Moreno, M. A. Guevara-Liceaga, A. F. Fuentes, J. Garcia-Barriocanal, C. Leon and J. Santamaria, *J. Solid State Chem.*, 2006, **179**, 928-934.
35. P. K. Moon and H. L. Tuller, *Solid State Ionics*, 1988, **28**, 470-474.
36. H. Takamura and H. L. Tuller, *Solid State Ionics*, 2000, **134**, 67-73.
37. K. W. Eberman, B. J. Wuensch and J. D. Jorgensen, *Solid State Ionics*, 2002, **148**, 521-526.
38. A. V. Shlyakhtina, A. V. Knotko, M. V. Boguslavskii, S. Y. Stefanovich, I. V. Kolbanev, D. V. Peryshkov and L. G. Shcherbakova, *Inorg. Mater.*, 2005, **41**, 406-411.
39. J. A. Diaz-Guillen, M. R. Diaz-Guillen, J. M. Almanza, A. F. Fuentes, J. Santamaría and C. León, *J. Phys.: Condens. Matter*, 2007, **19**, 356212 (356211-356211).
40. H. Yamamura, H. Nishino, K. Kakinuma and K. Nomura, *Solid State Ionics*, 2003, **158**, 359-365.
41. Z. G. Liu, J. H. Ouyang, Y. Zhou and X. L. Xia, *Electrochimica Acta*, 2009, **54**, 3968-3971.

42. Z. G. Liu, J. H. Ouyang, K. N. Sun and X. L. Xia, *Journal of Power Sources*, 2010, **195**, 7225-7229.
43. X. L. Xia, J. H. Ouyang and Z. G. Liu, *Journal of the American Ceramic Society*, 2010, **93**, 1074-1080.
44. H. Yamamura, H. Nishino, K. Kakinuma and K. Nomura, *Solid State Ionics*, 2007, **178**, 233-238.
45. A. V. Shlyakhtina, A. V. Knotko, M. V. Boguslavskii, S. Y. Stefanovich, I. V. Kolbanev, L. L. Larina and L. G. Shcherbakova, *Solid State Ionics*, 2007, **178**, 59-66.
46. A. V. Shlyakhtina, A. V. Levchenko, J. C. C. Abrantes, V. Y. Bychkov, V. N. Korchak, V. A. Rassulov, L. L. Larina, O. K. Karyagina and L. G. Shcherbakova, *Mater. Res. Bull.*, 2007, **42**, 742-752.
47. O. Porat, C. Heremans and H. L. Tuller, *Solid State Ionics*, 1997, **94**, 75-83.
48. K. E. J. Eurenius, E. Ahlberg, I. Ahmed, S. G. Eriksson and C. S. Knee, *Solid State Ionics*, 2010, **181**, 148-153.
49. K. E. J. Eurenius, E. Ahlberg and C. S. Knee, *Solid State Ionics*, 2010, **181**, 1258-1263.
50. Y. Liu, R. L. Withers and L. Noren, *J. Solid State Chem.*, 2004, **177**, 4404-4412.
51. V. V. Kharton, E. N. Naumovich and A. A. Vecher, *J. Solid State Electrochem*, 1999, **3**, 61-81.
52. V. V. Kharton, E. N. Naumovich, A. A. Yaremchenko and F. M. B. Marques, *J. Solid State Electrochem.*, 2001, **5**, 160-187.
53. K. R. Kendall, C. Navas, J. K. Thomas and H. C. zurLoye, *Solid State Ionics*, 1995, **82**, 215-223.
54. R. Punn, A. M. Feteira, D. C. Sinclair and C. Greaves, *J. Am. Chem. Soc.*, 2006, **128**, 15386-15387.
55. P. Shuk, H. D. Wiemhofer, U. Guth, W. Gopel and M. Greenblatt, *Solid State Ionics*, 1996, **89**, 179-196.
56. T. Takahashi and H. Iwahara, *J. Appl. Electrochem.*, 1973, **3**, 65-72.
57. M. Thompson, T. Herranz, B. Santos, J. F. Marco, F. J. Berry and C. Greaves, *J. Solid State Chem.*, 2010, **183**, 1985-1991.
58. H. Inaba and H. Tagawa, *Solid State Ionics*, 1996, **83**, 1-16.
59. S. Omar, E. D. Wachsman and J. C. Nino, *Solid State Ionics*, 2008, **178**, 1890-1897.
60. B. P. Mandal, A. Banerji, V. Sathe, S. K. Deb and A. K. Tyagi, *J. Solid State Chem.*, 2007, **180**, 2643-2648.
61. B. P. Mandal, P. S. R. Krishna and A. K. Tyagi, *J. Solid State Chem.*, 2010, **183**, 41-45.
62. D. Michel, M. Perez y Jorba and R. Collongues, *Mater. Res. Bull.*, 1974, **9**, 1457-1468.
63. A. V. Shlyakhtina, J. C. C. Abrantes, L. L. Larina and L. G. Shcherbakova, *Solid State Ionics*, 2005, **176**, 1653-1656.
64. A. F. Fuentes, K. Boulahya, M. Maczka, J. Hanuza and U. Amador, *Solid State Sciences*, 2005, **7**, 343-353.
65. K. J. Moreno, A. F. Fuentes, J. García-Barriocanal, C. León and J. Santamaría, *J. Solid State Chem.*, 2006, **179**, 323-330.
66. K. J. Moreno, A. F. Fuentes, M. Maczka, J. Hanuza and U. Amador, *J. Solid State Chem.*, 2006, **179**, 3805-3813.
67. K. J. Moreno, A. F. Fuentes, M. Maczka, J. Hanuza and U. Amador, *J. Solid State Chem.*, 2006, **179**, 3805-3813.
68. F. X. Zhang, B. Manoun and S. K. Saxena, *Mater. Lett.*, 2006, **60**, 2773-2776.

69. F. X. Zhang, J. Lian, U. Becker, R. C. Ewing, L. M. Wang, L. A. Boatner, J. Z. Hu and S. K. Saxena, *Phys. Rev. B*, 2006, **74**.
70. R. S. Kumar, A. L. Cornelius, M. F. Nicol, K. C. Kam, A. K. Cheetham and J. S. Gardner, *Appl. Phys. Lett.* , 2006, **88**.
71. F. X. Zhang, J. Lian, U. Becker, L. M. Wang, J. Z. Hu, S. Saxena and R. C. Ewing, *Chem. Phys. Lett.*, 2007, **441**, 216-220.
72. J. Lian, L. Wang, J. Chen, K. Sun, R. C. Ewing, J. M. Farmer and L. A. Boatner, *Acta Mater.*, 2003, **51**, 1493-1502.
73. J. Lian, J. Chen, L. M. Wang, R. C. Ewing, J. M. Farmer, L. A. Boatner and K. B. Helean, *Phys. Rev. B*, 2003, **68**, 134107.
74. A. Meldrum, C. W. White, V. Keppens, L. A. Boatner and R. C. Ewing, *Phys. Rev. B*, 2001, **63**, 104109 -
75. P. Lacorre, F. Goutenoire, O. Bohnke, R. Retoux and Y. Laligant, *Nature*, 2000, **404**, 856-858.
76. F. Goutenoire, O. Isnard, R. Retoux and P. Lacorre, *Chem. Mater.*, 2000, **12**, 2575-2580.
77. L. Malavasi, H. Kim, S. J. L. Billinge, T. Proffen, C. Tealdi and G. Flor, *J. Am. Chem. Soc.*, 2007, **129**, 6903-6907.
78. F. Goutenoire, O. Isnard, E. Suard, O. Bohnke, Y. Laligant, R. Retoux and P. Lacorre, *J. Mater. Chem.,*, 2001, **11**, 119-124.
79. S. Basu, P. S. Devi and H. S. Maiti, *Appl. Phys. Lett.*, 2004, **85**, 3486-3488.
80. L. Zhang, O. P. Thakur, A. Feteira, G. M. Keith, A. G. Mould, D. C. Sinclair and A. R. West, *Appl. Phys. Lett.*, 2007, **90**, 142914.
81. J. C. Boivin, *Int. J. Inorg. Mater.*, 2001, **3**, 1261-1266.
82. K. R. Kendall, C. Navas, J. K. Thomas and H. C. zurLoye, *Chem. Mater.*, 1996, **8**, 642-649.
83. E. Kendrick, M. S. Islam and P. R. Slater, *J. Mater. Chem.*, 2007, **17**, 3104-3111.
84. S. Nakayama, T. Kageyama, H. Aono and Y. Sadaoka, *J. Mater. Chem.*, 1995, **5**, 1801-1805.
85. E. Kendrick and P. R. Slater, *Mater. Res. Bull.*, 2008, **43**, 3627-3632.
86. A. J. Feighery and J. T. S. Irvine, *Solid State Ionics*, 1999, **121**, 209-216.
87. G. Ehora, S. Daviero-Minaud, M. C. Steil, L. Gengembre, M. Frere, S. Bellayer and O. Mentre, *Chem. Mater.*, 2008, **20**, 7425-7433.
88. S. D. Park, J. M. Vohs and R. J. Gorte, *Nature*, 2000, **404**, 265-267.
89. P. N. Dyer, R. E. Richards, S. L. Russek and D. M. Taylor, *Solid State Ionics*, 2000, **134**, 21-33.

2 Experimental and Characterisation Methods

2.1 Synthetic methods

Traditional solid state syntheses are governed by diffusion. Intimate grinding of reagents and the use of high temperatures help enhance the reaction. However, repeated grinding and firing is sometimes required before a pure product is obtained. Compared to the synthesis of organic compounds, two main differences exist. [1] Firstly, an organic reaction is usually carried out in a solvent, allowing reagents to become thoroughly mixed and therefore overcoming diffusion problems present in solid state reactions. Secondly, in an organic synthesis functional groups react, requiring rearrangement of only a small number of atoms. However, in a solid state reaction, the atoms often need to be completely rearranged.

Various solution based methods have been developed for the synthesis of oxides which allows thorough mixing of reagents. [2] The sol-gel or Pechini method is one example that has been widely used. Typically, this involves forming citrate complexes of the metals, followed by the addition of ethylene glycol, which undergoes a condensation reaction with the citric acid, to form a polyester. This polyester is then calcined to remove organic components, before firing at high temperatures. [2] 'Gel-aging', a process where the gel is left for a period of time, also helps the diffusion of reagents. [3]

Coprecipitation of an amorphous precursor involves dissolving reagents separately, before mixing together thoroughly and by adjusting the pH, the precursor may be precipitated. [2] Once a dry, solid precursor is obtained, reactions leading to the desired product may be monitored *in-situ* in the diffractometer.

Hydrothermal synthesis was first pioneered in geology, during research into the formation of minerals and it mimics the conditions in the Earth's mantle required for growth of minerals. [4] It takes place in a sealed autoclave at temperatures above the boiling point of the solvent and at increased pressures. [3] Generation of autogeneous pressure, due to the evolution of gases during the reaction creates unique reaction conditions. Sometimes a mineraliser, such as an inorganic salt is required to enhance solubility of particular reagents. [4] There are many advantages over conventional solid state routes, such as the isolation of metastable phases, the enhanced diffusion of

reagents, lower temperatures and shorter reaction times. However, due to reactions occurring in a sealed vessel, it is more difficult to measure reaction progress *in-situ*.[3, 4]

The main difference between the conventional method and solution based, 'chimie douce' methods is that the high temperature routes result in the formation of the most thermodynamically stable products, while the solution routes can yield metastable phases. An example of this is the formation of pyrochlore-type $Bi_2Ti_2O_7$, which is formed using a precursor method, but attempts of this synthesis at high temperatures results in the formation of $Bi_4Ti_3O_{12}$ and $Bi_2Ti_4O_{11}$.[5-7]

Occasionally single crystals may be grown from melt, through slow cooling (*e.g.* 0.05 °C min^{-1}) of the molten product. However, this is not always straightforward in solid state chemistry, due to sample decomposition, incongruent melting and phase transitions.

The work carried out in this thesis has utilised all of the above techniques to differing extents, with the conventional solid state route being the most common.

2.2 Structural characterisation methods

2.2.1 Diffraction

2.2.1.1 Powder X-ray diffraction

X-rays have a similar wavelength (*e.g.* 0.71073 Å MoKα and 1.5418 Å CuKα) to interatomic distances in solids (typically 0.5-2.5 Å), which makes them suitable for the determination of crystal structures of a variety of different compounds. The translation of the unit cell through 3D space creates the long range order required to form X-ray diffraction patterns. When no long range order is present, the compound is amorphous and no Bragg peaks, only broad features, are observed in the diffraction pattern.

The information obtained in the powder pattern is related to four aspects of a crystal structure:

1) Peak positions - contain information on size and shape of unit cell
2) Peak intensities - contain information on the types of atom present and their location within the unit cell
3) Peak width - contains information on size and strain of crystallites

4) Background - contains information on the local structure of the crystal.

In powder diffraction, the sample contains an infinite number of randomly orientated crystallites, which are representative of the sample to be characterised. X-rays are scattered by electrons and constructive interference of the scattered waves results in maxima being observed in the diffraction pattern.

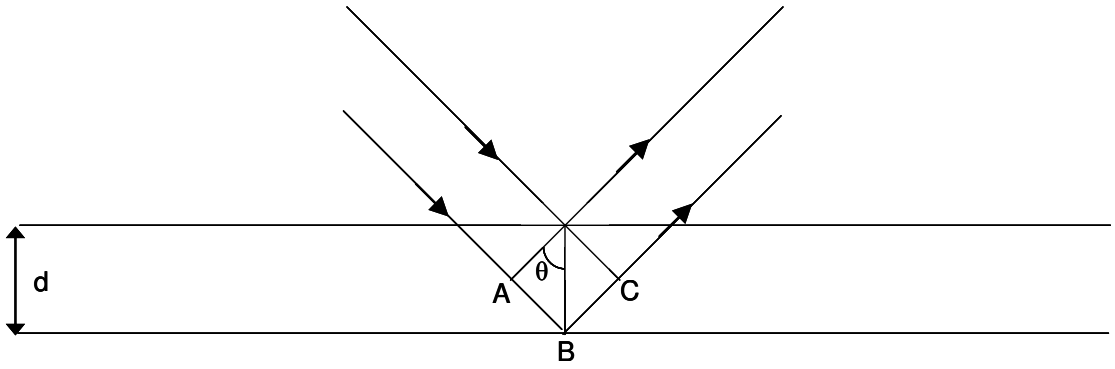

Figure 2.1: Derivation of Bragg's Law. The length ABC=2dsinθ

The superposition of diffracted X-rays which are 'in phase' or 'out of phase' leads to constructive or destructive interference. The basic condition of diffraction is given by Bragg's Law (Equation 2.1) and is illustrated in Figure 2.1.

$$\lambda = 2d_{hkl} \sin\theta \qquad (2.1)$$

Here d_{hkl} is the interplanar spacing, λ is the wavelength of the radiation used and θ is the diffraction angle. From this equation, we can calculate the position, usually expressed as the 2θ angle, of each (*hkl*) reflection in the powder pattern. This then allows the unit cell parameters to be determined via the relationships of d_{hkl} to *a, b, c,* α, β and γ.

The scattering factor, *f*, of an atom is directly related to its number of electrons (Equation 2.2) and decreases exponentially with 2θ. The amplitude of the wave scattered by an atom is given by f_a and f_e represents the scattering power of one electron.

$$f = \frac{f_a}{f_e} \qquad (2.2)$$

The structure factor, F_{hkl} (Equation 2.3), consists of two components. The f_n component is the scattering factor of the atom, *n,* and the summation of F_{hkl} therefore contains information on the types of atom present. The $e^{2\pi i(hx_n+ky_n+lz_n)}$ term contains

information regarding the atomic fractional coordinates (x_n, y_n, z_n) for each atom, n. The summation is carried out over all atoms in the unit cell.

$$F_{hkl} = \sum_{1}^{n} f_n e^{2\pi i(hx_n + ky_n + lz_n)} \quad (2.3)$$

The structure factor, F_{hkl}, is directly related to the intensities (I_{hkl}) observed in a powder pattern by Equation 2.4. Here the constant, k, contains terms such as absorption, reflection multiplicity, temperature factors, the Lorentz factor and the polarisation factor.

$$I_{hkl} = k\left|F_{hkl}\right|^2 \quad (2.4)$$

2.2.1.2 Powder neutron diffraction

Neutrons can also have wavelengths corresponding to interatomic distances, which allows them to be used in diffraction studies of crystalline materials. Unlike X-ray diffraction (where the scattering of the diffracted beam depends on the atomic number and hence is dominated by heavy metals) neutron scattering does not depend on atomic number. Neutron scattering therefore varies independently from not only the location of the atom in the periodic table, but with isotope, as the neutrons are scattered by the nuclei of atoms. Hence neutron diffraction is a suitable probe for determining accurate oxygen positions (or those of other light elements) in heavy metal oxides, due to the more comparable scattering length of oxygen to the metals. Neutrons are more penetrating than X-rays and therefore probe more of the bulk of the sample. Unlike X-rays, there is no intensity fall-off in neutron data at high angle, as scattering length does not depend on 2θ and hence temperature factors may be obtained more accurately. In this project, neutron diffraction has been carried out at the ISIS spallation neutron source, using the General Materials diffractometer (GEM) and the High Resolution Powder Diffractometer (HRPD).

2.2.2 Neutron total scattering

Usually, diffraction methods utilise information contained within the Bragg peaks of a diffraction pattern. This yields information on the average crystal structure. However, in doing this a wealth of information contained in the background, or diffuse scattering, is lost. In total scattering data analysis, both the Bragg peaks and diffuse scattering are included. By including the diffuse scattering in the analysis, deviations from the average structure may be determined and details of the local structure may be obtained.

In a total scattering experiment, extreme care has to be taken to subtract the correct background before data analysis can occur. Certain calibration runs must be done in order to accurately obtain the background, which is required in the normalisation procedure. Typically this involves a data collection on an empty vanadium can sample holder and a vanadium rod of the same dimensions as the sample holders to be used for the experiment.

In this project, total scattering data-sets were obtained for $Nd_2Zr_2O_7$ and $Bi_2Zr_{2-x}Ti_xO_7$ samples. For each $Bi_2Zr_{2-x}Ti_xO_7$ sample, a total of 6 hours of data were collected, corresponding to a current of 140 μAh per hour and a time of flight (TOF) range of 400-24000 μs. For $Nd_2Zr_2O_7$, 3 hours of data were collected.

Various functions are defined for use in a total scattering experiment. Here we will use the nomenclature outlined by Keen.[8] In a total scattering experiment, it is the scattering intensity which is measured, allowing the total scattering structure function, *F(Q)*, to be obtained (Equation 2.5).[9] The average number density is given by ρ_0 (which is the number of atoms in the unit cell divided by the unit cell volume). Q is the magnitude of the diffraction vector, r is the distance between a pair of atoms and $G(r)$ is the total radial distribution function.

$$F(Q) = \rho_0 \int_0^\infty 4\pi r^2 G(r) \frac{\sin Qr}{Qr} dr \qquad (2.5)$$

A normalised total scattering structure function, *S(Q)* can also be defined, (see Equation 2.6).[10] $4\pi \sum_{i=1}^{n} (c_i \bar{b}_i)^2$ is the total scattering cross section of the material, where c_i is the concentration of atom type i and $\bar{b}_i$ is the coherent neutron scattering length of atom type i. Here n represents the number of chemically distinct species.

$$S(Q)-1=\frac{F(Q)}{\sum_{i=1}^{n}(c_i\bar{b}_i)^2} \tag{2.6}$$

F(Q) is related to the total radial distribution function, *G(r)* (Equation 2.7), by a Fourier transform.[10] The total radial distribution function, *G(r)* (Equation 2.7), can be described as the probability of finding an atom at a distance *r* from another atom. An alternative expression for *G(r)* is given in Equation 2.8. g_{ij} represents the partial radial distribution functions.

$$G(r)=\frac{1}{(2\pi)^3\rho_0}\int_0^{\infty}4\pi Q^2F(Q)\frac{\sin Qr}{Qr}dQ \tag{2.7}$$

$$G(r)=\sum_{i,j=1}^{n}c_ic_j\bar{b}_i\bar{b}_j(g_{ij}(r)-1) \tag{2.8}$$

G(r) may also be broken down into individual contributions from pairs of atoms, *i.e.* the partial radial distribution functions, $g_{ij}(r)$ which are defined in Equation 2.9.[8] Here n_{ij} is the number of particles of type *j* and ρ_j is the average number density (ρ_0) multiplied by the concentration (c_j) of atom *j*. Atom type *j* is separated from atom type *i* at distances of *r* and $r + \Delta r$.[8]

$$g_{ij}(r)=\frac{n_{ij}(r)}{4\pi r^2dr\rho_j} \tag{2.9}$$

G(r) can also be described in terms of a total correlation function, *T(r)* as shown in Equation 2.10.

$$T(r)=4\pi r\rho_0\left[G(r)+\left(\sum_{i=1}^{n}c_i\bar{b}_i\right)^2\right] \tag{2.10}$$

Both the experimental *F(Q)* and *G(r)* are required for data analysis and are compared to the calculated *F(Q)* and *G(r)* during refinement of the structural model using a reverse Monte Carlo based computer program, RMCProfile.[10]

2.3 Instrumentation

2.3.1 Laboratory powder X-ray diffractometers

2.3.1.1 Siemens d5000

A Siemens d5000 diffractometer with CuKα_1 and CuKα_2 (1.5418 Å) radiation in flat-plate reflection geometry, operating at 40 kV and 40 mA, was used for preliminary characterisation. X-rays pass through both Soller slits and divergence slits (either fixed 1° or variable v6 or v20 slits), before reaching the sample. Diffracted X-rays then pass through a second set of divergence slits before reaching a detector (either the energy sensitive Sol-X detector or a scintillation detector). The energy sensitive detector selects the range of energies detected, hence eliminates problems due to the fluorescence of metals such as iron.

Samples for the d5000 diffractometer were prepared in two ways. In each case the sample was ground in a pestle and mortar, before using one of two sample holders. Bulk sample holders were used when the compound to be characterised could be pressed into bulk sample holders (without falling out) and the surface was made smooth with a glass microscope slide. Some of the samples did not stay in bulk sample holders; therefore an amorphous glass slide was smeared with a thin layer of Vaseline, before sieving the ground sample onto the slide using a 100 mesh sieve.

2.3.1.2 Bruker d8 Advance diffractometers

Two Bruker d8 Advance diffractometers have been used in this thesis, which have been assigned locally as the ‘d8’ and the ‘d9’.

A Bruker d8 diffractometer operating in Bragg-Brentano geometry at 40 kV and 40 mA using CuKα_1 radiation (1.5406 Å), equipped with a Ge (111) monochromator, was used for some characterisation. It was also equipped with an anti-scattering tube (preventing air scattering and divergence of the X-ray beam), fixed Soller slits and fixed 1° divergence slits. The diffracted X-ray beam was detected by the Vantec linear position sensitive detector, which had a minimum step size of 0.0085°.

An Anton Paar HTK1200 furnace was used for *in-situ* variable temperature studies. This was attached to the ‘d8’ diffractometer for all characterisation in this report apart from the variable temperature powder X-ray diffraction (VT-PXRD) experiment carried out on the doped bismuth vanadates (see Chapter 7), where the furnace was attached to

the 'd9' diffractometer. This furnace can operate at temperatures between room temperature and 1100 °C under different atmospheres. However all *in-situ* variable temperature powder X-ray diffraction in this thesis has been carried out in air. The heating profiles are controlled by Bruker XRD commander software.[11] Various heating profiles may be used; however in this work a 'ramp/scan' profile was used, whereby the furnace heated the sample to a set temperature, before recording a PXRD pattern whilst the set temperature remained constant. In typical variable temperature studies carried out in this report, diffraction patterns were obtained in 20 °C or 40 °C increments. Corrected temperatures were obtained using the polynomial calculated from the thermal expansion of Al_2O_3 by Simon Allen in his PhD thesis.[12] The polynomial is shown in Equation 2.11 and the coefficients are $a = 1.61 \times 10^{-7}$ K^{-2}, $b = -5.86 \times 10^{-4}$ K^{-1}, $c = 0.565$ and $d = -134$ K. T_{corr} represents the corrected temperature and T_{set} represents the chosen temperature in the diffractometer input file.

$$T_{corr} = T_{set} + \left(aT_{set}^3 + bT_{set}^2 + cT_{set} + d\right) \qquad (2.11)$$

Samples for the d8 diffractometer were prepared in an identical manner to the preparation of amorphous fused silica glass slides for the d5000 diffractometer. The silica slides were then mounted in an alumina sample holder. A VT-PXRD experiment has also been carried out on a bulk sample of Bi_6WO_{12}, where the sample was first pressed into a pellet and then placed into the alumina sample holder, using a silica ring to hold the pellet in place.

A second Bruker d8 diffractometer (named 'd9' in order to distinguish from the other d8 diffractometer) operating at 40 kV and 40 mA and using CuKα_1 and CuKα_2 (1.5418 Å) radiation, was used for most of the room temperature characterisation in this thesis. X-rays pass through Soller slits, variable divergence slits and antiscattering slits before reaching the sample. The diffracted beam then reaches the high resolution Lynx Eye detector, which consists of 192 silicon strips.

Samples were prepared for the 'd9' by grinding the sample in a pestle and mortar, before sieving over a Vaseline smeared zero-background silicon slide placed in an aluminium holder.

2.3.1.3 Measurement parameters

Table 2.1 shows the typical measurement parameters used for characterising samples throughout this report. Most Rietveld fits shown in this report use 30 minute d9 scans. The 50 minute d5000 measurement was used for routine identification of the sample, with the longer measurement being used for more accurate work and characterisation. Table 2.2 shows additional measurement parameters.

Table 2.1: Typical PXRD measurement parameters for data collection in this thesis.

Instrument	2θ range (º)	Step Size (º)	No. of Steps	Time/step (s)	Duration
D9	10-70	0.02053	2922	0.6	29 mins
D5000	10-70	0.02	3000	1	50 mins
D5000	5-120	0.02	5750	7.5	12h

Table 2.2: (a and b) typical measurement parameters used for collecting variable temperature data. (c) uses the same step size and 2θ range as a highly crystalline CeO_2 sample in order to carry out particle size determination.

	Instrument	2θ range (º)	Step Size (º)	Time/step (s)	Duration
a	D8	10-70	0.0170119	1	1h03min
b	D8	10-90	0.0170119	1	1h23min
c	D8	10-120	0.0085059	1	3h

In this thesis, laboratory PXRD data were given a code, 'd*_×××××', where d* denotes the instrument used (d5, d8 or d9) and '×××××' represents a data collection number. 'd5' represents the Siemens d5000 diffractometer.

2.3.2 Neutron diffractometers at the ISIS spallation souce

2.3.2.1 TOF neutron technique

In a spallation source (see Figure 2.2), the production of neutrons begins with the formation of hydride ions. The acceleration of hydride ions then occurs in a linear accelerator and the hydride ions are then stripped of electrons (to form protons), by aluminium oxide, as they enter the synchrotron. Protons are accelerated in the synchrotron ring, until they reach energies of 800 MeV. Protons with extremely high energies then hit a tungsten target, creating an intranuclear cascade, producing neutrons. These neutrons have a range of different energies (*i.e.* are polychromic), which are reduced by a hydrogen containing moderator, usually water or methane. This spread of neutron energies results in neutrons with a range of wavelengths.

Therefore at a time-of flight neutron source, such as ISIS, Bragg's law is solved by varying the wavelength of the neutrons. Unlike laboratory X-ray diffractometers, the detectors at instruments such as GEM and HRPD are not required to move, hence are located at a fixed 2θ position. The relationship between the wavelength and time of flight is given in Equation 2.12 where h is Planck's constant, m is the mass of a neutron, L is the path length of the diffractometer and t is the time of flight.

$$\lambda = \frac{ht}{mL} \tag{2.12}$$

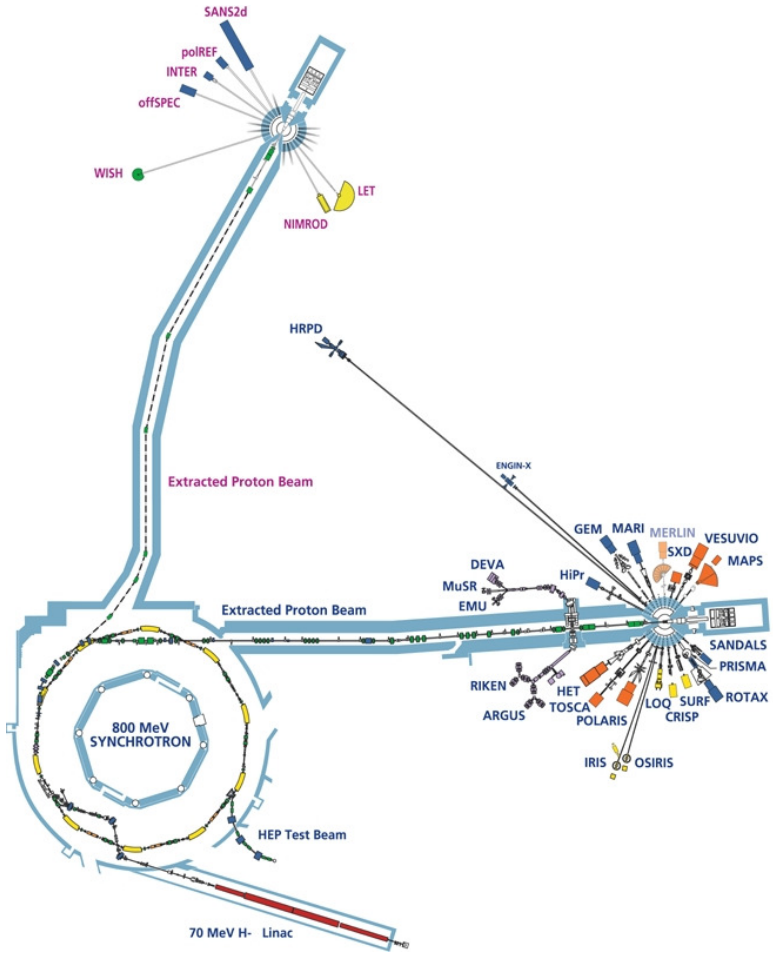

Figure 2.2: Diagram of ISIS taken from the ISIS website.

2.3.2.2 GEM diffractometer

The GEM diffractometer at ISIS was used to collect total scattering data. GEM uses a methane moderator at temperatures of around 100 K. Two choppers are used to prevent overlap of the neutron frames, resulting in a range of neutron wavelengths

between 0.05 Å and 3.40 Å.[13] Additionally, GEM has an oscillating radial collimator which reduces the background contribution. GEM has eight banks of detectors made from both ZnS and ^{6}Li.[13]

The ability of a diffractometer to collect high quality total scattering data is related to the maximum value and resolution of Q (given in Equation 2.13), the magnitude of the diffraction vector (or momentum transfer). As a high resolution in real space is inversely proportional to the Q_{max} (Equation 2.14), a high value of Q must be attainable in order to obtain good total scattering data. [14]

$$Q = \frac{4\pi \sin\theta}{\lambda} \tag{2.13}$$

$$\Delta r = \frac{\pi}{Q_{\max}} \tag{2.14}$$

Laboratory instruments using CuK_{α} radiation limit the maximum value of Q to approximately 8 Å^{-1}, which is too low for good total scattering experiments. Shorter wavelengths are required in order to achieve a high value of Q and this is typically achieved by using either synchrotron X-ray or neutron sources.

Several features of the GEM diffractometer (Figure 2.3) make it particularly suitable for collecting total scattering data.[13] These include a path length of 17.0 m, the large number of detectors (7290 in total), a wide range of angles covered (1.2 ° to 171.4 °) and a large area covered by the detectors, which give a high resolution in both real and reciprocal space.[10, 13] A Q value of up to 50 Å^{-1} is achievable at GEM, due to a large flux of short wavelength neutrons.[10, 14]

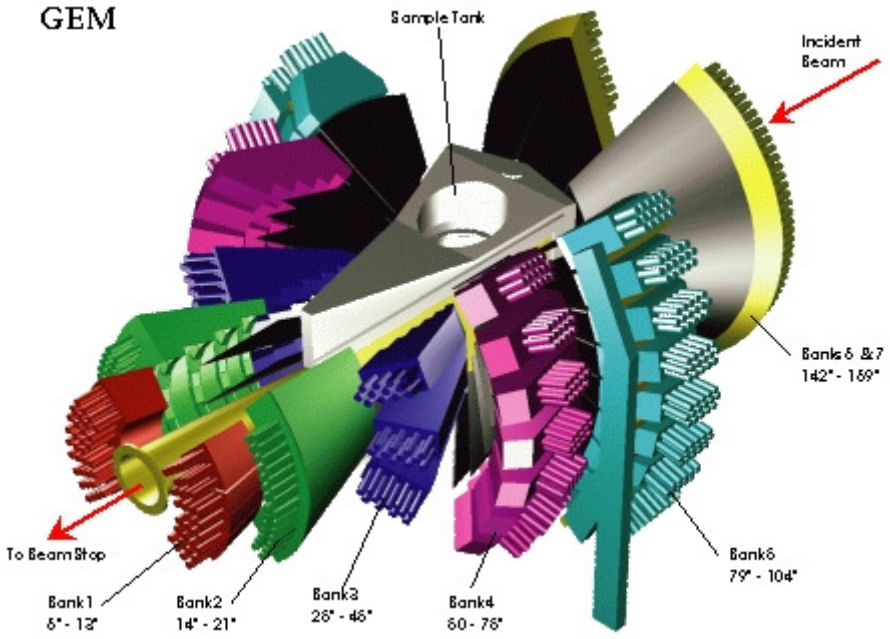

Figure 2.3: A diagram of the GEM diffractometer taken from the GEM website.

2.3.2.3 HRPD

HRPD has a 100 K methane moderator which slows down neutrons produced in the spallation process through interactions between neutrons and hydrogen atoms.[15] The error in the time of flight caused by the length of the methane moderator, is reduced by using a long path length of 100 m; therefore is a key factor in achieving a high resolution. Of the three fixed detector banks at 30°, 90°, and 168° ('backscattering') 2θ, it is the backscattering bank which offers the highest resolution, with $\Delta d/d = 4\text{-}5 \times 10^{-4}$.[15, 16] Detectors in the backscattering bank are made from ZnS and cover a range of angles from 160°-176°. Two choppers (operating at 50 Hz and 50/n Hz, where n typically is 5 or 10) are used to prevent overlap from neutron pulses, whilst a super mirror neutron guide improves neutron flux.[15, 16] With the maximum wavelength of the neutrons being approximately 10 Å, accessible d-spacings are in the range 0.3-16.5 Å, although the resolution varies with detector bank.[15, 16]

Variable temperature powder neutron diffraction data for Bi_6WO_{12} were collected on HRPD using a furnace. A room temperature scan of approximately 3-4 hours was carried out in the range 30 – 130 ms. Variable temperature PND data were collected in the range 60-800 ℃, in 40 ℃ intervals, with 12 mAh^{-1} of current per scan. Longer data collections were carried out at 700 ℃ and 800 ℃. Data were normalised by subtracting

a vanadium background (due to the vanadium can sample holder) using the MANTID software.

2.3.3 Synchrotron powder X-ray diffractometers

2.3.3.1 Synchrotron radiation

Synchrotron radiation is particularly useful as it has a high intensity, high resolution, high collimation, low beam divergence and tunable wavelengths. This is useful in powder diffraction studies in terms of detection of weak superstructure peaks (undetectable in the laboratory) and resolution of peaks which would usually appear broadened on laboratory diffractometers.

Synchrotron PXRD data in this thesis were collected at I11 at the Diamond Light Source. Diamond is a third generation synchrotron, with beam lines being sourced by either bending magnets or insertion devices, such as wigglers or undulators. Diamond operates at 3 GeV.

The production of synchrotron radiation begins with the generation of electrons. Electrons are injected into a linear accelerator (linac) reaching energies of 100 MeV, before entering the booster ring, where electrons reach energies of 3 GeV and finally enter the main storage ring. The booster ring, linac and storage ring are kept under vacuum to prevent electron energy loss due to collisions with air. Bending magnets keep the beam in orbit around the ring. Synchrotron radiation leaves the synchrotron at a tangent to the beam path, where bending magnets or insertion devices exist. Insertion devices are arrays of magnets which cause the electron beam to follow a sinusoidal path, resulting in the generation of synchrotron radiation.

2.3.3.2 I11 synchrotron powder X-ray diffractometer

I11 uses an in-vacuum undulator insertion device.[17] It operates with energies in the range 5-30 keV (which corresponds to wavelengths of 0.4-2.5 Å) with a double Si(111) monochromator cooled with liquid nitrogen.[17, 18] 45 Si (111) multiple analysing crystals arranged in 5 banks of 9 crystals are used on the diffractometer, which accurately define the 2θ angle.[17] For each analysing crystal, there is a detector made from a cerium activated $YAlO_3$ perovskite.[19] Detectors only have to move a small angle to record a whole powder pattern. [17]

Data were collected in capillary mode, in borosilicate capillaries. One particular advantage of capillary mode is the reduction of preferred orientation effects. To reduce effects caused by absorption, $\mu \times r$ was kept less than 1.5 (where μ is the absorption coefficient and r is the radius of the capillary). This required the use of 0.3mm capillaries. A cryostream N_2 blower was used to control the temperature. Data collected at I11 in this thesis used a wavelength of 0.82644 Å. No absorption edges of any of the elements under study were close to this wavelength.

2.4 Data analysis

2.4.1 Pawley refinement

When approximate unit cell parameters and space group are known, a Pawley refinement may be carried out.[20] No structural information is required. By supplying knowledge of the space group and unit cell parameters, the software is able to calculate the d-spacing (by refining the unit cell parameter) for allowed *hkl* reflections, to which the best possible intensity is assigned, in order to minimise the difference between the observed and calculated patterns. A good estimate of unit cell parameters of the phase is required to begin with. Pawley refinement is often used as a first step in structure solution in order to determine the metric symmetry of a phase, where approximate cell parameters are known from indexing.

2.4.2 Structure solution from powder diffraction data using simulated annealing

Structure solution of β-$Bi_2Sn_2O_7$ was attempted using the same methodology as used by Evans *et al.* in solving the α-$Bi_2Sn_2O_7$ crystal structure.[21] This used a procedure of simulated annealing combined with Rietveld refinement. Simulated annealing is often used in cases where the average substructure is known, but the appearance of weak superstructure peaks in the diffraction pattern suggest the presence of a larger cell (due to ordering of atoms). The relationship between the cell parameters of the average substructure and the superstructure may be expressed by a transformation matrix. Hence by using the transformation matrix to transform the average substructure, an approximate starting model for structure solution of the superstructure may be obtained. The γ-$Bi_2Sn_2O_7$ structure (pyrochlore) was transformed into orthorhombic and monoclinic non-centrosymmetric sub-groups of $Fd\bar{3}m$ using 'isodisplace'.[22] For each space group used, 10000 iterations of the anneal-refinement process were carried out.

In a cycle of annealing cell, parameters and atomic coordinates were randomly adjusted (within defined limits), with the maximum deviation from the ideal atomic coordinates being 0.5 Å. This shift in atomic coordinates was followed by a cycle of Rietveld refinement until convergence. This process was repeated for a set number of iterations. The large number of iterations used helps to reduce the likelihood of becoming 'stuck' in a local minimum.

2.4.3 Rietveld refinement

Rietveld refinement is used principally to refine crystal structures.[23] However, as described above, Rietveld refinement may be used as part of structure solution if an initial starting model is available.[21] In Rietveld refinement, a structural model is required, along with knowledge of the diffractometer parameters. Both structural and instrumental parameters can be refined. Parameters which may be refined and that are directly related to the structure include unit cell parameters, atomic coordinates, site occupancy and atomic displacement parameters (isotropic or anisotropic). Crystallite size, strain and preferred orientation, which are sample dependant, are also refineable. In addition, the scale factor, background, sample displacement, zero point, absorption and peak shape parameters may also be refined.

Rietveld refinement uses a least squares minimisation procedure. This works by minimising the difference between the observed diffraction pattern and that calculated from the structural model. Each cycle of the refinement procedure is fed back to the input program, thus improving the solution.

It is the residual, S_y (Equation 2.15), that is minimised during this least squares refinement. [24] y_i represents the intensity observed at the ith step and y_{ci} represents the calculated intensity at the ith step. w_i is the weighting factor (Equation 2.16).

$$S_y = \sum_i w_i (y_i - y_{ci})^2 \qquad (2.15)$$

$$w_i = \frac{1}{y_i} \qquad (2.16)$$

R factors are used as an indication of the quality of the refinement. Although there are several slightly different R factors which may be used, R weighted pattern (R_{wp}, given in Equation 2.17) is one of the favoured R factors as it is mathematically meaningful and is not biased to a structural model. [24]

$$R_{wp} = \left\{ \frac{\sum w_i \left(y_i(obs) - y_i(calc) \right)^2}{\sum w_i \left(y_i(obs) \right)^2} \right\}^{\frac{1}{2}} \quad (2.17)$$

Another R-factor which may be used to monitor the progress of refinement is R_{Bragg} (Equation 2.18). This is based on a structural model, from which intensities, I, are calculated and therefore is biased to the model being used. [24]

$$R_{bragg} = \frac{\sum I(obs) - I(calc)}{\sum I(obs)} \quad (2.18)$$

R_{exp} may also be defined and this gives the best value expected given the statistics of the data, as defined in Equation 2.19, where N is the number of observations and P is the number of parameters. Finally, a goodness of fit, '*GOF*' may also be used as an indicator of the quality of fit, where S_y is the residual that is minimised during Rietveld refinement (Equation 2.20).

$$R_{\exp} = \left[\frac{(N-P)}{\sum w_i y_{obs}^2} \right]^{\frac{1}{2}} \quad (2.19)$$

$$GOF = \left[\frac{S_y}{N-P} \right]^{\frac{1}{2}} = \frac{R_{wp}}{R_{\exp}} = \sqrt{\chi^2} \quad (2.20)$$

The background is fitted with a Chebychev polynomial function. Peak shapes are typically refined using a modified Thompson-Cox-Hastings pseudo-Voigt function (TCHZ). This function consists of both a Gaussian component (G) and a Lorentzian component (L), which can be represented in a simplified form by Equation (2.21). η is the mixing parameter and it determines the fraction of Gaussian and Lorentzian parameters in the function. [24]

$$TCHZ = \eta L + (1-\eta)G \quad (2.21)$$

Peak broadening arises due to the size and strain of the crystallites. Mathematically, the broadening of peaks can be described as a convolution of size, strain and instrumental components. The Scherrer equation gives information on crystallite size. In order to carry out crystallite size analysis, firstly the instrumental line broadening must be obtained from the XRD pattern of a highly crystalline and strain free material, such as Y_2O_3, quartz or CeO_2. This allows the instrumental peak shape and axial divergence values to be determined and they will then be fixed for subsequent

refinements. Following this, the size and strain may be determined, using Lorentzian and Gaussian functions respectively.

The software used for Rietveld refinement throughout this project is TOPAS Academic, using J-edit to prepare input files. [25]

2.4.4 Total scattering data analysis

Total scattering data analysis was carried out using RMCProfile version 5.[10] Prior to refinement, data were processed and normalised using the Gudrun program (based on the ATLAS programs).[26] RMCProfile uses a reverse Monte-Carlo procedure to fit the Bragg profile, normalised total scattering structure function (*S(Q)*) and total correlation function (*T(r)*) simultaneously. One of the advantages of RMCProfile is its ability to fit the Bragg profile, hence allowing the average structure to be retained and therefore preventing the generation of unreasonable configurations of atoms which only fit the local structure.[10]

A supercell, with dimensions larger than the unit cell of the material to be studied must be specified (*e.g.* $10 \times 10 \times 10$ the unit cell dimensions) as we are interested in deviations from the average structure. The RMCProfile refinement process involves the random movement of an atom from its position, which results in an increase or decrease in an agreement factor. The calculated and experimental *F(Q)* and *G(r)* are compared. If the agreement factor increases, as a result of the move, this move is rejected and given a smaller probability. Alternatively, if the agreement factor decreases, the move is accepted with a given probability.[14] The probability, *P*, is defined as shown in Equation 2.22 where χ^2_{RMC} is the RMC agreement factor.

$$P = e^{(-\Delta\chi^2_{RMC}/2)} \tag{2.22}$$

This process of moving an atom and accepting or rejecting the move continues until the deviations in R-factor are very small and oscillate around a minimum.[10] For Bragg profile fitting, data from bank 5 at GEM (91.3°) was used as it has the best counting statistics.

Various constraints and restraints can be used during RMCProfile refinement.[10] This helps to maintain the connectivity of atoms and hence prevent disintegration of the

crystal structure and therefore meaningless results. In RMCProfile simulations carried out in this thesis, a bond valence sum constraint was used.[27] This is particularly useful as it can introduce 'chemical sense' into the simulation and guide the refinement in the early stages to prevent unrealistic configurations from being obtained.[27] The individual bond valence can be described as outlined in Equation 2.23 where r_{ij} is the bond length and R_0 and b are ideal values which have previously been reported.[28, 29]

$$s_{ij} = e^{\frac{(R_0 - r_{ij})}{b}} \tag{2.23}$$

Therefore the sum of all individual bond valences, s_{ij}, gives the valence of the atom j.[28] Atom swap moves can be used in systems where there is a possibility of disorder between two atomic sites.

2.5 Impedance spectroscopy

2.5.1 Background and theory

The conductivity (σ) displayed by the sample (which has been pressed into a pellet) is related to its resistance by Equation 2.24, where ρ is the resistivity, l the length, A the area and R the resistance.

$$\sigma = \frac{1}{\rho} = \frac{l}{RA} \tag{2.24}$$

In an impedance spectroscopy measurement, the resistance is determined and providing that the dimensions of the sample are known, the conductivity may be calculated.

When an alternating sinusoidal voltage is applied across an electrolyte, an alternating sinusoidal current is produced, with a phase difference that is determined by the sample. The alternating voltage is given by Equation 2.25, where V is the voltage, V_0 is the amplitude, ω is the angular frequency (where $\omega = 2\pi f$, with f representing frequency) and t is time. The alternating current is given by Equation 2.26, where I is the current, I_0 is the amplitude and φ is the phase difference.

$$V = V_0 e^{i\omega t} \tag{2.25}$$

$$I = I_0 e^{i(\omega t - \phi)} \tag{2.26}$$

For a pure resistor, *R*, *i.e.* something that obeys Ohm's law (Equation 2.27), the phase difference of the current is zero.

$$R = \frac{V}{I} \tag{2.27}$$

However, in the case of oxide ion conductors (as is also common with other circuit elements), Ohm's law is not obeyed and the resistance has a dependence on the applied frequency and hence the term impedance, *Z,* (Equation 2.28), rather than resistance is used. Equation 2.28 can be simplified to Equation 2.29.

$$Z = \frac{V_0 e^{i\omega t}}{I_0 e^{i(\omega t - \varphi)}} \tag{2.28}$$

$$Z = \frac{V_0}{I_0} e^{i\varphi} \tag{2.29}$$

Impedance is a complex quantity and can be described by Equation 2.30, where *Z'* is the real component of the impedance (the resistance, *R*) and *Z''* is the imaginary part (which comprises of both the capacitance and the inductance). The term *X*, which represents the capacitance and inductance is defined in Equation 2.31, where *C* is the capacitance and *L* the inductance.

$$Z = Z' + iZ'' = R + iX \tag{2.30}$$

$$X = \omega L - \frac{1}{\omega C} \tag{2.31}$$

When a variable frequency is applied across an electrolyte, one or more semi-circles may be observed in the complex plane impedance plot. This is often modeled by a resistor and capacitor in parallel (as a physical representation of the electrolyte), although other circuit elements may be added to improve the model of the electrolyte.[30] Therefore the equation for impedance can be expressed as shown in Equation 2.32.

$$Z = R - \frac{i}{\omega C} \tag{2.32}$$

Depending on the capacitance, the intercepts of the semi-circle with the x-axis can be assigned to the resistance of the bulk, grain boundary or electrode response, see Table 2.3.[30] The capacitance can be calculated from the maximum of the arc if the frequency is known at this point, using the formula in Equation 2.33, where R is resistance (obtained from the intercept on the x-axis) and C is capacitance.[30]

$$\omega RC = 1 \qquad (2.33)$$

Table 2.3: Capacitance values and their assignment to components of the electrolyte.[30]

Phenomenon responsible	Capacitance (F cm^{-1})
Bulk	10^{-12} - 10^{-11}
Grain boundary	10^{-11}- 10^{-8}
Sample-electrode response	10^{-7}-10^{-5}

2.5.2 Experimental

Cylindrical pellets (measuring approximately 10 mm in diameter by 2 mm in thickness) were coated on both sides with conductive paste (silver, gold or platinum) and attached to platinum wire electrodes. The electrodes were then fired for 30 minutes to remove organic components (see Table 2.4 for the firing temperatures used for the different paste). Electrical conductivity was measured by an ac two probe method. A Solartron 1260 frequency response analyser in a frequency range 0.1-10.0 MHz was used. This was attached to a Probostat measurement cell. Data were analysed using Zview software.[31]

Table 2.4: Firing temperatures required for the conductive pastes used to attach the electrodes.

Conductive paste used to attach electrode	Firing temperature (°C)
Silver	400
Gold	515
Platinum	800

In the case of the $Bi_2Zr_2O_7$ – $Bi_2Ti_2O_7$, pellets were coated with silver conductive paste, as compounds in this system decompose below the firing temperature of the platinum conductive paste. Gold paste was used for bismuth vanadates. However, all other systems studied in this report use platinum conductive paste. The dimensions of the pellets were accurately determined, before attaching the electrode, using an electronic calliper.

2.6 Other characterisation methods

2.6.1 Electron microscopy

2.6.1.1 Scanning electron microscopy – energy dispersive X-ray analysis

Energy dispersive X-ray data for elemental analysis was collected on a Hitachi SU-70 scanning electron microscope, operating at 15 keV. Prior to data collection, the sample was typically pressed into a pellet and mounted onto a carbon stub before coating with either carbon or platinum, which acts as a conductive layer to prevent charging of the sample.

When electrons of a high energy 'hit' individual atoms in the sample, electronic transitions are induced, which gives rise to the generation of X-rays of wavelengths (and hence energies) characteristic to a particular atom. This allows quantification of elements present in the sample.

2.6.1.2 Transmission electron microscopy - electron diffraction

The high operating voltage of the TEM (with respect to the SEM) produces electrons with wavelengths suitable for diffraction studies. Due to the short wavelength of electrons (of the order of approximately 0.01 Å), in order to get diffraction from typical d-spacings, only small Bragg angles are required.

Samples were prepared for TEM by dispersing a small amount of sample in a volatile solvent such as propanol, before placing a drop on a holey carbon grid. A Jeol 2100F transmission electron microscope, operating at 200 keV was used to collect electron diffraction patterns. Electron diffraction patterns were collected by Dr. Budhika Mendis.

2.6.2 ^{91}Zr solid state NMR

^{91}Zr NMR spectra were collected by Dr. David Apperley (UK EPSRC national service) on a Varian VNMRS operating at 37.31 MHz for zirconium, using a WURST-QCPMG approach. This was required due to the quadrupolar nature of ^{91}Zr which results in a broad line width.[32]

2.6.3 Thermogravimetric analysis

Thermogravimetric analysis can be used to determine weight loss with increasing temperature, *e.g.* the loss of water in a sample or decomposition of a precursor. This is usually expressed as a percentage of the original mass. All TGA experiments were

carried out on a Perkin-Elmer Pyris 1, from room temperature to 700 °C. TGA measurements were carried out by Mr. Doug Carswell.

2.6.4 Inductively coupled plasma (ICP) analysis

Trace amounts of ions such as Bi^{3+}, Sn^{4+}, Zr^{4+} and Ti^{4+} in the precursor filtrate (*i.e.* in solution) were determined by ICP. ICP utilises a constant wavelength (λ = 160-800 nm) standard. A solution is dissociated into constituent ions and these ions are excited and emit light of a characteristic wavelength. This is a very sensitive technique and the lower limit for detecting ions is 0.2-100 ppb. All ICP experiments were carried out on a Jobin Yvon Ultima 2 ICP spectrometer.

2.6.5 Raman spectroscopy

Raman spectra were recorded by Dr. A. Beeby on a Jobin-Yovin Labram HR using an excitation wavelength of 633nm. Spectra were acquired and processed using the Horiba-Jobin-Yvon LabSpec 5 software package.

2.6.6 Second harmonic generation (SHG)

A laser can be used to determine whether a crystal is second harmonic generation active. In a centrosymmetric crystal, the polarisation of the crystal is linearly dependant on the electric field applied. However, for a non-centrosymmetric crystal, a laser signal may be generated with a frequency double that of the laser used (*i.e.* corresponding to the second harmonic). The polarisation, *P*, of a material is given by Equation 2.34, where χ is the linear electric susceptibility, *E* is the applied electric field and *d* is a coefficient.[33] This equation may be expanded as in Equation 2.35, where χ_{ij} is the electric susceptibility. It should be noted that further expansion of this polynomials in Equations 2.34 and 2.35 leads to terms which take into consideration higher order terms and coefficients.[33] For a SHG active material, the second-order coefficient is not equal to zero, *i.e.* $\chi_{ijk} \neq 0$.[33]

$$P = \chi E + dE^2 \qquad (2.34)$$

$$P_i = \chi_{ij} E_j + \chi_{ijk} E_j E_i \qquad (2.35)$$

SHG measurements were carried out at the University of Houston by Dr. Shiv Halasyamani. [33]

2.7 Geometry optimisation and DFT molecular dynamics simulations and analysis

2.7.1 Geometry optimisation

In a geometry optimisation, forces acting on the atoms of the system under study were minimised, by relaxing atomic positions, in order to find the lowest energy configuration. Geometry optimisation calculations were carried out using VASP, using the generalised gradient approach (GGA) using the Perdue-Burke-Ernzerhof (PBE) formalism.[34-37] A $1 \times 1 \times 1$ Monkhorst-Pack grid was used. In all calculations a fixed cell parameter was used. In the geometry optimisation procedure, forces are reduced until convergence is reached.

2.7.2 DFT molecular dynamics simulations and analysis

The first stage of molecular dynamics simulations was to carry out a geometry optimisation, as described above. The geometry optimised structure was taken as a starting point for molecular dynamics simulations. In an MD simulation the variation of atomic positions over time are calculated. This is achieved using Newton's laws of motions and relating the force on a particle to its acceleration, which allows the new atomic positions to be calculated, given that a fixed time step, Δt, is used.[38] Equation 2.36 and Equation 2.37 show the relationship for calculating the position, q, and momentum, p, of an atom (with mass m and acceleration a) after a given time interval, Δt. when the position or momentum at time t was known.[38]

$$q(t + \Delta t) = q(t) + \frac{p(t)}{m}\Delta t \qquad (2.36)$$

$$p(t + \Delta t) = p(t) + ma(t)\Delta t \qquad (2.37)$$

It is important to use a small time step, Δt (smaller than oxygen diffusion) as this allows accurate positions and momenta to be calculated which lie on the true trajectory.[38] If time steps are too large, atoms may approach too closely and structures which are energetically unfavourable, *i.e.* not on the trajectory, may be sampled.[38]

Ab-initio molecular dynamics calculations were performed using the Vienna Ab-initio Simulation Package (VASP).[34, 35] Calculations were carried out at the GGA level using the Perdew-Burke-Ernzerhof formalism. A $1 \times 1 \times 1$ Monkhorst-Pack grid was used. Visualisation of oxide migration pathways and changes in coordinates was

carried out using LAMP.[39] Mean-square displacements were calculated using nMOLDYN.[40]

2.8 References

1. A. Stein, S. W. Keller and T. E. Mallouk, *Science*, 1993, **259**, 1558-1564.
2. M. Kakihana and M. Yoshimura, *Bull. Chem. Soc. Jpn.*, 1999, **72**, 1427-1443.
3. R. I. Walton, *Chem. Soc. Rev.*, 2002, **31**, 230-238.
4. A. Rabenau, *Angew. Chem., Int. Ed. Engl.*, 1985, **24**, 1026-1040.
5. C. E. Bamberger, H. W. Dunn, G. M. Begun and S. A. Landry, *J. Solid State Chem.*, 1985, **58**, 114-118.
6. A. L. Hector and S. B. Wiggin, *J. Solid State Chem.*, 2004, **177**, 139-145.
7. I. Radosavljevic, J.S.O. Evans and A. W. Sleight, *J. Solid State Chem.*, 1998, **136**, 63-66.
8. D. A. Keen, *J. Appl. Cryst.*, 2001, **34**, 172-177.
9. P. F. Peterson, E. S. Bozin, T. Proffen and S. J. L. Billinge, *J. Appl. Cryst.*, 2003, **36**, 53-64.
10. M. G. Tucker, D. A. Keen, M. T. Dove, A. L. Goodwin and Q. Hui, *J. Phys.: Condens. Matter*, 2007, **19**, 335218.
11. Bruker AXS, Karlsruhe, 2000.
12. S. A. Allen, in *Department of Chemistry*, Durham University, Durham, 2003.
13. A. C. Hannon, *Nucl. Instrum. Methods Phys. Res. Sect. A*, 2005, **551**, 88-107.
14. T. Egami and S. J. L. Billinge, *Underneath the Bragg Peaks: Structural Analysis of Complex Materials*, Pergamon, Amsterdam, 2003.
15. R. M. Ibberson, W. I. F. David and K. S. Knight, *The High Resolution Neutron Powder Diffractometer (HRPD) at ISIS- A User Guide*, ISIS Crystallography, Didcot, 1992.
16. R. M. Ibberson, *Nuclear Instruments & Methods in Physics Research A*, 2009, **600**, 47-49.
17. S. P. Thompson, J. E. Parker, J. Potter, T. P. Hill, A. Birt, T. M. Cobb, F. Yuan and C. C. Tang, *Rev. Sci. Inst.*, 2009, **80**.
18. C. C. Tang, S. P. Thompson, T. P. Hill, G. R. Wilkin and U. H. Wagner, *Zeitschrift Fur Kristallographie*, 2007, 153-158.
19. N. Tartoni, S. P. Thompson, C. C. Tang, B. L. Willis, G. E. Derbyshire, A. G. Wright, S. C. Jaye, J. M. Homer, J. D. Pizzey and A. M. T. Bell, *J. Synchrotron Radiation*, 2008, **15**, 43-49.
20. G. S. Pawley, *J. Appl. Crystallogr.*, 1981, **14**, 357-361.
21. I. R. Evans, J. A. K. Howard and J. S. O. Evans, *J. Mater. Chem.*, 2003, **13**, 2098-2103.
22. B. J. Campbell, H. T. Stokes, D. E. Tanner and D. M. Hatch, *J. Appl. Crystallogr.*, 2006, **39**, 607-614.
23. H. M. Rietveld, *J. Appl. Crystallogr.*, 1969, **2**, 65-71.
24. *The Rietveld Method*, Oxford University Press, Oxford, 1993.
25. A. A. Coelho, Bruker AXS, Karlsruhe, 2000.
26. A. C. Hannon, W. S. Howells and A. K. Soper, *Inst. Phys. Conf. Ser.* , 1990, **107**, 193-211.
27. S. T. Norberg, M. G. Tucker and S. Hull, *J. Appl. Cryst.*, 2009, **42**, 179-184.
28. I. D. Brown and D. Altermatt, *Acta Cryst. B*, 1985, **41**, 244-247.
29. N. E. Brese and M. O' Keeffe, *Acta Cryst. B*, 1991, **47**, 192-197.

30. J. T. S. Irvine, D. C. Sinclair and A. R. West, *Adv. Mater.(Weinheim, Ger.)*, 1990, **2**, 132-138.
31. D. Johnson, Scribner Associates, Inc.
32. L. A. O'Dell and R. W. Schurko, *Chem. Phys. Lett.*, 2008, **464**, 97-102.
33. K. M. Ok, E. O. Chi and P. S. Halasyamani, *Chem. Soc. Rev.*, 2006, **35**, 710-717.
34. G. Kresse and J. Furthmuller, *Comput. Mater. Sci.* , 1996, **6**, 15-50.
35. G. Kresse and D. Joubert, *Phys. Rev. B*, 1999, **59**, 1758-1775.
36. J. P. Perdew, K. Burke and M. Ernzerhof, *Phys. Rev. Lett.*, 1996, **77**, 3865-3868.
37. J. P. Perdew, K. Burke and M. Ernzerhof, *Phys. Rev. Lett.*, 1997, **78**, 1396-1396.
38. C. J. Cramer, *Essentials of Computational Chemistry: Theories and Models*, Wiley, Chicester, 2004.
39. LAMP.The Large Array Manipulation Program. http://www.ill.eu/instruments-support/computing-for-science/cs-software/all-software/lamp
40. T. Rog, K. Murzyn, K. Hinsen and G. R. J. Kneller, *J. Comput. Chem*, 2003, **24**, 657-667.

3 Synthesis, Structure and Transport Properties of $Bi_2Zr_{2-x}Ti_xO_7$ Phases

3.1 Background

Sorokina and Sleight carried out studies on the solid solution of the $Bi_{2-x}Zr_xO_{3+x/2}$ system using a low temperature precursor route and reported the existence of a phase with a 1:1 ratio of Bi:Zr and a cubic cell parameter of 5.39 Å.[1] Most work has focused on the bismuth rich region of the $Bi_{2-x}Zr_xO_{3+x/2}$ system and Abrahams found tetragonal bismuth zirconates with compositions of $Bi_{2-x}Zr_xO_{3+x/2}$ (x = 0.05-0.17) whilst Meatza *et al.* extended this region to $Bi_{1.33}Zr_{0.67}O_{3.335}$.[2, 3] At 750 °C, $Bi_{1.85}Zr_{0.15}O_{3.075}$ transforms to a δ-Bi_2O_3 analogue, whilst $Bi_{1.33}Zr_{0.67}O_{3.335}$ undergoes the same transformation at 730 °C.[2, 3] Both $Bi_{1.89}Zr_{0.11}O_{3.055}$ and $Bi_{1.33}Zr_{0.67}O_{3.335}$ display high oxide ion conductivities of 1.01 S cm^{-1} at 700 °C (comparable to δ-Bi_2O_3) and 2.6×10^{-2} S cm^{-1} at 745 °C, respectively, where a fluorite-type structure is adopted. [2, 3]

Pyrochlore type bismuth titanate exists in stoichiometric ($Bi_2Ti_2O_7$) and non-stoichiometric ($Bi_{1.74}Ti_2O_{6.62}$) forms.[4, 5] The preparation of $Bi_{1.174}Ti_2O_{6.62}$ by Radosavljevic *et al.* and $Bi_2Ti_2O_7$ by Hector *et al.* follow two slightly different precursor routes.[4, 5] The precursor prepared by Radosavljevic *et al.* could be fired at 600 °C to produce a single phase product $Bi_{1.74}Ti_2O_{6.62}$.[5] In the method used by Hector, a single phase product could only be synthesised at 470 °C and an increase in temperature of just 10 °C resulted in partial pyrochlore decomposition and formation of $Bi_4Ti_3O_{12}$. [4, 5] Structure refinements of both the stoichiometric and non-stoichiometric bismuth titanate found that Bi^{3+} should be located on a position off the three-fold axis (96g or 96h respectively), as is common for Bi^{3+} containing pyrochlores. [4-6]

As discussed in Chapter 1, there are several examples of $M_2Ti_{2-x}Zr_xO_7$ compounds in the literature (where M = Y^{3+}, Gd^{3+}, Dy^{3+}), with the titanate end member possessing the pyrochlore structure and the zirconate end member having either the fluorite structure (M = Y^{3+}, Dy^{3+}) or the pyrochlore structure (M = Gd^{3+}).[7-9] Detailed studies on the $Y_2Ti_{2-x}Zr_xO_7$ system by Heremans *et al.* have shown that the cation and anion sublattices disorder independently with the anion sublattice disordering first.[7, 8] This has important implications for ionic conductivity as the disordering of the anion sublattice coincides with a large increase in conductivity, with an increase of approximately two orders of magnitude on going from $Y_2Ti_{1.6}Zr_{0.4}O_7$ to $Y_2Ti_{1.4}Zr_{0.6}O_7$

at 600 °C, although this is reduced to a change of approximately one order of magnitude at higher temperatures.[8] In the $Dy_2Ti_{2-x}Zr_xO_7$ system, an increase of approximately 1.5 orders of magnitude was found for $Dy_2Ti_{1.2}Zr_{0.8}O_7$, with respect to $Dy_2Ti_2O_7$, whilst the highest conductivity was 5×10^{-3} S cm^{-1} at 900 °C for $Dy_2Zr_2O_7$, two orders of magnitude higher than $Dy_2Ti_2O_7$.[9] As a cubic cell of approximately 5 Å has been reported for $Bi_2Zr_2O_7$ and $Bi_2Ti_2O_7$ has the pyrochlore structure, it is likely that the $Bi_2Zr_{2-x}Ti_xO_7$ system offers another opportunity for studying cation and anion ordering in a $M_2Ti_{2-x}Zr_xO_7$ system.[1, 4, 5]

The aim of this chapter was firstly to synthesise and characterise $Bi_2Zr_2O_7$ and mixed B cation compounds in the $Bi_2Zr_{2-x}Ti_xO_7$ system and hence determine whether the anion and cation sublattices disorder independently. A total scattering study will be carried out to determine the local structure in both $(BiZr)_2O_7$ and $Bi_2Ti_2O_7$. Finally, the variation of conductivity in the $Bi_2Zr_{2-x}Ti_xO_7$ system will be investigated.

3.2 Synthesis of $(BiZr)_2O_7$

3.2.1 Nitrate precursor method

The synthesis of $(BiZr)_2O_7$ was based on a precursor method described by Sorokina and Sleight.[1] The hydration level of zirconium oxynitrate was accurately determined by firing $ZrO(NO)_3 \cdot xH_2O$ overnight at 800 °C in order to decompose it to ZrO_2. $Bi(NO)_3 \cdot 5H_2O$ (1.00 g, 2.06 mmol, Aldrich, >98%) was dissolved in HNO_3 solution (70%, Fisher, ratio 5ml HNO_3 to 50 ml distilled water) and $ZrO(NO_3)_2 \cdot 2.5H_2O$ (0.57 g, 2.06 mmol, Aldrich, 99.99%) was dissolved in 50 ml water. The resulting solutions were mixed together, then neutralised with ammonium hydroxide. A white precipitate formed on neutralisation. This precipitate was stirred for several hours and aged overnight. Following this, the precipitate was stirred for approximately two hours, before filtering and then drying overnight in an oven at 95 °C. This white precursor was shown to be amorphous by XRD. The precursor was ground in a pestle and mortar and fired at 600 °C for 10 hours, yielding a yellow-orange solid.

3.2.2 Hydrothermal synthesis

This method was developed as a combination of two existing procedures.[10, 11] $Bi(NO_3)_3 \cdot 5H_2O$ (0.50 g, 1.03 mmol) and $ZrO(NO)_3 \cdot 2.5H_2O$ (0.29 g, 1.03 mmol) with 10 cm^3 3 M NaOH were stirred in a 20cm^3 Teflon liner for approximately 45 minutes.

This was placed in a steel autoclave and heated at 200 °C for 60 hours, under autogeneous pressure. The product obtained was a mixture of $(BiZr)_2O_7$ and monoclinic Bi_2O_3.

3.2.3 Sol-gel synthesis

The procedure described by Rao *et al.* in the synthesis of $La_2Zr_2O_7$ was attempted, replacing the lanthanum source with $Bi(NO_3)_3•5H_2O$.[12] Solutions of $Bi(NO_3)_3•5H_2O$ (1.00 g, 2.03 mmol) in dilute HNO_3 and $ZrO(NO_3)_2•2.5H_2O$ (0.57 g, 2.03 mmol) in water were mixed together, followed by the addition of citric acid in a 1:1 molar ratio with the metal ions (0.79 g, 4.12 mmol). Dilute ammonia was added to neutralise the solution, then the solution was heated in a water bath to form a viscous solution. Ethylene glycol (0.28 ml, 4.95 mmol) was added, in a molar ratio of 1.2 ethylene glycol: 1 metal ions, to form a gel. This was then heated on a hotplate at 100ºC until the gel began to solidify and then the temperature was increased until a solid was obtained. This solid was ground in a pestle and mortar, then fired overnight at 400 ºC, before firing for 5 hours at temperatures of 500 ºC, 600 ºC and 700 ºC. All products were impure and extremely poorly crystalline.

3.2.4 Conventional solid state synthesis

Bi_2O_3 (0.76 g, 1.63 mmol) and ZrO_2 (0.40 g, 3.25 mmol) were ground together in an agate pestle and mortar and fired at 500 ºC for 12 hours, 600 ºC (60 hours), 700 ºC (60 hours) and 800 ºC (12 hours). However, the products obtained were a mixture of either monoclinic or tetragonal Bi_2O_3 (depending on the temperature used) and monoclinic ZrO_2.

3.3 Synthesis of $Bi_2Ti_2O_7$

The method described by Radosavljevic *et al.* was followed.[5] $Bi(NO_3)_3•5H_2O$ (1.00 g, 2.06 mmol) and $Ti(OBu)_4$ (0.70 ml, 2.06 mmol) were dissolved in acetone to make 0.1 M solutions. The solutions were mixed together, heated to 50°C (with constant stirring) and the pH was adjusted to pH = 7 with NH_4OH. This was left overnight and then stirred. The solution became much more gelatinous on stirring. This was filtered and dried, then fired at 600°C for 16 hours, resulting in the formation of an off-white powder.

3.4 Synthesis of $Bi_2Zr_{2-x}Ti_xO_7$ mixed Phases

3.4.1 TiO_2 as the titanium source

$Bi(NO_3)_3$•$5H_2O$ (1.00 g, 2.06 mmol) and $ZrO(NO_3)_2$•$2.5H_2O$ (0.54 g, 1.96 mmol) were dissolved as for $(BiZr)_2O_7$. Attempts were made at dissolving the TiO_2 (0.008 g, 0.103 mmol) in acid at room temperature and under reflux conditions (HNO_3 solution at 120 °C) but were not successful. The only crystalline phases identified were $(BiZr)_2O_7$ and a small amount of the rutile TiO_2 polymorph.

3.4.2 Titanium metal as the titanium source

Titanium metal (0.005 g, 0.103 mmol) was dissolved in a ratio of 3 H_2O_2 (28%, 0.38 ml, 3.46 mmol) to 2 NH_3 (34%, 0.14 ml, 2.31 mmol) resulting in the formation of a yellow solution, based on procedures described by Hector and Camargo.[4, 13] $Bi(NO_3)_3$•$5H_2O$, dissolved in dilute HNO_3 solution, was added to the titanium solution, forming a deep red solution. This was followed by the addition of $ZrO(NO_3)_3$•$2.5H_2O$ (0.54 g, 1.96 mmol) solution. After stirring for a short length of time, the solution was neutralised by the slow addition of NH_4OH, which resulted in a colour change from a red solution to an orange precipitate, followed by a pale yellow precipitate. The resulting precipitate was stirred, left to age overnight, stirred again, then filtered by suction, dried and fired at 600 ºC for 10 hours.

3.4.3 Titanium butoxide as the titanium source

This method was chosen to prepare the $Bi_2Zr_{2-x}Ti_xO_7$ mixed phases. $Ti(OBu)_4$ (Fluka, 97.0%) was dissolved in acetone (Fisher, analytical grade), forming a milky-white solution. $Bi(NO_3)_35H_2O$ (1.00 g, 2.06 mmol) was dissolved in a solution of dilute HNO_3 (comprising 5 ml 70% HNO_3 and 50 ml water). $ZrO(NO_3)_2.xH_2O$ was dissolved in water. Bismuth and zirconium solutions were added to the titanium solution, forming a colourless solution, and the procedure was followed as for $(BiZr)_2O_7$. Inductively coupled plasma atomic emission spectroscopy measurements were carried out on several precursor filtrates and showed ion traces of the order 0.1-0.05 ppm; therefore it appears that the nominal compositions have been prepared.

It should also be noted that pure $Bi_2Ti_2O_7$ could be synthesised using the same method as the mixed phases. This is slightly different from the methods used by Radosavljevic and Hector and combines their procedures. $Bi(NO)_3$•$5H_2O$ was dissolved

in dilute nitric acid (as in Hector's paper) and $Ti(OBu)_4$ was dissolved in acetone (as carried out by Radosavljevic).[4, 5]

3.5 Characterisation of $(BiZr)_2O_7$

3.5.1 Laboratory PXRD data

Figure 3.1 shows a typical powder XRD pattern and Rietveld refinement of a single phase $(BiZr)_2O_7$ product with a fluorite structure, prepared by the precursor method described in 3.2.1. The structural model used for refinement is given in Table 3.1. The refined parameters included 18 background terms, specimen displacement height, scale factor, peak shape, lattice parameter and an overall temperature factor.

Table 3.1: Structural model used for $(BiZr)_2O_7$ refinement.

Atom	Site	x	y	z	Occupancy
Bi	4a	0	0	0	0.5
Zr	4a	0	0	0	0.5
O	8c	0.25	0.25	0.25	0.875

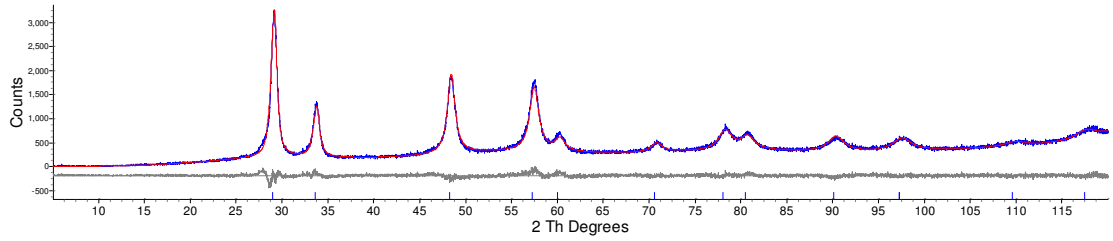

Figure 3.1: D5_07330: $(BiZr)_2O_7$. Rietveld refinement using simple fluorite-type structural model. a = 5.3254(4) Å, R_{wp} = 7.133%

In order to investigate the formation of this phase and its stability region, an *in-situ* variable temperature PXRD (VT-PXRD) study has been carried out (Figure 3.2). Starting from the amorphous precursor, the sample was heated in 20 ºC intervals and powder XRD patterns recorded. $(BiZr)_2O_7$ could be identified as a single phase, between 485 ºC and 580 ºC; above 580 ºC, $(BiZr)_2O_7$ began to decompose (Figure 3.2). Multi-phase Rietveld refinement showed that the decomposition products were γ-Bi_2O_3, monoclinic ZrO_2 and tetragonal ZrO_2. Tetragonal ZrO_2 is a high temperature polymorph, usually stable above temperatures of 1170 ºC, therefore it is likely that it has been stabilised by small amounts of bismuth.[14] The final XRD pattern taken at room temperature also has a reduced quantity of tetragonal ZrO_2.

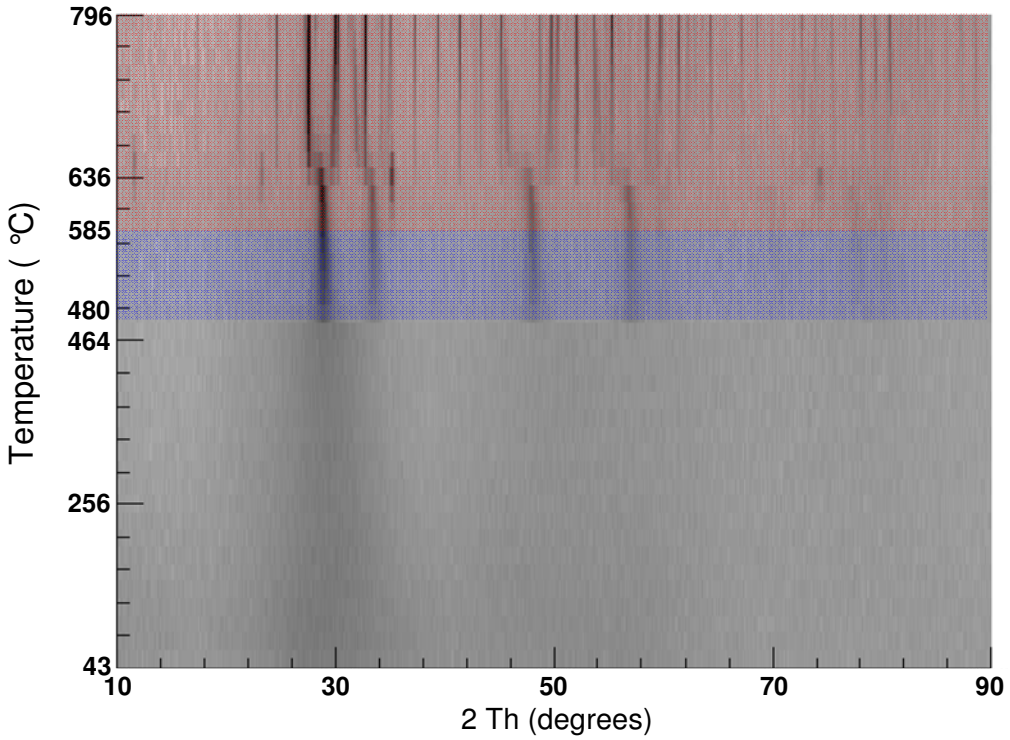

Figure 3.2: d8_03517: *In-situ* VT-PXRD of the $(BiZr)_2O_7$ precursor, showing the $(BiZr)_2O_7$ formation and stability range (shaded pale blue) and the onset of decomposition (shaded pale red).

A TGA experiment was carried out on a $(BiZr)_2O_7$ precursor. This showed a large mass loss between 200-300 ºC and a smaller mass loss between 400-500 ºC, due to the decomposition of the precursor (Figure 3.3). Constant weight was achieved after the second mass loss, suggesting the formation of the $(BiZr)_2O_7$ product at above 500 ºC. This is in excellent agreement with the results of our *in-situ* VT-PXRD study.

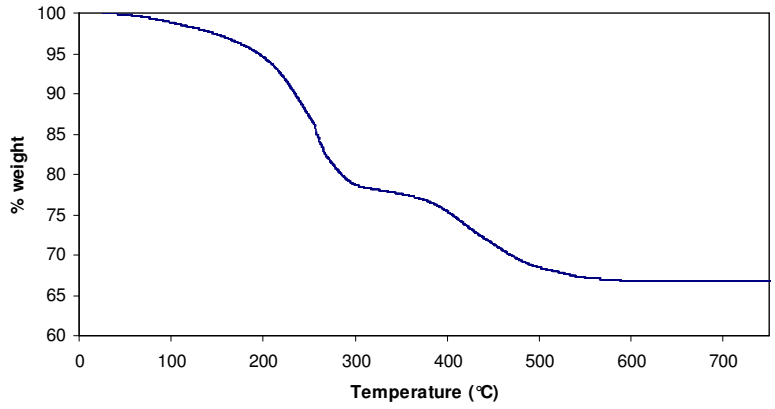

Figure 3.3: TGA results from $(BiZr)_2O_7$ precursor.

Broad peaks in the powder pattern of $(BiZr)_2O_7$ shown in Figure 3.1 suggest a small particle size in this product. In order to investigate the dependence of $(BiZr)_2O_7$ particle size on temperature from initial crystallisation to its decomposition, a further VT-PXRD experiment on the $(BiZr)_2O_7$ precursor was carried out using the same data collection

procedure as a scan recorded on a highly crystalline, strain free sample of CeO_2. This allows the crystallite size to be determined through Rietveld refinement. Results are shown in Figure 3.4. As expected, the crystallite size increased with increasing temperature, from <5 nm when this crystalline phase first appears, to about 20 nm, just before it starts to decompose.

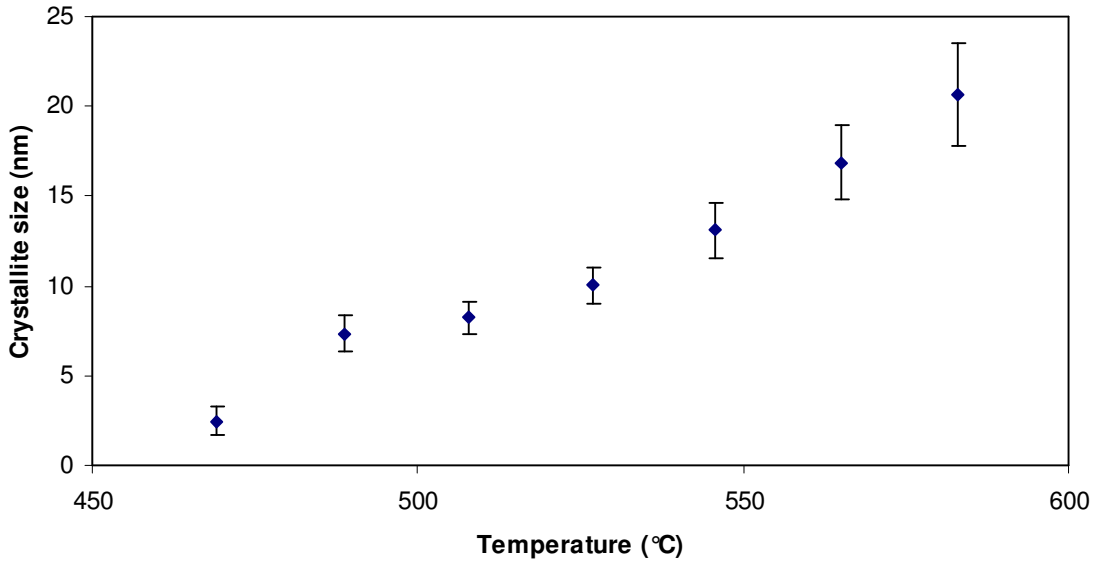

Figure 3.4: Variation of $(BiZr)_2O_7$ crystallite size (obtained from Rietveld refinement) with temperature.

In order to determine whether the fluorite-type $(BiZr)_2O_7$ is thermodynamically stable or kinetically stable, an annealing experiment was carried out. 2 g of $(BiZr)_2O_7$ were synthesised as described in section 3.2.1. This sample was repeatedly fired at 500 °C with intermittent grinding and XRD characterisation. This annealing temperature was chosen as it is well below the decomposition temperature of $(BiZr)_2O_7$, which was determined by *in-situ* VT-PXRD. The firing period lasted for a total of 270 hours. No pyrochlore ordering peaks or decomposition of the $(BiZr)_2O_7$ phase was observed in the XRD patterns. In addition to this, little change was observed in the crystallite size, despite 270 hours of annealing at 500 °C (Table 3.2). As no decomposition or pyrochlore ordering occurs within this time frame, fluorite $(BiZr)_2O_7$ can be regarded as being stable under the conditions and on the timescale investigated.

Table 3.2: Crystallite size of $(BiZr)_2O_7$ as a function of annealing time at 500 °C.

Total time annealed (h)	Crystallite size (nm)
0	12.8(1)
10	12.9(1)
22	13.0(1)
38	13.1(1)
54	12.3(1)
66	12.5(1)
126	12.8(1)
270	13.4(2)

3.5.2 Powder neutron diffraction data

Powder neutron diffraction data were collected on the GEM diffractometer at ISIS. Initial refinements showed that the sample was phase segregated, consisting of two fluorite phases with slightly different cell parameters. In the final refinement, 18 background parameters, a scale factor and an absorption coefficient were refined for each bank. One isotropic temperature factor was used per crystallographic site. The ratio of bismuth to zirconium present in each phase was obtained by refining the occupancy of the metal sites, using a restraint to preserve the overall $(BiZr)_2O_7$ stoichiometry. Data from banks 3, 4 and 5 were used in the final refinement. The fit obtained with two fluorite models is shown in Figure 3.5 for bank 5 data. One phase was slightly zirconium rich (zirconium occupancy of metal sites = 0.511(2)) and therefore had a smaller cell parameter (a = 5.2883(4) Å), whilst the second phase was slightly bismuth rich (bismuth occupancy of metal sites = 0.512(2)) and had a larger cell parameter (a = 5.3647(1) Å).

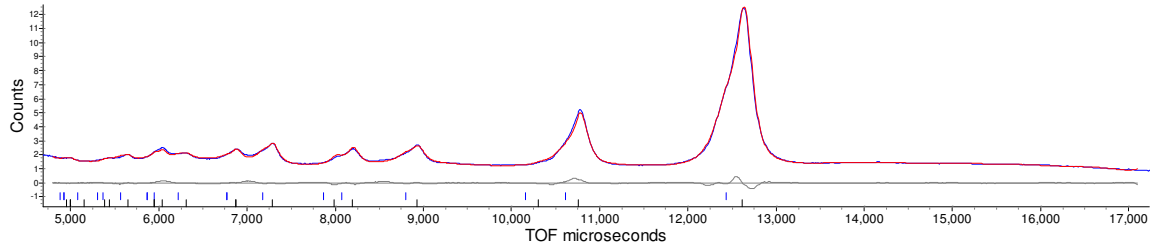

Figure 3.5: Rietveld fit for $(BiZr)_2O_7$ using powder neutron diffraction data. R_{wp} = 2.948%.

3.5.3 Total scattering data

RMCProfile refinements for $(BiZr)_2O_7$ were carried out starting with a fluorite configuration, which contained 12.5 % of anion sites as 'null scattering atoms' to take into the account the presence of vacancies. An $11 \times 11 \times 11$ supercell of the ideal fluorite structure (with P1 symmetry) was used as the starting configuration for RMC simulations. The program 'atomchoose' was used to randomly distribute Bi and Zr

cations, oxygen and oxygen vacancies across their ideal crystallographic sites, thereby creating a disordered supercell. Additionally, the 'atom swap' function was used during RMC refinements to swap bismuth atoms with zirconium atoms and oxygen atoms with oxygen vacancies The fits were carried out using two T(r) from neutron data: one up to 29 Å and the second used the same data but only up to 3 Å, with a higher weighting. The purpose of the second T(r) was to ensure RMC fits were chemically sensible on a local scale. Due to the phase segregation in $(BiZr)_2O_7$, the RMC fits did not use information from Bragg or S(Q). RMC fitting only used one phase, which could result in a distorted final configuration due to the presence of the two phases clearly present in the average structure. In addition bond valence sums were used to prevent species becoming over-bonded or under-bonded. Figure 3.6 shows the excellent agreement between the total scattering data and RMC fit.

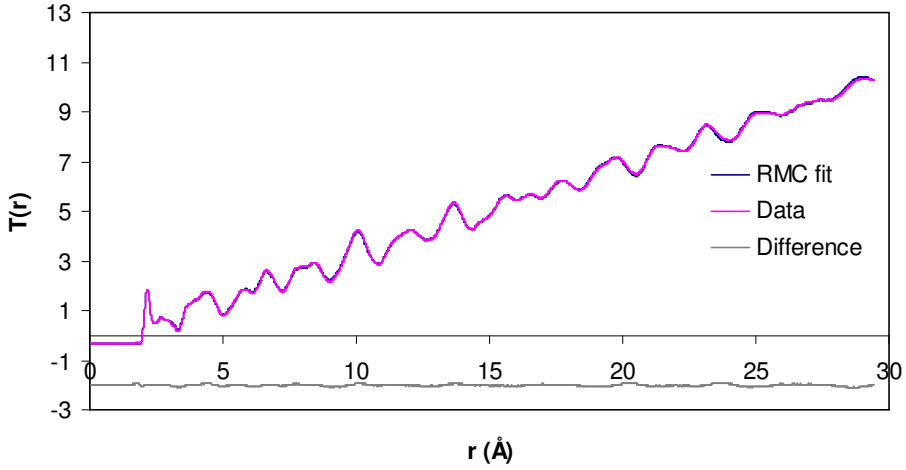

Figure 3.6: Fit to the T(r) obtained for $(BiZr)_2O_7$ using a fluorite starting configuration.

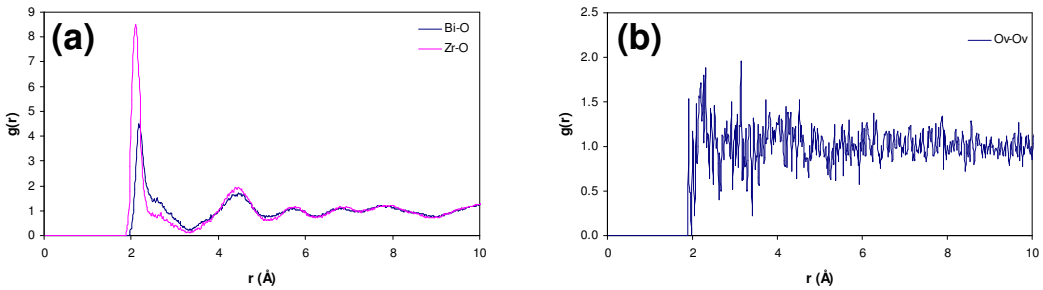

Figure 3.7: (a) Zr-O and Bi-O partial g(r) and (b) Ov-Ov partial g(r) as obtained from a RMCProfile fit using a $(BiZr)_2O_7$ fluorite starting configuration.

Figure 3.7a shows the Bi-O and Zr-O bond length distributions. The Bi-O distribution clearly shows the presence of two maxima, one at 2.20 Å and a second at 2.66 Å. For Zr-O, one bond length distribution maximum of 2.12 Å is observed. A small shoulder in the Zr-O bond length distribution is observed at 2.66 Å. This shoulder

is very small with respect to the Zr-O peak centred around 2.12 Å and is very different from the Bi-O distribution where the shoulder has an intensity of around 30 % of the main Bi-O maximum. Although RMC simulations show the differing bond lengths for Zr-O and Bi-O, only one peak is resolved in the T(r) at around 2.1 Å -2.2 Å. The coordination number of Bi and Zr was determined using the 'coord_gen' program, giving a value of 6.9 for bismuth and 7.4 for zirconium. The ideal fluorite has a coordination number of eight, so therefore in a defect fluorite such as $(BiZr)_2O_7$, the coordination number has to be lower to account for oxygen vacancies . As two peaks were observed in the Bi-O g(r), the coordination number can be broken down into two parts, firstly the region 1.96-2.40 Å and secondly the region 2.40 to 3.38 Å, which gives coordination numbers of 3.1 and 3.8, respectively. This indicates that there are three shorter Bi-O bonds and and 4 longer Bi-O bonds, however, overlap of the Bi-O g(r) peaks may introduce error into the calculation of the coordination number. The vacancy-vacancy g(r) is shown in Figure 3.7b. No clear peaks are seen, hence it is clearly visible that the vacancies are disordered throughout the system.

A pyrochlore model for $(BiZr)_2O_7$ has also been tested in RMCProfile refinements. The starting configuration was a $6 \times 6 \times 6$ supercell of the ideal pyrochlore structure. The fit to the total scattering data obtained when the pyrochlore model was used is shown in Figure 3.8. Again, an excellent agreement is achieved between the final RMC configuration and the data.

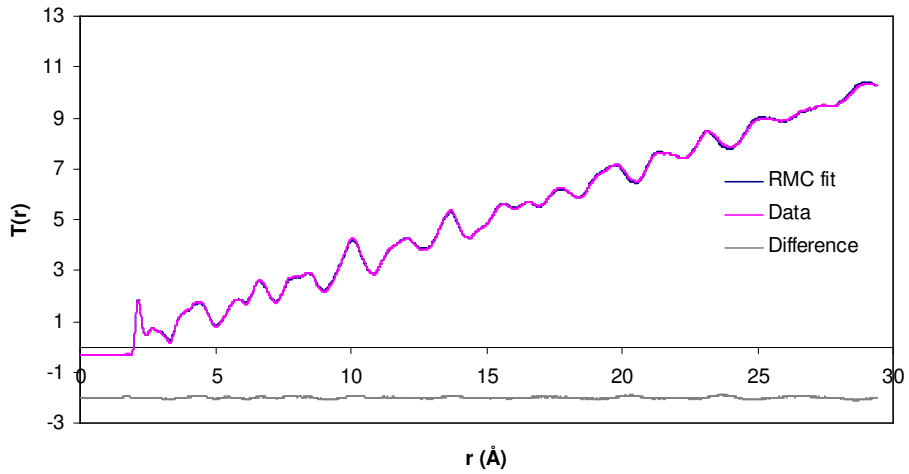

Figure 3.8: Fit to T(r) obtained for $(BiZr)_2O_7$ when a pyrochlore starting configuration was used.

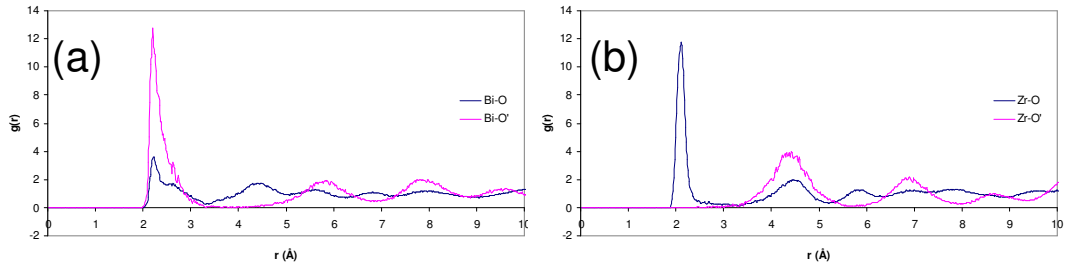

Figure 3.9: Bond length distributions from RMCProfile refinements using a pyrochlore model for $(BiZr)_2O_7$. (a) Bi-O and Bi-O' distributions and (b) Zr-O and Zr-O' distributions.

Figure 3.9 shows the bond-length distributions from RMCProfile refinements using a pyrochlore structure. A shoulder is clearly observed in the Bi-O bond length distribution (Figure 3.9a), which is similar to that observed for the RMC outputs when a fluorite configuration is used (Figure 3.7). When a fluorite configuration was used, a shoulder was present in the Zr-O bond length distribution (Figure 3.7) but this was not the case with RMC simulations with a pyrochlore configuration (Figure 3.9b). The Bi-O bond length distribution has maxima at 2.24 Å and a shoulder at 2.70 Å. Bi-O' has a maximum at 2.20 Å (where O' represents the oxygen on the 8a site). A maxima in the Zr-O bond length distribution was observed at 2.10 Å. As zirconium is not immediately coordinated by O', the first maximum in the Zr-O' distribution was observed at a longer distance of 4.38 Å.

A comparison between the fluorite and pyrochlore models is shown in Table 3.3. The bond lengths in the two models are almost identical and the Bi-O' distance in the pyrochlore model is only 0.04 Å longer than the pyrochlore Bi-O bond. Coordination numbers for bismuth (Bi-O: 5.61 and Bi-O': 1.93) and zirconium (5.66) were under-estimated in all cases. In a recent study on Bi_3YO_6, the underestimation of coordination number has been attributed to the displacement of atoms from their ideal crystallographic sites or the similarity of the neutron scattering lengths. In this case, zirconium and bismuth have similar neutron scattering lengths of 7.16 fm and 8.53 fm.

Table 3.3: Comparison of RMCProfile outcomes using fluorite and pyrochlore models for $(BiZr)_2O_7$.

	Fluorite	**Pyrochlore**
Bi-O coordination number	6.9	5.61
Bi-O' coordination number	N/A	1.93
Zr-O coordination number	7.4	5.66
Bi-O distance	2.20	2.20
Bi-O' distance	N/A	2.24
Zr-O distance	2.12	2.10

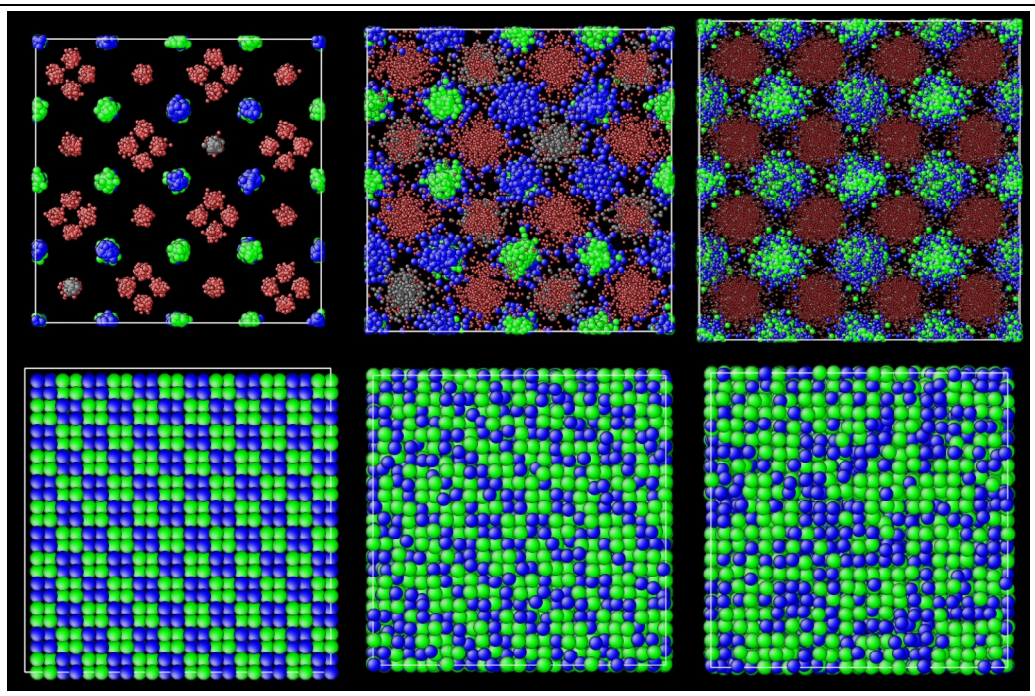

Figure 3.10: Left to right: (Left) ideal pyrochlore, (middle) RMC pyrochlore, (right) RMC fluorite. Top: RMC configuration condensed onto one unit cell for the pyrochlore configurations and a 2 × 2 × 2 supercell for the fluorite configuration. Bottom: cation arrangement on RMC supercell ($6a_p \times 6a_p \times 6a_p$ for pyrochlore and $11a_f \times 11a_f \times 11a_f$ for fluorite), where a_p~10Å and a_f ~5 Å. Bismuth blue, zirconium green, oxygen red, O' grey (pyrochlore), oxygen vacancies grey (fluorite).

Figure 3.10 shows only the final configurations from RMCProfile refinements. The fluorite arrangement of cations clearly shows clusters of Bi and Zr atoms, suggesting that it is not a completely random distribution. The pyrochlore cation arrangement shows cations are displaced from their ideal crystallographic sites, breaking the 'diagonal' motifs.

Figure 3.11a-d show the distribution of M-O-M and O-M-O angles from RMCProfile fitting, using both fluorite and pyrochlore models, compared to the angles in their respective starting configurations. In the ideal starting fluorite or pyrochlore configuration, no thermal motion is considered and all cations and anions sit on their ideal crystallographic sites.

Figure 3.11a shows the Bi-O-Bi angle distribution. The Bi-O-Bi fluorite angle distribution is slightly distorted to a lower angle (104°) than the ideal fluorite (109°), whilst the Bi-O-Bi pyrochlore angle distribution is distorted to a higher angle (96°) than the ideal pyrochlore (90°). Therefore the Bi-O-Bi angles for both fluorite and pyrochlore models fall between the ideal pyrochlore and ideal fluorite angles. Figure 3.11b shows the Zr-O-Zr angle distribution respectively. Figure 3.11b shows that the Zr-O-Zr angle from RMCProfile using the fluorite model is in good agreement with the ideal fluorite angle of 109°. RMCProfile refinements with the pyrochlore structure,

show that the Zr-O-Zr angle is distorted away from the ideal pyrochlore value of 138° to 123°, approximately midway between the expected values for the ideal pyrochlore and fluorite.

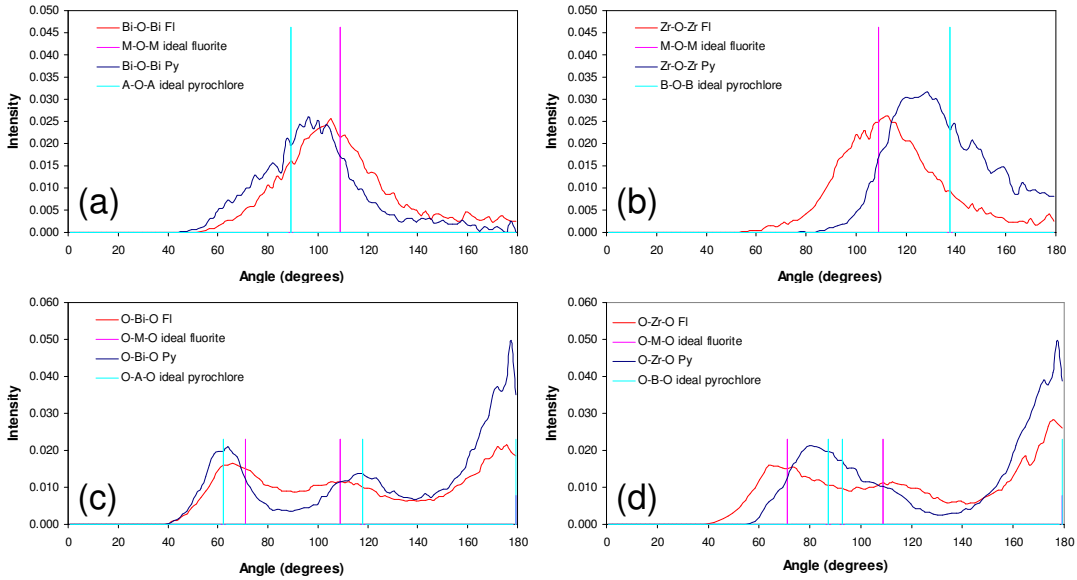

Figure 3.11 $(BiZr)_2O_7$ bond angle outputs from RMCProfile fitting. (a) Bi-O-Bi angles, (b) Zr-O-Zr angles, (c) O-Bi-O angles and (d) O-Zr-O angles. Ideal fluorite pink, ideal pyrochlore light blue. RMC fluorite red, RMC pyrochlore blue.

The O-Bi-O distributions for fluorite and pyrochlore are very similar (Figure 3.11c). Both show good agreement to their respective ideal fluorite or pyrochlore structures. The O-Zr-O angle distribution obtained is different depending on whether the fluorite or pyrochlore model is used (Figure 3.11d). One broad peak is observed for the pyrochlore model, centred at 82°, distorted from the ideal pyrochlore value of 90°. In the fluorite model, two peaks are seen, one at 71° and one at 109°, in excellent agreement with the expected fluorite values.

The angles obtained from RMC simulations with a pyrochlore configuration (indicated in Figure 3.11) show a distortion of angles away from the ideal pyrochlore values towards the angles expected for an ideal fluorite. However, when a fluorite configuration is used, there is less distortion of angles away from their ideal values. Therefore, results from our total scattering work on $(BiZr)_2O_7$ support $(BiZr)_2O_7$ having the fluorite structure.

3.6 Characterisation of $Bi_2Ti_2O_7$

3.6.1 Laboratory XRD data

The powder pattern of $Bi_2Ti_2O_7$ prepared by the precursor method described in section 3.3 is shown in Figure 3.12. Rietveld refinement was carried out using the structural model shown in Table 3.4. 18 background parameters, scale factor, specimen displacement, peak shape, an overall temperature factor, lattice parameter, y and z coordinates of the bismuth site and x coordinate of the 48f oxygen site were refined. The Rietveld fit obtained for $Bi_2Ti_2O_7$ is shown in Figure 3.12.

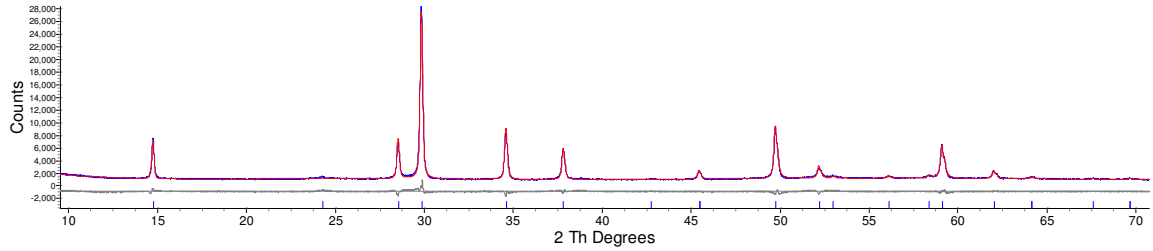

Figure 3.12: d9_03133: Rietveld refinement of $Bi_2Ti_2O_7$. R_{wp} = 4.639%, *a* = 10.3579(1) Å.

Table 3.4: Structural model used for $Bi_2Ti_2O_7$ refinements.

Atom	Site	x	y	z	Occupancy
Bi	96h	0	0.02745	0.97255	0.167
Ti	16d	0.5	0.5	0.5	1
O(1)	48f	0.125	0.125	0.43126	1
O(2)	8a	0.125	0.125	0.125	1

3.6.2 In-situ VT-PXRD data

The stability of $Bi_2Ti_2O_7$ was investigated through VT-PXRD (Figure 3.13). This showed that the product was stable up to 672 ºC. The decomposition products were determined by Rietveld refinement and found to be $Bi_4Ti_3O_{12}$ and $Bi_2Ti_4O_{11}$; however some $Bi_2Ti_2O_7$ remained until 796 ºC. This method of preparation appears to produce a more stable $Bi_2Ti_2O_7$ than that reported by Hector, which forms at 470 ºC, but begins to decompose at 480 ºC. An *in-situ* VT-PXRD study on the $Bi_2Ti_2O_7$ precursor shows that $Bi_2Ti_2O_7$ begins to form at 546 ºC.

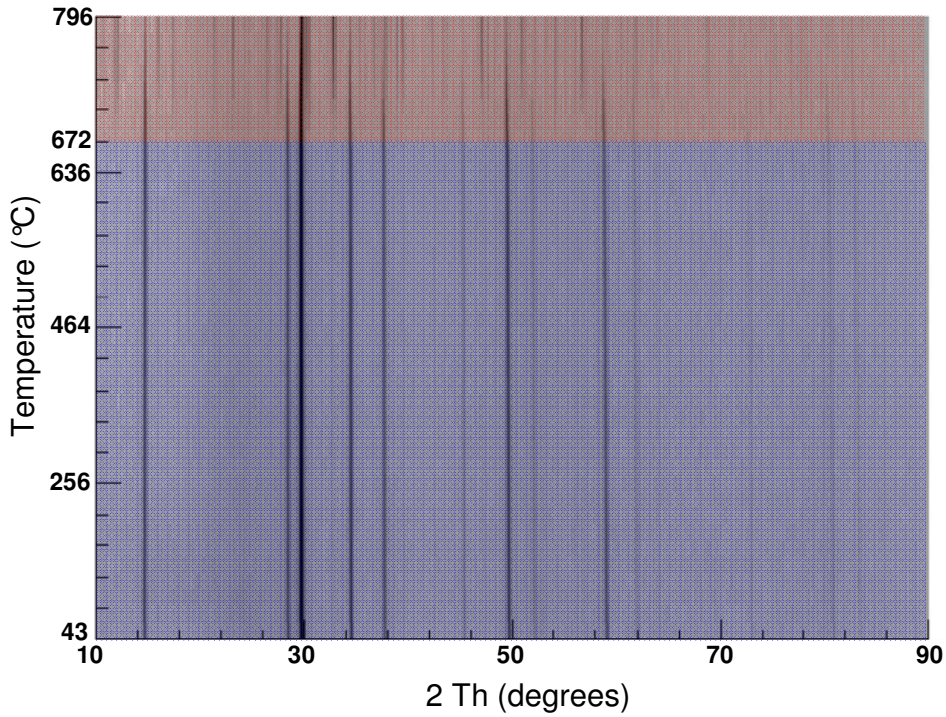

Figure 3.13: *In-situ* VT-PXRD of $Bi_2Ti_2O_7$. Decomposition occurs at 672 °C. Pale blue regions represent the stability range and the pale red regions show multiphase regions after decomposition.

3.6.3 Neutron powder diffraction data

Data were collected using the General Materials Diffractometer (GEM) at ISIS. Rietveld refinement was carried out using data from banks 3, 4, 5 and 6. 12 background parameters, absorption correction, sample peak shape, zero point error and scale factor were refined per bank. Additionally, the cell parameter, 48f oxygen x coordinate, y and z bismuth coordinates and one isotropic temperature factor per crystalllgraphic site were refined. The overall R_{wp} was 5.064 % and the fit to the bank 5 data is shown in Figure 3.14.

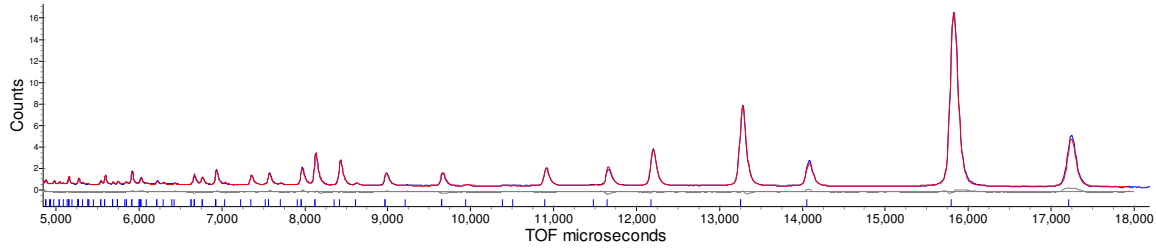

Figure 3.14: Rietveld fit to PND data obtained for $Bi_2Ti_2O_7$. Overall R_{wp} = 5.064%, *a* = 10.3480(8) Å. GEM bank 5 is shown.

3.6.4 Total scattering data

RMC refinements were carried out using a 6 × 6 × 6 pyrochlore supercell. During initial RMCProfile refinements, satisfactory fits could not be achieved when the Bragg, S(Q) and T(r) were simultaneously fitted. Therefore, in the final fits, only one T(r) (up

to 29 Å) was used in the refinements. The fit from RMCProfile refinement of $Bi_2Ti_2O_7$ using an ideal pyrochlore structure is shown in Figure 3.15. Excellent agreement between data and RMC fit was achieved.

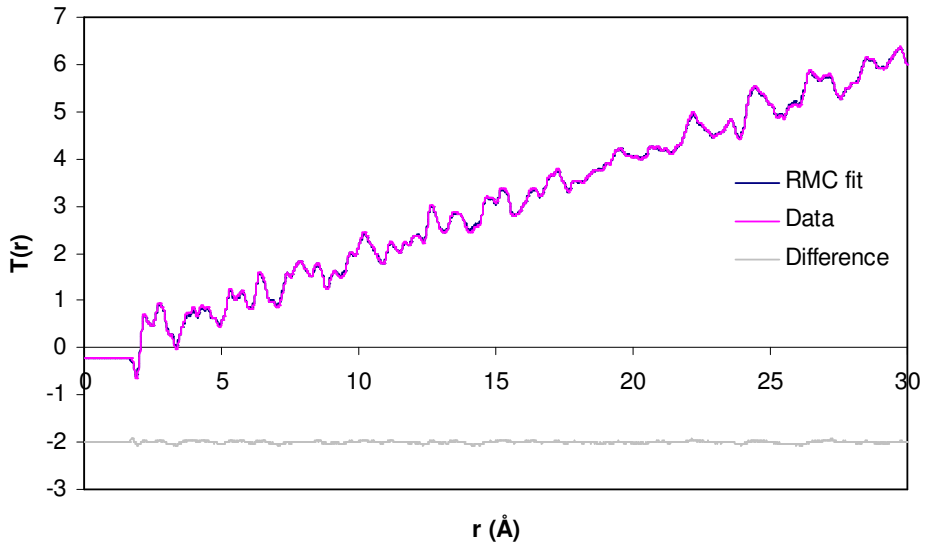

Figure 3.15: Fit to T(r) using $Bi_2Ti_2O_7$ pyrochlore starting configuration.

The bond length distributions are shown in Figure 3.16. Maxima were observed in the Ti-O distribution at 1.92 Å, in the Bi-O distribution at 2.16 Å and 2.68 Å and in the Bi-O' distribution at 2.22 Å. A second peak to the left of the peak at 1.92 Å in the Ti-O distribution was observed due to the closest approach cut-off in RMCProfile fitting. Bismuth and titanium coordination numbers were calculated using the 'coord_gen' program, which integrates under the partial g(r). This gave 5.7 Bi-O bonds, 1.9 Bi-O' bonds and 5.7 Ti-O bonds, which are slightly underestimated with respect to the ideal respective values of 6, 2 and 6. The local Bi-O environment can approximately broken up into two short bonds, with a maxima at 2.16 Å, three long bonds with a maxima at 2.68 Å and one very long bond with a maxima at 3.22 Å. The Bi-O' consists of a short bond with a maxima at 2.22 Å and a long bond with a maxima at 2.66 Å. The comparison of bond lengths from RMCProfile with those observed by Radosavljevic *et al.* is shown in Table 3.5.[5]

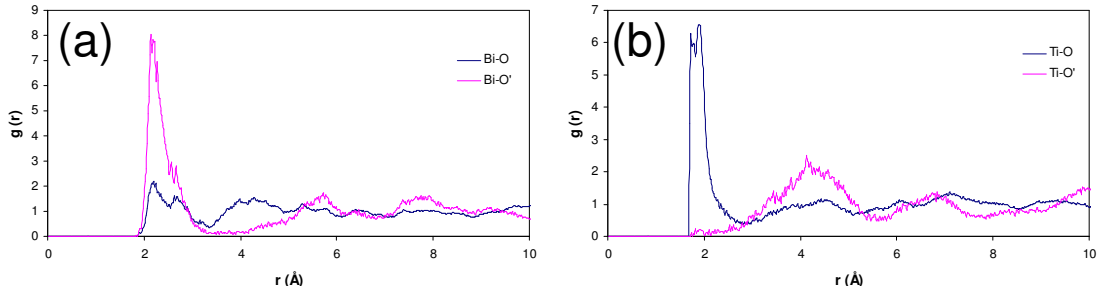

Figure 3.16: Bond length distributions obtained from $Bi_2Ti_2O_7$ RMC fit for (a) Bi-O, Bi-O', (b) Ti-O and Ti-O'.

Table 3.5: Bond length comparison for $Bi_2Ti_2O_7$ from RMCProfile refinements and published bond lengths from conventional Rietveld refinement.

	RMCProfile (Å)	Radosavljevic [5] model (Å)
Bi-O	2.16×2	2.28×2
	2.68×3	2.65×2
	3.22×1	2.97×2
Bi-O'	2.22×1	2.27×2
	2.66×1	

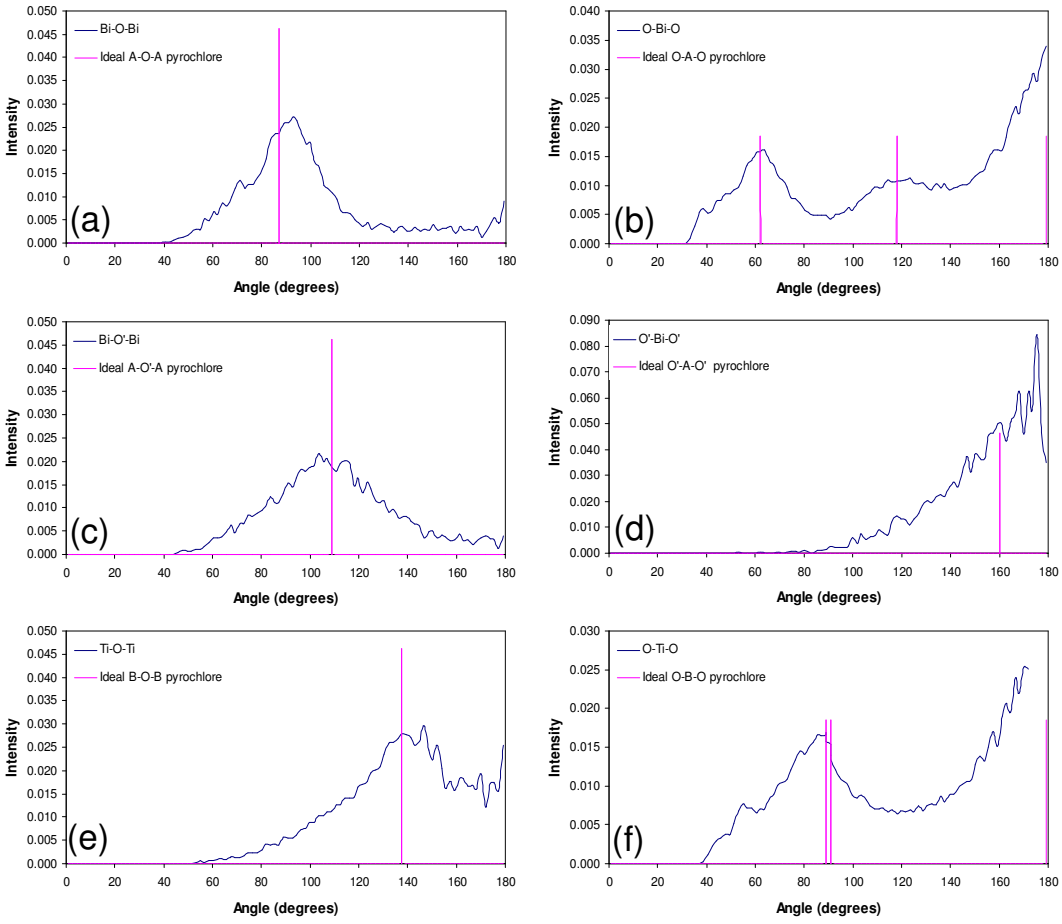

Figure 3.17: Angles from $Bi_2Ti_2O_7$ RMC output compared to ideal pyrochlore angles. (a) Bi-O-Bi, (b) O-Bi-O, (c) Bi-O'-Bi, (d) O'-Bi-O', (e) Ti-O-Ti, (f) O-Ti-O.

Figure 3.17a-f show selected angle distributions for $Bi_2Ti_2O_7$. Figure 3.17a shows a distribution of Bi-O-Bi angles centred around 98°, distorted from the ideal pyrochlore

angle of 90°. Good agreement between the RMCProfile output and the ideal pyrochlore is observed for O-Bi-O angles and Bi-O'-Bi angles (Figure 3.17b and c). The O'-Bi-O' angle distributions from RMCProfile simulations displayed a wide distribution of angles (Figure 3.17d). Rietveld refinement has shown that the O'-Bi-O' angle is distorted from its ideal angle of 180° to 160° by Radosavljevic *et al.* due to the displacement of bismuth from its three-fold axis.[5]

The Ti-O-Ti and O-Ti-O angle distributions show good agreement to the ideal pyrochlore structure (Figure 3.17e and f). The Ti-O-Ti angles in particular show a wide distribution of angles, although the maximum is centred at the expected value (Figure 3.17e). Radosavljevic *et al.* observed two different O-Ti-O angles centred around 90°, one at 92.5° and one at 87.5°, due to the value of the 48f x parameter, whilst the corresponding RMCProfile angle shows one broad angle distribution centred around 90°, with the trans oxygens centred around 180°.

Comparison of the O-O bond distributions for $(BiZr)_2O_7$ and $Bi_2Ti_2O_7$ are shown below (Figure 3.18). The $(BiZr)_2O_7$ peaks are broader than the peaks for $Bi_2Ti_2O_7$ indicating that the O-O environments are more disordered in $(BiZr)_2O_7$.

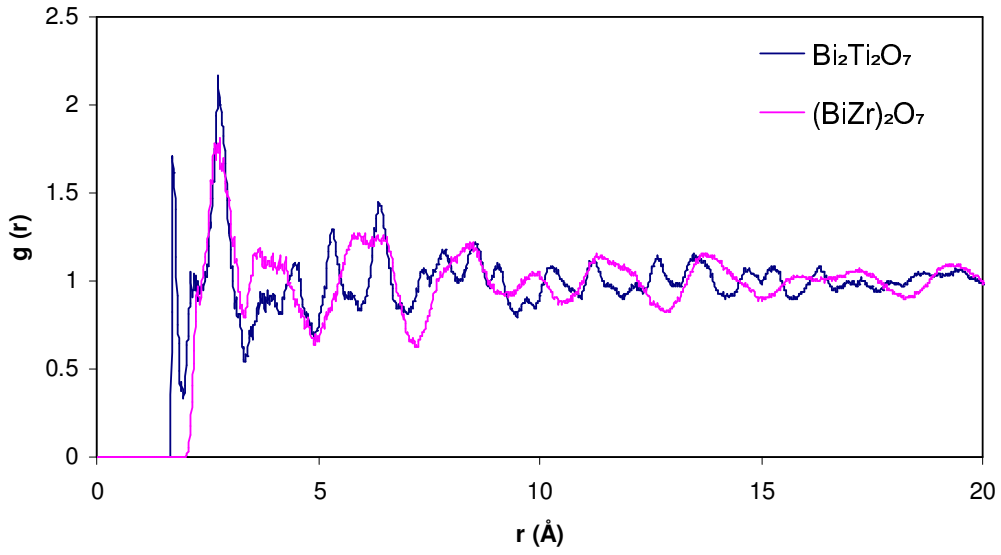

Figure 3.18: Oxygen-oxygen partial g(r) from RMCProfile refinements for $Bi_2Ti_2O_7$ and $(BiZr)_2O_7$.

The RMC configuration for $Bi_2Ti_2O_7$ is compared to the ideal pyrochlore $Bi_2Ti_2O_7$ model in Figure 3.19. It is clear to see in the $6 \times 6 \times 6$ supercell arrangement of cations, that the cations show a range of displacements compared to the ideal pyrochlore structure. This is expected as Rietveld refinement of the $Bi_2Ti_2O_7$ structure has shown

Bi^{3+} displacement from the (0,0,0) site.[4, 5] However, SHG measurements (carried out by P.S. Halasyamani) have shown that $Bi_2Ti_2O_7$ is SHG active. Even though $Bi_2Ti_2O_7$ has an average structure which can be described in centrosymmetric space group $Fd\bar{3}m$, the positive SHG signal proves that on a local scale the structure must be non-centrosymmetric, *i.e.* distorted from the ideal $Fd\bar{3}m$, as the Bragg scattering does not 'see' local disorder. This is consistent with the results of RMC modeling, which show a range of distortions from the ideal bond angles expected for a pyrochlore.

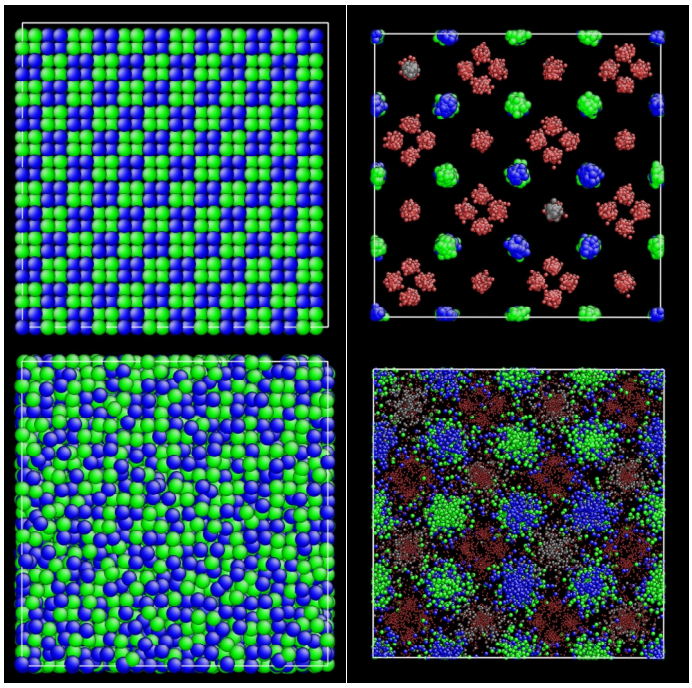

Figure 3.19: Comparison of the ideal pyrochlore structure with the RMC configuration for $Bi_2Ti_2O_7$. Top ideal pyrochlore, bottom RMC configuration of $Bi_2Ti_2O_7$. Left hand side: arrangement of cations in 6 x 6 x 6 supercell. Right hand side: RMC configuration condensed down onto one unit cell.

Second harmonic generation has also been reported for materials which have a centrosymmetric average structure, therefore the breaking of the inversion symmetry is caused by displacements on a local scale. An example of this is $Cd_2Nb_2O_7$, which is ferroelectric at low temperature.[15, 16] Below temperatures of approximately 180 K, this pyrochlore undergoes a phases transition to a tetragonal phase, with a space group of $I\bar{4}m2$, which is centrosymmetric.[16] Weller *et al.* have therefore attributed the presence of ferroelectricity to non-centrosymmetric distortions on a local scale.[16] Interestingly, a recent DFT geometry optimisation of $Bi_2Ti_2O_7$ has found the most stable structure to have non-centrosymmetric $Pna2_1$ symmetry, which supports our SHG result.[17] The $Pna2_1$ structure had two bismuth sites, and found that one shows a preference for the 96g bismuth site and the other for the 96h site (both of which are displaced from the three fold axis), but again a slight preference was observed for the 96h site.[17] A recent

PDF study on Hector's $Bi_2Ti_2O_7$ has also found a preference for the 96h crystallographic site, along with displacements of oxygen from the 8a site.[18] Using geometry optimisation, they found that $Bi_2Ti_2O_7$ with a structure *Cm* had the lowest energy and offered an improvement in the fit to the total scattering data over the average $Fd\bar{3}m$ model.[18] This also appears to be in-line with $Bi_2Ti_2O_7$ having non-centrosymmetric local distortions.

3.7 Characterisation of $Bi_2Zr_{2-x}Ti_xO_7$ mixed phases with laboratory PXRD

As there has been much interest in the literature in $M_2Zr_{2-x}Ti_xO_7$ phases, particularly with regard to their oxide ion conductivity, mixed $Bi_2Zr_{2-x}Ti_xO_7$ phases have been synthesised, in order to compare with the existing literature.[7-9, 19]

20 members of the $Bi_2Zr_{2-x}Ti_xO_7$ series (in x = 0.1 increments) have been synthesised using $Ti(OBu)_4$ as the titanium source, as described in section 3.4.3. PXRD shows a single fluorite phase for compositions up to and including x = 0.4 (see Figure 3.20a). Above this region, pyrochlore peaks start to appear. At x = 1.7 and above, a single phase pyrochlore region is present (see Figure 3.20b). The structural models used for refinement are given in Table 3.6 and Table 3.7. For all refinements (regardless of whether a fluorite or pyrochlore structure was used), 18 background terms, sample height, scale factor, peak shape, lattice parameters and an overall atomic displacement parameter were refined. For the pyrochlore, the y and z atomic coordinates of the bismuth site and the x coordinate of the 48f oxygen site were also refined.

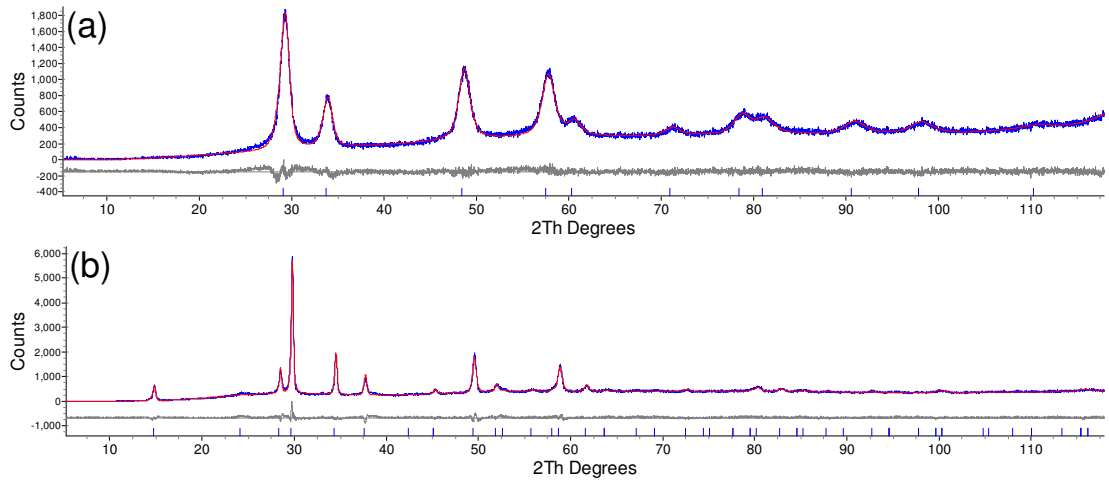

Figure 3.20: (a) d5_07560: $(BiZr_{0.8}Ti_{0.20})_2O_7$. Rietveld fit using a single fluorite model. R_{wp} = 6.913% (b) d5_07633: $Bi_2Zr_{0.3}Ti_{1.7}O_7$: Rietveld refinement using a single pyrochlore model. R_{wp} = 8.104%.

Table 3.6: Starting structural model used for refinements of mixed phases with the fluorite structure. In this case the compound is $(BiZr_{0.9}Ti_{0.1})_2O_7$.

Atom	Site	x	y	Z	Occupancy
Bi	4a	0	0	0	0.500
Zr	4a	0	0	0	0.450
Ti	4a	0	0	0	0.050
O	8c	0.25	0.25	0.25	0.875

Table 3.7: Starting structural model used for refinements of mixed phases with the pyrochlore structure. In this case the compound is $Bi_2(Zr_{0.10}Ti_{0.90})_2O_7$.

Atom	Site	x	y	z	Occupancy
Bi	96h	0	0.02745	0.97255	0.167
Ti	16d	0.5	0.5	0.5	0.900
Zr	16d	0.5	0.5	0.5	0.100
O(1)	48f	0.125	0.125	0.43126	1
O(2)	8a	0.125	0.125	0.125	1

The intermediate compositions (x = 0.5 to x = 1.6) were best modelled by the simultaneous presence of both fluorite and pyrochlore phases, as pyrochlore peaks could not be satisfactorily fitted (using either Rietveld or Pawley refinement) if only one phase was used, whilst a slight peak asymmetry on the main fluorite subcell reflections suggested the presence of two phases. Figure 3.21 show the variation of cell parameters from laboratory PXRD data, with the fluorite, pyrochlore and diphasic fluorite plus pyrochlore regions indicated. Rietveld refinement showed that cell parameters decrease approximately linearly with increasing titanium content, as expected due to the smaller size of Ti^{4+} (0.605 Å) compared to Zr^{4+} (0.72 Å, see Figure 3.21). [20] The $Bi_2Zr_{2-x}Ti_xO_7$ phase diagram is shown in Figure 3.22.

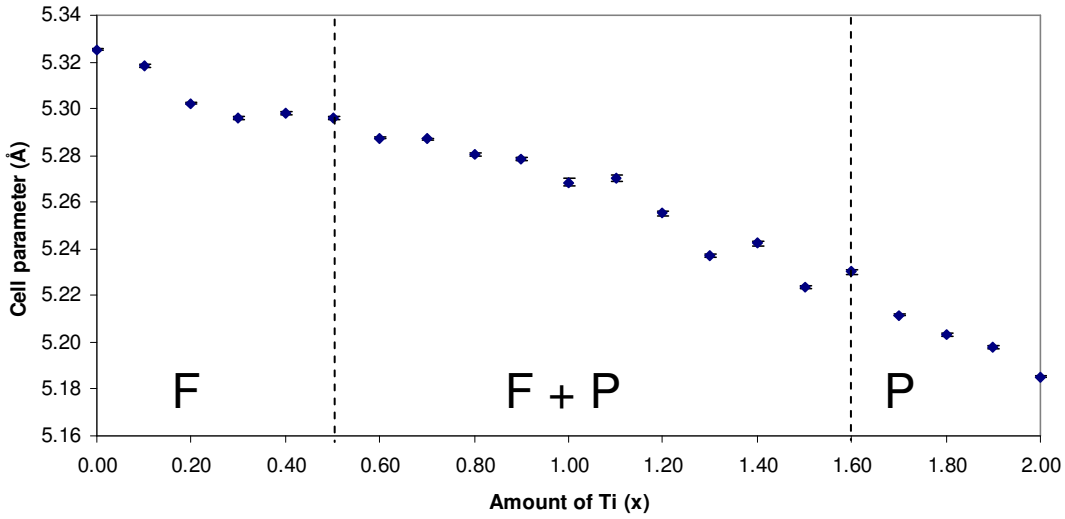

Figure 3.21: Variation of the $Bi_2Zr_{2-x}Ti_xO_7$ cell parameter with increasing titanium content. Single fluorite region is indicated by 'F', diphasic fluorite plus pyrochlore region is indicated by 'F+P' and single pyrochlore region is indicated by 'P'. For compositions with pyrochlore structure, the cell parameter was halved and for samples in the diphasic region, the cell parameter is an average of the halved pyrochlore cell parameter and the fluorite cell parameter.

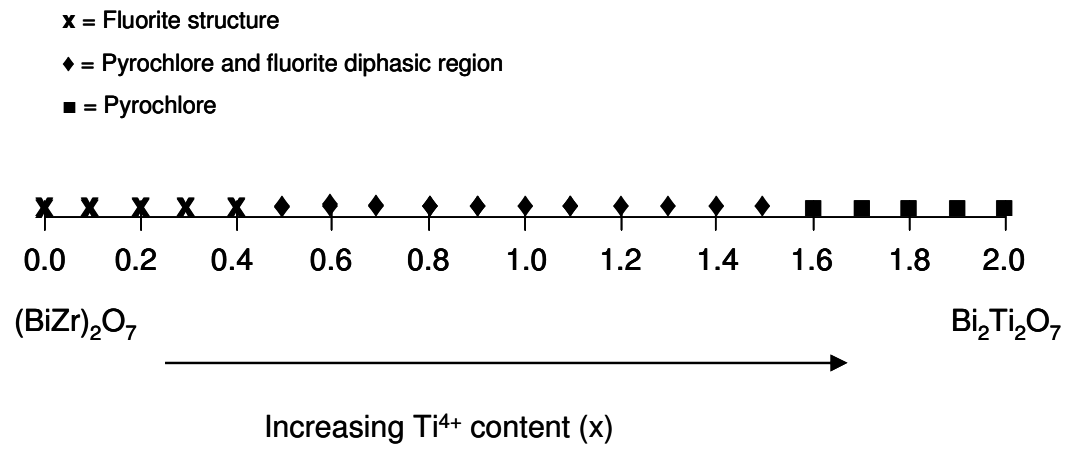

Figure 3.22: The $Bi_2Zr_{2-x}Ti_xO_7$ phase diagram. Crosses mark compositions with a fluorite structure and squares show compositions with a pyrochlore structure. Diphasic region is shown by diamonds.

Fluorite and pyrochlore phases have been found to coexist in two separate studies of the $Y_2Ti_{2-x}Zr_xO_7$ systems.[8, 21] Withers *et al.* found a diphasic fluorite – pyrochlore region between x =1.08 and x = 1.36 for the $Y_2Ti_{2-x}Zr_xO_7$ system.[21] Heremans *et al.* studied the $Y_2Ti_{2-x}Zr_xO_7$ system with powder neutron diffraction for x = 0.6, 0.9, 1.2 and 1.8.[8] The x = 0.6, 0.9 and 1.2 samples consisted of a pyrochlore phase and a small amount of fluorite phase, which had a cell parameter slightly larger than the *a*/2 of the pyrochlore. Synchrotron PXRD data of the x = 1.2 sample showed peak asymmetry, which was best modelled by using both a pyrochlore and a fluorite phase.[8] It has been suggested that the slow diffusion of cations during the synthetic process may explain formation of the diphasic pyrochlore-fluorite regions.[9] Although a precursor method followed by firing at high temperature (1350 °C) should favour the intimate mixing of cations (as employed by both Heremans *et al.* and Withers *et al.)*, in the synthetic method for $Y_2Ti_{2-x}Zr_xO_7$ outlined by Grey *et al.* single phases for compounds containing zirconium were only obtained after heating at higher temperatures of 1400 °C for 5-10 days , followed by a further firing at 1600 °C for 3 days.[8, 9, 22]

The pyrochlore-fluorite diphasic region found by Withers *et al.* and Heremans *et al.* are narrower in composition than the diphasic region we have found for the $Bi_2Ti_{2-x}Zr_xO_7$ system, although the diphasic region in the study by Heremans *et al.* is more comparable to the $Bi_2Ti_{2-x}Zr_xO_7$ system. However, in both studies, fewer compositions were structurally characterised than in our work on the $Bi_2Ti_{2-x}Zr_xO_7$ system. In the characterisation of the $Dy_2Ti_{2-x}Zr_xO_7$ system, no regions of fluorite and pyrochlore coexistence were reported.[9]

3.8 Impedance measurements

3.8.1 $Bi_2Zr_2O_7$

At low temperatures (Figure 3.23), one semi-circle arc and a shoulder at the low frequencies were observed in the complex impedance plot. The capacitance of these arcs were estimated using $\omega RC = 1$. The high frequency arc had a capacitance of 3.7 pF cm^{-1}, which was assigned to the bulk response. The shoulder was assigned to the grain boundary, given its capacitance of 8.0×10^{-10} F cm^{-1}.

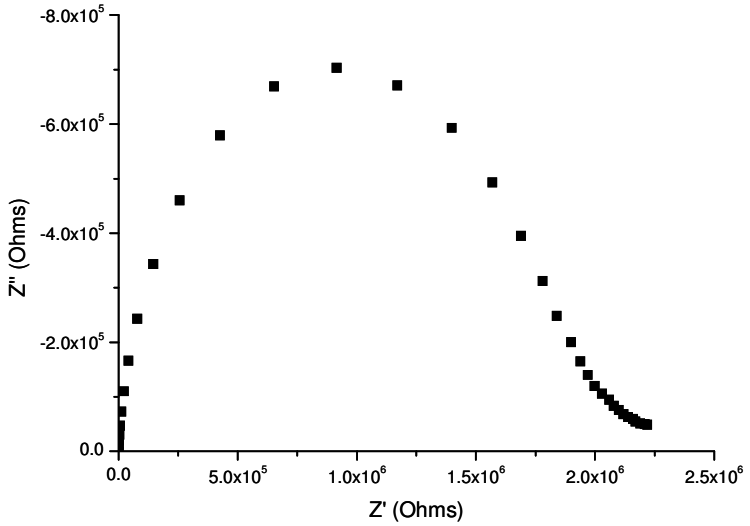

Figure 3.23: Complex impedance plot for $Bi_2Zr_2O_7$ at 259 °C.

As the materials decompose around 600 °C, impedance spectra were collected up to 578 °C. At high temperatures, the bulk response gradually disappeared and the grain boundary contribution was still visible. As no Warburg-type electrode response was observed and the capacitance at low frequencies was low, it was not immediately obvious whether the conductivity of $(BiZr)_2O_7$ was ionic. However, a study in the literature on the chemically related $Nd_2Zr_2O_7$ carried out a measurement under variable partial pressures of oxygen, which indicated that $Nd_2Zr_2O_7$ displayed oxide ion conductivity (due to the independence of conductivity with oxygen partial pressure), despite no electrode response being observed in the impedance data.[23] Therefore it is likely that there is an oxide-ion contribution to the total conductivity displayed by $(BiZr)_2O_7$.

3.8.2 $Bi_2Ti_2O_7$

At low temperature (398 °C), only one semi-circle arc was observed (Figure 3.24). This arc has a capacitance of 6.4×10^{-12} F cm^{-1} and has been assigned to the bulk.

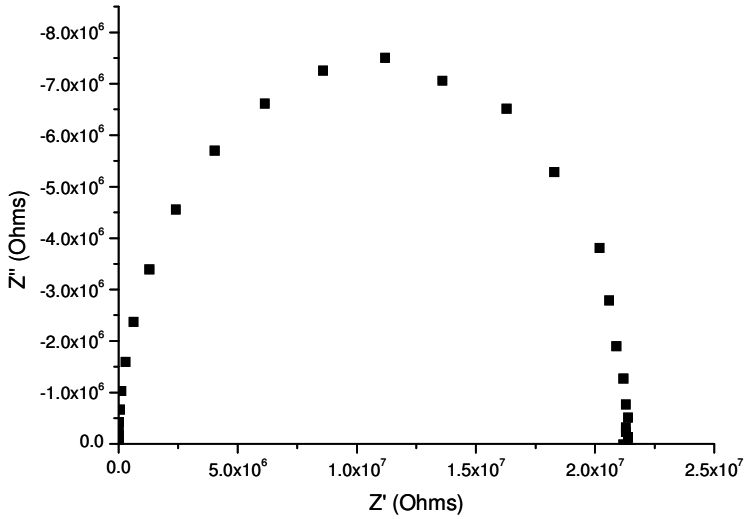

Figure 3.24: Complex impedance plot for $Bi_2Ti_2O_7$ at 398 °C.

At high temperatures (568 °C), only one semi-circle arc is observed, which had a capacitance of 8.1×10^{-12} F cm^{-1} (estimated using $\omega RC = 1$), typical of the bulk component. No significant electrode response was observed and at low frequencies the capacitance remained of the order of magnitude 10^{-9}-10^{-10} F cm^{-1}, indicating that oxide ion conductivity is not dominant.

3.8.3 Discussion

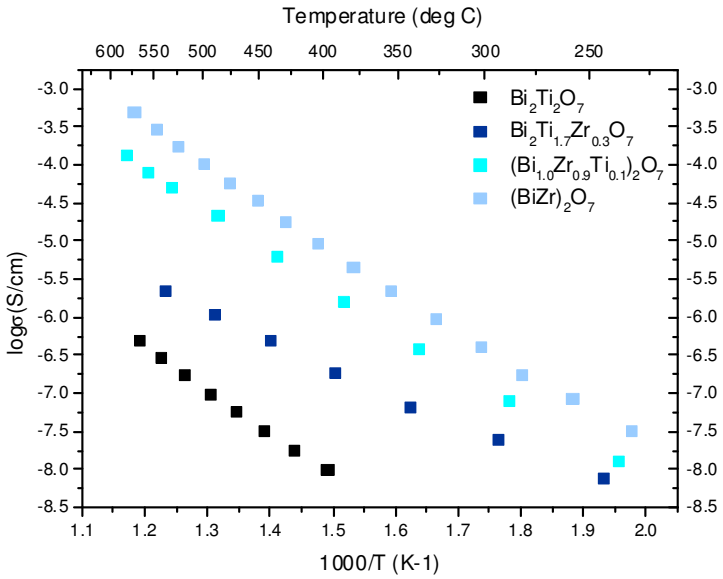

Figure 3.25: Variation of conductivity with temperature for members of the $Bi_2Zr_{2-x}Ti_xO_7$ system.

Figure 3.25 shows the variation of conductivity with temperature of pure single phase materials with compositions $Bi_2Ti_2O_7$, $Bi_2Ti_{1.7}Zr_{0.3}O_7$, $(BiZr_{0.9}Ti_{0.1})_2O_7$ and $(BiZr)_2O_7$. Pyrochlore $Bi_2Ti_2O_7$ was found to have the lowest conductivity of 5.1×10^{-7} S cm^{-1} at 568 °C. Doping with increasing amounts of Zr^{4+} resulted in a significant increase in conductivity, of a maximum 3 orders of magnitude, with the highest conductivity being obtained for $(BiZr)_2O_7$ (5.0×10^{-4} S cm^{-1} at 574 °C). This large increase in conductivity is probably due to the increase in ionic contribution to the total conductivity as a result of the structural change from pyrochlore to fluorite. Pyrochlore $Bi_2Ti_2O_7$ has an ordered array of oxide ions, but $(BiZr)_2O_7$ which crystallises as a fluorite, has the anions disordered. The increase in conductivity when Ti^{4+} is replaced by Zr^{4+} has also been reported in other $M_2Ti_{2-x}Zr_xO_7$ system, where M = Y^{3+}, Gd^{3+} and Dy^{3+}. [24] Conductivity values around 540 °C are summarised in Table 3.8.

Table 3.8: Conductivities of $Bi_2Zr_{2-x}Ti_xO_7$ samples around 540 °C.

Compound	Conductivity (S cm^{-1})	Temperature (°C)	Activation energy (eV)
$(BiZr)_2O_7$	3.0×10^{-4}	549	1.12(1)
$(Bi_{1.0}Zr_{0.9}Ti_{0.1})_2O_7$	5.1×10^{-5}	533	1.07(9)
$Bi_2Ti_{1.7}Zr_{0.3}O_7$	2.3×10^{-6}	540	0.75(2)
$Bi_2Ti_2O_7$	3.0×10^{-7}	544	1.18(2)

The conductivity displayed by the $Bi_2Zr_{2-x}Ti_xO_7$ system is low with respect to other pyrochlores. The low decomposition temperatures limit the conductivity range that can be explored. Extrapolation of the conductivity data for $(BiZr)_2O_7$ shows that a conductivity of 4.8×10^{-2} S cm^{-1} at 1000 °C (and 8.2×10^{-3} S cm^{-1} at 800 °C) would have been achieved had decomposition not occurred and this would have been comparable to other good $A_2B_2O_7$ oxide ion conductors.

Table 3.6 also shows the activation energies for the compounds studied in the $Bi_2Zr_{2-x}Ti_xO_7$ system, calculated from the 300 °C to 600 °C temperature range. These activation energies are typical to values found in the literature for pyrochlore and fluorite oxide ion conductors. For example, $Gd_2Zr_{2-x}Ti_xO_7$ has an activation energy which remains almost constant throughout the entire range of x = 0.0-2.0, at 0.8-0.9 eV.[25] The activation energy of $Gd_2(Zr_{1-x}Sn_x)O_7$ increases over the range 0.9-1.6 eV as the Sn^{4+} content is increased.[25]

3.9 Conclusions

Structural characterisation of $(BiZr)_2O_7$ and $Bi_2Ti_2O_7$ has been carried out using PXRD and total scattering data. $Bi_2Ti_2O_7$ is SHG active, which is only possible in space group $Fd\bar{3}m$ when there is a net displacement of cations from their ideal sites on a local scale, due to the destruction of the overall centre of inversion symmetry.

Compounds of the formula $Bi_2Zr_{2-x}Ti_xO_7$ have been synthesised and characterised for the first time. In the $Bi_2Zr_{2-x}Ti_xO_7$ structure, zirconium rich compositions have the fluorite structure up to x = 0.4. Titanium rich samples have the pyrochlore structure, in the region x = 1.7 to x = 2.0. Compounds in the intermediate composition region are a mixture of fluorite and pyrochlore phases.

Doping Zr^{4+} into $Bi_2Ti_2O_7$ increases the conductivity, with $(BiZr)_2O_7$ displaying a three-fold order of magnitude increase over $Bi_2Ti_2O_7$. The higher conductivity of $(BiZr)_2O_7$ with respect to $Bi_2Ti_2O_7$ is comparable to other $M_2Ti_{2-x}Zr_xO_7$ systems.[8, 9, 20]

3.10 References

1. S. L. Sorokina and A. W. Sleight, *Mat. Res. Bull.*, 1998, **33**, 1077-1081.
2. I. Abrahams, A. J. Bush, S. C. M. Chan, F. Krok and W. Wrobel, *J. Mater. Chem.*, 2001, **11**, 1715-1721.
3. I. de Meatza, J. P. Chapman, F. Mauvy, J. I. R. de Larramendi, M. I. Arriortua and T. Rojo, *Mater. Res. Bull.*, 2004, **39**, 1841-1847.

4. A. L. Hector and S. B. Wiggin, *J. Solid State Chem.*, 2004, **177**, 139-145.
5. I. Radosavljevic, J.S.O. Evans and A. W. Sleight, *J. Solid State Chem.*, 1998, **136**, 63-66.
6. T. A. Vanderah, I. Levin and M. W. Lufaso, *Eur. J. Inorg. Chem.*, 2005, 2895-2901.
7. B. J. Wuensch, K. W. Eberman, C. Heremans, E. M. Ku, P. Onnerud, E. M. E. Yeo, S. M. Haile, J. K. Stalick and J. D. Jorgensen, *Solid State Ionics*, 2000, **129**, 111-133.
8. C. Heremans, B. J. Wuensch, J. K. Stalick and E. Prince, *J. Solid State Chem.*, 1995, **117**, 108-121.
9. K. J. Moreno, M. A. Guevara-Liceaga, A. F. Fuentes, J. Garcia-Barriocanal, C. Leon and J. Santamaria, *J. Solid State Chem.*, 2006, **179**, 928-934.
10. D. Chen and R. Xu, *Mater. Res. Bull.*, 1998, **33**, 409-417.
11. Y. C. Mao, G. S. Li, X. Y. Sun and S. H. Feng, *J. Solid State Chem.*, 2000, **149**, 314-319.
12. K. K. Rao, T. Banu, M. Vithal, G. Swamy and K. R. Kumar, *Mater. Lett.*, 2002, **54**, 205-210.
13. E. R. Camargo, J. Frantti and M. Kakihana, *J. Mater. Chem.*, 2001, **11**, 1875-1879.
14. A. Gulino, S. LaDelfa, I. Fragala and R. G. Egdell, *Chem. Mater.*, 1996, **8**, 1287-1291.
15. F. Jona, G. Shirane and R. Pepinsky, *Phys. Rev.*, 1955, **98**, 903-909.
16. M. T. Weller, R. W. Hughes, J. Rooke, C. S. Knee and J. Reading, *Dalton Trans.*, 2004, 3032-3041.
17. C. H. Patterson, *Phys. Rev. B*, 2010, **82**.
18. D. P. Shoemaker, R. Seshadri, A. L. Hector, A. Llobet, T. Proffen and C. J. Fennie, *Phys. Rev. B*, 2010, **81**.
19. P. K. Moon and H. L. Tuller, *Solid State Ionics*, 1988, **28**, 470-474.
20. R. D. Shannon, *Acta Crystallogr. A*, 1976, **32**, 751-767.
21. Y. Liu, R. L. Withers and L. Noren, *J. Solid State Chem.*, 2004, **177**, 4404-4412.
22. N. Kim and C.P.Grey, *J. Solid State Chem.*, 2003, **175**, 110-115.
23. H. Yamamura, H. Nishino, K. Kakinuma and K. Nomura, *Solid State Ionics*, 2003, **158**, 359-365.
24. S. Kramer, M. Spears and H. L. Tuller, *Solid State Ionics*, 1994, **72**, 59-66.
25. T. H. Yu and H. L. Tuller, *Solid State Ionics*, 1996, **86-8**, 177-182.

4 Structure Solution of β-$Bi_2Sn_2O_7$ and Properties of $Bi_2Sn_2O_7$ Based Materials

4.1 Background

$Bi_2Sn_2O_7$ has three known polymorphs (Figure 4.1). [1] Above 680 °C, the high temperature γ form is stable. It has the pyrochlore structure (with a = 10.73 Å and V ≈ 1240 Å^3) and shows a displacement of the Bi^{3+} cation from the ideal A cation site, on the body diagonal of the cube. [2] The room temperature α form was initially indexed to a body-centred tetragonal cell with a = 15.05 Å, c = 21.5 Å and V ≈ 4900 Å^3, related to the γ-$Bi_2Sn_2O_7$ polymorph via a $\sqrt{2}a \times \sqrt{2}a \times 2a$ transformation matrix.[1] The structure has since been shown to have a complex monoclinic structure (although the cell parameters still correspond very closely to the $\sqrt{2}a \times \sqrt{2}a \times 2a$ distortion), with 176 atoms in the asymmetric unit, adopting the *Pc* space-group.[3] α-$Bi_2Sn_2O_7$ undergoes a phase transition to the β form at 90 °C.[1] The β-$Bi_2Sn_2O_7$ structure has not been reported in the literature; however, it could be indexed to a face centred cubic cell with a = 21.4 Å and V ≈ 9800 Å^3 (*i.e.* double the cell parameter of γ-$Bi_2Sn_2O_7$). [1, 3]

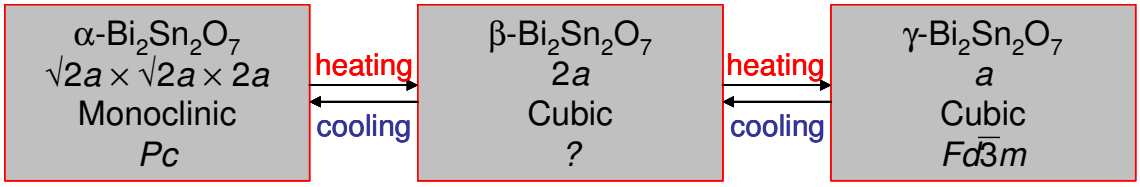

Figure 4.1: Phase transformations of $Bi_2Sn_2O_7$.[1-3]

No characterisation of the conductivity of $Bi_2Sn_2O_7$ has been reported in the literature to date. Therefore one of our aims was to explore both isovalent and aliovalent doping in $Bi_2Sn_2O_7$ by doping the Bi^{3+} site with Ca^{2+} and the Sn^{4+} site with Zr^{4+}. As an example of isovalent doping, it was shown in Chapter 3, that doping the B cation site in insulating $Bi_2Ti_2O_7$ with Zr^{4+} resulted in a structural change and a significant increase in ionic conductivity, of two to three orders of magnitude depending on the exact composition. The similarity of the ionic radii of Zr^{4+} (0.72 Å) and Sn^{4+} (0.69 Å) allows both ions to occupy the same crystallographic site. [4] This has been reported in several pyrochlores, such as the $Y_2(Zr_ySn_{1-y})_2O_7$ and $Gd_2Sn_{2-x}Zr_xO_7$ system studied by Wuensch.[5] The oxide ion conductivity of $Gd_2Sn_{2-x}Zr_xO_7$ increased with Zr^{4+} content.[6] Increasing the amount of Zr^{4+} in $Bi_2Sn_{2-x}Zr_xO_7$ increases the average B site

radius, which results in the radius ratio (r_A/r_B) decreasing and this may induce a transition to the fluorite structure type.

There are many literature examples of aliovalent doping increasing conductivity. $Yb_{1.8}Ca_{0.2}Ti_2O_{6.9}$ displays an oxide ion conductivity of 0.2 S cm^{-1} at 1000 °C which is the highest known conductivity for a pyrochlore.[7] $Gd_{1.8}Ca_{0.2}Ti_2O_{6.9}$ displays a high conductivity of 5×10^{-2} S cm^{-1} at 1000 °C, which is one of the highest conductivities observed for a pyrochlore, 2.5 orders of magnitude higher than $Gd_2Ti_2O_7$.[8,9] Low levels of Al^{3+} on the titanium site also increases conductivity in $Gd_2Ti_2O_7$.[9] Another example is in the calcium doped perovskites, $BaTi_{1-x}Ca_xO_{3-x}$, which exhibit higher conductivities than pure $BaTiO_3$. [10] In eight fold coordination, Ca^{2+} has a slightly smaller ionic radius of 1.12 Å compared to Bi^{3+}, which measures 1.17 Å.[4] This allows both Ca^{2+} and Bi^{3+} to occupy the same crystallographic site, which has been reported in the synthesis of a number of bismuth/calcium/vanadium oxides.[11,12,13] The aim of doping the bismuth site with calcium in $Bi_2Sn_2O_7$ was therefore to create oxide vacancies, in order to increase the conductivity.

Another factor which may influence the structure and properties of these materials, in addition to cation sizes and cation oxidation states, is the chemical nature of the cation. By carefully selecting cation combinations, it is possible to create compounds with an average site radius identical or close to radii of other cations. For example, a recent study showed that Pm^{3+} has an ideal radius to be doped into CeO_2, but as it is radioactive, a 1:1 ratio of Sm^{3+} and Nd^{3+} could be used instead.[14] Finally, this chapter looks at Bi_2ScNbO_7, as in six fold coordination the radii of Sc^{3+} to Nb^{5+} are 0.745 Å and 0.64 Å, respectively, so a 1:1 ratio of Sc^{3+} and Nb^{5+} gives an average radius of 0.693 Å, which is essentially identical to the ionic radius of Sn^{4+} (0.69 Å). Therefore the conductivity of $Bi_2Sn_2O_7$ and Bi_2ScNbO_7 can be compared along with that of doped analogues. The B-site cation stoichiometry and therefore the average B-site oxidation state may be also varied, thus controlling the oxygen content. This will create $Bi_2Sc_{1\pm x}Nb_{1\pm x}O_{7\pm\delta}$ phases with either oxygen excess or oxygen deficiency, depending on the ratio of Sc^{3+}: Nb^{5+}.

The aim of this chapter was firstly to attempt structure solution of β-$Bi_2Sn_2O_7$ from PND and synchrotron PXRD data. Secondly, the aim was to investigate the effect of aliovalent and isovalent doping in $Bi_2Sn_2O_7$ with Ca^{2+} and Zr^{4+} respectively. Finally,

the effect of the chemical nature of the cation on conductivity will be explored through comparison of Bi_2ScNbO_7 and related phases with $Bi_2Sn_2O_7$.

4.2 Synthesis of $Bi_2Sn_2O_7$

4.2.1 Conventional solid state synthesis

Stoichiometric quantities of Bi_2O_3 (1.214 g, 2.61 mmol) and SnO_2 (0.786 g, 5.22 mmol) required to make 2.00 g of product were intimately ground in a pestle and mortar and fired at 1100 °C for 16 h, following the procedure by Evans *et al.*.[3] The $Bi_2Sn_2O_7$ sample used for I11 data collection was the same as that used in 2003 to collect HRPD data and was calcined at 950 °C for 25 h to remove any absorbed impurities.

4.2.2 I11 synchrotron VT-PXRD data collection

Synchrotron PXRD data were collected using 0.3 mm borosilicate capillaries and a range of 2°-140° 2θ for all datasets. A two hour room temperature dataset and a four hour dataset at 470 K were collected for α-$Bi_2Sn_2O_7$ and β-$Bi_2Sn_2O_7$ respectively. Heating data were collected in the range 300 K - 490 K and cooling data in the range 470 K - 250 K, using a data collection time of two minutes per scan. A Cryostream Plus N_2 blower was used to control the temperature.

4.3 Structure solution of β-$Bi_2Sn_2O_7$

4.3.1 VT synchrotron PXRD data

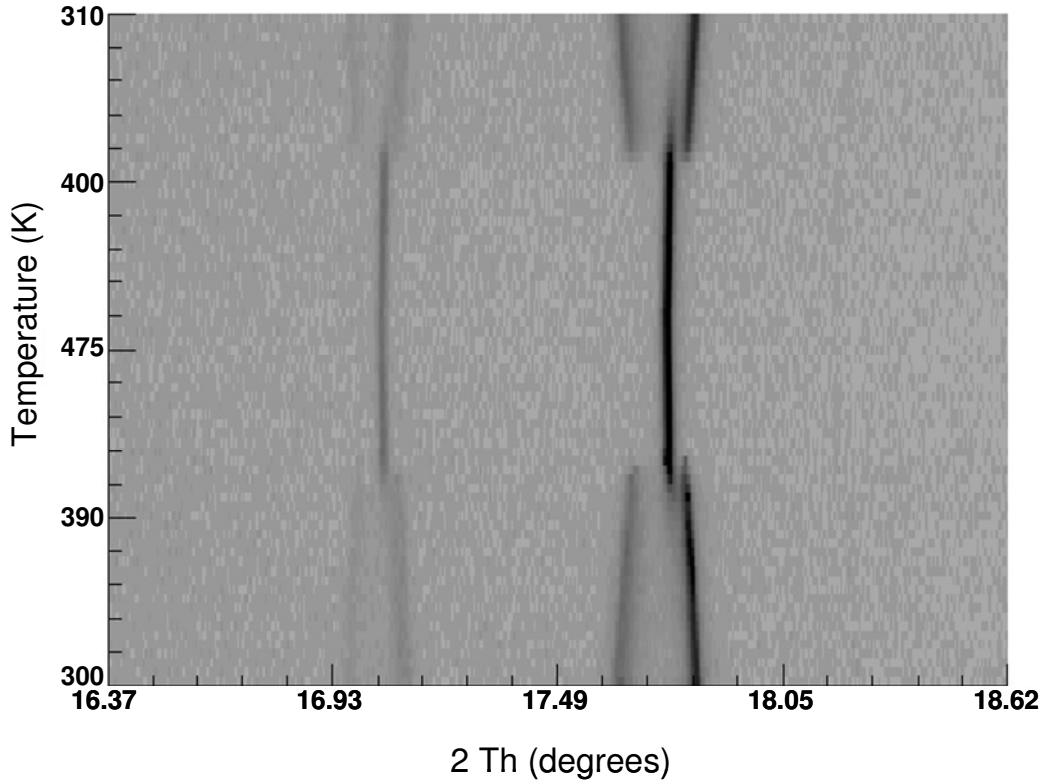

Figure 4.2: A small 2θ region of the heating and cooling I11 *in-situ* VT-PXRD data showing the α-$Bi_2Sn_2O_7$ - β-$Bi_2Sn_2O_7$ phase transition.

Figure 4.2 shows a Powder3D plot of the VT synchrotron PXRD data on heating and cooling $Bi_2Sn_2O_7$, in the region of the $\alpha - \beta$–$Bi_2Sn_2O_7$ transition. As the temperature increases, two peaks centred around 17.7° 2θ (present in the α-$Bi_2Sn_2O_7$ phase), merge into one peak for the β-$Bi_2Sn_2O_7$ phase at 420 K. Figure 4.2 also shows that there is a region where both the α and β phases coexist. This was found to be between 390 K and 415 K. As the temperature decreases, the single peak close to 17.7 ° 2θ (from β-$Bi_2Sn_2O_7$) splits into two at 395 K showing that the α –$Bi_2Sn_2O_7$ to β–$Bi_2Sn_2O_7$ transition is reversible and that again, there is a diphasic region, where both the α- and β-$Bi_2Sn_2O_7$ polymorphs are present. At temperatures of 335 K and lower, only α-$Bi_2Sn_2O_7$ is present. The diphasic region and hysteresis in phase transition temperature, indicate that this is a first order phase transition.

Analysis of the VT data was carried out using 'Multitopas_files', an in-house routine for sequential Rietveld refinement.[15] The α-$Bi_2Sn_2O_7$ structural model and the cooling

data were used. 15 background parameters, zero point, one overall isotropic temperature factor and cell parameters (*a*,*b*,*c* and β) were refined. The data analysis was split into two regions, one at low temperatures where the α-$Bi_2Sn_2O_7$ phase was present, and one at high temperature, where β-$Bi_2Sn_2O_7$ was present. The α-$Bi_2Sn_2O_7$ model was used for both the α- and β-$Bi_2Sn_2O_7$ phases. Figure 4.3 shows the variation of cell parameters with temperature for both α- and β-$Bi_2Sn_2O_7$. Of particular note is the difference between the *a* and *b* cell parameters (blue and pink) of β-$Bi_2Sn_2O_7$, indicating that the cell cannot be tetragonal.

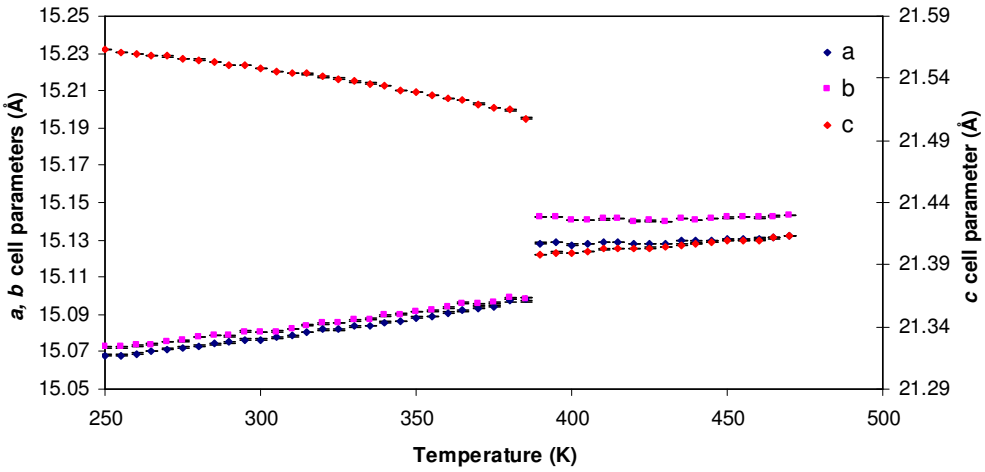

Figure 4.3: Variation of *a*, *b* and *c* cell parameters of $Bi_2Sn_2O_7$ with temperature.

Figure 4.4a shows the variation of cell volume with temperature. A discontinuity of volume is observed at the α-β-$Bi_2Sn_2O_7$ phase transition, which is in-line with previously published data for α-$Bi_2Sn_2O_7$.[3] Figure 4.4b shows the variation of the beta angle with temperature. As the temperature increases, the α-$Bi_2Sn_2O_7$ beta angle increases, until it approaches, but does not reach 90.0° after the phase transition, when only β-$Bi_2Sn_2O_7$ is present. This suggests that β-$Bi_2Sn_2O_7$ is not cubic, tetragonal or orthorhombic.

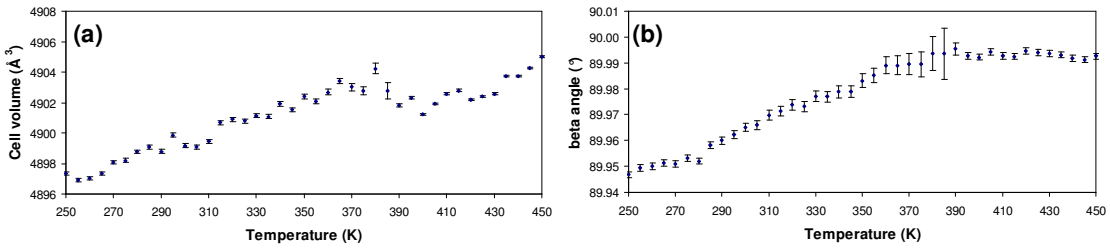

Figure 4.4: Variation of (a) volume and (b) β angle in $Bi_2Sn_2O_7$ with temperature.

4.3.2 Pawley fits of β-$Bi_2Sn_2O_7$

Although the structure of β-$Bi_2Sn_2O_7$ is unknown, it was indexed to a cubic unit cell using single crystal XRD data, with a = 21.4 Å by Sleight *et al.*.[1] Following the collection of synchrotron powder XRD data, the first stage in the structure solution was to determine the metric symmetry. One of the proposed space groups for β-$Bi_2Sn_2O_7$ was $F\bar{4}3c$, with a $2a \times 2a \times 2a$ relationship to the pyrochlore γ-$Bi_2Sn_2O_7$.[16] A Pawley refinement was carried out in space group $F\bar{4}3c$, using a cubic lattice parameter of approximately 21.4 Å and 12 background terms with I11 data. On closer inspection, it was immediately obvious that there were not only extra weak reflections present that are not fitted by $F\bar{4}3c$, but peak splitting, implying a lower symmetry. This is shown in Figure 4.5, in expanded sections of the Pawley fit.

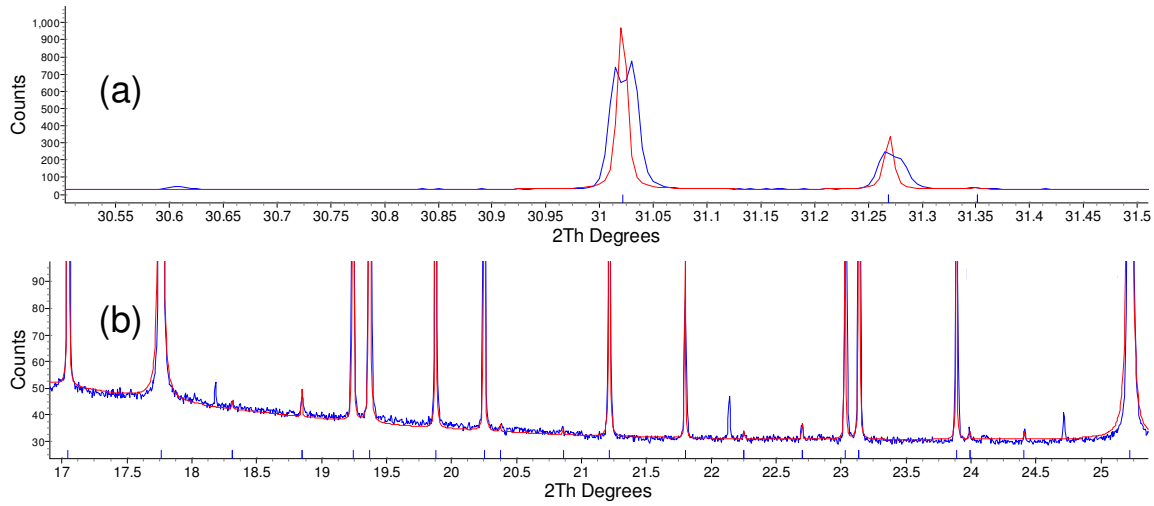

Figure 4.5: Zoomed regions of Pawley fit for β-$Bi_2Sn_2O_7$ in space group $F\bar{4}3c$. (a) Unaccounted peak splitting and (b) un-fitted peaks indicate that $F\bar{4}3c$ cannot be the correct space group.

A Pawley fit was attempted in $P23$, the lowest symmetry cubic space group, using the same parameters and $2a \times 2a \times 2a$ cell as described above for $F\bar{4}3c$. The peaks that were unaccounted for in Figure 4.5b using $F\bar{4}3c$ were fitted in $P23$. Peak splitting was still observed and could not be accounted for in this space group (see Figure 4.6). Therefore, despite being thought to be cubic for many years, β-$Bi_2Sn_2O_7$ cannot be cubic.[1, 16] Pawley fits were then carried out in the lowest symmetry tetragonal space group, $P4$ and the lowest symmetry orthorhombic space group, $P222$ using the same parameters as in earlier Pawley fits. Cell parameters were changed from the $2a \times 2a \times 2a$ cell originally thought for 'cubic' β-$Bi_2Sn_2O_7$ to the $\sqrt{2}a \times \sqrt{2}a \times 2a$ cell which describes α-$Bi_2Sn_2O_7$. The $\sqrt{2}a \times \sqrt{2}a \times 2a$ cell was slightly distorted prior to the Pawley refinement in $P222$, so that $a \neq b$, as required for orthorhombic symmetry.

Figure 4.6 shows the fit to the 31° peak for *P*23, *P*4 and *P*222 and it is clear to see that in *P*23 and *P*4, only one peak has been calculated at this position, hence the structure cannot be cubic or tetragonal, which is consistent with the results from the variable temperature experiment. In *P*222 two peaks were calculated at 31°. As all extra peaks and peak splitting could be accounted for in *P*222, the metric symmetry of β-$Bi_2Sn_2O_7$ is orthorhombic (Figure 4.6c).

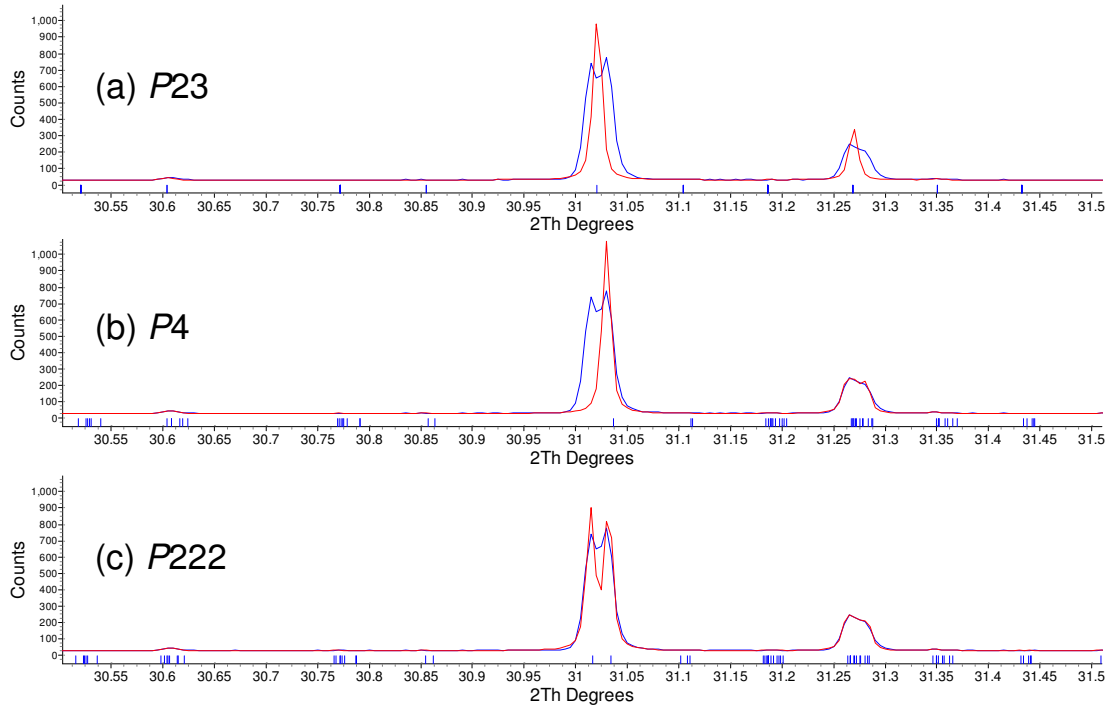

Figure 4.6: Pawley fits of β-$Bi_2Sn_2O_7$. Fit to 31° peak in space groups (a) *P*23 (cubic), (b) *P*4 (tetragonal), (c) *P*222 (orthorhombic).

SHG measurements by Sleight *et al.* indicated that β-$Bi_2Sn_2O_7$ is non-centrosymmetric, hence β-$Bi_2Sn_2O_7$ cannot belong to space group *P*222.[1] Possible orthorhombic non-centrosymmetric space groups, which are sub-groups of $Fd\bar{3}\,m$ and consistent with this √2a × √2a × 2a transformation were identified using 'isodisplace', following symmetry descent from the high temperature, high symmetry pyrochlore γ-$Bi_2Sn_2O_7$.[17]

4.3.3 Structure solution of β-$Bi_2Sn_2O_7$ using simulated annealing in orthorhombic and monoclinic and space groups

The pyrochlore γ-$Bi_2Sn_2O_7$ structure was transformed into the allowed ten orthorhombic space groups (all non-centrosymmetric sub-groups of $Fd\bar{3}\,m$) using 'isodisplace'.[17] The space groups used were *Pmm*2, *Pmc*2_1, *Pcc*2, *Pma2*, *Pca*2_1, *Pnc*2, *Pmm*2_1, *Pba*2, *Pna*2_1 and *Pnn*2.

Structure solution was attempted using simulated annealing with both synchrotron PXRD (I11) and PND (HRPD) data. Neutron data were collected in 2003 by I. Evans. Only data from the HRPD backscattering bank were used due to its high resolution. For the I11 synchrotron PXRD data, 16 background parameters were used, whilst a total of six were used for the HRPD PND data. Peak shapes were fixed at the values obtained from a Pawley fit using the appropriate space group, for both I11 and HRPD data. Scale factor, cell parameters and one isotropic temperature factor per atom type were refined. As the orthorhombic space groups are polar and therefore have floating origins in the z direction, the z coordinate of Bi1 was fixed in every input file to fix the origin. The remainder of the coordinates were allowed to deviate 0.5 Å from their ideal crystallographic sites. Bond length restraints were used for Bi-O, Bi-O', Sn-O, Sn-O', O-O, O-O' and O'-O' distances, which prevented bond lengths from becoming too small. 10000 iterations of annealing were carried out, which took approximately one day on a PC. Figure 4.7a shows the variation in R_{wp} for each of the 10 orthorhombic space groups for the 20 solutions with the lowest R_{wp}.

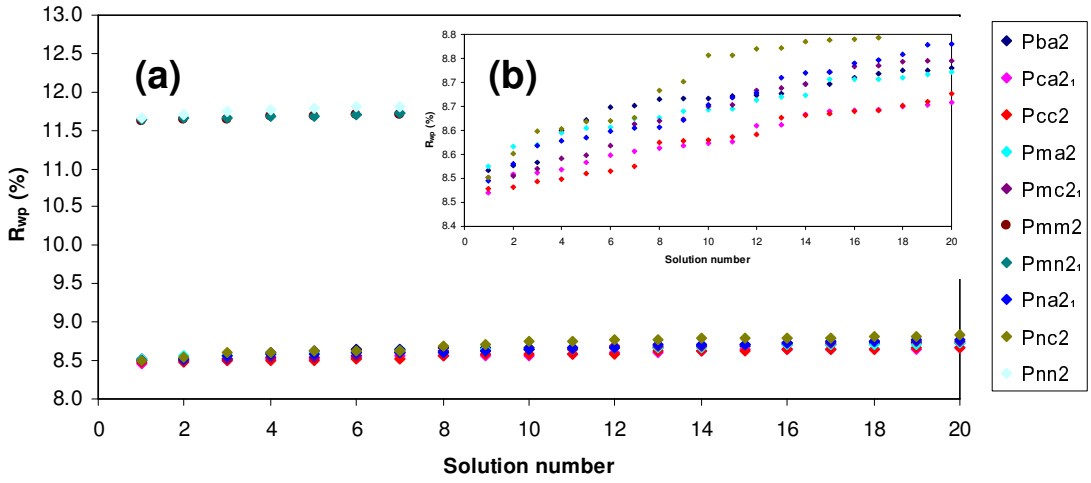

Figure 4.7: Simulated annealing of β-$Bi_2Sn_2O_7$: 20 solutions with the lowest R_{wp} for (a) 10 orthorhombic space groups (b) orthorhombic space groups excluding *Pnn*2, *Pmm*2 and *Pmn*2_1.

Figure 4.7a shows that the orthorhombic space groups could be divided into two groups: one containing only *Pnn*2, *Pmm*2 and *Pmn*2_1 space groups which had solutions with a high R_{wp} around 11.5% and a second group containing the remaining space groups with R_{wp}'s around 8.5%. Figure 4.7b shows that the R_{wp}'s of the remaining orthorhombic space groups are very similar. To try and distinguish between the space groups, the visual quality of fit was inspected. Diagnostic peaks were chosen, which

were unsatisfactorily fitted in both the HRPD and I11 data. Figure 4.8 show fits from two of the orthorhombic space groups tested and the remaining eight space groups (not shown) have a similar quality of fit. As can be seen in Figure 4.8, when d = 1.809 Å (26.4 ° or 87365 μs) and 1.783 Å (26.8 ° or 86134 μs), neither the synchrotron nor the neutron diffraction data are properly fitted. Refining peak shapes did not improve the quality of fit. This indicates that the discrepancy is caused by problems with the structural model; therefore the structure does not have orthorhombic symmetry.

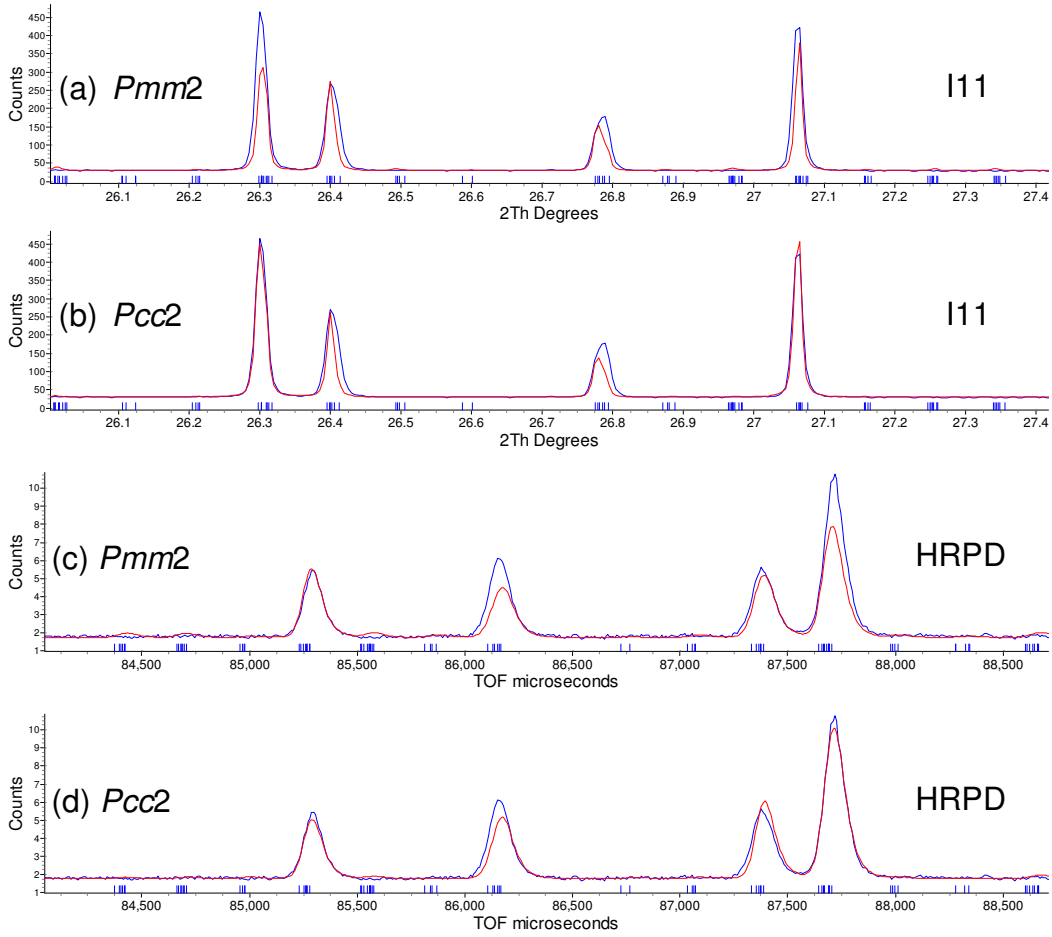

Figure 4.8: Fits to I11 (a and b) and (b and c) HRPD data in orthorhombic space groups *Pmm*2 and *Pcc*2.

Due to the poor fits obtained using the orthorhombic sub-groups, four non-centrosymmetric monoclinic space groups (which are sub-groups of *Fd*3 *m*) were identified as possibilities for β-$Bi_2Sn_2O_7$ using 'isodisplace'.[17] These were *P*2, *P*2$_1$, *Pc* and *Pm*. Simulated annealing input files were set up for these monoclinic space groups, as described for the orthorhombic space groups. Annealing was carried out on a PC and took approximately 3 days per space group. Figure 4.9 shows the 20 iterations with the lowest R_{wp}, with little difference being observed between *Pc* and *P*2. The lowest R_{wp}

and number of unique atoms are summarised in Table 4.1. *Pc* marginally had the lowest R_{wp}.

Table 4.1: Monoclinc space groups with the lowest R_{wp} obtained after 10000 cycles of annealing and the number of unique atoms (after refinement of peak shape).

Space group	Space group number	R_{wp} (%)	Number of unique atoms
Pm	7	5.856	176
Pc	6	4.475	176
$P2_1$	4	4.703	216
*P*2	3	4.608	184

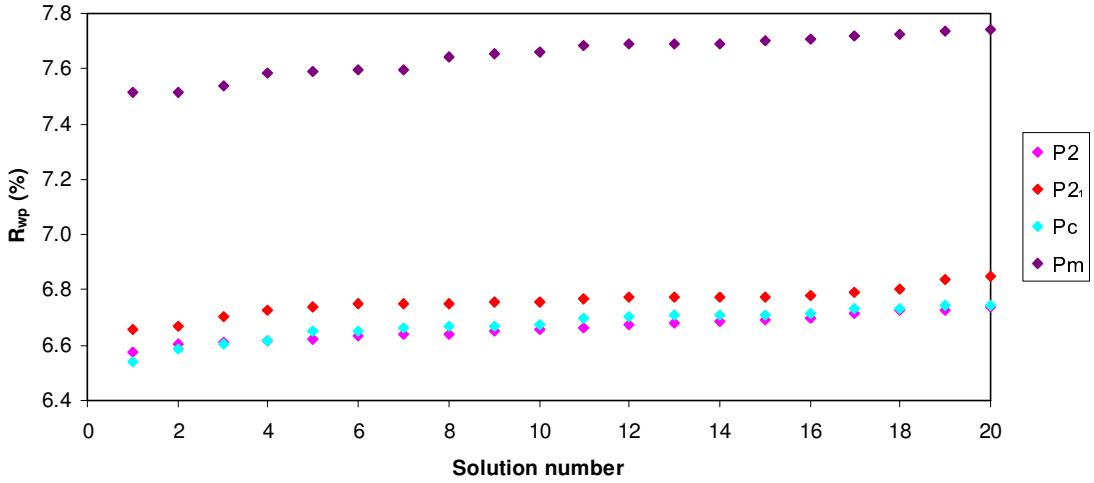

Figure 4.9: Simulated annealing of β-$Bi_2Sn_2O_7$: 20 solutions with lowest R_{wp} for monoclinic space groups.

There is a slight preference for the structural model using *Pc*, which is the space group of the α-$Bi_2Sn_2O_7$ structure. The visual quality of a small region of the Rietveld fits using monoclinic space groups are shown in Figure 4.10 and Figure 4.11 and are clearly better than those shown in Figure 4.8 for the orthorhombic space groups.

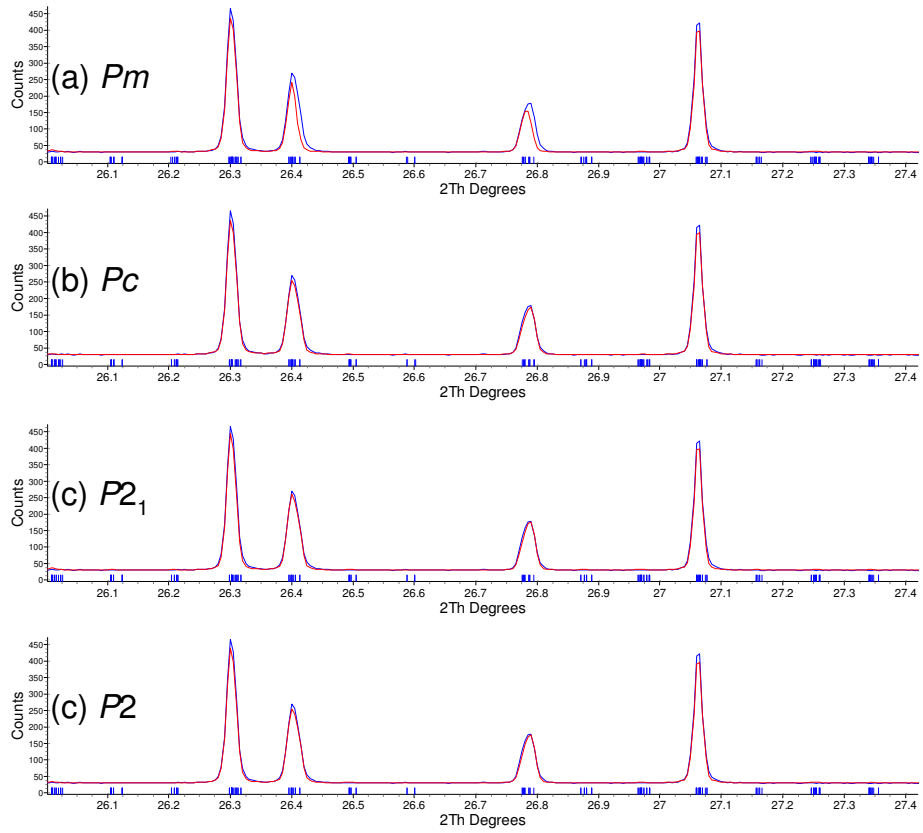

Figure 4.10: Fits to I11 data from simulated annealing of β-$Bi_2Sn_2O_7$ in monoclinic space groups.

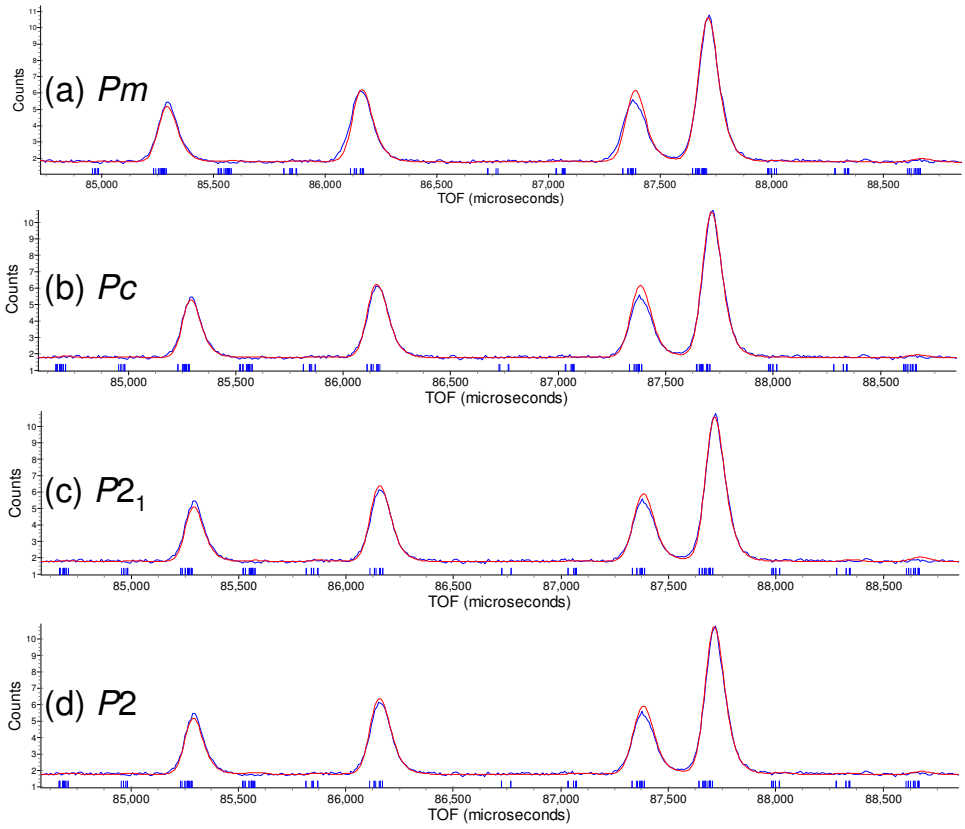

Figure 4.11: Fits to HRPD data from simulated annealing of β-$Bi_2Sn_2O_7$ in monoclinic space groups.

The enlarged range of the Rietveld fit using the *Pc* structural model is shown in Figure 4.12 . Excellent agreement between the data and model is observed.

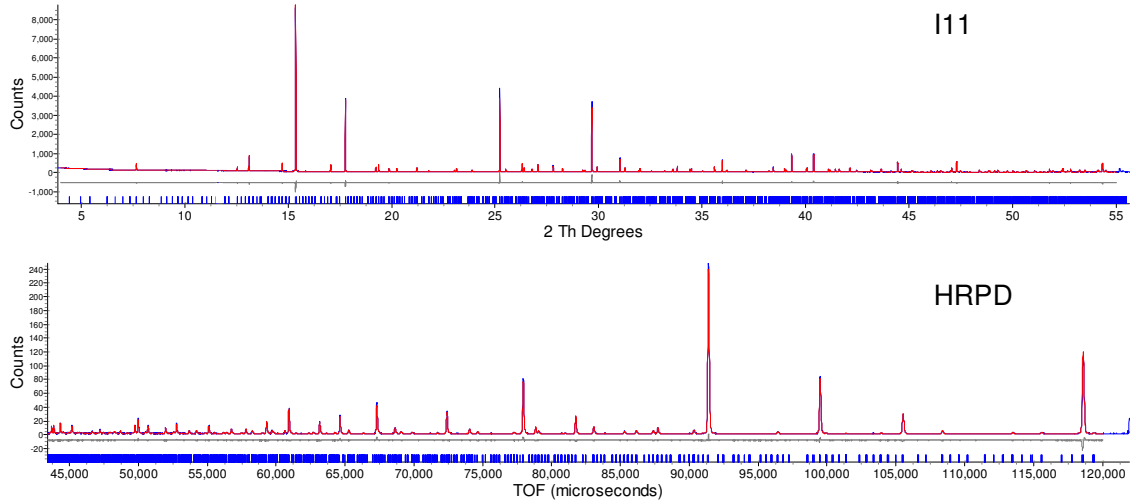

Figure 4.12: Rietveld fit for (a) I11 synchrotron PXRD data and (b) HRPD NPD data using the *Pc* structural model for β-$Bi_2Sn_2O_7$. Overall R_{wp} = 4.475%

Of the four monoclinic space groups tested, there is little difference between *Pc*, *P*2 and $P2_1$, as shown in Table 4.1, Figure 4.10 and Figure 4.11. A slight preference is observed for the fit in *Pc*, which is also the space group for α-$Bi_2Sn_2O_7$. It should be noted that there are several examples in the literature of isosymmetric phase transitions, whereby atomic coordinates change but the space group does not and are observed in materials which exhibit a first order phase transition.[18, 19] An example of this includes the *Cc*-*Cc* transition in $BiFeO_3$.[18, 19] Therefore it is possible that the α-β-$Bi_2Sn_2O_7$ phase transition may involve a *Pc*-*Pc* transition.

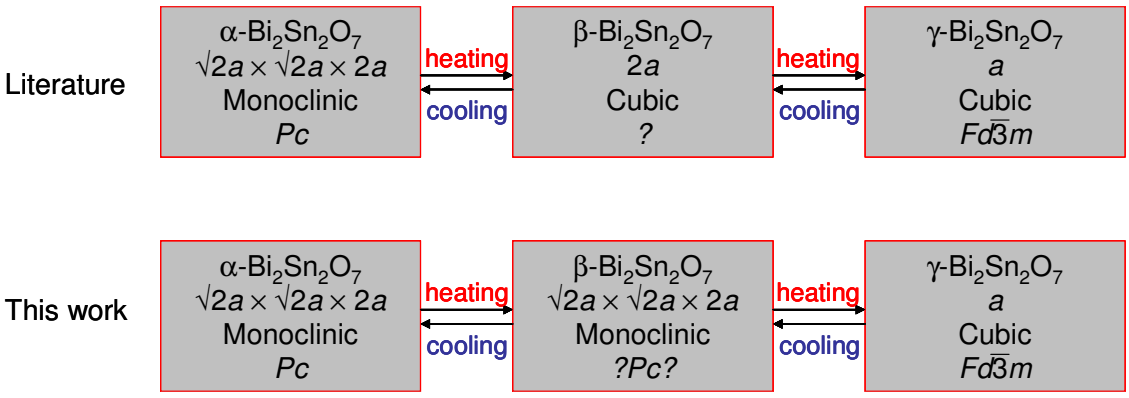

Figure 4.13: Phase transitions of $Bi_2Sn_2O_7$ and relationship between the structures, highlighting our work which suggests an isosymmetrical phase transition for the α-$Bi_2Sn_2O_7$ to β-$Bi_2Sn_2O_7$ phase transition.

In summary, in this work we have shown for the first time that β-$Bi_2Sn_2O_7$ is not cubic (Figure 4.13), in contrast to the existing literature, where β-$Bi_2Sn_2O_7$ has been

thought to be cubic for many years.[1, 16] It seems possible that the α-$Bi_2Sn_2O_7$ to β-$Bi_2Sn_2O_7$ transition involves a *Pc-Pc* transition, but further work is required in order to confirm this.

4.4 $Bi_2Sn_{2-x}Zr_xO_7$ mixed phases

There are several examples in the literature where isovalent doping on the B cation site increases the conductivity.[6, 20, 21] In particular, increasing the zirconium content in $Gd_2Sn_{2-x}Zr_xO_7$ increased the conductivity by one order of magnitude.[6] Therefore the $Bi_2Sn_{2-x}Zr_xO_7$ system has been explored to investigate the possibility of zirconium doping increasing the conductivity.

4.4.1 Synthesis of $Bi_2Sn_{2-x}Zr_xO_7$

Two methods were used in the synthesis of $Bi_2Sn_{2-x}Zr_xO_7$ compounds. One method used a traditional solid state route, whilst the other employed a precursor method.

4.4.1.1 Conventional solid state synthesis

Stoichiometric quantities (to produce 1.00 g of product) of Bi_2O_3 (Aldrich, 99.9%), ZrO_2 (Aldrich, 99.9%) and SnO_2 (Aldrich, 99.9%) were ground and fired at temperatures between 900 °C and 1100 °C for 16 hours.[3] $Bi_2Sn_{2-x}Zr_xO_7$ compositions in the range x = 0-1.6 in x = 0.2 intervals were prepared. The synthetic conditions and outcomes have been summarised in Table 4.2.

The limit of doping was found to be x = 1.0. It therefore appears that the solid solution can not be extended to the most zirconium rich compositions through a conventional solid state reaction. This is in line with our previous unsuccessful attempts to synthesise $(BiZr)_2O_7$ through a conventional solid state route, as described in Chapter 3.

Table 4.2: Summary of $Bi_2Sn_{2-x}Zr_xO_7$ products obtained through conventional solid state synthesis.

x	T (°C)	Product	Structure type
0.0	1100	$Bi_2Sn_2O_7$	α-$Bi_2Sn_2O_7$
0.2	1100	$Bi_2Sn_{1.8}Zr_{0.2}O_7$	α-$Bi_2Sn_2O_7$
0.4	1100	$Bi_2Sn_{1.6}Zr_{0.4}O_7$	α-$Bi_2Sn_2O_7$
0.6	1100	$Bi_2Sn_{1.4}Zr_{0.6}O_7$	α-$Bi_2Sn_2O_7$
0.8	1100	$Bi_2Sn_{1.2}Zr_{0.8}O_7$	β-$Bi_2Sn_2O_7$
1.0	1100	Bi_2SnZrO_7	β-$Bi_2Sn_2O_7$
1.2	1100	$Bi_2Sn_{0.8}Zr_{1.2}O_7$ +ZrO_2	β-$Bi_2Sn_2O_7$
1.4	950	$Bi_2Sn_{0.6}Zr_{1.4}O_7$ + ZrO_2	β-$Bi_2Sn_2O_7$
1.6	900	$Bi_2Sn_{0.4}Zr_{1.6}O_7$ + β Bi_2O_3 + ZrO_2	β-$Bi_2Sn_2O_7$

4.4.1.2 Precursor method

Stoichiometric quantities of $Bi(NO_3)_3 \bullet 5H_2O$, $ZrO(NO_3)_2 \bullet 2.5H_2O$ and $Sn(OBu)_4$ (to produce 2.00 g of product) were dissolved as follows: $Bi(NO_3)_3 \bullet 5H_2O$ (Aldrich, >98%) was dissolved in a dilute nitric acid solution (5 ml 70% HNO_3 and 50 ml H_2O) and $ZrO(NO_3)_2 \bullet 2.5H_2O$ (Aldrich, 99.99%) was dissolved in 40 ml H_2O. $Sn(OBu)_4$ was added to 50 ml acetone (Fisher, analytical grade) and heated gently, with continuous stirring, but the tin complex did not dissolve. The bismuth and zirconium solutions were added to the solution containing the undissolved tin complex, then neutralised with NH_4OH. The resulting white precipitate was stirred for approximately four hours and aged overnight. Following this, the mixture was stirred for a further two hours before filtering under vacuum and washing with distilled water. The resulting white precipitate was dried for four hours at 95 °C, ground and fired at 600 °C for 10 hours.

Table 4.3: Summary of products obtained using the precursor method for $Bi_2Sn_{2-x}Zr_xO_7$ compounds.

x	T (°C)	Product	Structure
0.0	600	$Bi_2Sn_2O_7$	$Bi_2Sn_2O_7$ type
0.2	600	$Bi_2Sn_{1.8}Zr_{0.2}O_7$	$Bi_2Sn_2O_7$ type
0.4	600	$Bi_2Sn_{1.6}Zr_{0.4}O_7$	$Bi_2Sn_2O_7$ type
0.6	600	$Bi_2Sn_{1.4}Zr_{0.6}O_7$	$Bi_2Sn_2O_7$ type
0.8	600	$Bi_2Sn_{1.2}Zr_{0.8}O_7$	$Bi_2Sn_2O_7$ type
1.0	600	Bi_2SnZrO_7	$Bi_2Sn_2O_7$ type
1.2	600	$Bi_2Sn_{0.8}Zr_{1.2}O_7$	$Bi_2Sn_2O_7$ type
1.4	600	$Bi_2Sn_{0.6}Zr_{1.4}O_7$	$Bi_2Sn_2O_7$ type
1.6	600	$Bi_2Sn_{0.4}Zr_{1.6}O_7$	Fluorite + ZrO_2
1.8	600	$Bi_2Sn_{0.2}Zr_{1.8}O_7$	Phase segregated fluorite + ZrO_2

Compositions of $Bi_2Sn_{2-x}Zr_xO_7$ in the range $x = 0.0$-1.8 in 0.2 intervals were prepared. Table 4.3 shows the synthetic conditions and outcomes of the $Bi_2Sn_{2-x}Zr_xO_7$ precursor method.

4.4.2 Structural characterisation of $Bi_2Sn_{2-x}Zr_xO_7$ phases prepared by a conventional route

Compositions in the range $Bi_2Sn_2O_7$ – Bi_2SnZrO_7 ($x = 0.0$-1.0) could be successfully synthesised via the high temperature route. In a typical refinement, twelve background parameters, sample height, peak shape, cell parameters and one overall isotropic temperature parameter were refined. Refinements used α-$Bi_2Sn_2O_7$ as the structural model, with the occupancy of the tin sites adjusted to account for Zr^{4+} substitution.

Figure 4.14 shows a Rietveld fit for $Bi_2Sn_{1.8}Zr_{0.4}O_7$ and Bi_2SnZrO_7. As the Zr^{4+} content was increased, the peaks centred around 33.5° merge, indicating the transformation from α- to β-$Bi_2Sn_2O_7$ (see Figure 4.15). From PXRD, $Bi_2Sn_{2-x}Zr_xO_7$ has the α-$Bi_2Sn_2O_7$ structure in the region $x = 0$-0.6 and the β-$Bi_2Sn_2O_7$ structure in the region $x = 0.8$-1.4, although the $x = 1.2$ and $x = 1.4$ samples contained a ZrO_2 impurity. Despite compounds with $x = 0.8$ or greater showing the β-$Bi_2Sn_2O_7$ structure, the α-$Bi_2Sn_2O_7$ structural model was used in Rietveld refinement. As the amount of zirconium is increased in the $Bi_2Sn_{2-x}Zr_xO_7$ system, the cell volume increases (Figure 4.16). This is in agreement with the slightly larger ionic radius of Zr^{4+} (0.72 Å) compared to Sn^{4+} (0.69 Å) in six fold coordination.[4] A change in slope is observed at $x = 0.6$, caused by the change of the crystal structure from α-$Bi_2Sn_2O_7$ to β-$Bi_2Sn_2O_7$ induced by Zr^{4+} doping. Interestingly, chemical doping of both the Bi^{3+} site (by Pb^{2+} and Cd^{2+}) and the Sn^{4+} site (by Ga^{3+}, Rh^{3+}, Sc^{3+}, In^{3+}, Ru^{4+}, Sb^{5+}, $Nb^{5+}$and Ta^{5+}) has previously been reported to stabilise β-$Bi_2Sn_2O_7$ to room temperature.[1]

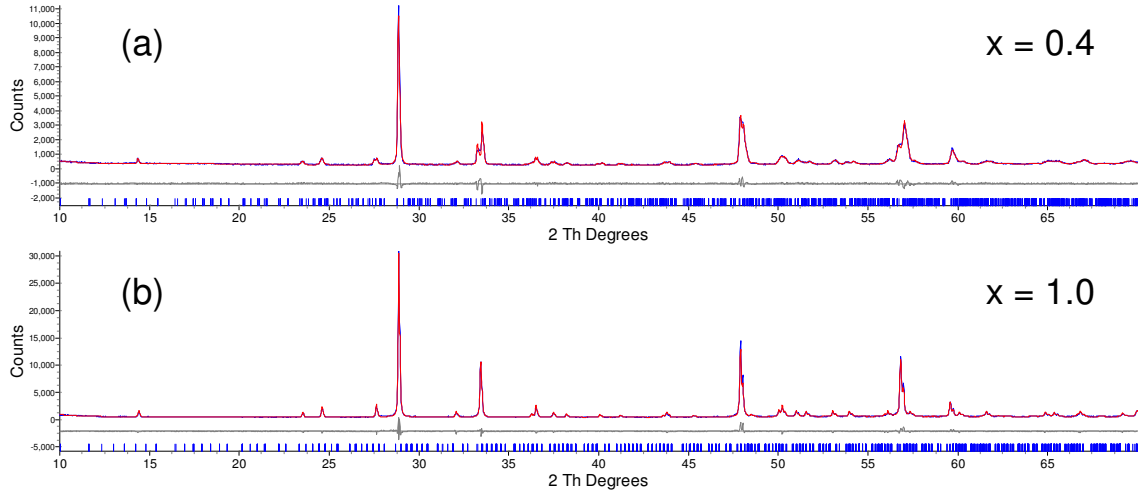

Figure 4.14: (a) d9_04773: $Bi_2Sn_{1.6}Zr_{0.4}O_7$ Rietveld refinement using the α-$Bi_2Sn_2O_7$ model. (b) d9_04743: Bi_2SnZrO_7 Rietveld refinement using the α-$Bi_2Sn_2O_7$ model.

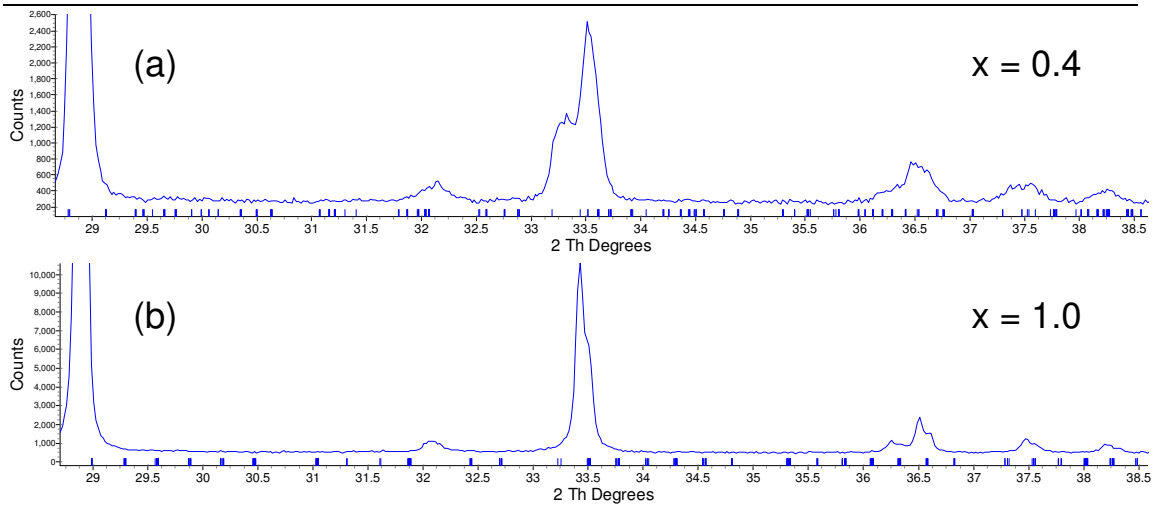

Figure 4.15: (a) d9_04773: $Bi_2Sn_{1.6}Zr_{0.4}O_7$ zoomed region showing peak centred around 33.5 °, characteristic of α-$Bi_2Sn_2O_7$. (b) d9_04743: Bi_2SnZrO_7 zoomed region showing peak centred around 33.5 °, characteristic of β-$Bi_2Sn_2O_7$

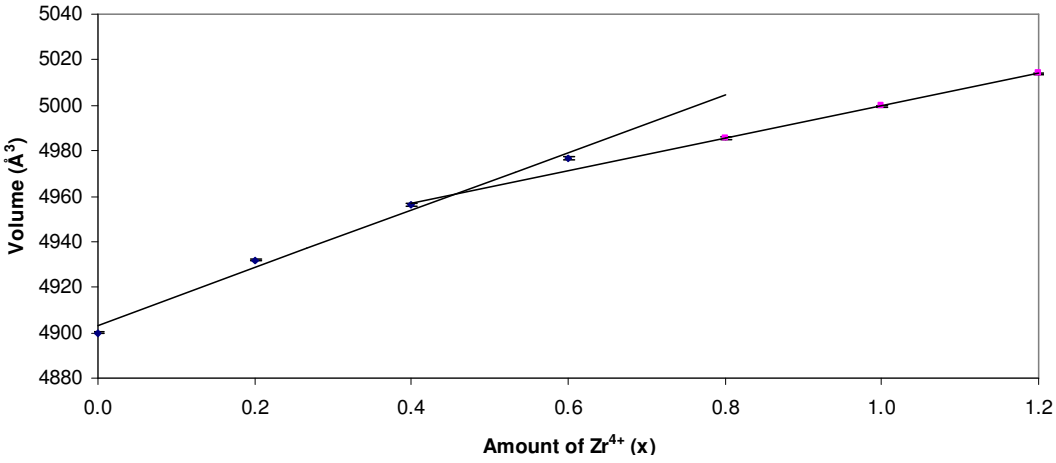

Figure 4.16: Variation of cell volume of $Bi_2Sn_{2-x}Zr_xO_7$ (synthesised via the conventional solid state route) with increasing zirconium content.

4.4.3 Structural characterisation of $Bi_2Sn_{2-x}Zr_xO_7$ phases prepared by a precursor route

We have discovered that it is possible to synthesise $Bi_2Sn_{2-x}Zr_xO_7$ phases via the precursor method described in 4.4.1.2. In contrast to the samples prepared at high temperatures (1100 °C), the samples prepared via the precursor method (600 °C) were less crystalline. Samples with x = 0-1.4 had the $Bi_2Sn_2O_7$ structure, whilst those with x = 1.6 and 1.8 have the fluorite structure. It is impossible to distinguish between the α-$Bi_2Sn_2O_7$ and β-$Bi_2Sn_2O_7$ polymorphs for samples prepared via the precursor route, due to peak broadening due to small crystallite size. $Bi_2Sn_{0.2}Zr_{1.8}O_7$ and $Bi_2Sn_{0.4}Zr_{1.6}O_7$ have the fluorite structure, but also show a small percentage of ZrO_2.

An example of the fluorite-type structural model used for the refinement of the zirconium rich samples (x =1.6 and 1.8) prepared by the precursor method is shown in Table 4.4. In a typical refinement, lattice parameters, specimen displacement height,

scale factor, an overall temperature factor, size, strain and 18 background parameters were refined. A Rietveld plot is shown in Figure 4.17

Table 4.4: Structural model used for refinements for compounds with the fluorite structure. In this case the model is for $Bi_2Sn_{0.2}Zr_{1.8}O_7$.

Atom	Site	x	y	z	Occupancy
Bi	4a	0	0	0	0.5
Zr	4a	0	0	0	0.45
Sn	4a	0	0	0	0.05
O	8c	0.25	0.25	0.25	0.875

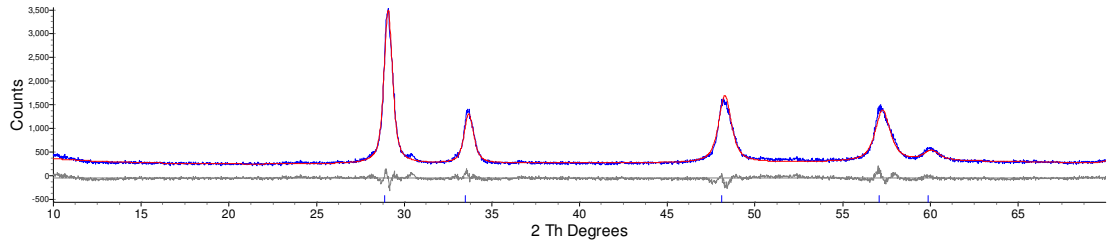

Figure 4.17: d9_04911: $Bi_2Sn_{0.4}Zr_{1.6}O_7$ synthesised by a precursor method. Refinement using a fluorite structural model. R_{wp} = 7.514%

Figure 4.18 shows the phase diagrams for the $Bi_2Sn_{2-x}Zr_xO_7$ systems when synthesised through both conventional and precursor methods. Despite PXRD showing a small quantity of ZrO_2 and slight phase segregation for the zirconium rich compositions, the level of impurity or phase segregation is still small with respect to the impurities observed for the $Bi_2Sn_{0.4}Zr_{1.6}O_7$ composition prepared through the conventional solid state route. Therefore it appears that the Zr^{4+} solubility in $Bi_2Sn_2O_7$ has been increased by using a precursor route.

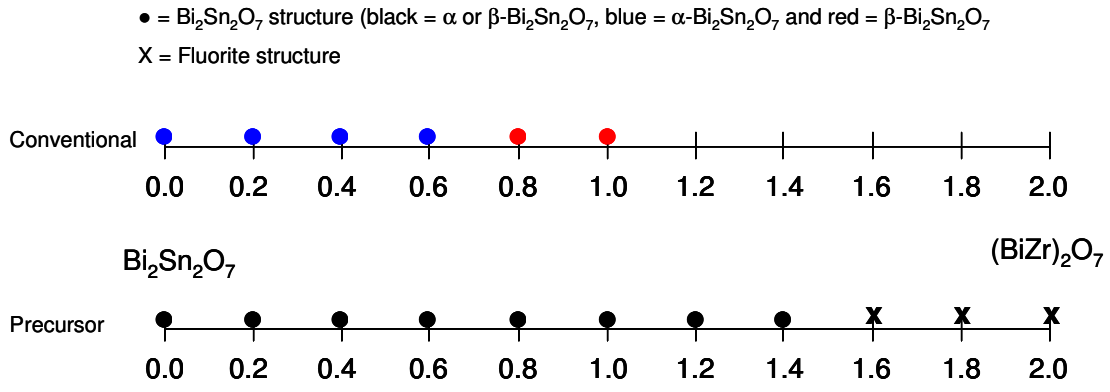

Figure 4.18: Phase diagram for the $Bi_2Sn_{2-x}Zr_xO_7$ system prepared by conventional and precursor methods. Circles indicate $Bi_2Sn_2O_7$ and are colour coded according to the polymorph adopted: Black either α-$Bi_2Sn_2O_7$ or β-$Bi_2Sn_2O_7$, blue α-$Bi_2Sn_2O_7$ and red β-$Bi_2Sn_2O_7$. Crosses indicate the fluorite structure type.

4.4.4 High temperature (VT) structural behaviour

The behaviour of the $Bi_2Sn_{2-x}Zr_xO_7$ phases (prepared by conventional solid state synthesis) was explored at elevated temperatures using VT-PXRD. Figure 4.19 shows the plot for $Bi_2Sn_{1.6}Zr_{0.4}O_7$, which is typical for other members of the series.

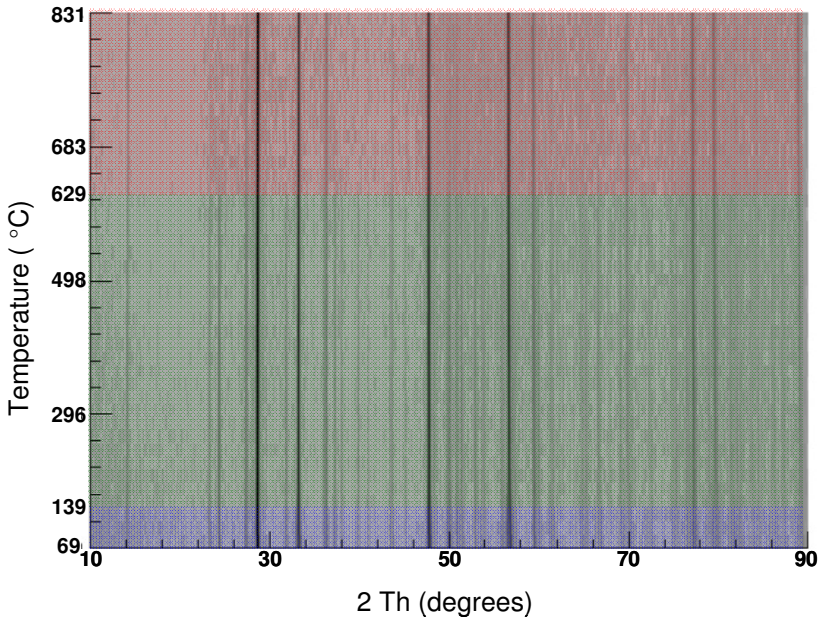

Figure 4.19: d8_03718: VT-PXRD plot for $Bi_2Sn_{1.6}Zr_{0.4}O_7$. Blue patterns show stability of α phase, green patterns show stability of β phase and red patterns show the stability of the pyrochlore phase.

$Bi_2Sn_{1.6}Zr_{0.4}O_7$ is stable in the temperature region up to 839 °C, as no phase segregation or decomposition was observed. As for pure $Bi_2Sn_2O_7$, two phase transitions are observed in $Bi_2Sn_{1.6}Zr_{0.4}O_7$; firstly the α→β transition at 139 °C and secondly the β→γ transition at 629 °C, which are very close to the transition temperatures observed in pure $Bi_2Sn_2O_7$ by Evans *et al.*[3] In pure $Bi_2Sn_2O_7$ the α→β transition occurs at 137 °C and the β→γ transition at 627 °C. No transformation to a fluorite structure was observed over the temperature range studied for any compound in the $Bi_2Sn_{2-x}Zr_xO_7$ system, despite the reduction in cation radius ratio caused by zirconium doping on the B site.

4.4.5 Impedance results

All pellets in the $Bi_2Sn_{2-x}Zr_xO_7$ system had densities around 70%. The impedance spectra of $Bi_2Sn_2O_7$, $Bi_2Sn_{1.6}Zr_{0.4}O_7$, $Bi_2Sn_{1.4}Zr_{0.6}O_7$ and $Bi_2Sn_{1.2}Zr_{0.8}O_7$ can all be described in the same way. At low temperatures, one semi-circle arc is observed, which has a capacitance of the order of magnitude 10^{-12} F cm^{-1}, estimated using the formula

$\omega RC = 1$ and this arc may be modelled with a resistor and capacitor in parallel. Given the capacitance of 10^{-12} F cm^{-1}, this arc was assigned to the bulk response.

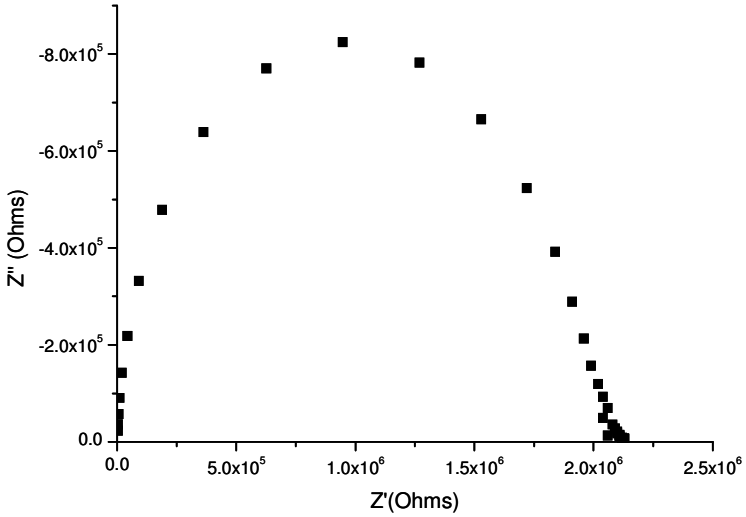

Figure 4.20: Complex impedance plot of $Bi_2Sn_2O_7$ at 470 °C.

Figure 4.20 shows a low temperature complex impedance plot for $Bi_2Sn_2O_7$ which is typical for other members of the $Bi_2Sn_{2-x}Zr_xO_7$ system. At temperatures higher than 700 °C, a second semi-circle arc appears which was assigned to the grain boundary response. At low frequencies, as the capacitance remained low, of the order of magnitude 10^{-10}-10^{-8} and no Warburg type electrode response was observed, ionic conductivity was not dominant.

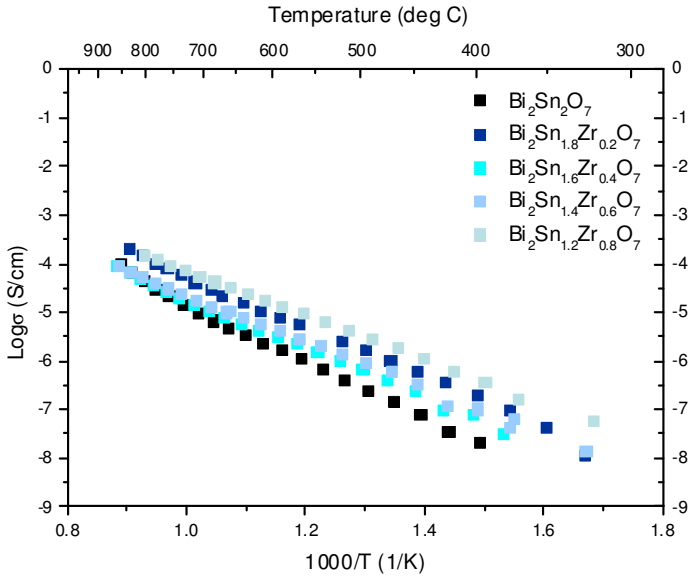

Figure 4.21: Variation of conductivity with temperature in the $Bi_2Sn_{2-x}Zr_xO_7$ system.

Figure 4.21 shows the variation of conductivity with temperature. From the graph, it is clear to see that $Bi_2Sn_2O_7$ exhibits the lowest conductivity and therefore doping the B

site with zirconium increases the conductivity. However, the highest conductivity is observed for the x = 0.8 sample (1.6×10^{-4} S cm^{-2} at 800 °C) which is the most zirconium-rich, followed by $Bi_2Sn_{1.8}Zr_{0.2}O_7$, $Bi_2Sn_{1.4}Zr_{0.6}O_7$ and $Bi_2Sn_{1.6}Zr_{0.4}O_7$. The change in conductivity between $Bi_2Sn_2O_7$ and $Bi_2Sn_{1.2}Zr_{0.8}O_7$ is approximately one order of magnitude, which is similar to the increase seen in the $Gd_2Sn_{2-x}Zr_xO_7$ system.[6] The low conductivity in the $Bi_2Sn_{2-x}Zr_xO_7$ systems may be explained through the fully ordered anion array in the pyrochlore related structure and the fact that isovalent doping with Zr^{4+} does not create any additional oxygen vacancies.

4.5 $Bi_{2-x}Ca_xSn_2O_{7-x/2}$

As discussed in Chapter 1, aliovalent doping of the A cation site has increased the ionic conductivity in a number of cases.[8] For example $Yb_{1.8}Ca_{0.2}Ti_2O_{6.9}$ currently has the highest oxide ion conductivity for a pyrochlore.[7] $Gd_{1.8}Ca_{0.2}Ti_2O_{6.9}$ also has a high conductivity, 2.5 orders of magnitude greater than that of the parent $Gd_2Ti_2O_7$.[8] As aliovalent doping increases the number of vacancies, calcium doping in the $Bi_{2-x}Ca_xSn_2O_{7-x/2}$ system has been explored in order to determine whether the conductivity of $Bi_2Sn_2O_7$ will be increased.

4.5.1 Synthesis of $Bi_2Sn_2O_7$ and $Bi_{2-x}Ca_xSn_2O_{7-x/2}$

$Bi_2Sn_2O_7$ was synthesised via a method described by Evans *et al.*.[3] Stoichiometric amounts of Bi_2O_3 (1.21 g, 2.61 mmol, Aldrich, 99.9%) and SnO_2 (0.79 g, 5.21 mmol, Aldrich, 99.9%) were ground together in a pestle and mortar and fired at 1100 °C for 16 hours. Stoichiometric quantities of CaO (Aldrich, 99.9%), Bi_2O_3 (Aldrich, 99.9%) and SnO_2 (Aldrich, 99.9%) to produce either a 1.00 g or 2.00 g product were ground together in a pestle and mortar for the Ca doped samples, with the temperature and firing duration remaining the same. Compositions in the series $Bi_2Sn_2O_7$ – $Bi_{1.2}Ca_{0.8}Sn_2O_7$ were explored in x = 0.1 intervals. All products were yellow in colour.

4.5.2 Structural characterisation of $Bi_{2-x}Ca_xSn_2O_{7-x/2}$

The PXRD patterns show that when x = 0.3 or more, $CaSnO_3$ forms as an additional phase. α-$Bi_2Sn_2O_7$ was used as the structural model for Rietveld refinement, with the occupancy of the bismuth sites adjusted appropriately to account for the Ca^{2+} doping. Lattice parameters, specimen displacement height, scale factor, overall atomic displacement parameter, peak shape and 18 background terms were included in the refinements. At room temperature, the β-$Bi_2Sn_2O_7$ phase is present. A Rietveld fit for

$Bi_{1.9}Ca_{0.1}Sn_2O_{6.95}$ is shown in Figure 4.22. Figure 4.23 shows the linear decrease in cell volume with increasing calcium content, as expected for the substitution of the slightly smaller Ca^{2+} ion for Bi^{3+}.

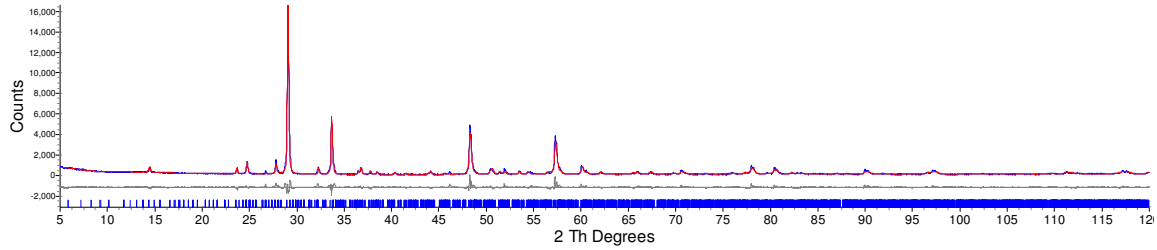

Figure 4.22: (a) d5_08512: $Bi_{1.9}Ca_{0.1}Sn_2O_{6.95}$: Rietveld refinement using the α-$Bi_2Sn_2O_7$ structural model.

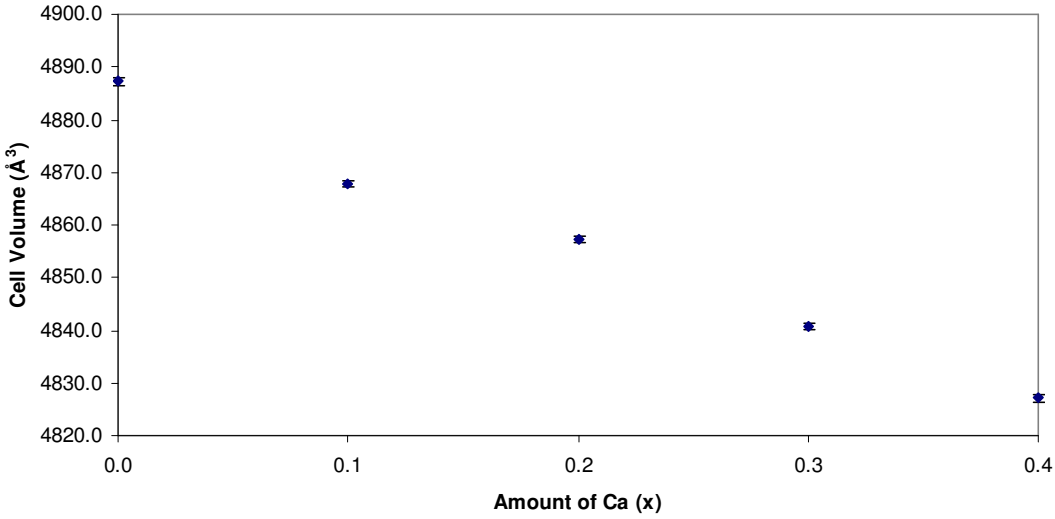

Figure 4.23: Variation of cell volume with increasing calcium content.

4.5.3 High temperature structural behaviour

In-situ VT-PXRD studies were carried out on the $x = 0.1$ and 0.2 Ca samples in the $Bi_{2-x}Ca_xSn_2O_{7-x/2}$ series. Figure 4.24 shows the VT-PXRD pattern obtained for $Bi_{1.8}Ca_{0.2}Sn_2O_{6.90}$.

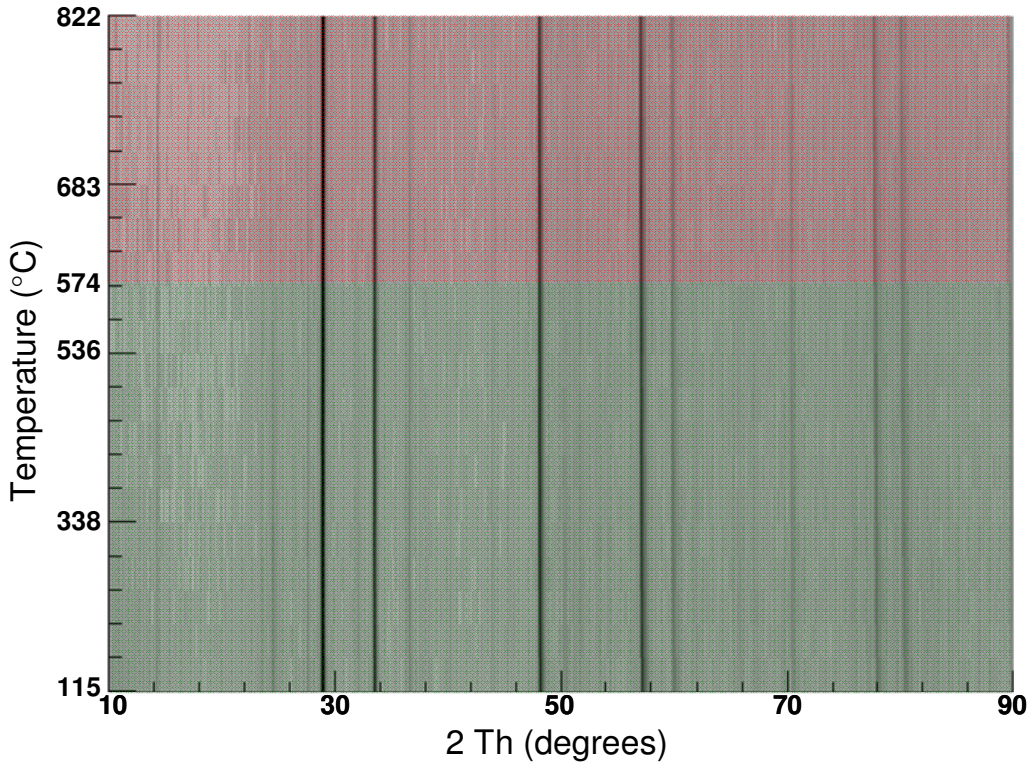

Figure 4.24: d8_03758: VT-PXRD pattern of $Bi_{1.8}Ca_{0.2}Sn_2O_{6.90}$. Green patterns show stability region of β phase, whilst red patterns show the stability of the pyrochlore phase (up to 822 °C).

As was seen for the $Bi_2Sn_{2-x}Zr_xO_{7-x/2}$ phases, no decomposition or phase segregation was observed. At room temperature, the β-$Bi_2Sn_2O_7$ phase is present. The β→γ transition occurs at 574 °C, which is lower than the β→γ transition temperature reported in the literature for pure $Bi_2Sn_2O_7$ (627 °C).[1, 3]

4.5.4 Impedance results

4.5.4.1 $Bi_{1.9}Ca_{0.1}Sn_2O_{6.95}$

At low temperatures, one semi-circle arc, with a second overlapping semi-circle arc was observed (Figure 4.25). The capacitances were estimated using the formula $\omega RC = 1$. The first arc had a capacitance of 4.1×10^{-12} F cm^{-1} and was assigned to the bulk contribution. The bulk arc could be modeled with a resistor (R) and capacitor (C) in parallel. The overlapping arc was assigned to the grain boundary response, as it had a capacitance of 4.0×10^{-9} F cm^{-1}.

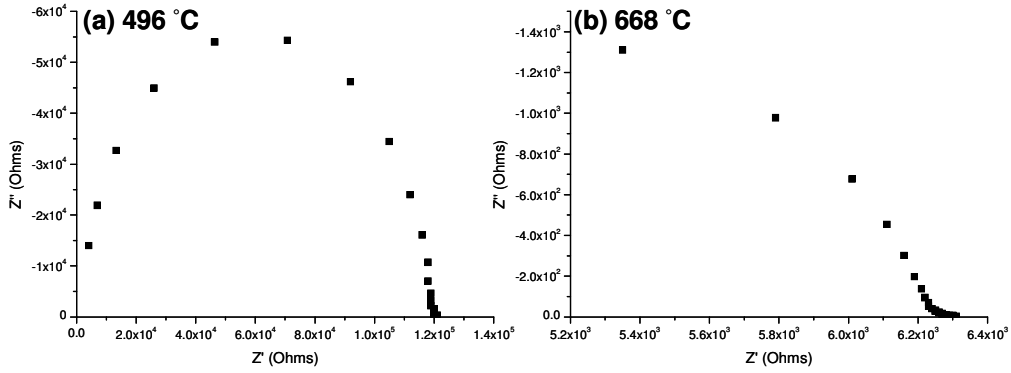

Figure 4.25: $Bi_{1.9}Ca_{0.1}Sn_2O_{6.95}$ complex impedance plots at (a) 496 °C and at (b) 668 °C.

Above 500 ° C the bulk response gradually disappears. At temperatures above 600 °C, a third arc is observed at high frequency, with a capacitance of 7.7×10^{-6} F cm^{-1}, which is typical of the electrode response and indicates the presence of ionic conductivity (Figure 4.25b).

4.5.4.2 $Bi_{1.8}Ca_{0.2}Sn_2O_{6.90}$

At low temperatures one large arc is observed. The arc is not perfect and is elongated. Two plateaus are seen in the graph of capacitance versus frequency, suggesting that there are two components. The capacitances of the arcs were estimated using the formula $\omega RC = 1$. The high frequency arc had a capacitance of 4.2 x 10^{-12} F cm^{-1} so was assigned to the bulk, whilst the low frequency arc had a capacitance of 1.6 x 10^{-11} F cm^{-1} and was assigned to the grain boundary response.

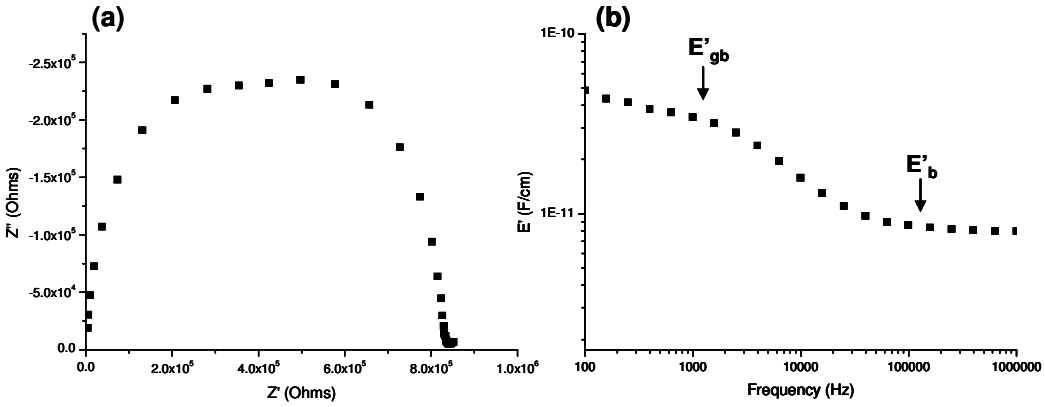

Figure 4.26: (a) Complex impedance plot for $Bi_{1.8}Ca_{0.2}Sn_2O_{6.9}$ and (b) variation of capacitance (E') with frequency for $Bi_{1.8}Ca_{0.2}Sn_2O_{6.9}$ showing two plateaus, indicative of the bulk (E'_b) and grain boundary (E'_{gb}) responses.

With increasing temperature the bulk disappears. Above 546 ° C , a third semi-circle arc appears at low frequency. At 642 °C this arc has a capacitance of 1.1 x 10^{-7} F cm^{-1}, typical of the electrode response and indicative of ionic conductivity. The densities of all pellets in the $Bi_{2-x}Ca_xSn_2O_{7-x/2}$ series were in the region of 70-75%.

4.5.4.3 Discussion

The maximum conductivity was obtained for the Ca = 0.1 sample. Increasing the calcium content further resulted in a decrease in conductivity. A similar situation has been observed in the $Nd_{2-x}Sr_xZr_2O_{7-x/2}$ system, where $Nd_{1.9}Sr_{0.1}Zr_2O_{6.95}$ has a slightly higher conductivity than $Nd_2Zr_2O_7$, however increasing the strontium content to $Nd_{1.8}Sr_{0.2}Zr_2O_{6.9}$ led to a decrease in conductivity. This was attributed to formation of a $SrZrO_3$ impurity phase.[22] Hence for our $Bi_{1.8}Ca_{0.2}Sn_2O_{6.90}$ sample it is possible that there may be a $CaSnO_3$ impurity present that has not been detected by PXRD.

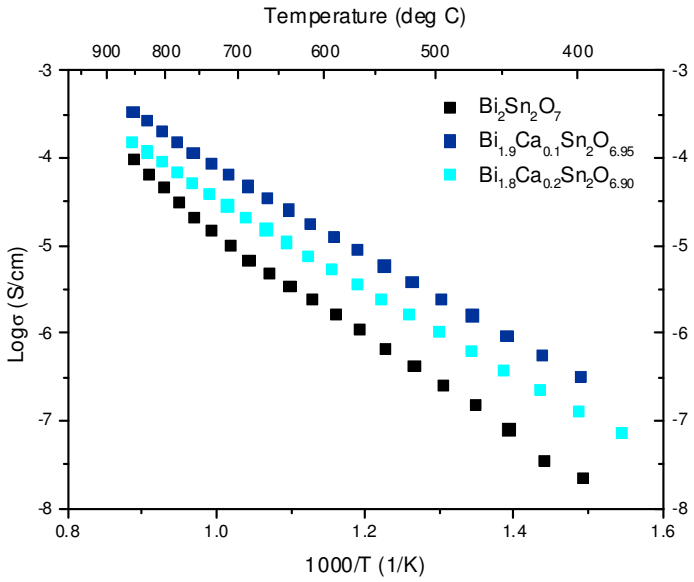

Figure 4.27: Variation of conductivity with temperature for the $Bi_{2-x}Ca_xSn_2O_{7-x/2}$ system.

Table 4.5: Conductivity of samples in the $Bi_{2-x}Ca_xSn_2O_{7-x/2}$ system around 800 °C.

Compound	Conductivity (S cm^{-1})	Temperature (°C)	Activation energy (eV)
$Bi_2Sn_2O_7$	4.7×10^{-5}	805	1.21(1)
$Bi_{1.9}Ca_{0.1}Sn_2O_{6.95}$	2.1×10^{-4}	808	1.064(8)
$Bi_{1.8}Ca_{0.2}Sn_2O_{6.90}$	9.3×10^{-5}	809	1.078(9)

The conductivities of the $Bi_{2-x}Ca_xSn_2O_{7-x/2}$ compounds are approximately two orders of magnitude lower than other Ca^{2+} doped pyrochlores.[7, 9] For example, at 740 °C, $Yb_{1.8}Ca_{0.2}Ti_2O_{6.9}$ has a high conductivity for a pyrochlore of 4×10^{-2} S cm^{-1}.[7] Another calcium doped pyrochlore, $Gd_{1.8}Ca_{0.2}Ti_2O_{6.9}$ achieves a conductivity of 1.7×10^{-2} S cm^{-1} at 800 °C estimated from the graph reported by Tuller *et al.*.[8] Table 4.5 also shows the activation energies for compounds in the $Bi_{2-x}Ca_xSn_2O_{7-x/2}$ system. Doping with Ca^{2+} decreases the activation energy with respect to $Bi_2Sn_2O_7$. The Ca = 0.1 and 0.2 samples have almost identical activation energies. The increase in conductivity for

$Bi_{1.9}Ca_{0.1}Sn_2O_{6.95}$ is approximately 0.75 orders of magnitude, which is comparable to the increase observed for $Yb_{1.8}Ca_{0.2}Ti_2O_{6.9}$ with respect to $Yb_2Ti_2O_7$.[7]

4.6 Bi_2ScNbO_7 and related phases

As in six fold coordination Sc^{3+} has a radius of 0.745 Å and Nb^{5+} has a radius of 0.64 Å, a 1:1 ratio of Sc^{3+} and Nb^{5+} gives an average cation radius of 0.693 Å, which is essentially identical to that of Sn^{4+} (0.69 Å).[4] As the structure and properties of these materials depends on not only cation sizes and oxidation states, but chemical nature of the cation, Bi_2ScNbO_7 offers an ideal comparison with $Bi_2Sn_2O_7$ to explore how the cation nature effects the properties of the parent compounds and doped analogues.

4.6.1 Synthesis of Bi_2ScNbO_7 and related phases

Table 4.6: Dopant, synthetic conditions and synthetic outcomes for Bi_2ScNbO_7 related phases.

Dopant	*x*	T (°C)	Duration (hrs)	Product
Ca^{2+}	0.05, 0.10	1000	24	
		1050	20	$Bi_{2-x}Ca_xScNbO_{7-x/2}$
	0.15	1000	36	
		1050	10	$Bi_{2-x}Ca_xScNbO_{7-x/2}$
	0.20	1000	36	
		1050	10	
		1100	10	$Bi_{2-x}Ca_xScNbO_{7-x/2}$
Sc^{3+}	0.05	1000	36	
		1025	14	
		1050	10	$Bi_2Sc_{1+x}Nb_{1-x}O_{7-x}$
	0.10	1000	36	
		1025	14	
		1050	10	
		1100	10	$Bi_2Sc_{1+x}Nb_{1-x}O_{7-x}$
	0.15	1100	48	$Bi_2Sc_{1+x}Nb_{1-x}O_{7-x}$
	0.20	1100	24	$Bi_2Sc_{1+x}Nb_{1-x}O_{7-x}$ + Sc_2O_3
Zr^{4+}	0.05	1050	22	$Bi_2ScNb_{1-x}Zr_xO_{7-x/2}$
	0.10, 0.15	1050	24	$Bi_2ScNb_{1-x}Zr_xO_{7-x/2}$
	0.20	1050	12	$Bi_2ScNb_{1-x}Zr_xO_{7-x/2}$ + ZrO_2

The synthesis of Bi_2ScNbO_7 was based on a literature procedure by Cann *et al.*.[23] Stoichiometric quantities of Bi_2O_3 (1.40 g, 3.00 mmol), Sc_2O_3 (0.21 g, 1.50 mmol) and Nb_2O_5 (0.40 g, 1.50 mmol) were ground together in an agate pestle and mortar and fired for 36h at 800 °C, 12h at 900 °C, 48h at 950 °C and 10h at 1000 °C, with intermittent grinding. A pure pyrochlore phase was obtained. In the synthesis of $Bi_2Sc_{1+x}Nb_{1-x}O_{7-x}$, $Bi_{2-x}Ca_xScNbO_{7-x/2}$ and $Bi_2ScNb_{1-x}Zr_xO_{7-x/2}$ stoichiometric quantities of the required oxides (Bi_2O_3, Sc_2O_3, Nb_2O_5, CaO and ZrO_2) were ground together in a pestle and mortar. Firing temperature, duration and synthetic outcome are summarised in Table 4.6.

4.6.2 Bi_2ScNbO_7

4.6.2.1 Structural characterisation

Two structural models were tested for Bi_2ScNbO_7. The first placed Bi^{3+} on the 'ideal' A cation site of (0,0,0) and the second model displaced bismuth from the origin on the three-fold axis, on a 96h site (0, *y*, 1-*y*) . In the refinement of each model, 18 background parameters, sample height, peak shape, scale factor, one overall isotropic temperature factor, cell parameters and atomic coordinates were refined.

Table 4.7: Model obtained from Rietveld refinement of Bi_2ScNbO_7 with Bi^{3+} displaced from the three-fold axis.

Atom	Site	x	y	z	Occupancy
Bi	96h	0	0.0248(3)	0.9752(3)	0.167
Sc	16d	0.5	0.5	0.5	0.5
Nb	16d	0.5	0.5	0.5	0.5
O	48f	0.4316(6)	0.125	0.125	1
O	8a	0.125	0.125	0.125	1

Figure 4.28a shows the Rietveld fit obtained for the Bi_2ScNbO_7 phase in $Fd\bar{3}m$. The best fit was achieved when the Bi cation is displaced from the origin, as is common for many Bi^{3+} containing pyrochlores, such as $Bi_2Ti_2O_7$ and γ-$Bi_2Sn_2O_7$.[2, 22] When bismuth is not displaced from the origin, certain reflections, such as the (442) and (062) reflections, are not fitted.[24] Figure 4.28b shows an enlarged region of the Rietveld fit obtained when Bi^{3+} is not displaced from the origin and Figure 4.28c shows the Rietveld fit when the Bi^{3+} cation is displaced to a 96h site, as in $Bi_2Ti_2O_7$.[25] A recent laboratory PXRD and electron diffraction study by Liu *et al.* has shown the presence of the (062) and (248) reflections, which are forbidden in $Fd\bar{3}m$. Although no Rietveld refinement was carried out, the presence of these reflections was attributed to displacive disorder on the O'A_2 sublattice, which is common in bismuth pyrochlores and allows Bi^{3+} to be displaced from the ideal (0,0,0) site on the three-fold axis.[26] Additionally, a structural study of the chemically similar pyrochlore, Bi_2InNbO_7, using NPD and PXRD has shown the displacement of Bi^{3+} to a 96h site.[27]

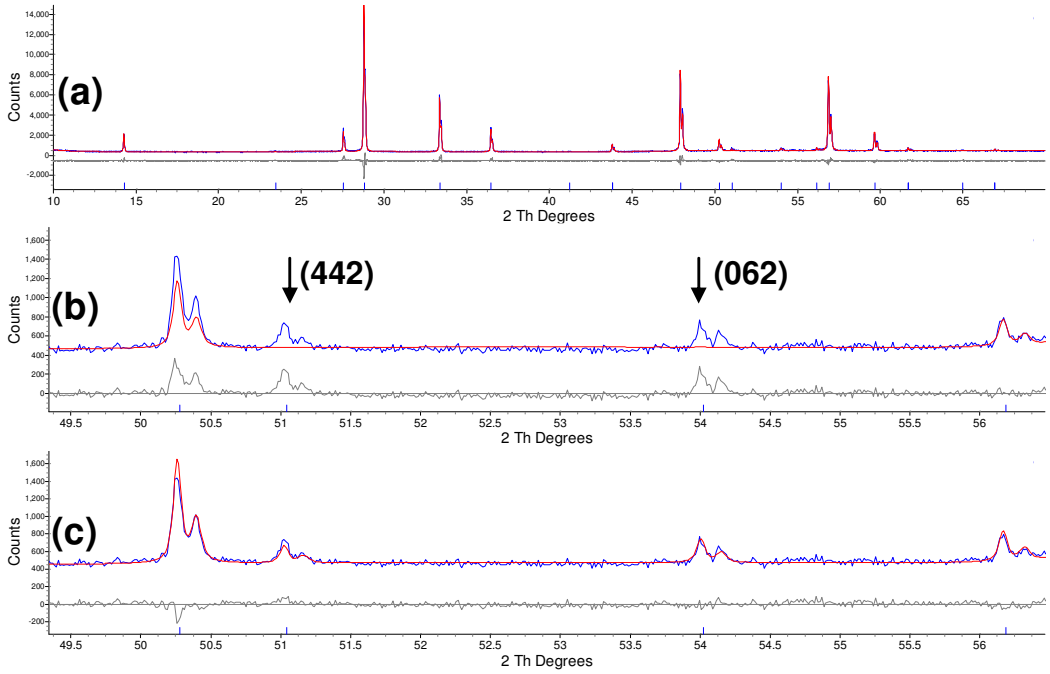

Figure 4.28: d9_03203: (a) Rietveld refinement for Bi_2ScNbO_7, using a model where bismuth is displaced from the origin R_{wp} = 6.501%, *a* = 10.72710(9) Å. (b) Enlarged region of fit when a model does not have bismuth displaced from the origin. R_{wp} = 9.846%, *a* = 10.7268(1) Å. (c) Enlarged region of fit when a model is used that has bismuth displaced from origin. (442) and (062) reflections are now fitted. R_{wp} = 6.501%, *a* = 10.72710(9) Å

4.6.2.2 Impedance

The density of the Bi_2ScNbO_7 pellet was 89%. Figure 4.29 shows the complex impedance plot for Bi_2ScNbO_7 at 387 °C. At low temperatures, one large semi-circle arc and one partially overlapping semi-circle arc were observed in the complex impedance plot, which could both be modelled by a resistor (R) and capacitor (C) in parallel. The capacitances of the arcs were estimated using the formula $\omega RC = 1$. The high frequency arc has a capacitance of 2.4×10^{-11} F cm^{-1} and the capacitance of the low frequency arc was 9.3×10^{-9} F cm^{-1}, therefore they were assigned to the bulk and grain boundary, respectively. No electrode response was observed, therefore the conductivity was dominated by the electronic contribution.

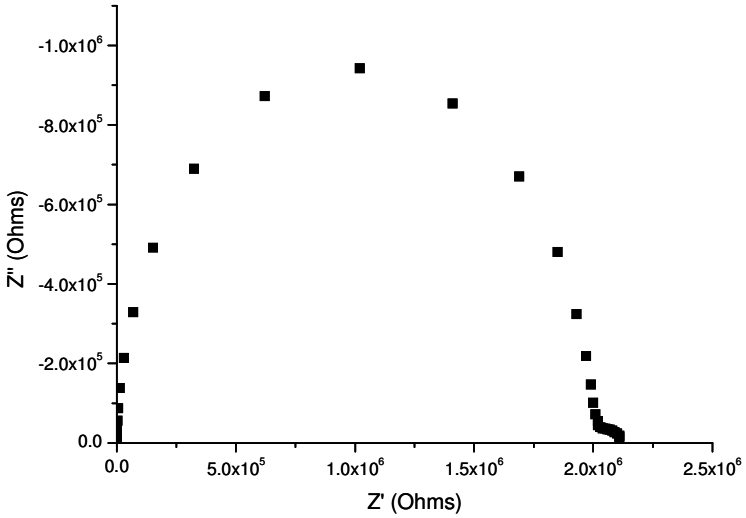

Figure 4.29: Complex impedance plot for Bi_2ScNbO_7 at 387 °C.

Figure 4.30 shows the variation of conductivity with temperature for both pure Bi_2ScNbO_7 and $Bi_2Sn_2O_7$. An increase in conductivity of one order of magnitude is observed when Sn^{4+} is replaced with a 1:1 ratio of Sc^{3+} to Nb^{5+}. Therefore the chemical nature of the cation, not only its radius, affects the physical properties. Kennedy *et al.* have attributed trends in the cell volume of stannate pyrochlores to a higher degree of covalency in the Sn-O bond, which may partially explain the lower conductivity of $Bi_2Sn_2O_7$. [28] Abrahams *et al.* have measured the ionic conductivity of some bismuth niobate oxides and found that the niobium rich compositions displayed a degree of electronic conductivity.[29] Therefore, it is possible that the increase in conductivity seen for Bi_2ScNbO_7 (with respect to $Bi_2Sn_2O_7$) is partially due to an increased electronic component of the total conductivity.

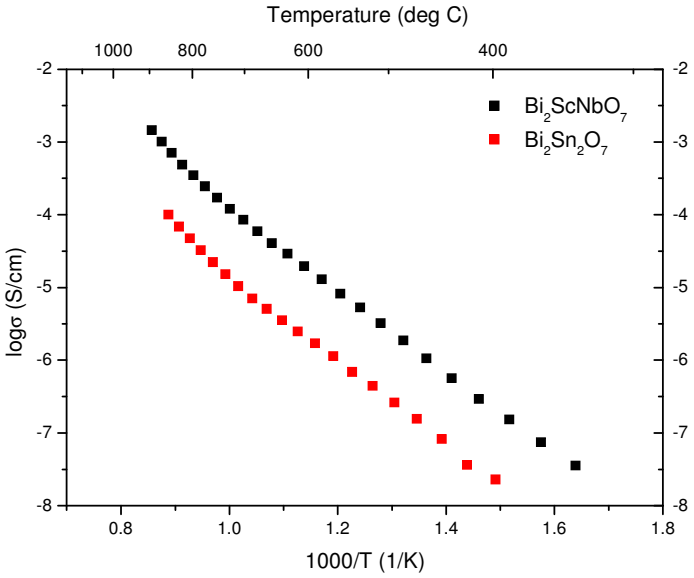

Figure 4.30: Plot of the variation of conductivity with temperature for the two parent members $Bi_2Sn_2O_7$ and Bi_2ScNbO_7.

There have been several studies on the effect the nature of the cation has on the conductivity. For example, a 1:1 ratio of Ga^{3+} and Sb^{5+} has an average cation radius of 0.61 Å, almost identical to the radius of Ti^{4+} (0.605 Å).[30] Therefore the conductivity of the $Gd_2(GaSb)_{1-x}Zr_{2x}O_7$ system affords a suitable comparison with the $Gd_2Ti_{2-x}Zr_xO_7$ system, as they have identical radius ratios.[30] The conductivity of the $Gd_2(GaSb)_{1-x}Zr_{2x}O_7$ system has a lower conductivity than the $Gd_2Ti_{2-x}Zr_xO_7$ system and at x = 0.4 the difference is approximately three orders of magnitude lower, indicating that chemical nature affects the conductivity.[30] However, the magnitude of the difference in conductivity between the two systems decreases with increasing zirconium content.[30]

4.6.3 Characterisation of Bi_2ScNbO_7 doped analogues with Rietveld refinement

In the following sections, all $Bi_2Sc_{1+x}Nb_{1-x}O_7$, $Bi_{2-x}Ca_xScNbO_{7-x/2}$ and $Bi_2ScNb_{1-x}Zr_xO_{7-x/2}$ phases have been characterised by Rietveld refinement. In all cases, the following parameters were refined: 18 background parameters, specimen displacement height, peak shape, cell parameter and one overall isotropic temperature factor. The structural model was based on that of Bi_2ScNbO_7 with Bi^{3+} displaced to a 96h site. Occupancies of the B cation site and oxygen sites were adjusted accordingly to take the appropriate substitution into account.

4.6.4 $Bi_2Sc_{1+x}Nb_{1-x}O_{7-x}$

Structural characterisation

Phase pure samples with compositions $Bi_2Sc_{1+x}Nb_{1-x}O_{7-x}$ (x =0.05-0.15) were prepared. Rietveld refinement was carried out using the parameters described in section 4.6.3 and a typical Rietveld fit is shown in Figure 4.31.

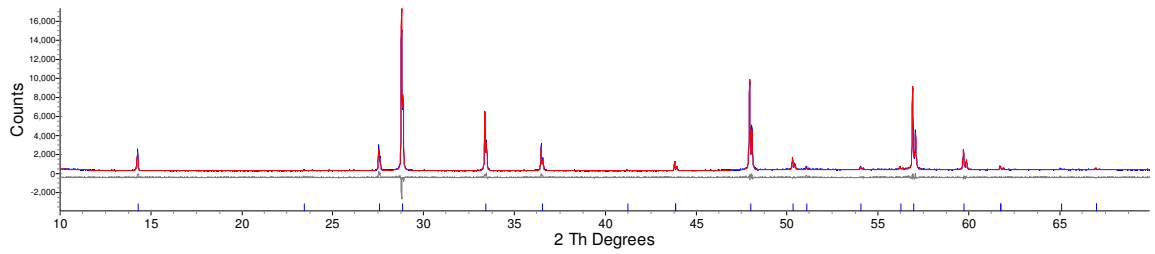

Figure 4.31: d9_03284: Rietveld refinement for $Bi_2Sc_{1.05}Nb_{0.95}O_{6.95}$, R_{wp} = 6.447%.

4.6.4.1 Impedance

Increasing the ratio of scandium to niobium introduced oxygen deficiency into the pyrochlore structure and therefore should be expected to increase oxide ion conductivity. All pellets in the $Bi_2Sc_{1+x}Nb_{1-x}O_{7-x}$ series had densities around 80%. At low temperatures one semi-circle arc and a low frequency tail were observed in the complex impedance plot of $Bi_2Sc_{1.05}Nb_{0.95}O_{6.95}$ (Figure 4.32). The capacitance was estimated using $\omega RC = 1$, and a value of 1.1x 10^{-11} F cm^{-1} was obtained at 420 ° C for the large arc, typical of the bulk response. The bulk arc could be modelled with a resistor (R) and capacitor (C) in parallel. The tail had a capacitance of 7.2 x 10^{-8} F cm^{-1}, indicating the grain boundary component.

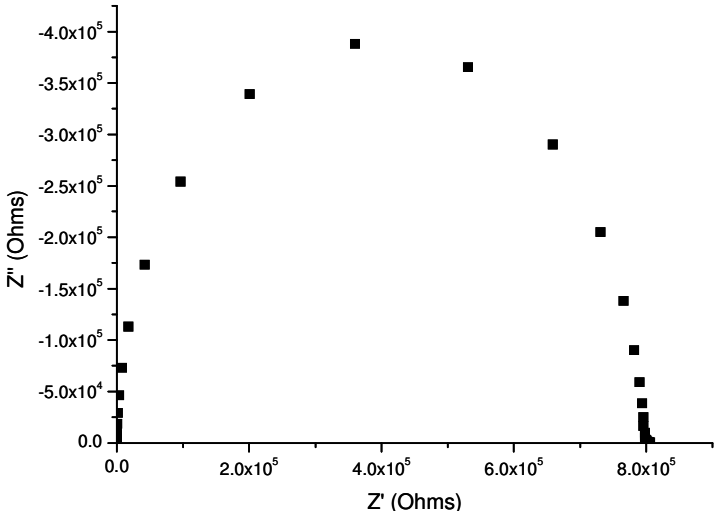

Figure 4.32: Complex impedance plot for $Bi_2Sc_{1.05}Nb_{0.95}O_{6.95}$ at 420 °C.

The bulk response gradually disappeared with heating. At low frequencies (less than 10 Hz) the capacitance remained in the order of magnitude 10^{-8}-10^{-9} F cm^{-1}, which suggests that the ionic contribution to conductivity is not dominant. $Bi_2Sc_{1.05}Nb_{0.95}O_{6.95}$ showed a conductivity very similar to parent member, Bi_2ScNbO_7 (see Figure 4.33), despite having an oxygen deficiency.

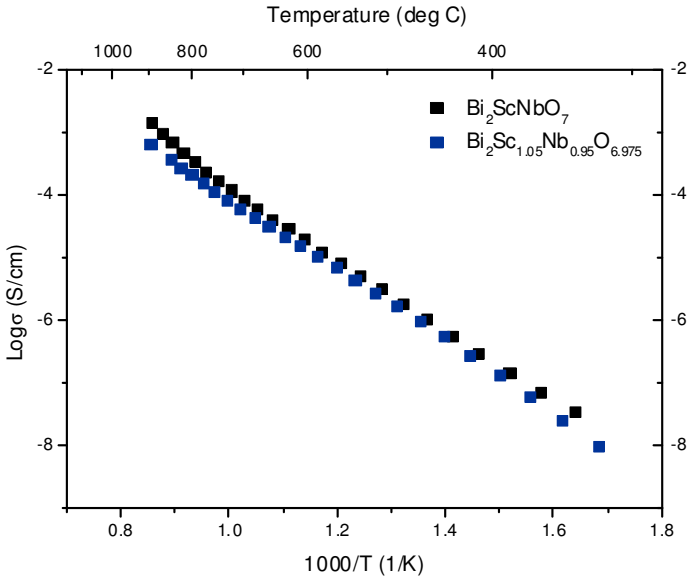

Figure 4.33: Plot of variation of conductivity with temperature in the $Bi_2Sc_{1+x}Nb_{1-x}O_{7-x}$ system.

4.6.5 $Bi_{2-x}Ca_xScNbO_{7-x/2}$

4.6.5.1 Structural characterisation

Figure 4.34 shows a Rietveld plot for $Bi_{1.9}Ca_{0.1}ScNbO_{6.95}$, typical for compositions in this series. Refinements were carried out using the model with Bi^{3+} displaced from (0,0,0), as in Table 4.7 and using the parameters described in 4.6.3. No impurity phases were detected.

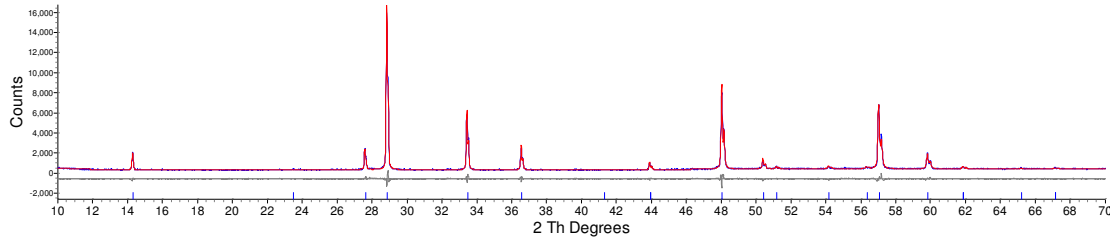

Figure 4.34: d9_03232: Rietveld refinement for $Bi_{1.9}Ca_{0.1}ScNbO_{6.95}$. R_{wp} = 5.862%.

Figure 4.35 shows the variation of cell parameters with increasing Ca^{2+} content. A small percentage of Sc_2O_3 was detected in the Rietveld refinement of $Bi_{1.8}Ca_{0.2}ScNbO_{6.9}$. This indicates the onset of phase segregation and therefore the limit of the solid solution. The decrease in cell parameters is expected, due to the substitution of Bi^{3+} (1.17 Å) with the smaller Ca^{2+} (1.12 Å).[4]

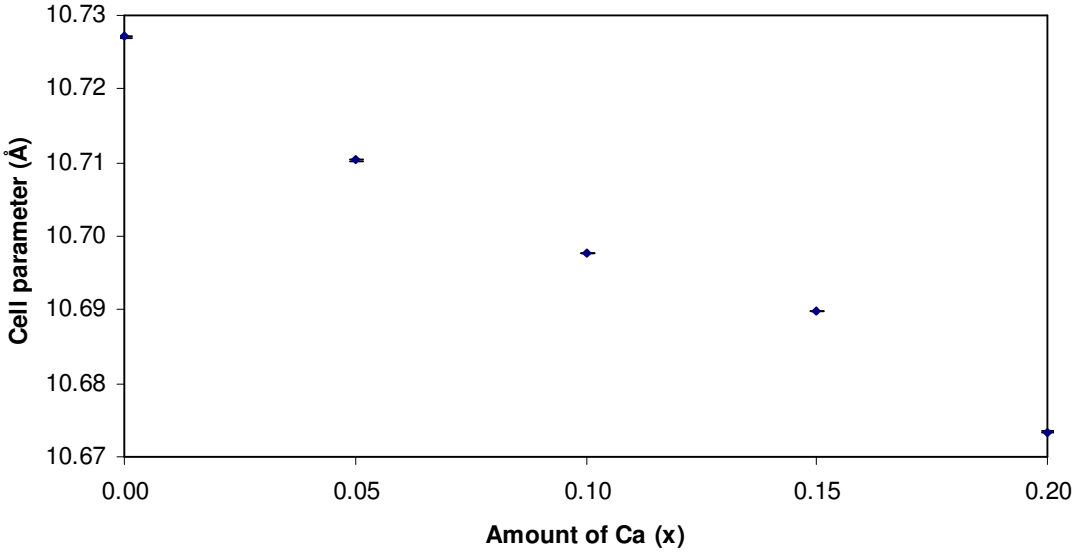

Figure 4.35: Plot of cell parameters versus composition for the $Bi_{2-x}Ca_xScNbO_{7-x/2}$ system.

4.6.5.2 Impedance

At low temperatures, one semi-circle arc with a small shoulder at high frequency was observed in the complex impedance plot of $Bi_{1.95}Ca_{0.05}ScNbO_{6.975}$. The capacitances were estimated using $\omega RC = 1$. At 412 °C the large semi-circle arc had a capacitance of 1.2×10^{-11} F cm^{-1}, which is typical of the bulk. The low frequency shoulder had a capacitance of 7.3×10^{-9} F cm^{-1} and was therefore assigned to the grain boundary response. At low frequencies the capacitance remained of the order of magnitude 10^{-8} F cm^{-1}, hence the conductivity was dominated by the electronic contribution.

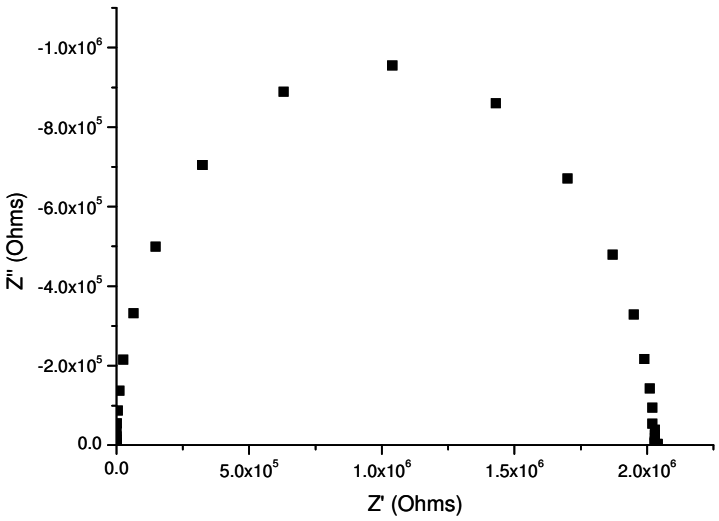

Figure 4.36: Complex impedance plot for $Bi_{1.95}Ca_{0.05}ScNbO_{6.975}$ at 412 °C.

The bulk response gradually disappeared with increasing temperature, with the grain boundary response still visible. At very low frequencies, the capacitance was of the order of magnitude 10^{-8} F cm^{-1}, hence the ionic contribution to the conductivity was not

dominant. The complex impedance plots for $Bi_{1.90}Ca_{0.10}ScNbO_{6.95}$ may be described in the same way as for $Bi_{1.95}Ca_{0.05}ScNbO_{6.975}$. The densities of the pellets were around 80%.

Aliovalent doping with Ca^{2+} on the bismuth site, as in the $Bi_{2-x}Ca_xSn_2O_{7-x/2}$ system introduces oxygen vacancies and hence should increase the conductivity. This was not the case for $Bi_{2-x}Ca_xScNbO_{7-x/2}$ and doping with calcium had little effect on the conductivity, with the stoichiometric parent compound marginally having the highest conductivity in the system (see Figure 4.37).

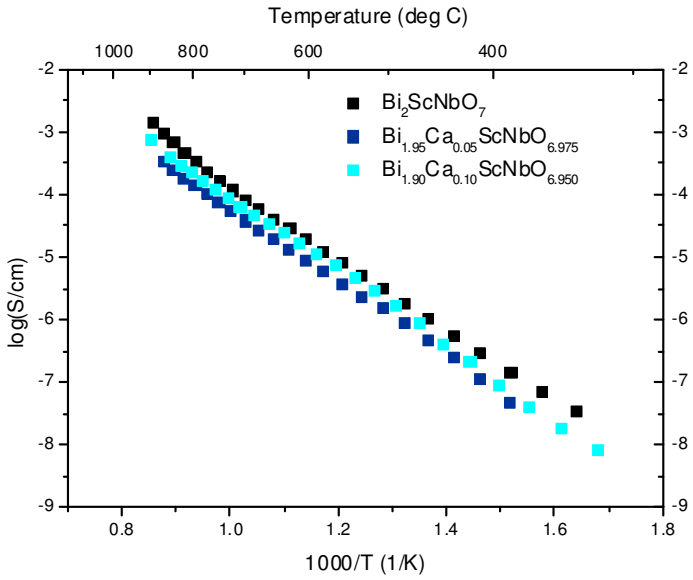

Figure 4.37: Plot of the variation of conductivity with temperature for the $Bi_{2-x}Ca_xScNbO_{7-x/2}$ system.

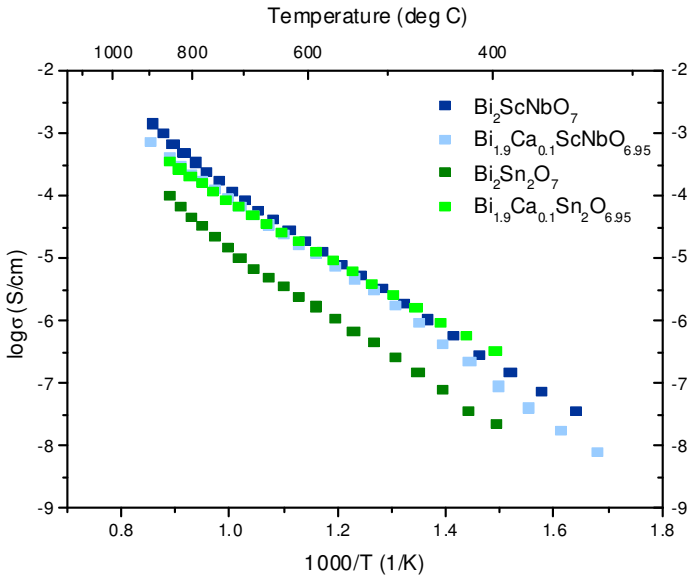

Figure 4.38: Comparison of the conductivities for Bi_2ScNbO_7 and $Bi_2Sn_2O_7$ and their 0.1 Ca doped analogues.

As discussed earlier, the conductivity of $Bi_2Sn_2O_7$ is increased when the A cation site is doped with Ca^{2+}, reaching a maximum for $Bi_{1.90}Ca_{0.10}Sn_2O_{6.95}$. As can be seen in Figure 4.38, when $Bi_2Sn_2O_7$ is doped with Ca^{2+} (*i.e.* $Bi_{1.90}Ca_{0.10}Sn_2O_{6.95}$), the conductivity is now very similar to that obtained by Bi_2ScNbO_7 and at higher temperatures is identical to $Bi_{1.90}Ca_{0.10}ScNbO_{6.95}$.

4.6.6 $Bi_2ScNb_{1-x}Zr_xO_{7-x/2}$

4.6.6.1 Structural characterisation

Another possibility for creating oxygen deficiency is by replacing Nb^{5+} on the B site with Zr^{4+}. A typical Rietveld fit for compounds in this series is shown in Figure 4.39. Rietveld refinement was carried out using the model described in Table 4.7 and the parameters described in 4.6.3.

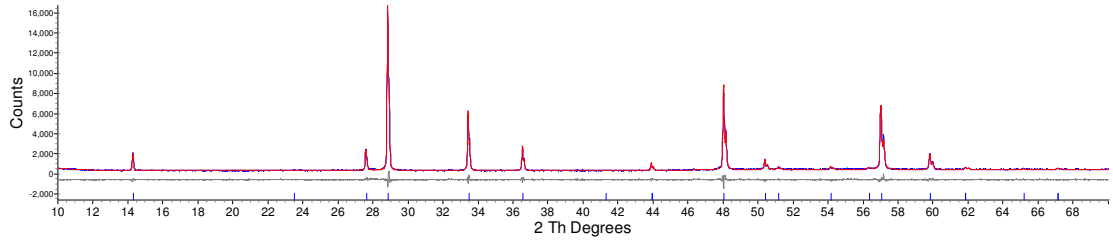

Figure 4.39: d9_03333: Rietveld refinement of $Bi_2ScNb_{0.9}Zr_{0.1}O_{6.95}$. R_{wp} = 5.831%.

4.6.6.2 Impedance

At low temperatures, one semi-circle arc was observed in the complex impedance plot for $Bi_2ScNb_{0.95}Zr_{0.05}O_{6.975}$ (Figure 4.40), which could be modelled using a resistor and capacitor in parallel. At 427 °C the capacitance was estimated to be 1.3×10^{-11} F cm^{-1} using $\omega RC = 1$ and was assigned to the bulk. As there was no Warburg-type electrode response and the capacitance remained low at low frequencies, the conductivity was dominated by the electronic contribution.

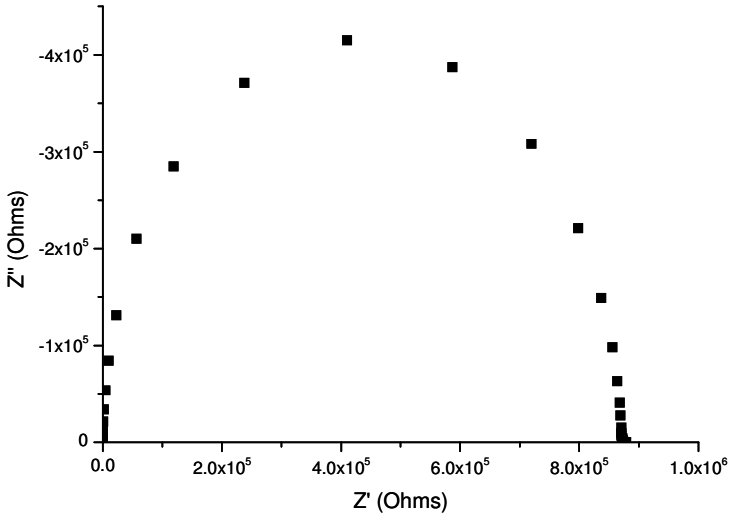

Figure 4.40: Complex impedance plot for $Bi_2ScNb_{0.95}Zr_{0.05}O_{6.975}$ at 427 °C.

With increasing temperature, the arc corresponding to the bulk gradually disappears and a second semi-circle arc appears. This arc has a capacitance of 9.3 x 10^{-9} F cm^{-1} and was assigned to the grain boundary response. The complex impedance plots for other members of the $Bi_2ScNb_{1-x}Zr_xO_{7-x/2}$ series can be described in the same way. All pellets in the $Bi_2ScNb_{1-x}Zr_xO_{7-x/2}$ series had densities of around 80%.

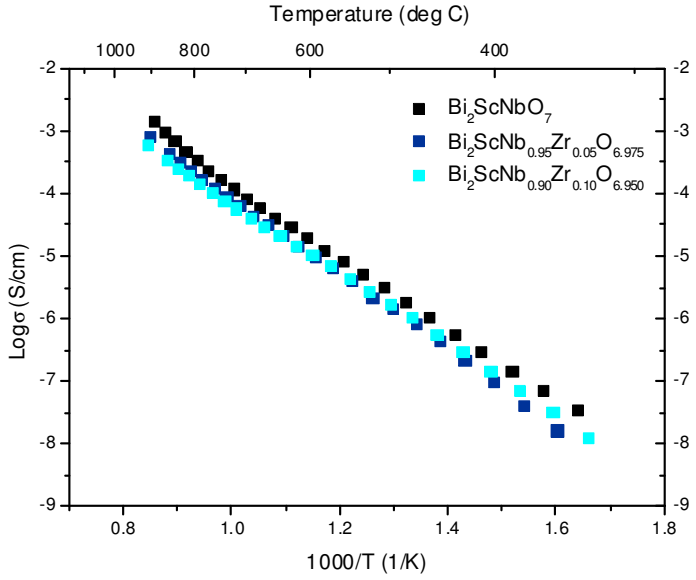

Figure 4.41: Plot of variation of conductivity versus temperature for the $Bi_2ScNb_{1-x}Zr_xO_{7-x/2}$ system.

Figure 4.41 shows the variation in conductivity for Bi_2ScNbO_7, $Bi_2ScNb_{0.95}Zr_{0.05}O_{6.975}$ and $Bi_2ScNb_{0.90}Zr_{0.10}O_{6.95}$. Once more, a similar trend is observed as in the $Bi_2Sc_{1+x}Nb_{1-x}O_{7-x}$ and $Bi_{2-x}Ca_xScNbO_{7-x/2}$ systems, whereby the change in conductivity is very small and the parent Bi_2ScNbO_7 has the highest conductivity, which may be due to some vacancy-dopant association.[31]

4.7 Conclusions

The coexistence of the α- and β-$Bi_2Sn_2O_7$ phases and hysteresis in α-β phase transition temperature show that this phase transition is a first order phase transition. Analysis of synchrotron PXRD data has shown for the first time that β-$Bi_2Sn_2O_7$ is not cubic and Pawley fits have shown that β-$Bi_2Sn_2O_7$ is metrically orthorhombic.

Structure solution using PND and synchrotron PXRD data has been attempted in orthorhombic and monoclinic non-centrosymmetric sub-groups of $Fd\bar{3}m$. Although β-$Bi_2Sn_2O_7$ is metrically orthorhombic, structure solution in orthorhombic sub-groups of $Fd\bar{3}m$ showed significant misfit to both the PND and synchrotron PXRD data, indicating that the true symmetry of β-$Bi_2Sn_2O_7$ is lower. Structure solution in the monoclinic sub-groups showed a much improved fit to the PND and synchrotron PXRD data and a small preference was observed for *Pc*.

The formation of the α-$Bi_2Sn_2O_7$ or β-$Bi_2Sn_2O_7$ polymorph may also be induced by chemical doping. In the $Bi_2Sn_{2-x}Zr_xO_7$ system, the α-$Bi_2Sn_2O_7$ phase is present in the region x = 0-0.6 and β-$Bi_2Sn_2O_7$ is present in the region x = 0.8-1.0. Ca^{2+} doping also stabilises β-$Bi_2Sn_2O_7$ to room temperature. The $Bi_{1.9}Ca_{0.1}Sn_2O_{6.95}$ and $Bi_{1.8}Ca_{0.2}Sn_2O_{6.9}$ compounds show the β-$Bi_2Sn_2O_7$ structure. Bi^{3+} is displaced from the 3-fold axis in Bi_2ScNbO_7 as is common in many bismuth containing pyrochlores.

Various different doping strategies have been explored for $Bi_2Sn_2O_7$ and Bi_2ScNbO_7. Ca^{2+} doping of $Bi_2Sn_2O_7$ results in the highest oxide ion conductivity being observed for $Bi_{1.9}Ca_{0.1}Sn_2O_{6.95}$. No increases in the conductivity were seen in Bi_2ScNbO_7 doped phases with respect to the parent Bi_2ScNbO_7. However, Bi_2ScNbO_7 shows an increase in conductivity of approximately one order of magnitude greater than $Bi_2Sn_2O_7$, which has an identical radius ratio to Bi_2ScNbO_7. This indicates that the chemical nature of the cation influences the properties of a material and not only oxidation states or radius ratio.

4.8 References

1. R. D. Shannon, J. D. Bierlein, J. L. Gillson, G. A. Jones and A. W. Sleight, *J. Phys. Chem. Solids*, 1980, **41**, 117-122.
2. R. H. Jones and K. S. Knight, *J. Chem. Soc., Dalton Trans.*, 1997, 2551-2555.
3. I. R. Evans, J. A. K. Howard and J. S. O. Evans, *J. Mater. Chem.*, 2003, **13**, 2098-2103.
4. R. D. Shannon, *Acta Crystallogr. A*, 1976, **32**, 751-767.
5. B. J. Wuensch, K. W. Eberman, C. Heremans, E. M. Ku, P. Onnerud, E. M. E. Yeo, S. M. Haile, J. K. Stalick and J. D. Jorgensen, *Solid State Ionics*, 2000, **129**, 111-133.

6. T. H. Yu and H. L. Tuller, *Solid State Ionics*, 1996, **86-8**, 177-182.
7. A. V. Shlyakhtina, P. Fedtke, A. Busch, I. V. Kolbanev, T. Barfels, M. Wienecke, A. E. Sokolov, V. A. Ulianov, V. A. Trounov and L. G. Shcherbakova, *Solid State Ionics*, 2008, **179**, 1004-1008.
8. S. A. Kramers and H. L. Tuller, *Solid State Ionics*, 1995, **82**, 15-23.
9. S. Kramer, M. Spears and H. L. Tuller, *Solid State Ionics*, 1994, **72**, 59-66.
10. L. Zhang, O. P. Thakur, A. Feteira, G. M. Keith, A. G. Mould, D. C. Sinclair and A. R. West, *Appl. Phys. Lett.*, 2007, **90**, 142914.
11. I. Radosavljevic, J. A. K. Howard, A. W. Sleight and J. S. O. Evans, *J. Mater. Chem.*, 2000, **10**, 2091-2095.
12. I. R. Evans, S. Tao, J. T. S. Irvine and J. A. K. Howard, *Chem. Mater.*, 2002, **14**, 3700-3704.
13. J. S. O. Evans and A. W. Sleight, *Int. J. Inorg. Mater.*, 2000, **2**, 375-377.
14. S. Omar, E. D. Wachsman and J. C. Nino, *Solid State Ionics*, 2008, **178**, 1890-1897.
15. J. S. O. Evans, Durham, 1999, p. Fortran 77 routine.
16. B. J. Kennedy, Isamunadar and M. M. Elcombe, *Mater. Sci. Forum*, 1998, **278**, 762-767.
17. B. J. Campbell, H. T. Stokes, D. E. Tanner and D. M. Hatch, *J. Appl. Crystallogr.*, 2006, **39**, 607-614.
18. A. G. Christy, *Acta Crystallogr. B*, 1995, **51**, 753-757.
19. J. F. Scott, *Adv. Mater.*, 2010, **22**, 2106-2107.
20. C. Heremans, B. J. Wuensch, J. K. Stalick and E. Prince, *J. Solid State Chem.*, 1995, **117**, 108-121.
21. K. J. Moreno, M. A. Guevara-Liceaga, A. F. Fuentes, J. Garcia-Barriocanal, C. Leon and J. Santamaria, *J. Solid State Chem.*, 2006, **179**, 928-934.
22. K. V. G. Kutty, C. K. Matthews, T. N. Rao and U. V. Varadaraju, *Solid State Ionics*, 1995, **80**, 99 - 110.
23. D. P. Cann, C. A. Randall and T. R. Shrout, *Solid State Commun.*, 1996, **100**, 529-534.
24. T. A. Vanderah, I. Levin and M. W. Lufaso, *Eur. J. Inorganic Chem.*, 2005, 2895-2901.
25. I. Radosavljevic, J.S.O. Evans and A. W. Sleight, *J. Solid State Chem.*, 1998, **136**, 63-66.
26. Y. Liu, R. L. Withers, H. B. Nguyen, K. Elliott, Q. J. Ren and Z. H. Chen, *J. Solid State Chem.*, 2009, **182**, 2748-2755.
27. Q. D. Zhou, B. J. Kennedy, V. Ting and R. L. Withers, *J. Solid State Chem.*, 2005, **178**, 1575-1579.
28. B. J. Kennedy, B. A. Hunter and C. J. Howard, *J. Solid State Chem.*, 1997, **130**, 58-65.
29. M. Malys, M. Holdynski, F. Krok, W. Wróbel, J. R. Dygas, C. Pirovano, R. N. Vannier, E. Capoen and I. Abrahams, *J. Power Sources*, 2009, **194**, 16-19.
30. H. Takamura and H. L. Tuller, *Solid State Ionics*, 2000, **134**, 67-73.
31. J. A. Kilner, *Solid State Ionics*, 2000, **129**, 13-23.

5 Synthesis and Characterisation of $Nd_2Zr_2O_7$

5.1 Background

The synthesis of $Nd_2Zr_2O_7$ has been reported several times in the literature, using precursor and conventional solid state methods.[1-5] When prepared using a conventional solid state route at 1400 °C, $Nd_2Zr_2O_7$ is well known to possess the pyrochlore structure.[1] However, there have been conflicting reports of whether $Nd_2Zr_2O_7$ has the pyrochlore or fluorite structure when prepared using precursor methods.[2-5] For example, Battacharya *et al.* report the fluorite structure when synthesised at 750 °C, whilst Zhang *et al.* assign $Nd_2Zr_2O_7$ prepared at 600 °C to the pyrochlore structure.[3, 5] Structural characterisation of $Nd_2Zr_2O_7$ samples prepared by precursor methods have mainly utilised laboratory PXRD for phase identification only, whilst few other local probes have been used and no neutron diffraction studies have been carried out.[3-5] $Nd_2Zr_2O_7$ samples prepared via a precursor method show peak broadening in PXRD data, indicative of small crystallite size, hence broad, weak pyrochlore superstructure peaks will be difficult to detect by PXRD. In order to fully characterise $Nd_2Zr_2O_7$ prepared via precursor method, local structure techniques must also be used.

The most comprehensive structural study of $Nd_2Zr_2O_7$ prepared by a precursor method is a recent synchrotron PXRD study by Lee *et al.*.[2] This found that $Nd_2Zr_2O_7$ possesses the fluorite structure when synthesised between 700 °C and 1000 °C, but when $Nd_2Zr_2O_7$ is synthesised at temperatures greater than 1100 °C, $Nd_2Zr_2O_7$ has the pyrochlore structure. $Nd_2Zr_2O_7$ is already well known to undergo a pyrochlore-fluorite order-disorder transition at 2300 °C, which is probably due to the r_A/r_B value for $Nd_2Zr_2O_7$ (r_A/r_B = 1.54) being close to the fluorite-pyrochlore boundary of 1.46. [6] Therefore, it may be possible that the polymorph adopted by $Nd_2Zr_2O_7$ may be controlled by the choice of synthetic route.

There are examples in the literature where the synthetic route adopted determines the product or polymorph obtained. For example, pyrochlore type $Bi_2Ti_2O_7$ may only be prepared through precursor routes, whilst the solid state synthesis of this stoichiometric ratio gives a mixture of $Bi_4Ti_3O_{12}$ and $Bi_2Ti_4O_{11}$.[7-9] The synthesis of the cubic polymorph of $ZrMo_2O_8$ can be obtained via a precursor route, but conventional solid state synthesis gives monoclinic $ZrMo_2O_8$ below 670 K and trigonal $ZrMo_2O_8$ above 670 K.[8-10]

The aim of this chapter was firstly to use a precursor route to synthesise $Nd_2Zr_2O_7$, rather than the conventional high temperature method. Secondly, the aim was to carry out structural characterisation of $Nd_2Zr_2O_7$ in order to determine whether $Nd_2Zr_2O_7$ prepared via the precursor method was a fluorite (with disordered cations and anions) or pyrochlore (with ordered cations and anions) by using average and local structure probes. Techniques to be used included X-ray, neutron and electron diffraction, neutron total scattering, Raman spectroscopy and NMR spectroscopy. The use of many different average and local structure techniques will offer a significant improvement on existing literature structural characterisation.

5.2 Synthetic routes to $Nd_2Zr_2O_7$

5.2.1 Nitrate precursor method

The hydration level of $ZrO(NO_3)_2 \bullet xH_2O$, was determined by firing $ZrO(NO_3)_2 \bullet xH_2O$ overnight at 800 °C, in order to form ZrO_2 and enabling x to be calculated. Equimolar amounts of $Nd(NO_3)_3 \bullet 6H_2O$ (0.90 g, 2.06 mmol, Aldrich, 99.9%) and $ZrO(NO_3)_3 \bullet 2.5H_2O$ (0.57 g, 2.06 mmol, Aldrich, 99.99%) were dissolved separately in 25 ml water. The two solutions were mixed together and stirred thoroughly before neutralising the mixture with NH_4OH. A lilac gel was formed and this was stirred for several hours, aged overnight, stirred for approximately two hours before filtering under vacuum. The solid was dried at 95 °C and then fired at 600 °C for ten hours, which yielded a blue compound. This product was then fired at 700 °C and 900 °C for 10 hours at each temperature, with intimate grinding between firings.

A large sample was prepared for neutron diffraction using 13.7 mmol of both $Nd(NO_3)_3 \bullet 6H_2O$ (12.03 g, Aldrich, 99.9%) and $ZrO(NO_3)_3 \bullet 2.5H_2O$ (7.59 g, Aldrich, 99.9%), each dissolved separately in 100 ml water. The precursor was prepared as above and then fired at 800 °C for 16 hours. A blue polycrystalline powder was formed. Two further large samples were prepared in the same way. After the initial firing at 800 °C, one sample was annealed at 800 °C for 300 hours and the other sample was annealed at 1000 °C for 300 hours. In the following discussion these samples will be referred to as indicated in Table 5.1.

Table 5.1: Abbreviations used for $Nd_2Zr_2O_7$ after different heat treatments.

Synthetic route	Abbreviation
$Nd_2Zr_2O_7$ fired for 16 h at 800 °C	NZO-800A
$Nd_2Zr_2O_7$ annealed at 800 °C	NZO-800B
$Nd_2Zr_2O_7$ annealed at 1000 °C	NZO-1000B

5.2.2 Conventional solid state synthesis

ZrO_2 (0.85 g, 6.86 mmol, Aldrich, 99.9%) and Nd_2O_3 (1.15 g, 3.43 mmol, Honeywell, 99%) were fired at 900 °C to remove absorbed water. The oxides were then ground together and fired at 1400 °C for 80 hours, with intermittent grinding.[1, 10] A blue powder was formed.

5.3 Structural characterisation with laboratory PXRD

Firing the precursor at 600 °C yielded a very poorly crystalline compound, with broad peaks (Figure 5.1a). Further heating of this sample to 700 °C and 900 °C (Figure 5.1b and c) resulted in a fluorite phase being obtained at each temperature. Firing the sample (made by the precursor route) at 1100 °C resulted in the formation of a more crystalline sample and the appearance of weak pyrochlore peaks, indicating that the sample has transformed from a fluorite to pyrochlore. After increasing the firing temperature to 1200 °C (Figure 5.1d) for a total of 16 hours, the intensity of the pyrochlore peaks did not increase.

Table 5.2 and Table 5.3 show the structural models used for $Nd_2Zr_2O_7$ refinements. In addition to the variable parameters in the above models, the cell parameter, 18 background terms, scale factor, overall temperature factor and specimen displacement height were refined.

Table 5.2: Structural model used for fluorite type $Nd_2Zr_2O_7$ refinements (as for Figure 5.1 b and c).

Atom	Site	x	y	z	Occupancy
Nd	4a	0	0	0	0.5
Zr	4a	0	0	0	0.5
O	8c	0.25	0.25	0.25	0.875

Table 5.3: Structural model used for pyrochlore $Nd_2Zr_2O_7$ refinements (as for Figure 5.1d).

Atom	Site	x	y	z	Occupancy
Nd	16c	0	0	0	1
Zr	16d	0.5	0.5	0.5	1
O(1)	48f	0.43126	0.125	0.125	1
O(2)	8a	0.125	0.125	0.125	1

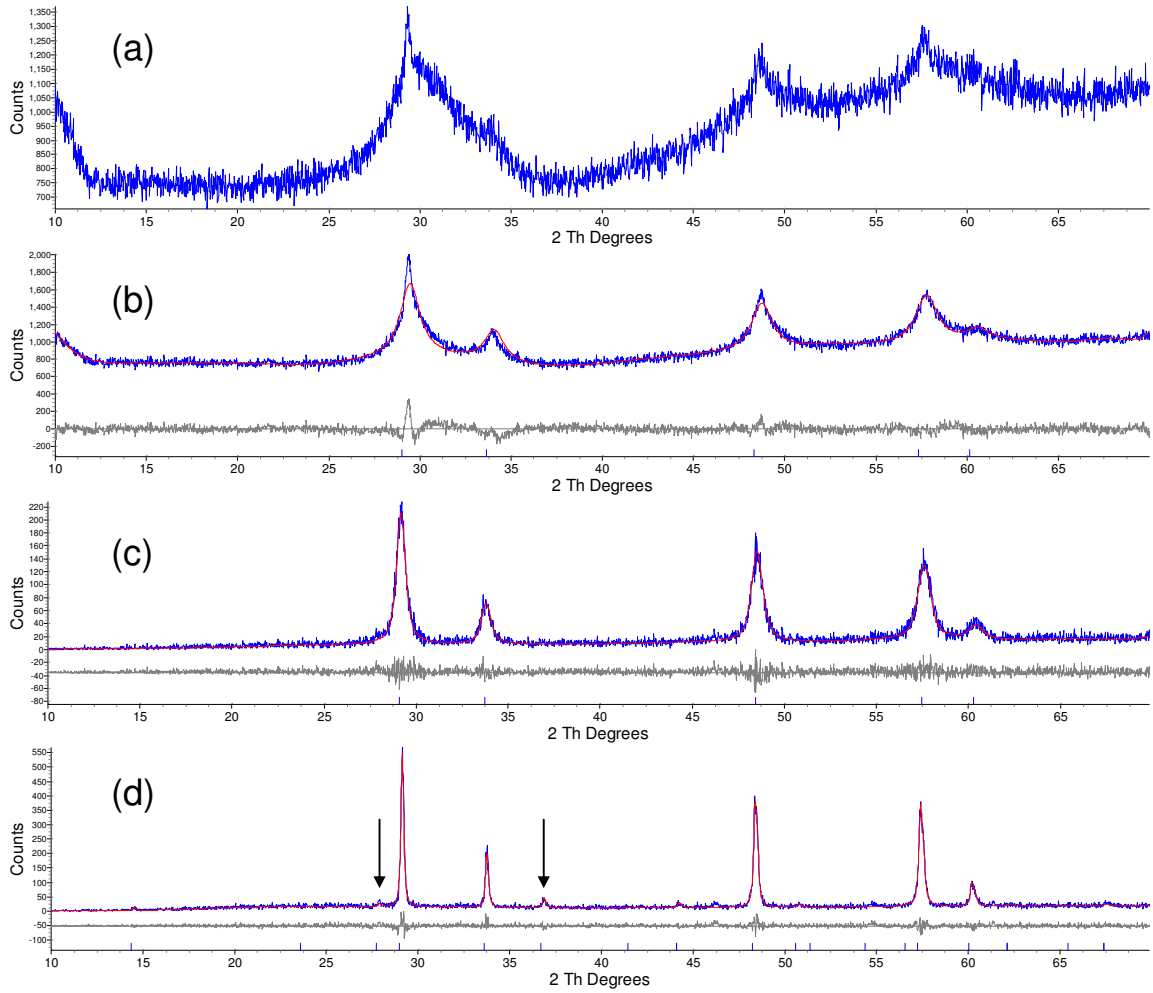

Figure 5.1: $Nd_2Zr_2O_7$ after firing at different temperatures. (a) d9_02696: $Nd_2Zr_2O_7$ after firing at 600 ℃. (b) and (c) are refinements using a fluorite model. (b) d9_02697: $Nd_2Zr_2O_7$ after firing at 700 ℃. (c) d5_07671: $Nd_2Zr_2O_7$ after firing at 900 ℃. (d) d5_07691: $Nd_2Zr_2O_7$ after firing at 1200 ℃, refinement using a pyrochlore model.

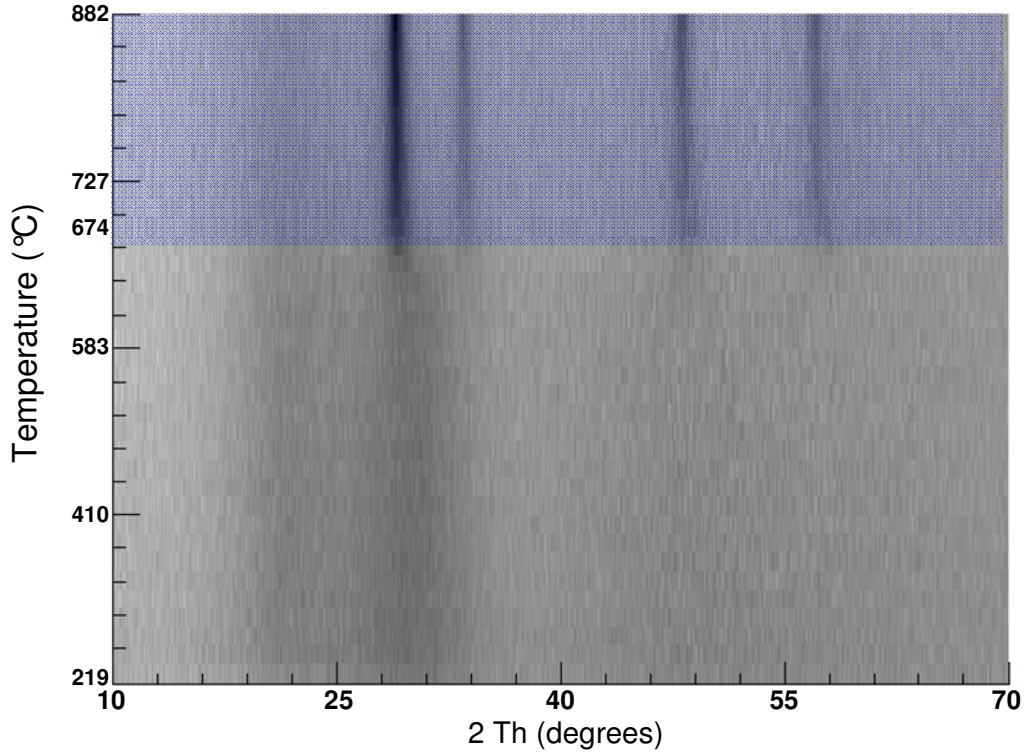

Figure 5.2: d8_03593: *In-situ* VT-PXRD study of the $Nd_2Zr_2O_7$ precursor. $Nd_2Zr_2O_7$ forms at 674 °C. Below this temperature, the sample is amorphous. $Nd_2Zr_2O_7$ stability range is shaded in pale blue.

Variable temperature PXRD was carried out on the amorphous $Nd_2Zr_2O_7$ precursor, from room temperature to 900 °C, in order to determine the onset of formation of the crystalline product. Data show that the fluorite type structure forms at 674 °C (Figure 5.2). Above this temperature, the peak width decreases, showing an increase in crystallinity. No pyrochlore superstructure peaks or decomposition products were observed in the temperature region studied. Rietveld refinement was carried out on $Nd_2Zr_2O_7$ synthesised *in-situ* in the diffractometer, after cooling to room temperature. Specimen displacement height, peak shape, 18 background parameters, cell parameter and one overall temperature factor were refined. Figure 5.3 shows the Rietveld fit obtained, which gave a fluorite cell with $a = 5.311(8)$ Å and $R_{wp} = 11.065$ %.

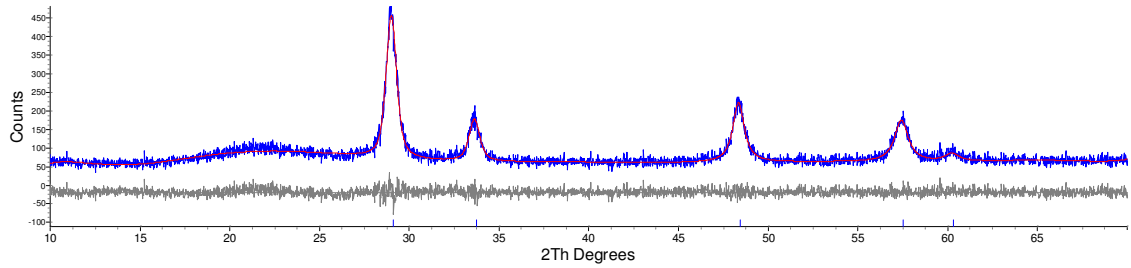

Figure 5.3: d8_03593 range 37 (19 °C): $Nd_2Zr_2O_7$ synthesised *in-situ* in the diffractometer, post VT-PXRD and after cooling to room temperature. Rietveld refinement using a fluorite structural model. R_{wp} = 11.065%, *a* = 5.311(8) Å.

In order to investigate the stability of the apparently fluorite-type $Nd_2Zr_2O_7$, an annealing experiment was carried out. A sample of $Nd_2Zr_2O_7$ synthesised via the precursor route described in section 5.2.1 was fired at 800 °C with intermittent regrinding. The affect of prolonged annealing was monitored through XRD. Despite annealing for over 300 hours, no transformation to the pyrochlore structure has been observed (Figure 5.4). Crystallite size analysis, carried out via Rietveld refinement has shown only a very small change in crystallite size, from 9-11 nm (Table 5.4).

Table 5.4: Crystallite size of $Nd_2Zr_2O_7$ obtained from Rietveld refinement.

Time annealed (h)	Crystallite Size (nm)
16	9.16(9)
28	9.36(8)
58	9.91(9)
118	11.5(1)
134	11.05(9)
146	11.4(1)
162	11.0(1)
174	10.17(7)
242	10.80(8)
309	10.89(9)

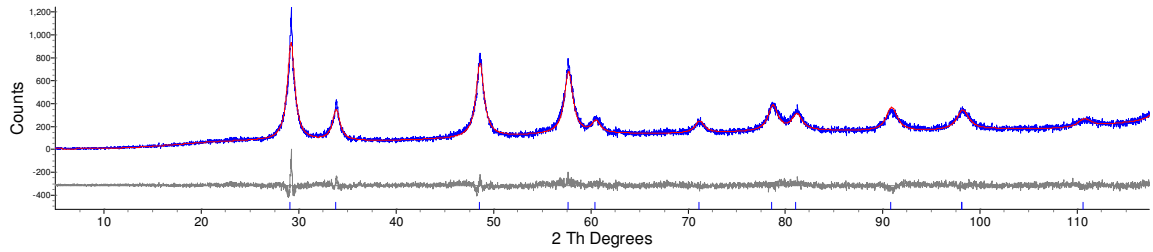

Figure 5.4: d5_07882: Fluorite type $Nd_2Zr_2O_7$ after annealing for 309 hours at 800 °C. Rietveld refinement for a fluorite structure. R_{wp} = 9.389 %, *a* = 5.3014(4) Å.

It therefore appears that from the laboratory PXRD data analysis, $Nd_2Zr_2O_7$ prepared by the precursor method and annealed at 800 °C possesses a fluorite-type structure. The question still remains as to whether this $Nd_2Zr_2O_7$ is actually a true fluorite, or whether it is a pyrochlore, with the crystallite size sufficiently small and the peaks therefore

sufficiently broad to prevent the observation of the weak pyrochlore supercell reflections. However, taking the radius ratio rules into account it may be possible that $Nd_2Zr_2O_7$ can adopt both structure types, as the r_A/r_B value for $Nd_2Zr_2O_7$ is 1.54, close to the fluorite-pyrochlore boundary of 1.46, but just within the pyrochlore stability field.

5.4 Neutron diffraction studies

5.4.1 $Nd_2Zr_2O_7$ 'as synthesised' (NZO 800A) and $Nd_2Zr_2O_7$ annealed at 800 °C (NZO 800B)

Neutron diffaction data were collected on the General Materials Diffractometer (GEM) at the ISIS spallation source. Table 5.2. shows the model used for refinement for both NZO 800A and NZO 800B. In the refinement for both NZO 800A and NZO 800B, 3 banks of data were included (91.3°, 63.6° and 35.0° banks). 15 background parameters, a scale factor, 3 peak shape parameters and an absorption coefficient were refined for each bank. In addition, the cell parameter and two isotropic temperature factors (one for the metal site and one for the oxygen site) were refined. Figure 5.5a and b show Rietveld fits of NZO 800A and NZO 800B respectively. Neutron diffraction data are consistent with a $Nd_2Zr_2O_7$ fluorite model.

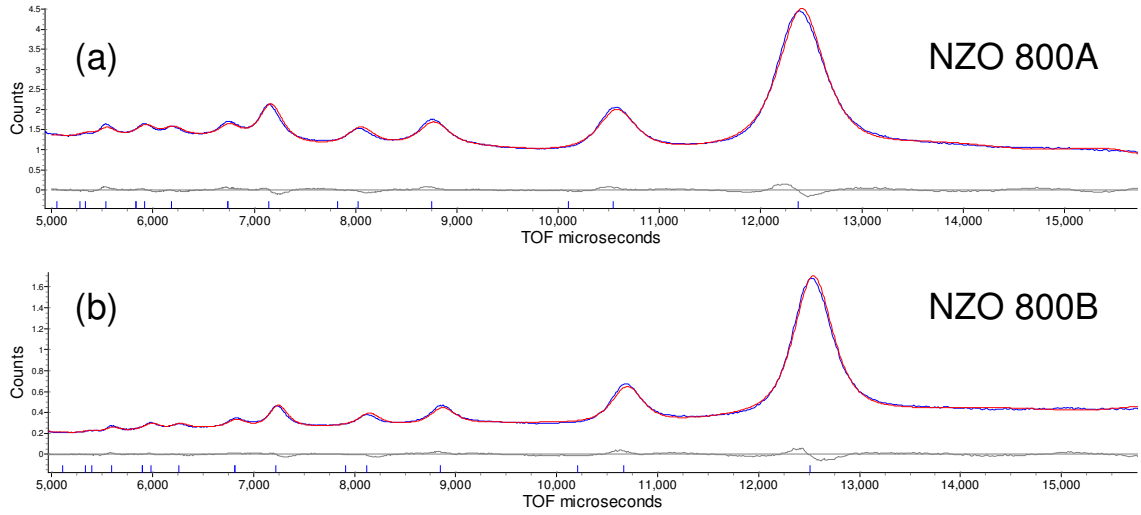

Figure 5.5: GEM43539: Refinement for NZO 800A using a fluorite model and 3 banks of data. Bank 5 (91.3°) is shown. R_{wp} =2.317%, *a* = 5.2590(2) Å. (b) GEM43540: Rietveld refinement for NZO 800B. using 3 banks of data and a fluorite model. R_{wp} = 2.476%, *a* =5.3176(1) Å. Bank 5 (91.3°) is shown.

5.4.2 $Nd_2Zr_2O_7$ annealed at 1000 °C (NZO 1000)

When $Nd_2Zr_2O_7$ is annealed at high temperatures, weak pyrochlore reflections are observed in the diffraction pattern. In the chemically related compound $Nd_2Hf_2O_7$, the crystal structure determination reported disorder on the oxygen sublattice, where some

of the oxygen atoms from the 48f site are displaced to the normally vacant 8b (O3) site.[11]

Taking the possibility of similar oxygen disorder into consideration, two pyrochlore type models for NZO 1000 were refined against the neutron data (banks 3, 4 and 5) and laboratory X-ray data: model 1 with oxygen present on the 48f and 8a sites only (as normal) and model 2 with oxygen present on all three oxygen sites (see Table 5.5 and Table 5.6 respectively). For both models, the cell parameter, 48f x parameter, zero point error, scale factor, absorption correction, 6 background parameters per bank, one isotropic temperature factor per metal site, one equated isotropic temperature factor for all oxygen sites and peak shape were refined for the model 1. In addition, fractional occupancies of the three unique oxygen sites were refined for model 2, using a restraint to prevent deviations from the nominal stoichiometry.

Table 5.5: Model 1 obtained for refinements with no oxygen disorder, *i.e.* oxygen only occupying the 48f and 8a crystallographic sites.

Atom	Site	x	y	z	Occupancy
Nd	16c	0	0	0	1
Zr	16d	0.5	0.5	0.5	1
O(1)	48f	0.41120(5)	0.125	0.125	1
O(2)	8a	0.125	0.125	0.125	1

Table 5.6: Model 2 obtained for refinement of $Nd_2Zr_2O_7$ when oxygen is disordered across the 48f, 8a and 8b crystallographic sites.

Atom	Site	x	y	z	Occupancy
Nd	16c	0	0	0	1
Zr	16d	0.5	0.5	0.5	1
O(1)	48f	0.4126(5)	0.125	0.125	0.9670(8)
O(2)	8a	0.125	0.125	0.125	0.99(3)
O(3)	8b	0.375	0.375	0.375	0.21(3)

Figure 5.6a and b show the Rietveld fits obtained for models 1 and 2, respectively. Refinement results gave R_{wp} of 6.042% for model 1. However, addition of the third oxygen site gave an improved R_{wp} of 5.515%, supporting model 2 with the oxygen sublattice disorder. Table 5.7 shows the key refinement results. The occupation of the O3 site in $Nd_2Zr_2O_7$ is similar to the situation in the chemically related $Nd_2Hf_2O_7$ pyrochlore and the theoretical study by Catlow and Wilde, which showed that oxygen migration from the 48f site to the vacant 8b site is energetically most favourable.[11, 12]

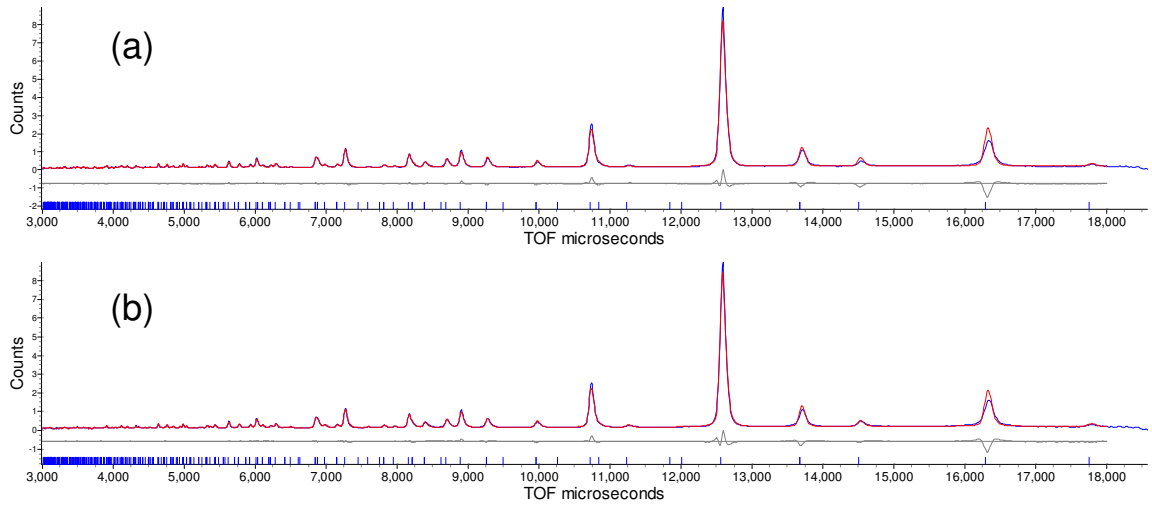

Figure 5.6: GEM43541: Rietveld refinement of NZO 1000. (a) Model 1, R_{wp} = 6.042%. (b) Model 2, R_{wp} = 5.515%

Table 5.7: Comparison of the key refinement results for $Nd_2Zr_2O_7$ annealed at 1000 °C.

	Model 1: without O(3)	**Model 2: with O(3)**
a (Å)	10.67711(6)	10.67706(5)
R_{wp} (%)	6.042	5.515
48f x	0.41120(5)	0.41264(5)
Occupancy O1	1	0.9670(8)
Occupancy O2	1	0.993(3)
Occupancy O3	1	0.210(3)
B_{eq} Oxygen (Å^2)	1.29(1)	1.15(1)

In the recent synchrotron PXRD study of $Nd_2Zr_2O_7$ by Lee *et al.*, Rietveld refinement results found cation antisite disorder in $Nd_2Zr_2O_7$.[2] The antisite disorder decreased as the synthesis temperature increased. To explore the possibility of the NZO 1000 sample having cation antisite disorder, Rietveld refinement was used to determine the amount of Zr^{4+} on the Nd^{3+} site and *vice-versa* by refining the occupancy of the cation sites, for both model 1 and model 2. This resulted in only a very small insignificant decrease in R-factor. The difference between our $Nd_2Zr_2O_7$ pyrochlore models and Lee's pyrochlore model is probably due to the different thermal history and preparation conditions of the sample.

5.5 Complementary techniques

5.5.1 Electron diffraction

Electron diffraction data were collected on NZO 800A. Only ring patterns could be obtained, due to individual grains of $Nd_2Zr_2O_7$ being agglomerates. The ring pattern, shown in Figure 5.7, shows no pyrochlore reflections (which would lead to a doubling of the unit cell parameter) and indexes to a 5.46 Å face centred cubic unit cell, hence it is consistent with NZO 800A having a fluorite type structure.

Zone axis patterns were collected for NZO 1000 (Figure 5.8). These diffraction patterns indexed to a 11.08 Å face centred cubic cell, as expected for a pyrochlore. This is bigger than values from PXRD and PND and given that the same sample was used for collection of electron diffraction data, this probably due to some error in the calibration of the microscope.[13]

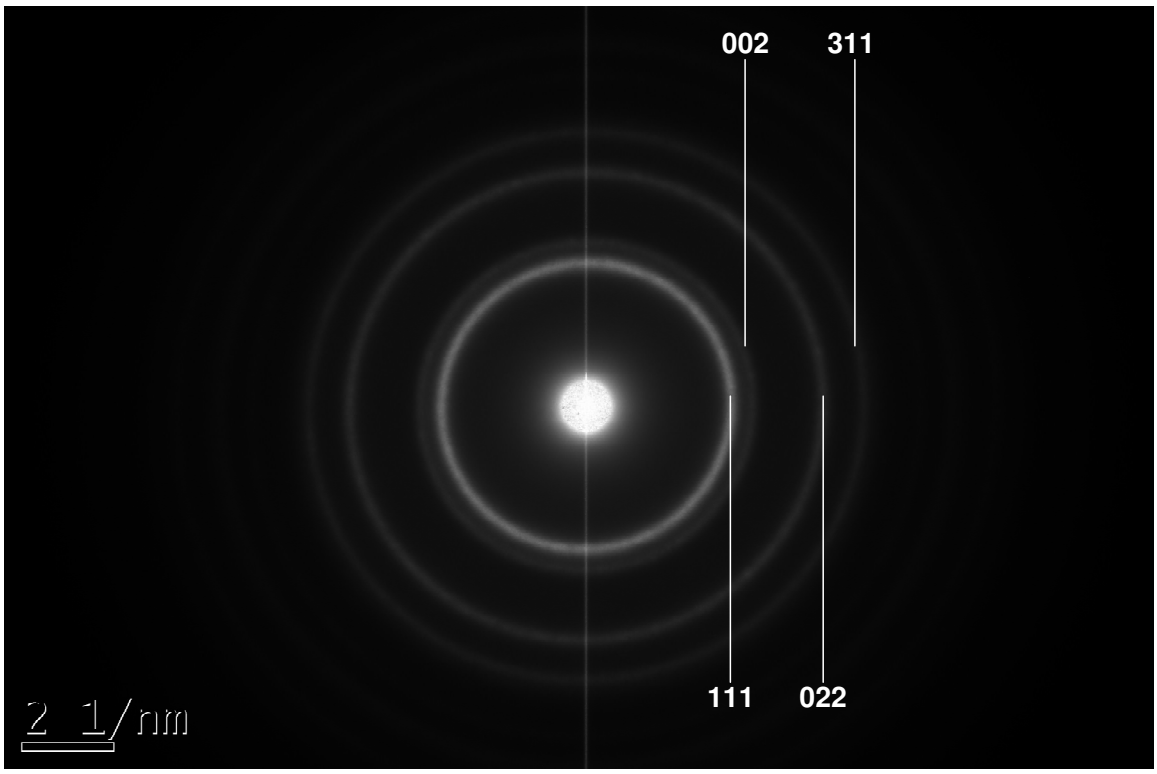

Figure 5.7: Electron diffraction pattern of NZO 800A, which indexes to a 5.46Å face centred cubic unit cell.

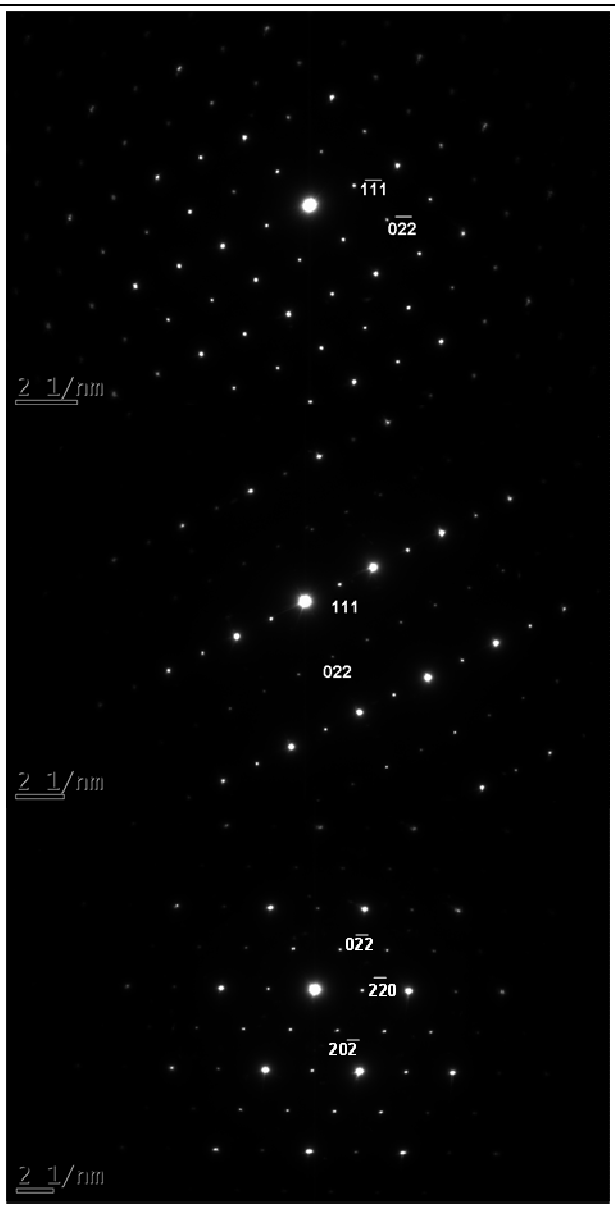

Figure 5.8: Electron diffraction patterns of NZO 1000. The patterns index to a 11.08 Å face centred cubic cell.

5.5.2 ^{91}Zr solid state NMR

Techniques that look at the local structure have also been utilised in order to gather further evidence to help determine whether NZO 800A is fluorite or pyrochlore. ^{91}Zr NMR spectra have been collected using a QCPMG-WURST approach by David Apperley (using the EPSRC funded UK national service). The groups of 'spikelets' observed in each of the spectra (which are produced by this kind of NMR experiment) can be viewed as one broadened peak per spectrum. Figure 5.9 and Figure 5.10 show ^{91}Zr solid state NMR spectra for NZO 800A and NZO 800B. Both spectra are similar and consist of one broad peak. The broad peaks observed for NZO 800A and NZO 800B are typical of disorder and a distribution of different local Zr environments.

In the pyrochlore structure, only one peak would be observed, due to the presence of only one zirconium site. The spectrum of NZO 1000 (Figure 5.11) has narrower full-width at half maximum (approximately 100 kHz) than the two fluorite-type NZO 800A and NZO 800B (approximately 250 kHz), suggesting the local structure is more ordered for NZO 1000 than in the two fluorite-type compounds. However, the NZO 1000 spectrum (Figure 5.11) clearly has a much lower signal to noise ratio than the NZO 800A and NZO 800B spectra, therefore the apparent narrower full width at half maximum of the peak in the NZO 1000 spectrum should be treated with caution.

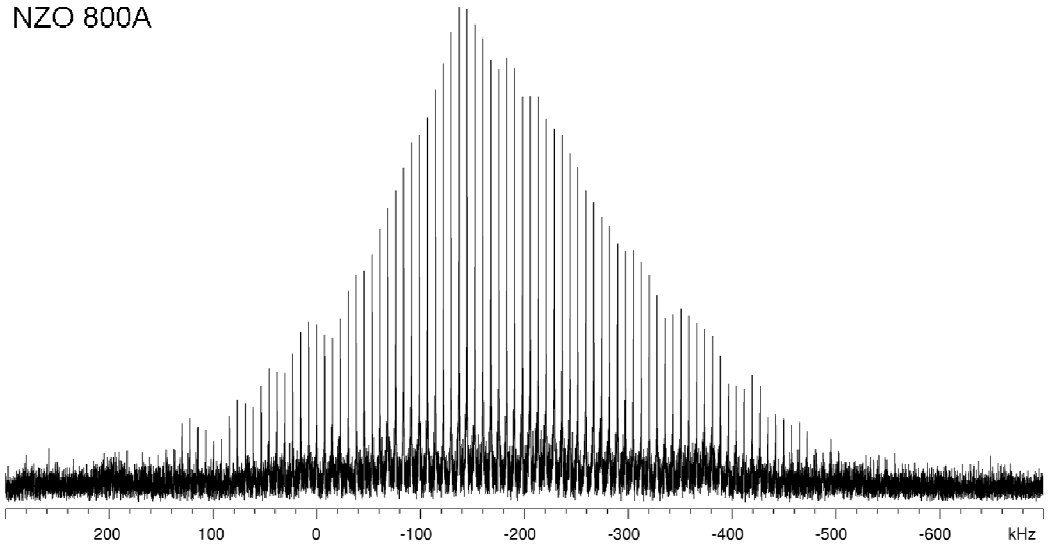

Figure 5.9: ^{91}Zr solid state NMR spectrum of NZO 800A.

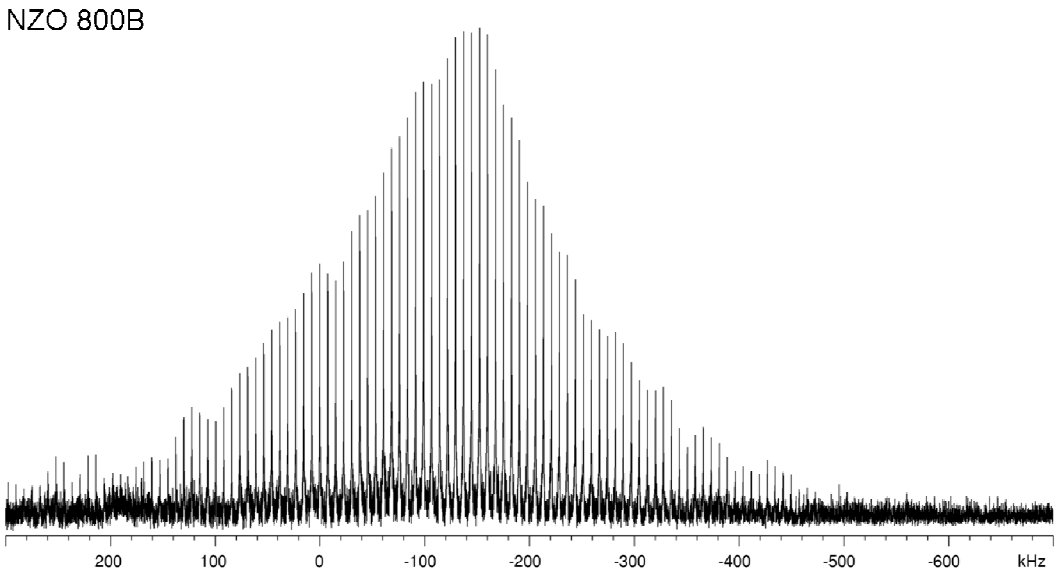

Figure 5.10: ^{91}Zr solid state NMR spectrum of NZO 800B.

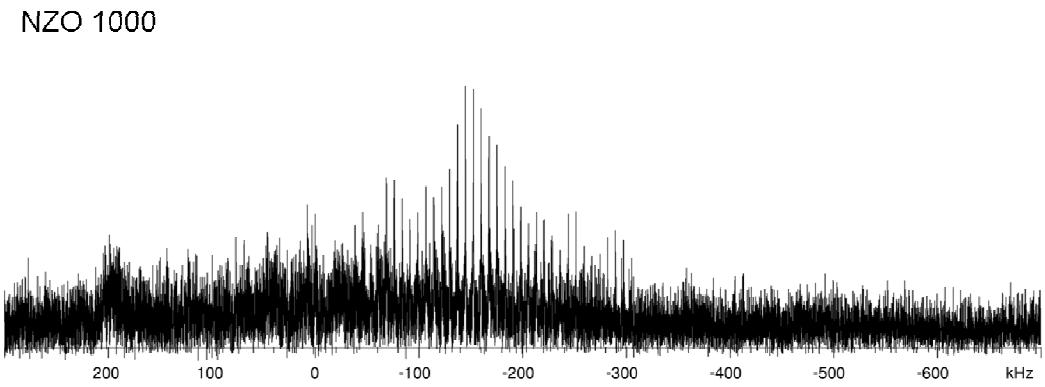

Figure 5.11: ^{91}Zr solid state NMR spectrum of NZO 1000.

5.5.3 Raman spectroscopy

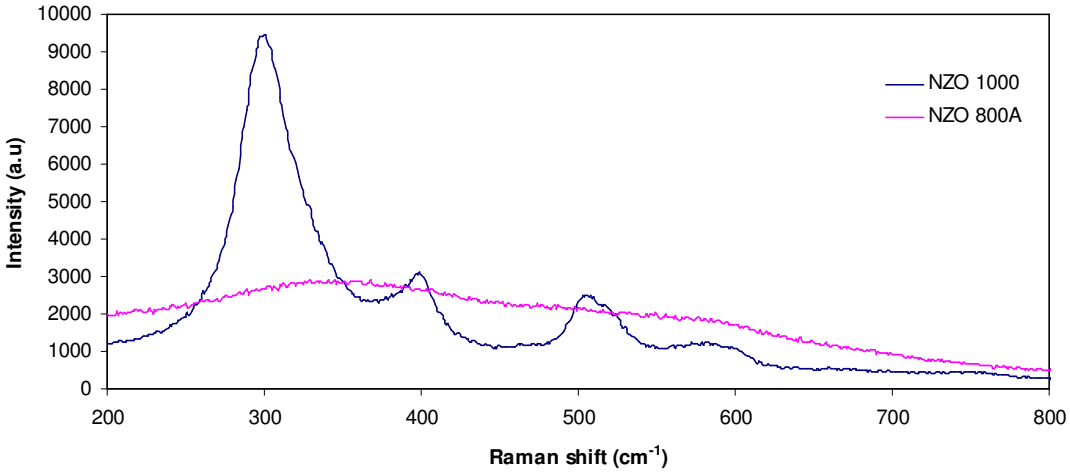

Figure 5.12: Raman spectra of NZO 1000 and NZO 800A.

Figure 5.12 shows the Raman spectrum of NZO 1000, which is typical of pyrochlore spectra reported in the literature.[14] For NZO 800A, only a broad feature was observed in the Raman spectrum (Figure 5.12). Broadening of Raman bands can be attributed to both small particle size effects (illustrated in a study of ceria) and local disorder. [14-17] Defect fluorites often show broadened Raman bands, even when samples appear very crystalline in the XRD patterns, due to the local scale disorder.[12, 16] Increased broadening of Raman bands has been reported as pyrochlores disorder upon doping, firstly to a disordered pyrochlore and then to a fluorite.[12, 16, 17] In the case of NZO 800A, the broadening of Raman bands is presumably a combination of small particle size and local disorder. A similar situation was observed in a study on the $Gd_{2-x}Ce_xZr_2O_7$ system, where XRD studies showed a fluorite lattice with broadened peaks (and a crystallite size of 5-7 nm) with correspondingly broadened Raman spectra.[17]

5.5.4 Neutron total scattering

RMCProfile refinements were carried out using both the fluorite and pyrochlore models, using the dataset collected for NZO 800A. One T(r) was used up to 29 Å. Figure 5.13 shows the fit to the total scattering data obtained during RMCProfile refinements when a pyrochlore model was used for $Nd_2Zr_2O_7$. The pyrochlore model used was a $6 \times 6 \times 6$ supercell of $Nd_2Zr_2O_7$ with a pyrochlore structure. Excellent agreement was achieved between the data and the model.

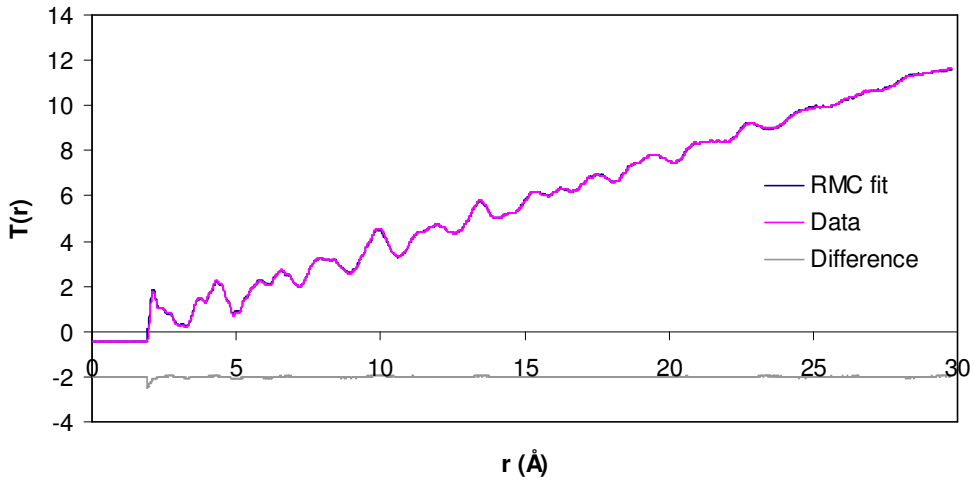

Figure 5.13: Fit to T(r) for NZO 800A using a pyrochlore model.

Figure 5.14 and Figure 5.15 show the Nd-O and Zr-O bond length distributions respectively. In Figure 5.14, the Nd-O bond length distribution maximum is at 2.14 Å whilst the Nd-O' bond length distribution maximum is 2.33 Å (O' represents oxygen on the 8a site). As shown in Figure 5.14, maxima in the bond length distributions of Zr-O and Zr-O' were found to be 2.08 Å and 4.38 Å respectively, as expected as the O' oxygen is not in the immediate coordination sphere of zirconium. Coordination numbers were calculated using the 'coord_gen' programme which integrates under the partial g(r). The coordination numbers were as follows: Nd-O: 5.6, Nd-O': 1.74 and Zr-O: 6.2, in good agreement with the ideal pyrochlore structure which has six Nd-O bonds, two Nd-O' bonds and six Zr-O bonds. Under-estimation of coordination number in Bi_3YO_6 has previously been attributed to displacement of atoms from their crystallographic sites or the similarity of the neutron scattering lengths.[18] Here, neodymium and zirconium have similar scattering lengths of 7.69 fm and 7.16 fm, respectively and this is therefore probably the cause of the slight under-estimation of coordination number.

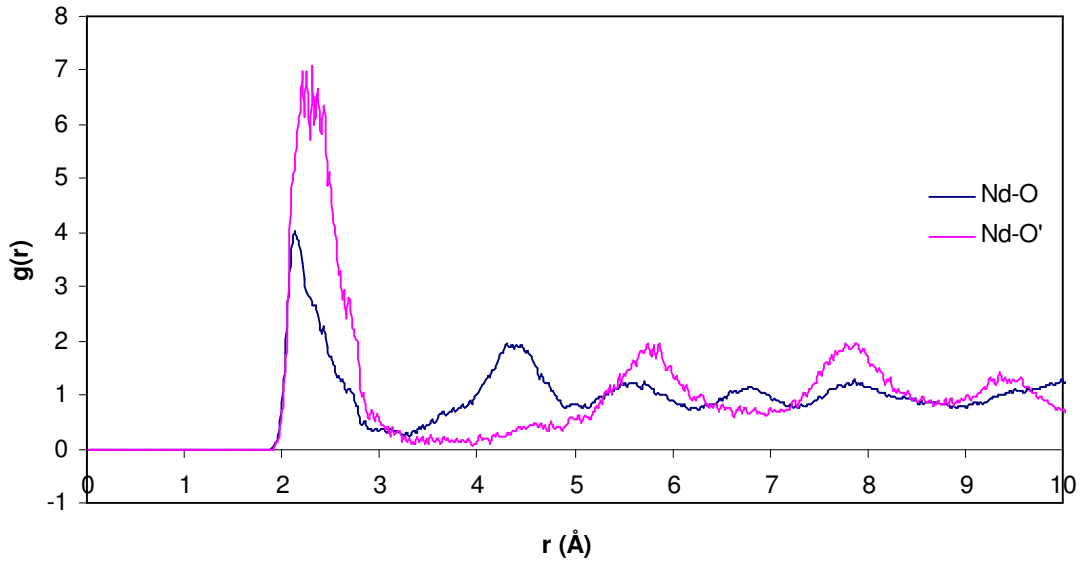

Figure 5.14: Nd-O and Nd-O' partial g(r) which indicate bond length distributions. These have been obtained from RMC simulations using a $Nd_2Zr_2O_7$ pyrochlore starting configuration.

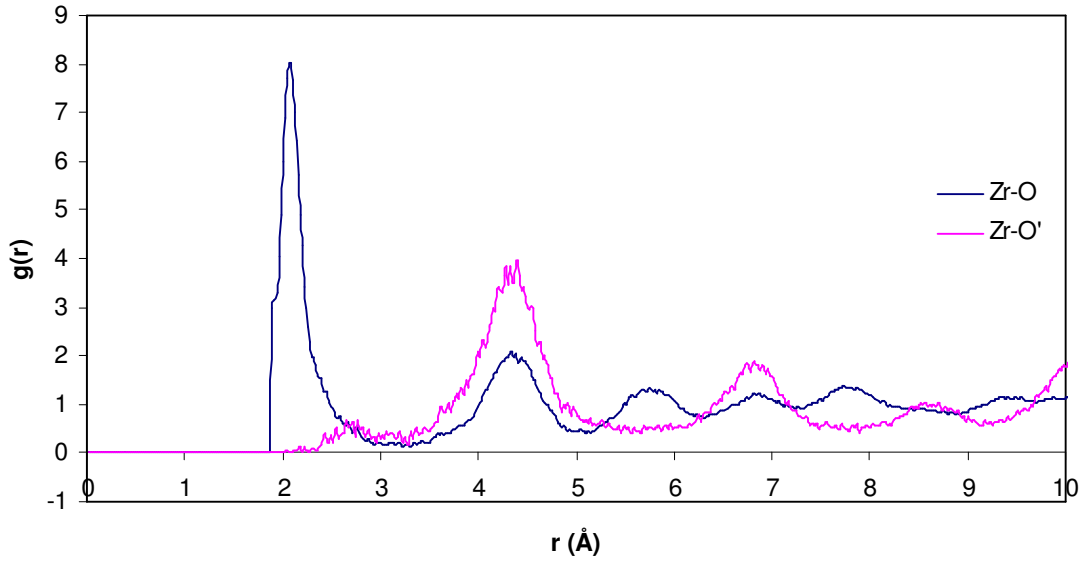

Figure 5.15: Zr-O and Zr-O' bond length distributions which have been obtained from RMC simulations using a $Nd_2Zr_2O_7$ pyrochlore starting configuration.

RMCProfile simulations for $Nd_2Zr_2O_7$ were also carried out using the fluorite model. A starting configuration with Nd and Zr randomly distributed over the cation crystallographic sites and oxygen and oxygen vacancies randomly distributed over the anion sites was created using the 'atomchoose' program. The fluorite model used was an $11 \times 11 \times 11$ supercell of $Nd_2Zr_2O_7$ with the fluorite structure. The 'atom swap' function in RMCProfile was used to swap neodymium atoms with zirconium atoms and oxygen with oxygen vacancies. One T(r) was used up to 29 Å. Figure 5.16 shows the

fit to the total scattering data when a fluorite model is used. Again, an excellent agreement between the data and the model was obtained.

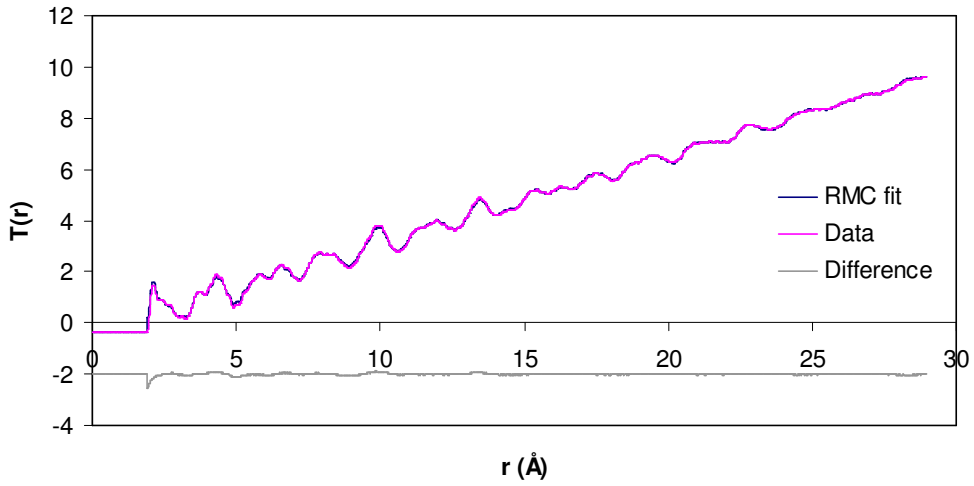

Figure 5.16: Fit to $Nd_2Zr_2O_7$ T(r) using a fluorite starting configuration.

The Nd-O and Zr-O bond length distribution are shown in Figure 5.17. The Nd-O bond length distribution shows a maximum at 2.20 Å and the Zr-O distribution shows a maximum at 2.10 Å. The coordination numbers for Nd and Zr were calculated to be 6.9 and 7.3 respectively. In a perfect fluorite, MO_2, the cations have a coordination number of 8, but in fluorite type $Nd_2Zr_2O_7$, 12.5% of the anion sites are vacant, hence the coordination number will be reduced, with the average value being 7.

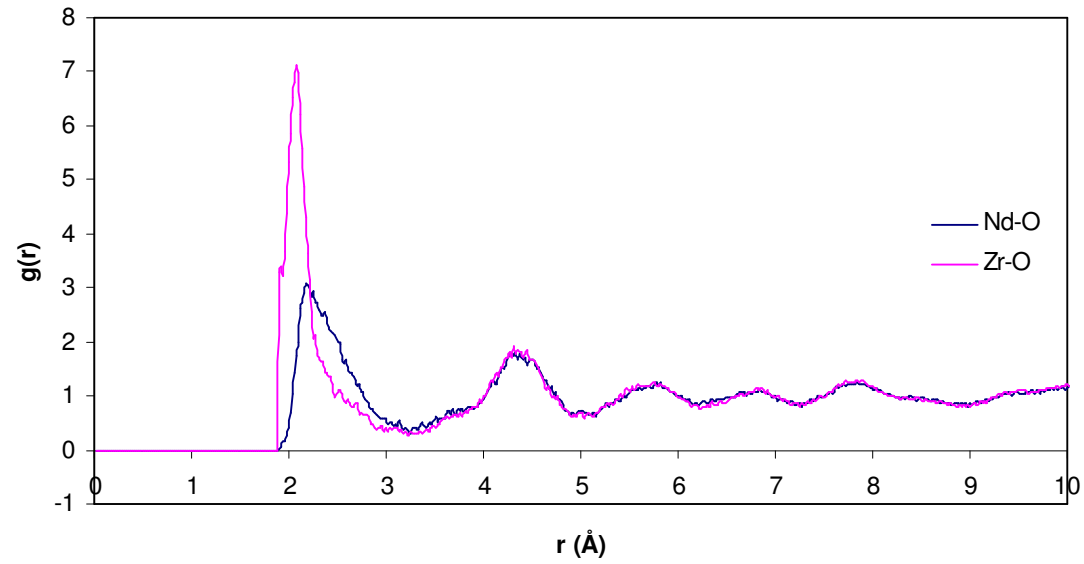

Figure 5.17: Nd-O and Zr-O bond length distributions from RMC simulations using a fluorite starting configuration for $Nd_2Zr_2O_7$.

As there is not a clear preference for fluorite or pyrochlore from the fit to the T(r), a comparison between the fluorite and pyrochlore models has been made (Table 5.8). The difference in bond length distribution maxima between the two models was small.

Table 5.8: Coordination numbers and bond lengths for fits to $Nd_2Zr_2O_7$ total scattering data using both pyrochlore and fluorite models.

	Fluorite	Pyrochlore
Nd-O coordination number	6.9	5.6
Nd-O' coordination number	N/A	1.7
Zr-O coordination number	7.3	6.2
Nd-O distance	2.20	2.14
Nd-O' distance	N/A	2.33
Zr-O distance	2.10	2.08

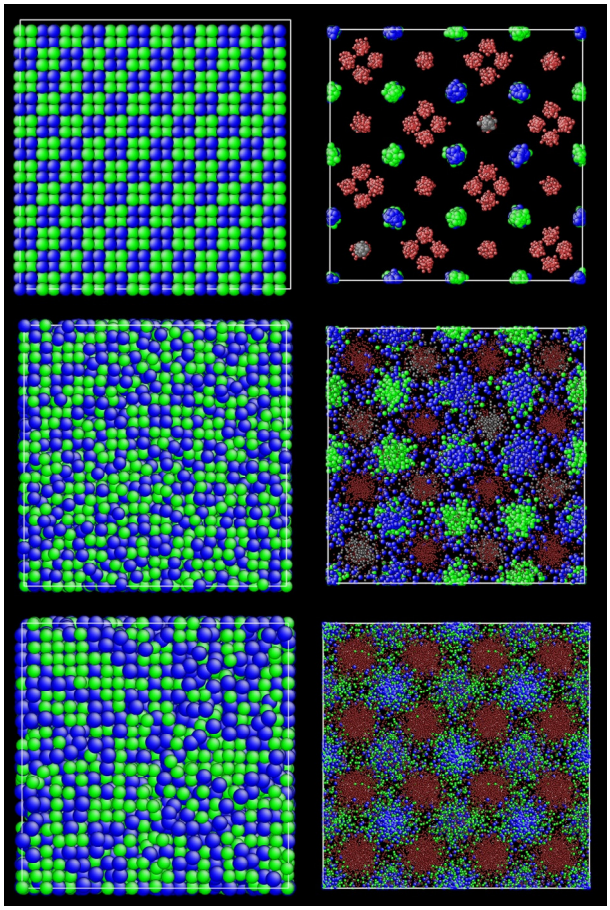

Figure 5.18: Views of final configurations obtained from RMCProfile refinements compared with the ideal pyrochlore configuration. Ideal pyrochlore starting configuration top, RMC pyrochlore middle, RMC fluorite bottom. Left hand side: cation ordering for RMC supercells (pyrochlore $6a_p \times 6a_p \times 6a_p$, fluorite $11a_F \times 11a_F \times 11a_F$). Right hand side: RMC configurations condensed into one unit cell for ideal pyrochlore and RMC pyrochlore. The fluorite configuration is condensed onto a $2a_F \times 2a_F \times 2a_F$ supercell. Blue spheres are Nd atoms, green spheres Zr, red spheres O, grey spheres O' (for pyrochlore) and vacancy (for fluorite). a_F ~5Å fluorite cell, a_P ~10 Å pyrochlore cell.

Figure 5.18 shows views of the final RMC configurations obtained from both the fluorite and pyrochlore starting models. In the fluorite configuration, there appears to be some diagonal chains of Nd and Zr atoms which resemble pyrochlore ordering and

also clustering of Nd and Zr atoms, rather than a completely random distribution of cations (Figure 5.18). When the configurations are condensed into one unit cell, both the fluorite and pyrochlore unit cell shows that some cations are displaced from the ideal cation sites, into areas which are usually unoccupied by the cation.

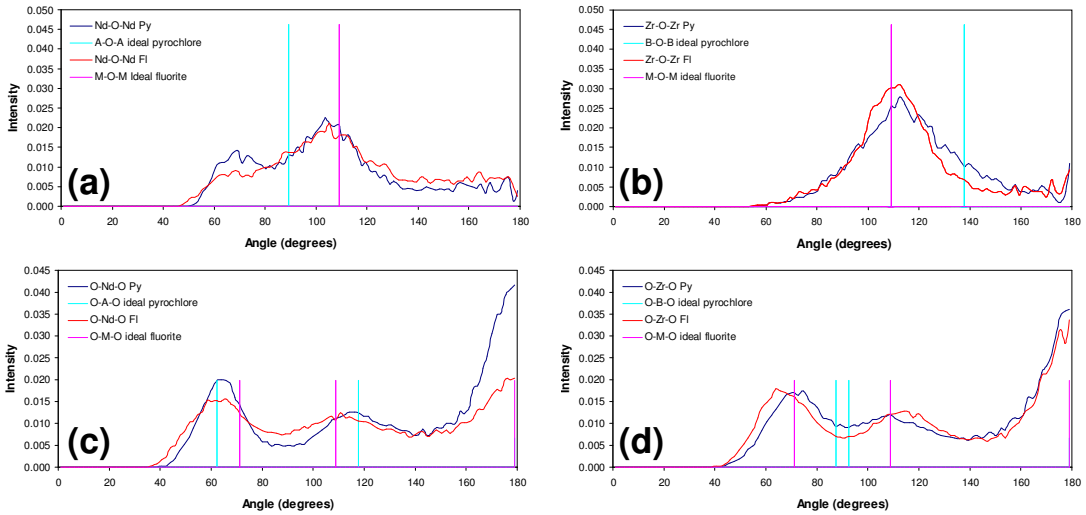

Figure 5.19: Comparison of M-O-M and O-M-O angles for $Nd_2Zr_2O_7$ obtained from RMCProfile simulations using both fluorite and pyrochlore structures, compared to the ideal values. (a) Nd-O-Nd, (b) Zr-O-Zr, (c) O-Nd-O, (d) O-Zr-O. The angular distributions obtained from RMC simulations are represented by red and dark blue curves for the pyrochlore and fluorite configurations respectively, whilst the corresponding angles in the ideal pyrochlore and fluorite structure are shown as pink and light blue vertical lines.

Bond angle distributions obtained from RMC modeling reflect local disorder in the RMC configurations and have been compared to the ideal pyrochlore and ideal fluorite values. The Nd-O-Nd angle distribution shows a distortion from both the ideal fluorite and pyrochlore structure (Figure 5.19a). The RMC pyrochlore model shows two maxima at 77° and 104°, distorted from the single peak at 90° expected for an ideal pyrochlore. The fluorite model shows a broad distribution of angles, although the maximum observed in the fit from RMCProfile refinements is at 105°, only slightly lower than the 109° expected in an ideal fluorite.

Figure 5.19b shows the Zr-O-Zr angle distribution. The RMCProfile outputs are almost identical, regardless of whether the fluorite or pyrochlore model was used. Comparison with the Zr-O-Zr angles in the fluorite and pyrochlore structure shows that for an ideal fluorite, the expected Zr-O-Zr angle is 109°, whilst in an ideal pyrochlore this angle is expected to be 138°. Figure 5.19b clearly shows that the RMC pyrochlore Zr-O-Zr angle distribution corresponds more closely to the ideal fluorite than the ideal pyrochlore. The RMC fluorite has a maximum at 110° and the RMC pyrochlore has a maximum at 112°.

Figure 5.19c shows the O-Nd-O angle distributions. The ideal fluorite and pyrochlore angles are very similar to each other, which has also been reflected in the RMC outputs. Both the fluorite and pyrochlore outputs from RMCProfile refinements show two peaks, with the fluorite peaks being broader and overlapping more than the pyrochlore peaks, indicating that there was a larger distribution of O-Nd-O environments when the fluorite model was used.

Figure 5.19d shows the O-Zr-O angle distribution. In the ideal pyrochlore configuration, the are two O-Zr-O angles of 87.3° and 92.7°, which are slightly distorted from the perfect octahedral value of 90° because of the value of the 48f x parameter. For an ideal fluorite these angles are 71° and 109°. Figure 5.19d clearly shows the distortion of the O-Zr-O angles in the RMC pyrochlore away from 90°, with maxima at 73° and 109°. For the RMC fluorite configuration, maxima were centred at 66° and 114°. The O-Zr-O angles obtained from the RMC fit using the pyrochlore model clearly resemble the fluorite angle distribution more closely.

In summary, good RMC fits can be obtained when both fluorite and pyrochlore models are used. When a pyrochlore starting configuration was used, the bond angles distort to the angles expected for a fluorite, which supports NZO 800A having a fluorite structure.

5.5.5 DFT geometry optimisation calculations

Geometry optimisation calculations were carried out in both the fluorite and pyrochlore structures. For the fluorite structure, a $2 \times 2 \times 2$ supercell was used with zirconium atoms and neodymium atoms randomly distributed to account for the disorder across the cation sites. The atoms in the unit cell are allowed to move, in order to minimise the energy of the system. After convergence, the total energy of the structure may be divided by the number of atoms, in order to calculate the energy per atom. The structure with the lowest energy per atom is the most stable.

Table 5.9: Results from geometry optimisation of $Nd_2Zr_2O_7$

Pyrochlore energy per atom (eV)	-9.003583
Fluorite energy per atom (eV)	-8.887424

The results are shown in Table 5.9 and they show that pyrochlore $Nd_2Zr_2O_7$ has a lower energy per atom and therefore is more stable than fluorite $Nd_2Zr_2O_7$. All calculations converged and the difference in energy at convergence was much smaller than the difference in energy observed between the two structures.

5.6 Discussion

The synthesis of $Nd_2Zr_2O_7$ with a small particle size has been reported several times in the literature using slightly different precursor methods.[2-5] A comparison of some of the results are shown in Table 5.10. The synthesis of $Nd_2Zr_2O_7$ using a precursor route (similar to our synthetic procedure), followed by different heat treatments (in the 700 °C to 1400 °C region) has recently been reported by Lee *et al.*.[2] In the Rietveld refinement, only synchrotron PXRD data was used, despite oxygen positions and occupancies being refined. Neutron diffraction data would have allowed more accurate and reliable oxygen parameters to be obtained. In the study by Lee *et al.*, the fluorite and pyrochlore models were both tested against the data collected for $Nd_2Zr_2O_7$ fired at 1000 °C, and a preference was found for the fluorite model, which is opposite to that observed in our study.[2] The pyrochlore model at 1100 °C included cation anti-site defects and occupancy of the O3 site (which is normally vacant). The occupancy of the O3 site was greater than that found in our study of NZO 1000; however, this may be due to the prolonged annealing of our sample at 1000 °C, which is in contrast to the 24 h of annealing in the study by Lee *et al.*.[2] With increasing firing temperatures, the occupancy of the O3 site and cation anti-site defects decreased. An increase in crystallite size with temperature was also observed.

Table 5.10: Comparison of $Nd_2Zr_2O_7$ polymorphs obtained, the temperatures of formation and the characterisation techniques used. (Y= yes, N = no).

	Lee[2]	**Bhattacharya[3]**	**Zhang[5]**	**Rao[4]**
Fluorite observed?	Y	Y	N	
Pyrochlore observed?	Y	Y	Y	
Fluorite formation temperature (°C)	700	750	N/A	500
Pyrochlore formation temperature (°C)	1100	900	600	500
Data	Synchrotron PXRD	Lab PXRD	Lab PXRD Electron diffraction	Lab PXRD FT-IR
Rietveld?	Y	N	N	N

The existence of a fluorite phase was reported at 750 °C by Bhattacharya *et al.* and at 700 °C by Lee *et al.*[2, 3] Bhattacharya reported the existence of a pyrochlore phase at 900 °C, with the pyrochlore peaks having extremely low intensity.[3] Zhang *et al.* synthesised $Nd_2Zr_2O_7$ using a precursor procedure followed by firing for only 10 minutes at 600 °C and assigned a pyrochlore structure, despite PXRD showing that the sample had extremely poor crystallinity.[5] Rao *et al.* reported the formation of $Nd_2Zr_2O_7$

at 500 ℃, but did not explicitly state whether the product had the fluorite or pyrochlore structure and no Rietveld refinement was carried out.[4] From our work, we report $Nd_2Zr_2O_7$ formation at 674 °C, which is slightly lower than that reported by Lee *et al.* and Bhattacharya *et al.*.[2, 3]

Lee *et al.* only used synchrotron PXRD as a characterisation technique, which gives information about the average structure and not the local structure. Therefore our structural characterisation of NZO 800A and NZO 1000 is much more complete, given the range of average and local structure techniques used.

It should be noted that a similar behaviour has been observed in $Gd_2Zr_2O_7$.[19] Like $Nd_2Zr_2O_7$, $Gd_2Zr_2O_7$ has a cation radius ratio of 1.46 (on the pyrochlore-fluorite boundary) and is also known to undergo an order-disorder transformation at 1530 ℃.[6] When synthesised by a precursor route and fired at 700-1200 ℃, $Gd_2Zr_2O_7$ has the fluorite structure.[19] When fired at 1300 ℃ and 1400 ℃ for five hours, a mixture of fluorite and pyrochlore $Gd_2Zr_2O_7$ is found, whilst increasing the duration of firing at these temperatures to twenty four hours results in the formation of a single pyrochlore phase.[19] Results from Rietveld refinement show that the cation anti-site disorder and occupancy of the normally vacant O(3) site decrease with temperature.[19] However, only synchrotron XRD was used for structural characterisation and no local structure probes were used.

Additionally, Shlyakhtina *et al.* have also reported the synthesis of fluorites using a precursor route, which then transform to pyrochlores at high temperatures.[20] Moreno *et al.* have used mechanochemical synthesis which also appears to produce fluorites, some of which transform to pyrochlores at high temperature.[21-23] However, in the work by both Shlyakhtina *et al.* and Moreno *et al.*, structural characterisation has mainly involved laboratory PXRD (although Shlyakhtina also used infra-red spectroscopy as a local probe), therefore it is impossible to say whether these compounds are definitely fluorites or not due to small particle sizes.[20, 21, 23]

5.7 Conclusions

In-situ VT-PXRD has shown that $Nd_2Zr_2O_7$ crystallises at 674 °C. After prolonged annealing at 800 °C, no decomposition products or phase transformations were observed. *Ex-situ* firing at 1000 °C resulted in the appearance of weak pyrochlore peaks. From neutron diffraction data, NZO 800A and NZO 800B crystallise as fluorites, whilst NZO 1000 crystallises as a pyrochlore with a disordered oxygen sublattice, where oxygen is displaced from a 48f site to an 8b site.

Electron diffraction found a 5.46 Å cell for NZO 800A (from a ring pattern) and a 11.08 Å cell for NZO 1000 (from zone axis patterns), whilst Raman spectroscopy gave spectra consistent with a pyrochlore for NZO 1000 and a broad band for NZO 800A which is similar to that observed for other defect fluorites.[17] ^{91}Zr NMR spectra of NZO 800A and NZO 800B show broad peaks, indicating a distribution of zirconium environments.

RMCProfile refinements for NZO 800A using both a fluorite and pyrochlore starting model favours the fluorite structure. When a pyrochlore configuration is used, the final bond angle distributions are distorted to those of a fluorite.

Structural characterisation of our NZO 800A sample has used more techniques than previously reported in the literature. NZO 800A with a fluorite structure is supported by X-ray, neutron and electron diffraction, which give information on the average structure and also total scattering analysis, Raman spectroscopy and NMR spectroscopy, which give information on the local structure.

5.8 References

1. E.J. Harvey, K.R. Whittle, G.R. Lumpkin, R.I. Smith and S.A.T. Redfern, *J. Solid State Chem.*, 2005, **178**, 800-810.
2. Y. H. Lee, H. S. Sheu and H. C. I. Kao, *Mater. Chem. Phys.*, 2010, **124**, 145-149.
3. A. K. Bhattacharya, A. Hartridge, K. K. Mallick and J. L. Woodhead, *J. Mater. Sci.*, 1994, **29**, 6076-6078.
4. K. K. Rao, T. Banu, M. Vithal, G. Swamy and K. R. Kumar, *Mater. Lett.*, 2002, **54**, 205-210.
5. A. Y. Zhang, M. K. Lu, Z. S. Yang, G. J. Zhou and Y. Y. Zhou, *Solid State Sciences*, 2008, **10**, 74-81.
6. D. Michel, M. Perez y Jorba and R. Collongues, *Mater. Res. Bull.*, 1974, **9**, 1457-1468.
7. C. E. Bamberger, H. W. Dunn, G. M. Begun and S. A. Landry, *J. Solid State Chem.*, 1985, **58**, 114-118.
8. A. L. Hector and S. B. Wiggin, *J. Solid State Chem.*, 2004, **177**, 139-145.
9. I. Radosavljevic, J.S.O. Evans and A. W. Sleight, *J. Solid State Chem.*, 1998, **136**, 63-66.
10. C. Lind, A. P. Wilkinson, Z. B. Hu, S. Short and J. D. Jorgensen, *Chem. Mater.*, 1998, **10**, 2335-2337.
11. R. Ubic, I. Abrahams and Y. Hu, *J. Am. Ceram. Soc.*, 2008, **91**, 235-239.
12. P. J. Wilde and C. R. A. Catlow, *Solid State Ionics*, 1998, **112**, 173-183.
13. C. T. Schamp and W. A. Jesser, *Ultramicroscopy*, 2005, **103**, 165-172.
14. B. P. Mandal, P. S. R. Krishna and A. K. Tyagi, *J. Solid State Chem.*, 2010, **183**, 41-45.
15. J. E. Spanier, R. D. Robinson, F. Zheng, S. W. Chan and I. P. Herman, *Phys. Rev. B*, 2001, **64**, 245407.
16. B. P. Mandal, N. Garg, S. M. Sharma and A. K. Tyagi, *J. Solid State Chem.*, 2006, **179**, 1990-1994.

17. B. P. Mandal, R. Shukla, S. N. Achary and A. K. Tyagi, *Inorg. Chem.*, 2010, **49**, 10415-10421.
18. I. Abrahams, X. Liu, S. Hull, S. T. Norberg, F. Krok, A. Kozanecka-Szmigiel, M. S. Islam and S. J. Stokes, *Chem. Mater.*, 2010, **22**, 4435-4445.
19. Y. H. Lee, H. S. Sheu, J. P. Deng and H. C. I. Kao, *J. Alloys and Compounds*, 2009, **487**, 595-598.
20. A. V. Shlyakhtina, L. G. Shcherbakova, A. V. Knotko and A. V. Steblevskii, *J. Solid State Electrochem.*, 2004, **8**, 661-667.
21. K. J. Moreno, A. F. Fuentes, J. García-Barriocanal, C. León and J. Santamaría, *J. Solid State Chem.*, 2006, **179**, 323-330.
22. K. J. Moreno, A. F. Fuentes, M. Maczka, J. Hanuza and U. Amador, *J. Solid State Chem.*, 2006, **179**, 3805-3813.
23. K. J. Moreno, M. A. Guevara-Liceaga, A. F. Fuentes, J. Garcia-Barriocanal, C. Leon and J. Santamaria, *J. Solid State Chem.*, 2006, **179**, 928-934.

6 Synthesis, Characterisation, Simulations and Properties of Bi_6WO_{12} and Related Oxide Ion Conductors

6.1 Background

Oxide ion conductivity in the Bi_2O_3-WO_3 system was first reported by Takahashi and Iwahara in 1973.[1] $Bi_7WO_{13.5}$ showed the highest conductivity (approximately 0.14 S cm^{-1} at 900 °C), but Bi_6WO_{12} was also reported to have a high oxide ion conductivity in the range 400 °C to 900 °C, with $\sigma = 0.1$ S cm^{-1} at 900 °C, of the same order of magnitude as yttria stabilized zirconia and β-$La_2Mo_2O_9$. However, only very basic XRD studies were published, which reported that both Bi_6WO_{12} and $Bi_7WO_{13.5}$ have a fluorite related structure.[1]

Bi_6WO_{12} falls within the region of Bi_2O_3-WO_3 solid solution classified as Type 1b ($\sqrt{5} \times \sqrt{5} \times 2$ fluorite superstructure) by Zhou.[2] There has been some debate in the literature regarding the extent of this solid solution, with Zhou, Watanabe and Ling reporting it to exist between $Bi_{12}WO_{16.5}$-Bi_6WO_{12}, $Bi_{7.4}WO_{14.1}$-$Bi_{5.6}WO_{11.4}$, and $Bi_{7.4}WO_{14.25}$-$Bi_{5.25}WO_{9.375}$ respectively.[3, 4] Ling *et al.* have recently published the structure of $Bi_{8.2}WO_{15.3}$, which has the Type 1b structure, therefore extending their solid solution region further.[5] Crystal structures of three different compositions belonging to the fluorite superstructure Type 1b have been published. Ling has published the structures of $Bi_{5.85}WO_{11.59}$ and $Bi_{8.2}WO_{15.3}$ (they will be referred to as Ling 1998 and Ling 2010, respectively), whilst Nespolo has published the structure of $Bi_7WO_{13.5}$.[3, 5-7] Although some early studies reported a space group of $I4_1/a$, Ling and Nespolo both report a space group of $I4_1$.[3, 7]

A number of differences exist between the three structures, indicating that there are still uncertainties with the true structure. The key differences between the models are summarised in Table 6.1. Nespolo *et al.* solved the structure for $Bi_7WO_{13.5}$ using single crystal X-ray data only, where the metals dominate the diffraction data and the accurate determination of oxygen parameters can be difficult.[7] Although Ling *et al.* used both powder neutron diffraction and powder synchrotron X-ray diffraction for $Bi_{5.85}WO_{11.59}$, a complete refinement could not be carried out.[6] In the case of $Bi_{8.2}WO_{15.3}$, single crystal synchrotron XRD and single crystal neutron diffraction have been used for

structure solution and complete refinement was possible. Unlike previous studies, this refinement used rigid bodies to model WO_6 octahedra.

Table 6.1: Summary of the differences between the three published Type 1b bismuth tungstate structures.

	Nespolo [7]	Ling 1998 [3]	Ling 2010 [5]
Data	Single crystal XRD	Synchrotron PXRD and PND	Single crystal ND and single crystal synchrotron XRD
Bi/W mixed site	8b	4a	4a
Number of partially occupied oxygen sites	3	3	7 (surrounding mixed metal site)
Temperature factors (U_{eq})	Large range for oxygen (0.022-2Å^2)	Equated. Metal sites 0.0243 Å^2 and oxygen sites 0.138 Å^2	Oxygens equated according to whether they belong to a MO_6 or MO_8, where M = mixed metal site. Range 0.022 to 0.371 Å^2

In both of Ling's models, Bi was placed on four 8b sites, whilst W and the mixed Bi:W site occupied 4a crystallographic sites.[6] However, Nespolo only placed Bi on 3 × 8b sites, with the final 8b site being occupied by both Bi and W. The remainder of the Bi was placed on a 4a site, with the remainder of W (as in the Ling model) being placed on a different 4a site.[7] Nespolo's $Bi_7WO_{13.5}$ and Ling's $Bi_{5.85}WO_{11.89}$ models contained 10 oxygen sites. Six of the oxygen U_{eq} values in Nespolo's model (from X-ray data) are approximately one magnitude smaller than those obtained in the Ling 1998 model, which used neutron data. Nespolo's model contains oxygen U_{eq} with a large range of values (from 0.022 to 2 Å^2). Ling (1998) was unable to refine any oxygen positions from neutron data, whilst Nespolo was only able to refine six oxygen positions. Oxygen vacancies in both the Nespolo and Ling $Bi_{5.85}WO_{11.89}$ models have been concentrated around W^{6+} to reduce the coordination number.[7] In the $Bi_{8.2}WO_{15.3}$ model, there are seven partially occupied sites which are centred around the mixed cation site.[5]

In their work on Aurivillius-type Bi_2WO_6, Mairesse *et al.* have reported an increase in ionic conductivity when Nb^{5+} or Ta^{5+} substitutes W^{6+}. The highest conductivity was found for the $Bi_2W_{0.95}Nb_{0.05}O_{5.975}$ and $Bi_2W_{0.95}Ta_{0.05}O_{5.975}$ samples, with both showing an increase of approximately three orders of magnitude at 300 °C and 1.5 orders of magnitude at 800 °C. At 800 °C, the oxide ion conductivity displayed by both $Bi_2W_{0.95}Nb_{0.05}O_{5.975}$ and $Bi_2W_{0.95}Ta_{0.05}O_{5.975}$ was 5.0×10^{-3} S cm^{-1}.[8] Atomistic

modeling by Islam *et al.* has also shown that Nb^{5+} and Ta^{5+} are the energetically preferred substituents for the W^{6+} site in Bi_2WO_6 and that La^{3+} is the energetically preferred substituent for the Bi^{3+} site.[9]

The aim of this work was to firstly to investigate the Bi_6WO_{12} structure and carry out molecular dynamics simulations in order to explore oxide ion diffusion pathways. Secondly, the effect of isovalent and aliovalent doping on the oxide ion conductivity was explored.

6.2 Synthetic routes to Bi_6WO_{12}

6.2.1 Conventional solid state synthesis

Stoichiometric quantities of Bi_2O_3 and WO_3 were ground in a pestle and mortar, then fired at 800 °C for six hours followed by 10 hours firing at 900 °C. Bi_6WO_{12} was also prepared by firing the oxides at 800 °C for 48h. Energy dispersive X-ray analysis was used to confirm the ratio of Bi:W and gave excellent agreement with the expected 6:1 Bi:W ratio.

6.2.2 Single crystal growth

Approximately 0.6g of Bi_6WO_{12} was fired at its melting point of 1025 °C for one hour. The sample was then cooled to room temperature at a rate of 3 °C per hour, until a temperature of 500 °C was reached. Cooling continued to room temperature at a rate of 10 °C per hour. Energy dispersive X-ray analysis was used to determine the Bi: W ratio, after taking an average over five crystals and this showed that they were bismuth deficient, with an average of Bi:W ratio of 5.56(3) : 1.

6.2.3 Synthesis of doped analogues

All doped samples were prepared by solid state synthesis from stoichiometric quantities of oxides: Bi_2O_3, WO_3, Nb_2O_5, Ta_2O_5, ZrO_2, CaO and Er_2O_3. Target compositions, synthetic conditions and outcomes are summarised in Table 6.2.

Table 6.2: Target compositions, synthetic conditions and outcomes for Bi_6WO_{12} doped phases.

Dopant	*x*	T(°C)	Time (hrs)	Product obtained
Ca^{2+}	0.05, 0.10	900	24	$Bi_{6-x}Ca_xWO_{12-x/2}$
	0.20	900	12	$Bi_{6-x}Ca_xWO_{12-x/2}$
	0.30, 0.40, 0.50	900	16	$Bi_{6-x}Ca_xWO_{12-x/2}$, $CaWO_4$
Nb^{5+}	0.05	900	10	$Bi_6W_{1-x}Nb_xO_{12-x/2}$
	0.10	900	20	$Bi_6W_{1-x}Nb_xO_{12-x/2}$
	0.15	900	22	$Bi_6W_{1-x}Nb_xO_{12-x/2}$
	0.20	900	22	$Bi_6W_{1-x}Nb_xO_{12-x/2}$, $Bi_{1.7}Nb_{0.3}O_{3.3}$
	0.30, 0.40	900	22	$Bi_6W_{1-x}Nb_xO_{12-x/2}$, $Bi_{1.7}Nb_{0.3}O_{3.3}$
Ta^{5+}	0.05, 0.10	900	30	$Bi_6W_{1-x}Ta_xO_{12-x/2}$
	0.15, 0.20	900	34	$Bi_6W_{1-x}Ta_xO_{12-x/2}$, Bi_2WO_6
Zr^{4+}	0.05,0.10, 0.15	900	10	$Bi_6W_{1-x}Zr_xO_{12-x}$
	0.20,0.25, 0.30	900	10	$Bi_6W_{1-x}Zr_xO_{12-x}$
	0.35, 0.40	900	30	$Bi_6W_{1-x}Zr_xO_{12-x}$
Er^{3+}	0.05, 0.10	900	10	$Bi_{6-x}Er_xWO_{12}$
	0.15, 0.20	900	10	$Bi_{6-x}Er_xWO_{12}$
	0.30, 0.40	900	30	$Bi_{6-x}Er_xWO_{12}$, Bi_2WO_6
Er^{3+} and Zr^{4+}	0.05, 0.10	900	20	$Bi_{6-x}Er_xW_{1-y}Zr_yO_{12-y}$
($x = y$)	0.15, 0.20	900	20	$Bi_{6-x}Er_xW_{1-y}Zr_yO_{12-y}$
Er^{3+} and Zr^{4+}	$x = 0.05$ $y = 0.10$	900	20	$Bi_{6-x}Er_xW_{1-y}Zr_yO_{12-y}$
($x \neq y$)	$x = 0.10$ $y = 0.05$	900	20	$Bi_{6-x}Er_xW_{1-y}Zr_yO_{12-y}$
	$x = 0.15$ $y = 0.20$	900	20	$Bi_{6-x}Er_xW_{1-y}Zr_yO_{12-y}$
	$x = 0.20$ $y = 0.15$	900	20	$Bi_{6-x}Er_xW_{1-y}Zr_yO_{12-y}$

6.3 Room temperature structural characterisation of Bi_6WO_{12}

6.3.1 Synchrotron PXRD data

Synchrotron PXRD data were collected at the I11 beamline at Diamond. 18 background parameters, zero point error, scale factor, size/strain parameters, cell parameters and one overall isotropic temperature factor were refined. Both the Ling 2010 and the Nespolo models were tested, with cation and anion occupancies adjusted in order to represent the Bi_6WO_{12} stoichiometry. Figure 6.1a shows the fit to the synchrotron data using Ling's model.

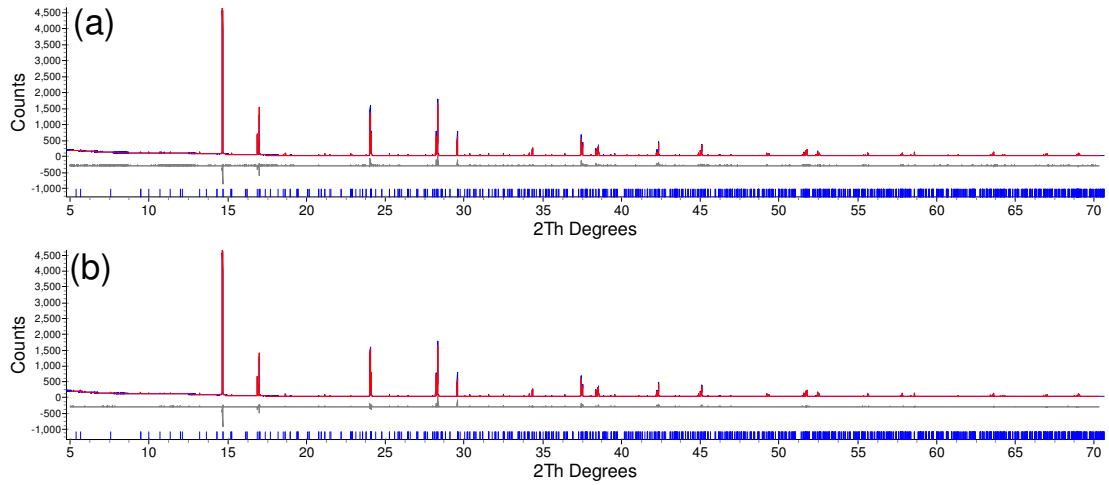

Figure 6.1: Fit to Bi_6WO_{12} synchrotron PXRD data using (a) Ling's 2010 model. R_{wp} = 6.944 %. (b) Nespolo's model. R_{wp} = 6.855 %.

The refinements using Nespolo's models used the same parameters as described above for Ling's model. Figure 6.1b shows the fit obtained. A slight preference for Nespolo's model was observed. No extra superstructure peaks were observed in the synchrotron data which may have been caused by ordering of Bi^{3+} and W^{6+} on different crystallographic sites.

6.3.2 Room temperature PND HRPD data

Two models were tested in the refinements of Bi_6WO_{12} against neutron data. The first model used was Ling's 2010 model. Twelve background terms, scale factor, cell parameters, one overall temperature factor for the metal sites, one overall isotropic temperature factor for the oxygen sites and atomic coordinates were refined. The occupancy of both cation and anion crystallographic sites were adjusted to account for the Bi_6WO_{12} stoichiometry. The occupancies of the fourteen partially occupied oxygen sites surrounding the mixed metal site were adjusted to correlate with the cation ratio, in the same way as reported by Ling for his $Bi_{8.2}WO_{15.3}$ composition.[5]

Using Ling's 2010 model, a R_{wp} of 11.143 % was achieved. The fit is shown in Figure 6.2. It is clear from Figure 6.2, that there is a discrepancy in intensity of the main peak (at approximately 96000 μs) which corresponds to the (244) reflection.

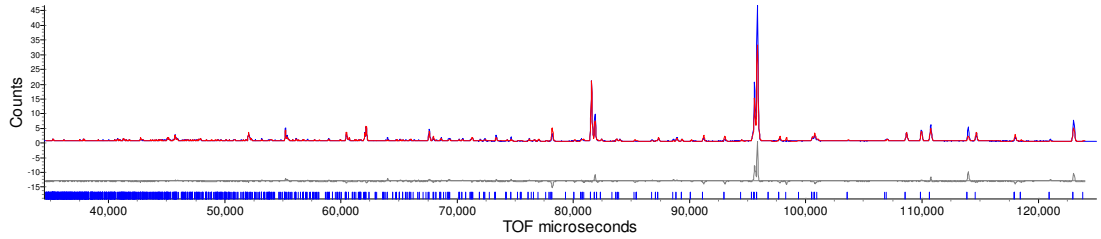

Figure 6.2: Rietveld refinement for Bi_6WO_{12} using Ling's 2010 model and HRPD data, R_{wp} = 11.143 %.

The second model used was Nespolo's model. The same parameters were refined as those described above for Ling's 2010 model. The occupancy of the cation and anion sites were adjusted for the Bi_6WO_{12} stoichiometry. The modified Nespolo model is shown in Table 6.3.

Table 6.3: Nespolo's model, adjusted for Bi_6WO_{12} stoichiometry.

Site	x	y	z	Occupancy
Bi1	0.000	0.000	0.007	1.000
W1	0.000	0.000	0.505	1.000
Bi2	0.289	0.106	0.987	0.786
W2	0.289	0.106	0.987	0.214
Bi3	0.705	0.395	0.275	1.000
Bi4	0.203	0.397	0.014	1.000
Bi5	0.795	0.103	0.252	1.000
O1	0.119	0.036	0.099	0.600
O2	0.846	0.424	0.156	1.000
O3	0.062	0.314	0.085	1.000
O4	0.937	0.152	0.162	1.000
O5	0.265	0.291	0.149	1.000
O6	0.729	0.233	0.127	1.000
O7	0.433	0.106	0.184	0.600
O8	0.561	0.348	0.107	1.000
O9	0.621	0.038	0.140	1.000
O10	0.374	0.457	0.143	0.368

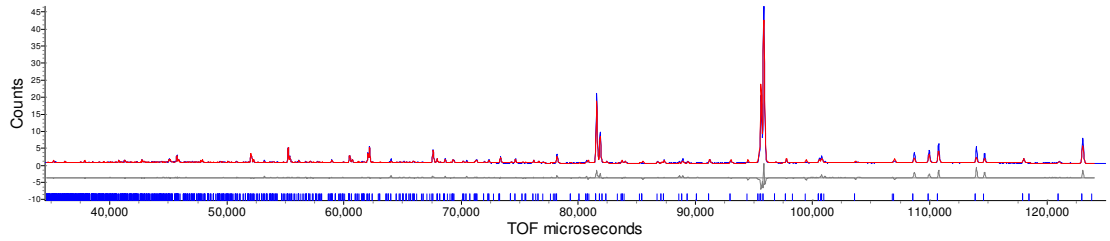

Figure 6.3: Refinement of Bi_6WO_{12} using Nespolo's model and HRPD data. R_{wp} = 8.041%.

The fit obtained with Nespolo's model is shown in Figure 6.3. The R_{wp} (8.041 %) is much lower than that obtained using Ling's model (R_{wp} = 11.143 %) and the fit is visually much better than Ling's model. The preference for Nespolo's model is greater than that observed for X-ray data. This will be partly due to the enhanced contrast between bismuth and tungsten, given the neutron scattering lengths (and therefore a preference for the cation ordering in Nespolo's model), but also because of the differences in the oxygen sublattice, which is much more sensitive to neutron diffraction. As can be seen in Figure 6.3, there is still discrepancy in the observed and calculated intensities in the region 100000 μs to 125000 μs when Nespolo's model is used, suggesting that this model is still not perfect and that there are probably problems with oxygen positions, site occupancies and displacement parameters.

6.3.3 Combined refinements using neutron and synchrotron X-ray data

A combined refinement file using I11 synchrotron PXRD and HRPD NPD data was set up. A total of 21 background parameters, zero point error, size and strain were refined for the I11 data. For the HRPD data, twelve background parameters and an absorption correction were refined. Cell parameters, atomic coordinates (from Nespolo's model), one overall isotropic temperature factor for all metal atoms and a second overall isotropic temperature factor for all oxygen atoms were refined. The fits to the neutron data and the fit to the synchrotron XRD data are shown in Figure 6.4. The overall R_{wp} was 7.145% for the combined refinement.

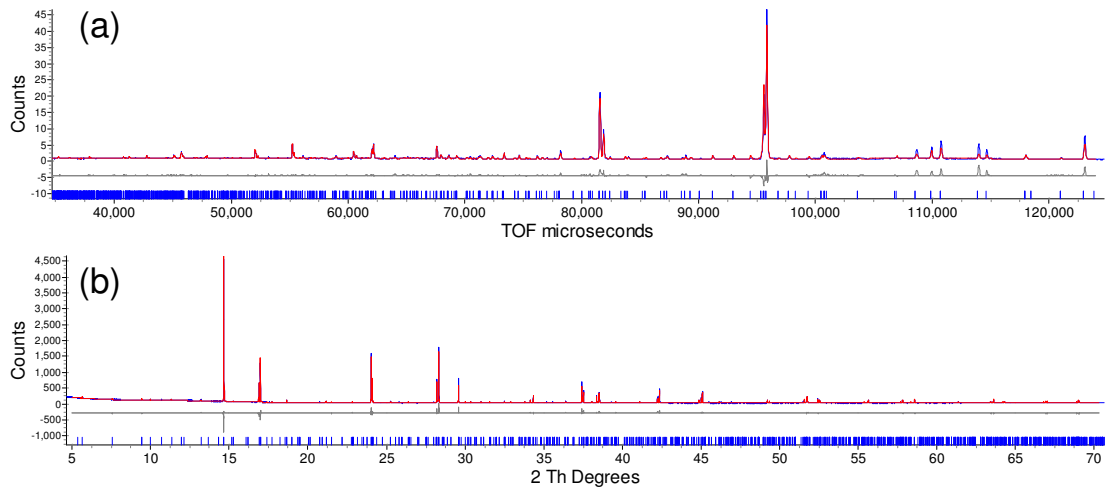

Figure 6.4: Fit to (a) HRPD neutron data and (b) I11 synchrotron XRD data from combined refinement for Bi_6WO_{12}. Overall R_{wp} = 7.145%

Our structural model for Bi_6WO_{12} favours the cation ordering as found in Nespolo's model for $Bi_7WO_{13.5}$ and this model will be used for further structural work.

6.3.4 Description of the Bi_6WO_{12} room temperature structure

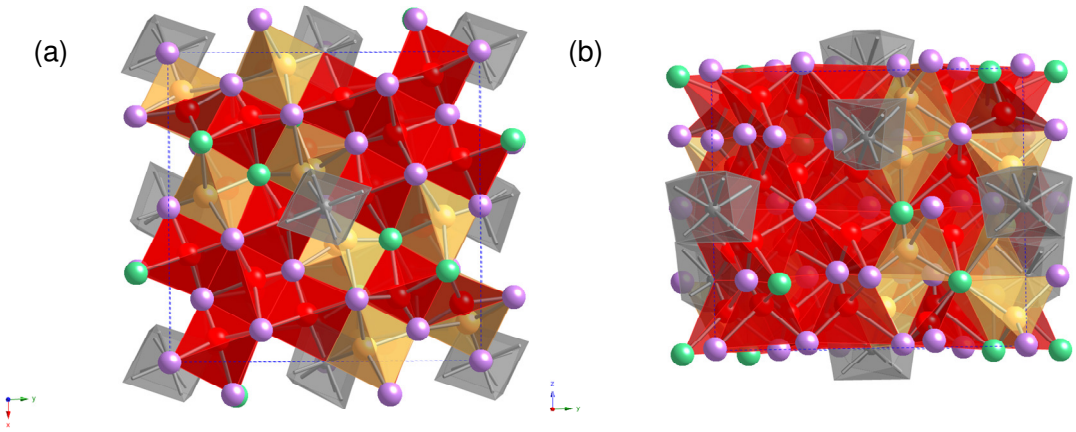

Figure 6.5: (a) *ab* plane and (b) *ac* plane of model for Bi_6WO_{12}. Red polyhedra are OBi_4 tetrahedra, orange polyhedra are OBi_4 tetrahedra with the oxygen site being partially occupied, grey polyhedra are WO_x units from fully occupied W site. Purple spheres are bismuth atoms and green spheres are the mixed bismuth/tungsten site.

The structural model for Bi_6WO_{12}, which gives the best agreement with our data can be described as a network of edge sharing OBi_4 tetrahedra and isolated WO_x units (Figure 6.5). Partially occupied oxygen sites at the centre of OBi_4 tetrahedra are shown in orange, whilst the fully occupied tungsten site is at the centre of the grey polyhedra. Fully occupied oxygen sites at the centre of OBi_4 tetrahedra and are shown in red.

The fully occupied tungsten site is coordinated by eight oxygen sites, but four of these oxygen sites are partially occupied, which may result in the local tungsten coordination number being reduced to as low as four. Three out of eight oxygen sites which coordinate the mixed cation site are partially occupied. Therefore it can be envisioned that the local coordination number of tungsten on the mixed cation site can be reduced to five.

6.4 High temperature structural characterisation of Bi_6WO_{12}

6.4.1 Laboratory VT-PXRD on Bi_6WO_{12}

In-situ variable temperature PXRD data were collected on a bulk sample of Bi_6WO_{12} up to 848 °C (Figure 6.6). No decomposition was observed in the temperature range studied. Some extra weak peaks from the silica ring sample holder were observed in the diffraction pattern.

Sequential Rietveld refinement over the temperature range studied was carried out using the in-house routine 'Multi-topas'.[10] For each temperature range, cell parameters, an overall temperature factor, sample height, peak shape and eighteen background parameters were refined. Our model for Bi_6WO_{12} was used.

.

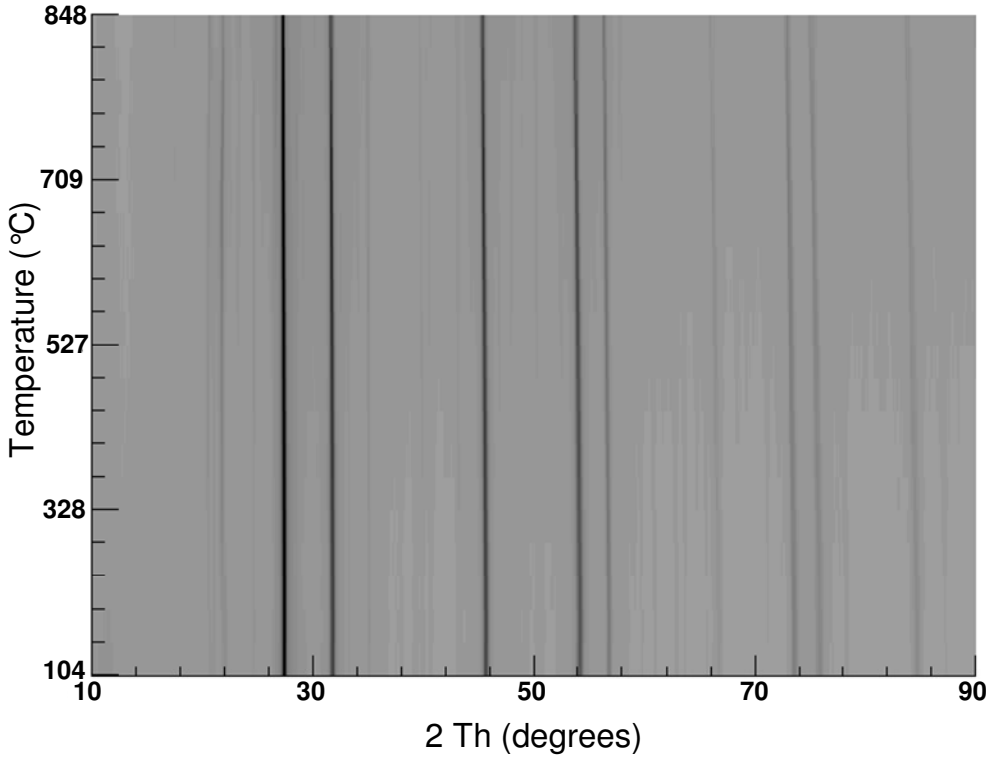

Figure 6.6: d8_04022: *In-situ* VT-PXRD for Bi_6WO_{12} in the temperature range 104 °C to 848 °C. No decomposition products or phase transitions were observed.

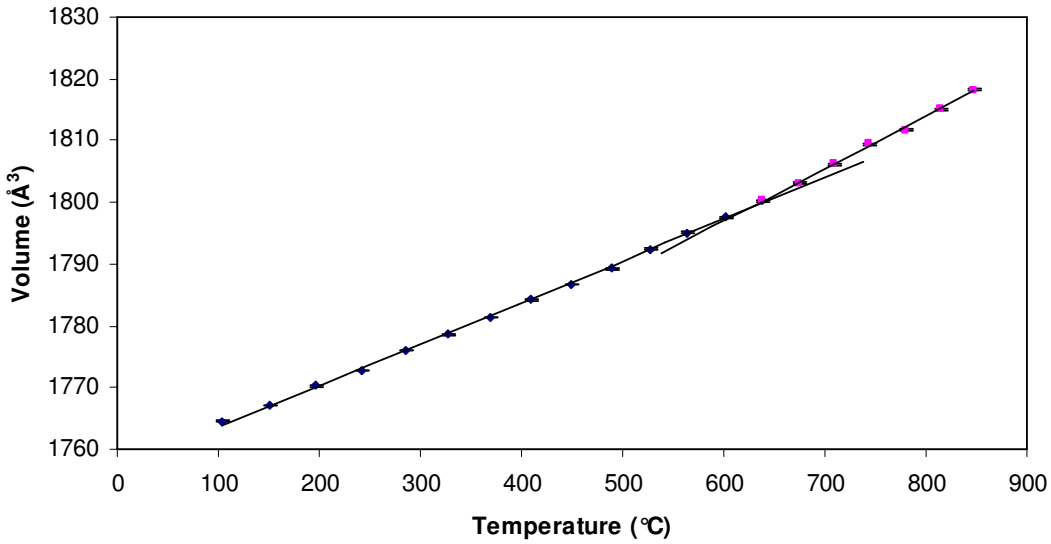

Figure 6.7: Variation of cell volume of Bi_6WO_{12} with temperature, highlighting the change in gradient at high temperature.

Figure 6.7 shows the variation of cell volume with temperature. A change in slope was observed at 640 °C. However, there was no visible change in the diffraction pattern at or around this temperature, suggesting that any structural changes which may occur cannot be long-range in order and can only be on a local, short range scale.

6.4.2 700 °C and 800 °C HPRD data

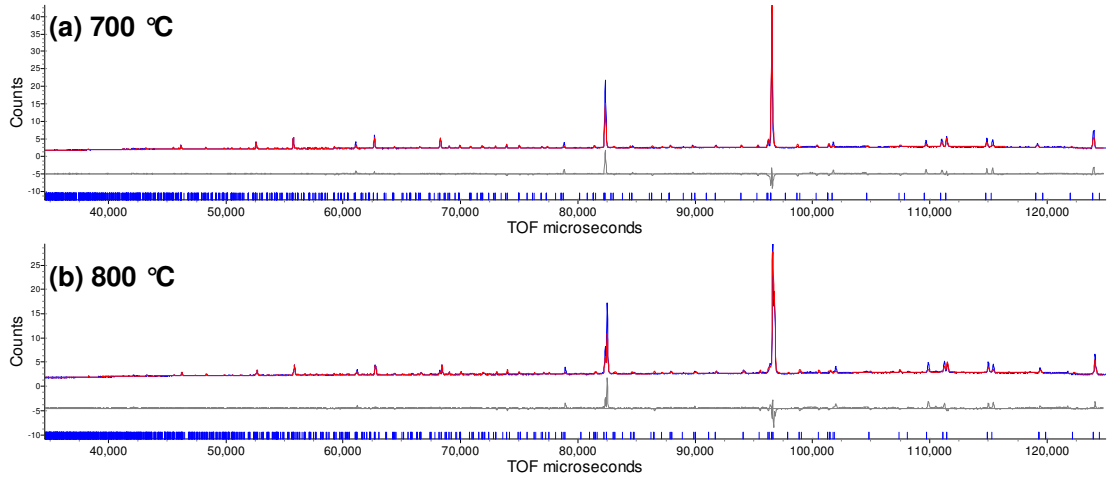

Figure 6.8: Rietveld fit of Bi_6WO_{12} at (a) 700 °C, R_{wp} = 4.167% (b) 800 °C, R_{wp} = 3.779 %.

Refinements using our Bi_6WO_{12} model were carried out on the data collected at 700 °C and 800 °C, using the parameters described in 6.3.3. The fits to the neutron data are shown in Figure 6.8 No decomposition products or phase transitions were observed in the data, therefore Bi_6WO_{12} remains tetragonal at high temperature. However, there

are still some discrepancies in the 100000 μs to 120000 μs region and around 80000 μs-85000 μs, which are probably due the discrepancies on the oxygen sublattice.

6.5 Bi_6WO_{12} impedance results

The oxide ion conductivity of Bi_6WO_{12} between 400 °C and 900 °C was first reported by Takahashi and Iwahara.[1] We carried out an impedance measurement on our own Bi_6WO_{12} sample to use as a benchmark for comparison with the new, doped materials. The density of the pellet was around 90 %.

At low temperatures, one large semi-circle arc and a Warburg-type electrode response was seen in the complex impedance plot for Bi_6WO_{12} (Figure 6.9a). The capacitance of the arc was calculated to be 2.2 pF cm^{-1}, using the formula $\omega RC=1$. The shape of the high frequency arc was unsymmetrical. The graph of capacitance versus frequency shows two plateaus (Figure 6.9b) indicating that there are two components present in this region, one with a capacitance of 9.99×10^{-12} F cm^{-1} (bulk contribution) and the second having a capacitance of 5.25×10^{-11} F cm^{-1} (grain boundary contribution). The high frequency spike was assigned to the electrode response as it has a capacitance of 2.25×10^{-7} F cm^{-1}, a value which is typically displayed by oxide ion conductors.

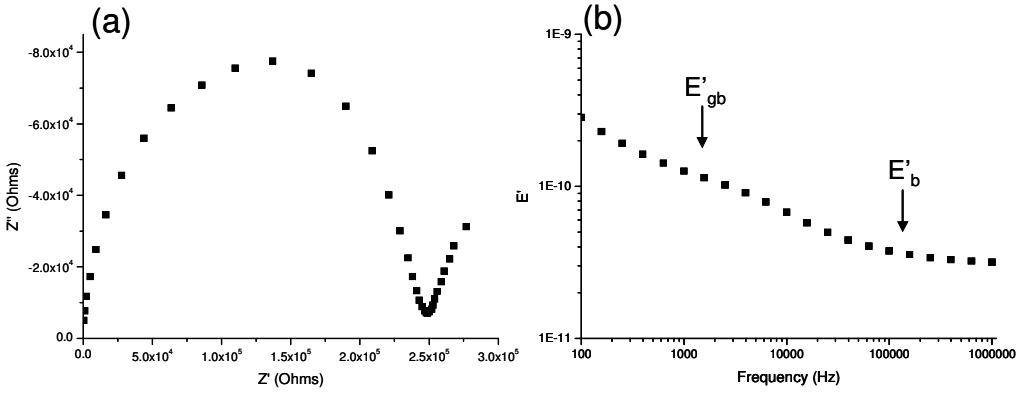

Figure 6.9: (a) Complex impedance plot for Bi_6WO_{12} at 193 °C. (b) Graph of capacitance versus frequency for Bi_6WO_{12} at 193 °C, which shows two plateaus and they have been assigned to the bulk (E'_b) and the grain boundary (E'_{gb}).

At high temperatures, only one semi-circle arc was observed due to the collapse of the electrode response spike into a semi-circle arc, hence the resistance was obtained at the high frequency intercept. The arc had a capacitance of 1.618×10^{-6} F cm^{-1}, which is typical for the electrode response and ionic conductivity.

Figure 6.10 shows the Arrhenius plot of conductivity for Bi_6WO_{12}. A slight decrease in gradient (due to a lowering in activation energy) was observed at 660 °C. The activation energy was calculated to be 0.838(9) eV at temperatures below 660 °C and 0.71(2) eV at temperatures above 660 °C. This agrees quite closely with the change in slope in the unit cell volume dependence on temperature observed around 640 °C. As there was no change in the PXRD patterns, the decrease in activation energy must therefore come from disorder on a local scale.

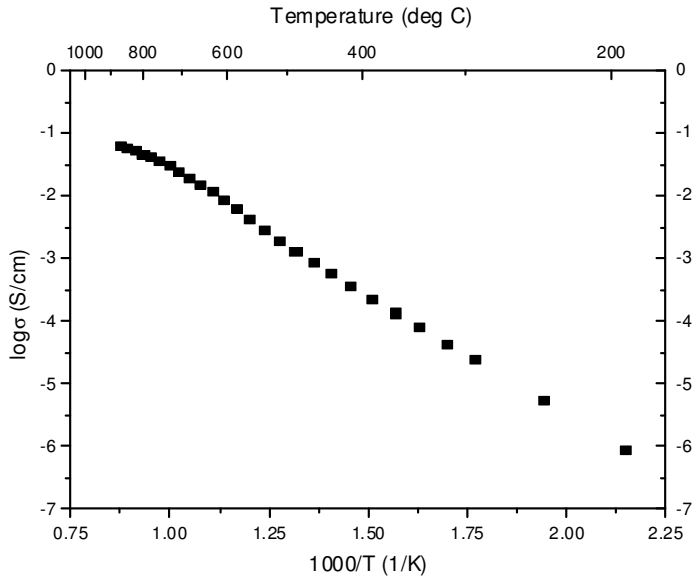

Figure 6.10: Arrhenius plot of conductivity for Bi_6WO_{12}.

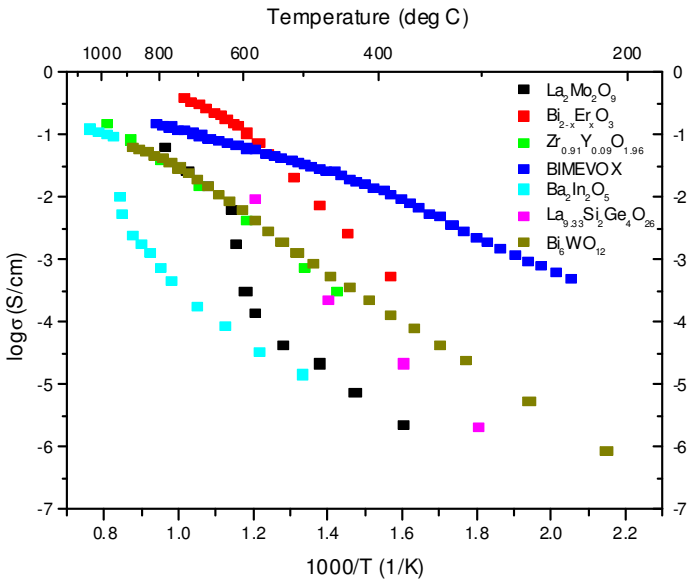

Figure 6.11: Comparison of oxide ion conductivity for Bi_6WO_{12} with that of other good oxide ion conductors.[11-14]

Figure 6.11 gives a comparison of the conductivity of our Bi_6WO_{12} sample compared with other well known oxide ion conductors. It shows that Bi_6WO_{12} has a high oxide ion conductivity, of the same order of magnitude as YSZ, which is used in commercial applications. In order to gain further insight into the oxide ion conduction pathway, molecular dynamics simulations were carried out, in the hope that this may identify how the conductivity may be enhanced by the appropriate doping of either the Bi^{3+} or W^{6+} cation sites.

6.6 Molecular dynamics simulations

Molecular dynamics (MD) simulations have been carried out in order to determine whether oxide ion conductivity is via OBi_4 'fluorite-like' tetrahedra, WO_x units, or both. The initial structure used for MD simulations was based on Ling's 1998 model, which was optimised before MD.[3] When all crystallographic sites are fully occupied, this corresponds to $M_{40}O_{80}$ in space group P1. As cation sites may not be partially occupied or include vacancies, the closest stoichiometry to 6 Bi: 1 W is 35 Bi: 5 W, which would require 67.5 oxygen atoms. As partially occupied sites may not be used in simulations, 68 oxygen atoms were used, giving the formula $Bi_{35}W_5O_{68}$. Therefore, with respect to the fully occupied $M_{40}O_{80}$ stoichiometry, twelve oxygen atoms must be removed. Four oxygens were removed from the O6, O9 and O10 sites, which were partially occupied in the ideal crystal structure, therefore these sites can be regarded as having an occupation of 50 %. A MD time step of 2 fs was used and 25 000 steps were run, resulting in a simulation 50 000 fs in duration. Molecular dynamics trajectories have been visualised in LAMP and mean square displacements have been calculated in nMOLDYN.[15, 16]

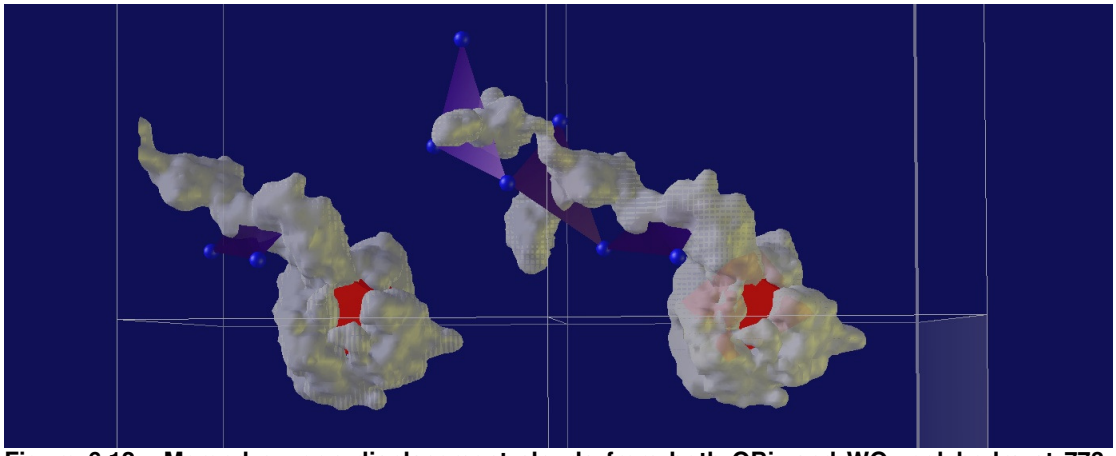

Figure 6.12: Merged oxygen displacement clouds from both OBi_4 and WO_x polyhedra at 773 K. WO_x polyhedra are orange, whilst OBi_4 polyhedra are blue. Bismuth atoms are blue spheres.

Figure 6.12 shows a view of selected oxygen displacement clouds at 773 K. It clearly shows a large displacement cloud due to the rotation of WO_x polyhedra, which is

merged with the displacement clouds of OBi_4 units. This indicates that both WO_x and OBi_4 units are involved in the diffusion process. However, as can be seen in Figure 6.12, the merged diffusion clouds do not form a diffusion pathway across the unit cell. It appears that the exchange of oxygen occurs between the WO_x and OBi_4 units, which is supported in the simulations by the ability of tungsten to support coordination numbers of five and six (see Figure 6.13). The exhibition of variable coordination number is also thought to be important in the oxide ion conduction process in $La_2Mo_2O_9$.[17]

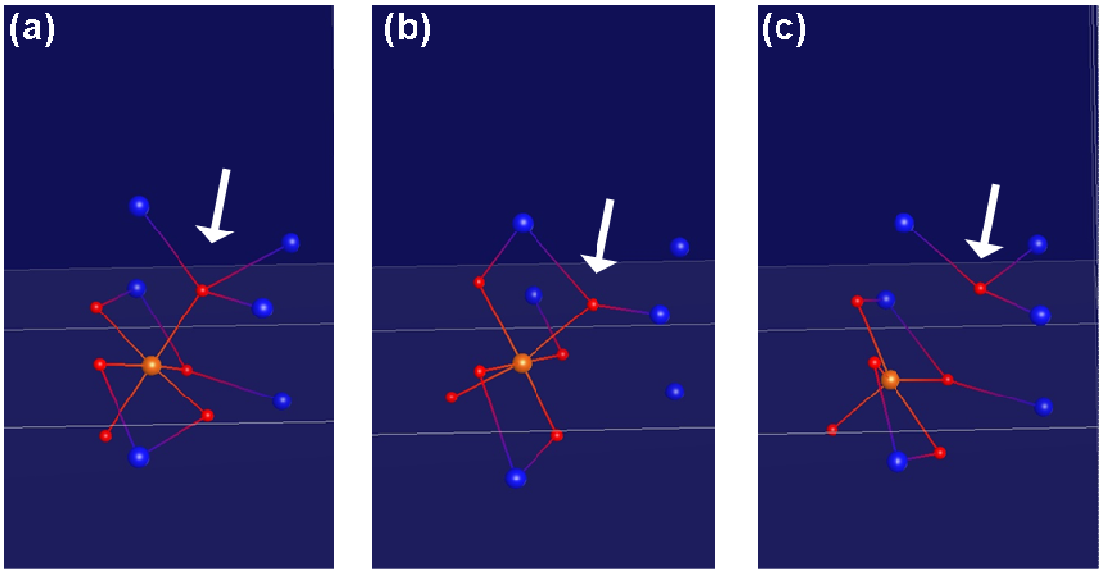

Figure 6.13: Changes in coordination of tungsten at 773 K. Left to right: (a) tungsten in six fold coordination, (b) tungsten in six fold coordination with elongated bond lengths, (c) finally tungsten in five fold coordination. Orange spheres are tungsten atoms, red spheres oxygen atoms and blue spheres are bismuth atoms.

At 973 K, the oxygen diffusion clouds now merge together to form a continuous pathway between the WO_x polyhedra and OBi_4 units, as shown in Figure 6.14.

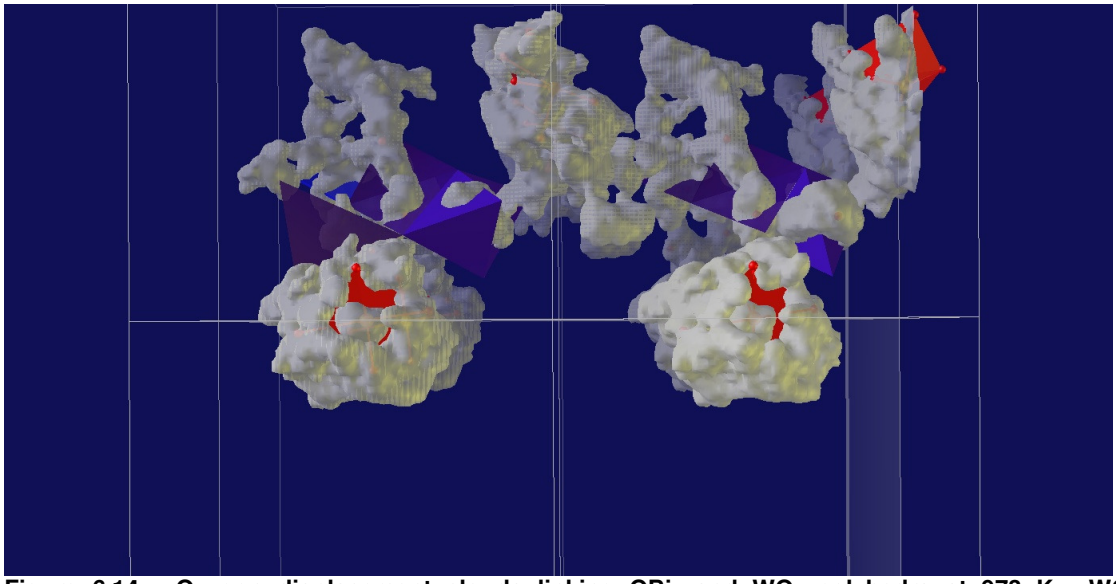

Figure 6.14: Oxygen displacement clouds linking OBi_4 and WO_x polyhedra at 973 K. WO_x polyhedra are orange, OBi_4 polyhedra are blue.

At 1173 K, diffusion also occurs directly between the WO_x polyhedra (Figure 6.15). Figure 6.16 shows diffusion between WO_x and OBi_4 units at 1173 K.

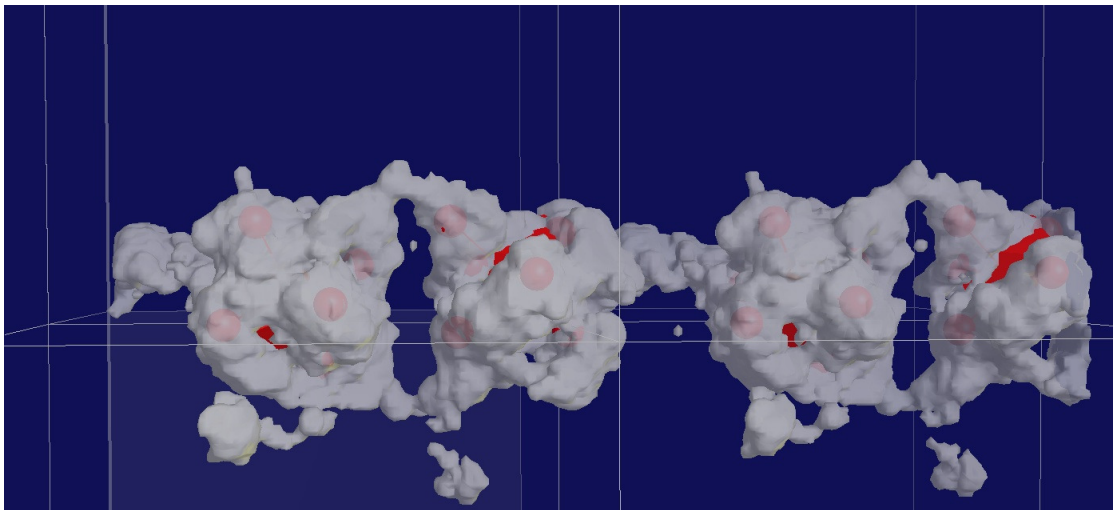

Figure 6.15: Oxygen displacement clouds from WO_x polyhedra only at 1173 K. Red spheres are oxygen atoms and orange polyhedra represent WO_x polyhedra.

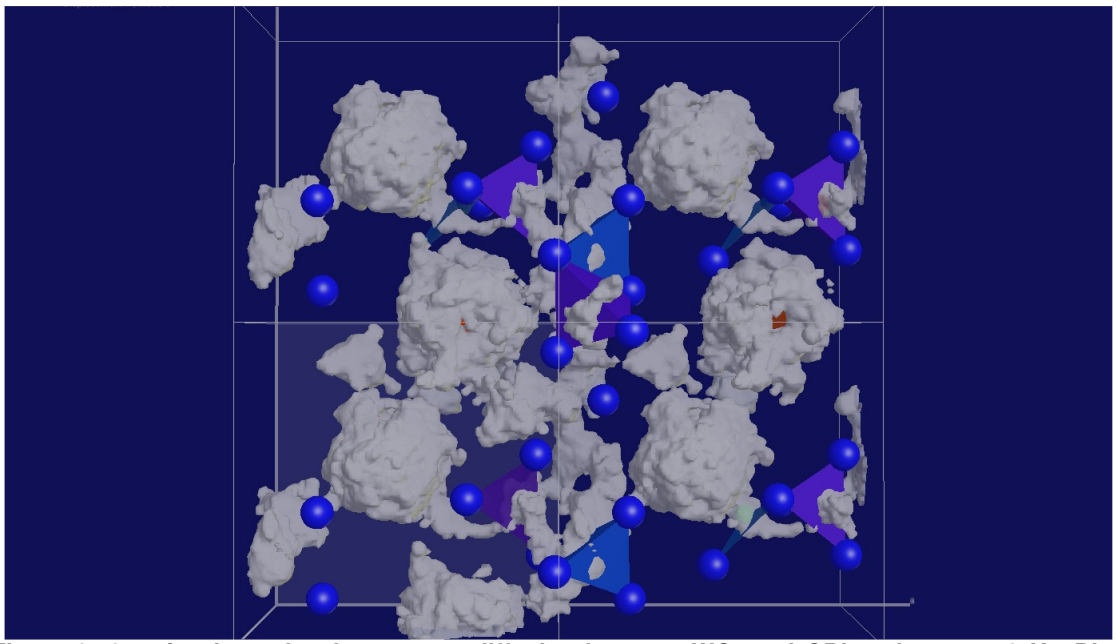

Figure 6.16: *ab* plane showing oxygen diffusion between WO_x and OBi_4 units at 1173 K. Blue spheres are bismuth atoms, blue polyhedra are OBi_4 units and orange polyhedra are WO_x units.

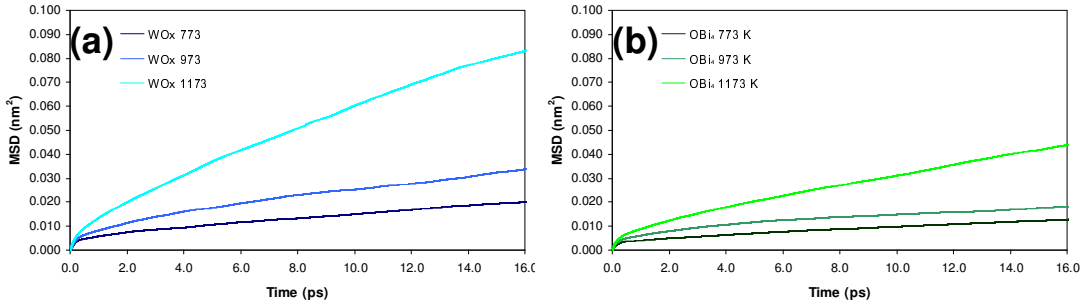

Figure 6.17: Mean square displacements (MSDs) for oxygen atoms in (a) WO_x units and (b) OBi_4 polyhedra.

In order to quantify whether oxide ion motion is diffusional or vibrational, the mean square displacement (MSD) can be calculated. The MSDs for oxygen atoms from WO_x polyhedra and OBi_4 polyhedra are shown in Figure 6.17. The largest MSD is observed for WO_x units at 1173 K, which is consistent with diffusion occurring between WO_x units and exchange between WO_x and OBi_4. At each temperature, the MSDs of the WO_x units are higher than the MSDs of the OBi_4 units.

In summary, molecular dynamics studies have found that both the OBi_4 and WO_x subunits are involved in the oxide ion migration pathways responsible for conductivity. Therefore doping studies will be carried out on both the bismuth and tungsten sites.

6.7 Doped Bi_6WO_{12} analogues

As molecular dynamics studies have found that both the OBi_4 and WO_x sites are involved in the oxide ion conduction pathways, both the bismuth and tungsten sites have been doped in order to try and increase ionic conductivity. We have doped the bismuth site with Er^{3+} and Ca^{2+} and the tungsten site with Nb^{5+} and Zr^{4+}. We have also simultaneously doped the bismuth and tungsten sites with Er^{3+} and Zr^{4+} respectively.

Phase composition of all products was checked by Rietveld refinement. In a typical refinement, 18 background terms, sample height, scale factor, cell parameters, peak shape and an overall isotropic temperature factor were refined. In each case the structural model used for refinement was based on Nespolo's model, with cation and anion occupancies adjusted in order to take into account the new composition.

6.7.1 $Bi_{6-x}Ca_xWO_{12-x/2}$ phases

6.7.1.1 Structural characterisation

$Bi_{6-x}Ca_xWO_{12-x/2}$ phases with x = 0.05, 0.1, 0.2, 0.3, 0.4 and 0.5 were synthesised as discussed in section 6.2.3. For x = 0.05 to x = 0.3, a single tetragonal phase based on Bi_6WO_{12} was observed. PXRD patterns of $Bi_{5.6}Ca_{0.4}WO_{11.8}$ and $Bi_{5.5}Ca_{0.5}WO_{11.75}$ showed a trace impurity of $CaWO_4$. Rietveld refinement was carried out using the parameters described in 6.7. A typical Rietveld fit is shown in Figure 6.18.

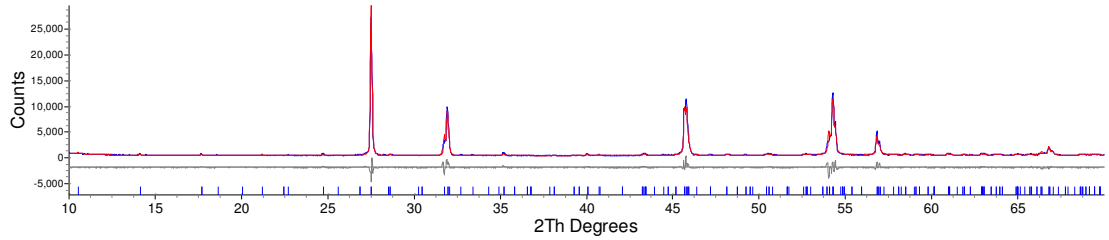

Figure 6.18: d9_03821: Rietveld fit for $Bi_{5.8}Ca_{0.2}WO_{11.9}$. R_{wp} = 9.740 %.

6.7.1.2 Impedance

Pellets with densities of around 90% could be prepared for $Bi_{6-x}Ca_xWO_{12-x/2}$. At 241 °C the complex impedance plot of $Bi_{5.9}Ca_{0.1}WO_{11.95}$ comprised of a single semi-circle arc and a Warburg-type spike (Figure 6.19). The capacitance of the large semi-circle arc was estimated to be 8.9×10^{-11} F cm^{-1} using the formula $\omega RC = 1$ and was therefore assigned to the bulk response. The capacitance of the spike was 10^{-7}-10^{-6} F cm^{-1} at frequencies of 2.5 Hz or less, indicating that ionic conductivity is present.

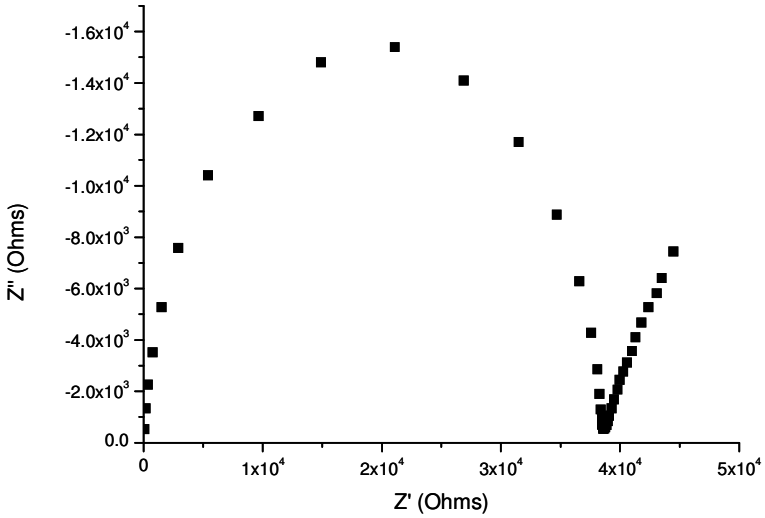

Figure 6.19: Complex impedance plot for $Bi_{5.9}Ca_{0.1}WO_{11.95}$ at 241 °C.

At high temperatures, the bulk response completely disappeared and the spike corresponding to the electrode response collapsed into a semi-circle arc with a high capacitance.

Despite Ca^{2+} doping increasing the number of oxygen vacancies, no increase in conductivity was observed for $Bi_{6-x}Ca_xWO_{12-x/2}$ phases. This may be due to some dopant-vacancy association.[18]

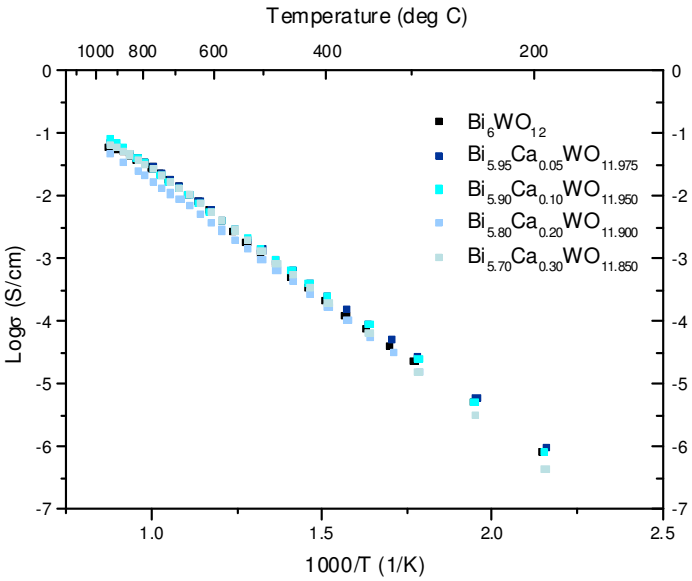

Figure 6.20: Arrhenius plots for $Bi_{6-x}Ca_xWO_{12-x/2}$ phases.

6.7.2 $Bi_6W_{1-x}Nb_xO_{12-x/2}$ phases

6.7.2.1 Structural characterisation

$Bi_6W_{1-x}Nb_xO_{12-x/2}$ phases (where x = 0.05, 0.10, 0.15, 0.20, 0.30 and 0.40) were synthesised. The $Bi_6W_{0.7}Nb_{0.3}O_{11.85}$ and the $Bi_6W_{0.6}Nb_{0.4}O_{11.80}$ samples showed $Bi_{1.7}Nb_{0.3}O_{3.3}$ as an impurity phase. Rietveld refinement was carried out using the parameters described in 6.7. Figure 6.21 shows a typical Rietveld fit.

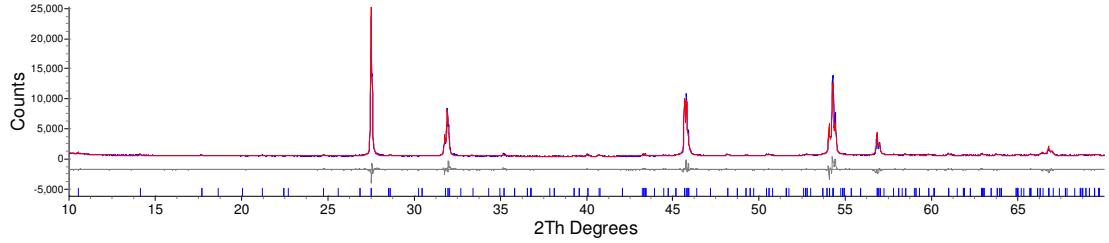

Figure 6.21: d9_03745: $Bi_6W_{0.9}Nb_{0.1}O_{11.95}$. R_{wp} = 8.692%

6.7.2.2 Impedance

All pellets had densities around 90%. One semi-circle arc and a Warburg-type electrode response were observed in the complex impedance spectrum for $Bi_6W_{0.95}Nb_{0.05}O_{11.975}$ at 290 °C (Figure 6.22). The capacitance of the larger semi-circle arc was estimated to be 7.4 × 10^{-11} F cm^{-1} using the formula $\omega RC = 1$, hence it was attributed to the bulk response. At low frequencies, the capacitance of the spike was of the order of magnitude 10^{-7}-10^{-6} F cm^{-1}, typical of ionic conductivity.

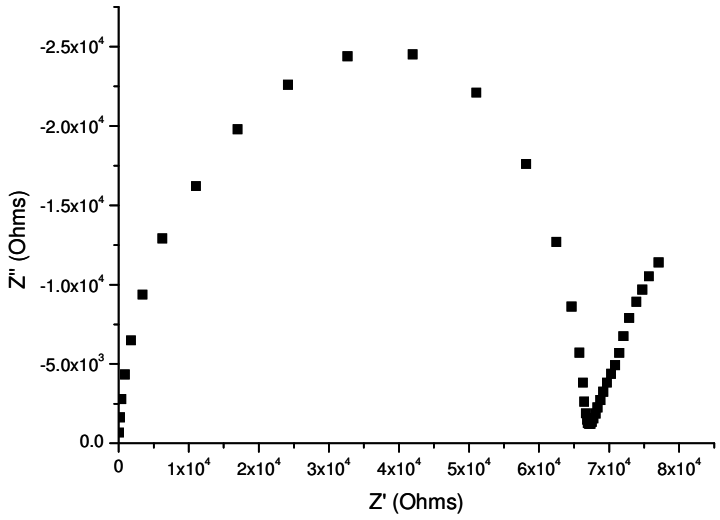

Figure 6.22: Impedance plot for $Bi_6W_{0.95}Nb_{0.05}O_{11.975}$ at 290 °C.

At high temperatures, the bulk contribution gradually disappeared, leaving only the electrode response. Therefore the high frequency intercept was taken as the bulk resistance.

Despite Nb^{5+} doping increasing the number of oxygen vacancies, no increase in conductivity was observed for $Bi_6W_{1-x}Nb_xO_{12-x/2}$ phases. Figure 6.23 shows the Arrhenius plots for $Bi_6W_{0.95}Nb_{0.05}O_{11.975}$ and $Bi_6W_{0.90}Nb_{0.10}O_{11.95}$, which shows a decrease in conductivity with Nb^{5+} doping.

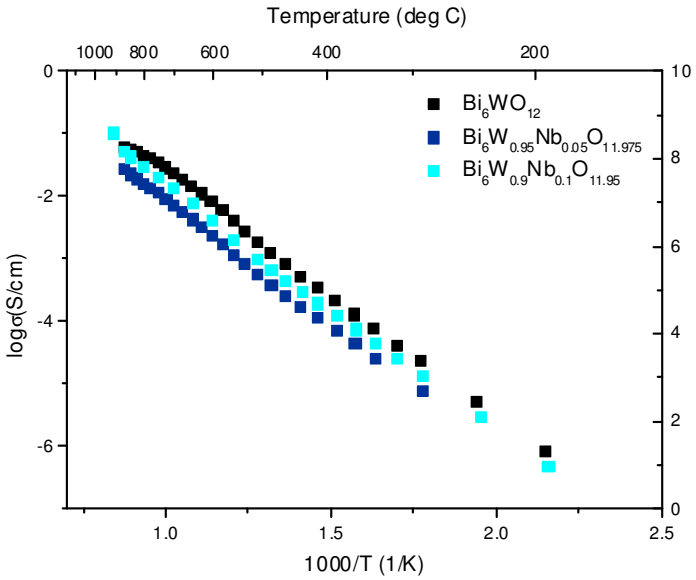

Figure 6.23: Arrhenius plots for members of the $Bi_6W_{1-x}Nb_xO_{12-x/2}$ system.

6.7.3 $Bi_6W_{1-x}Zr_xO_{12-x}$ phases

6.7.3.1 Structural characterisation

Eight samples in the $Bi_6W_{1-x}Zr_xO_{12-x}$ system (with x = 0.05, 0.10, 0.15, 0.20, 0.25, 0.30, 0.35 and 0.40) have been synthesised. PXRD data on both $Bi_6W_{0.65}Zr_{0.35}O_{11.65}$ and $Bi_6W_{0.60}Zr_{0.40}O_{11.60}$ showed that they contained Bi_2WO_6 and ZrO_2 as impurity phases. Rietveld refinement was carried out using the parameters described in 6.7. A typical Rietveld fit is shown in Figure 6.24.

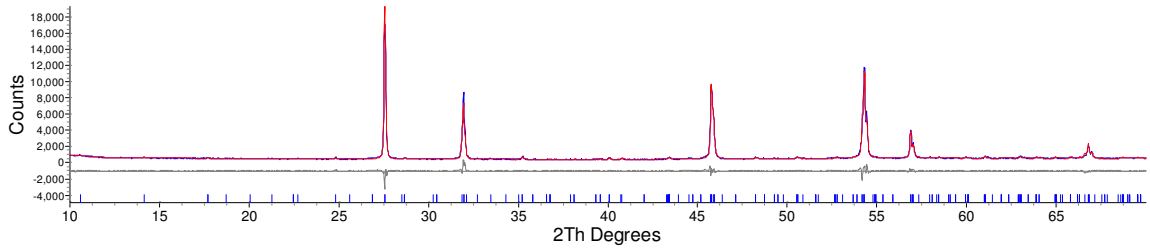

Figure 6.24: d9_03900: Rietveld refinement for $Bi_6W_{0.90}Zr_{0.10}O_{11.90}$. R_{wp} = 6.838%.

A graph of cell volume against Zr^{4+} content is shown in Figure 6.25. A decrease in cell volume is observed as the Zr^{4+} content is increased, which is unexpected given the larger radius of Zr^{4+} (0.72 Å) compared to W^{6+} (0.60 Å), but may probably be explained through the change in unit cell volume being a balance between incorporation of the larger Zr^{4+}, the creation of oxide vacancies and electrostatic effects due to charge differences.

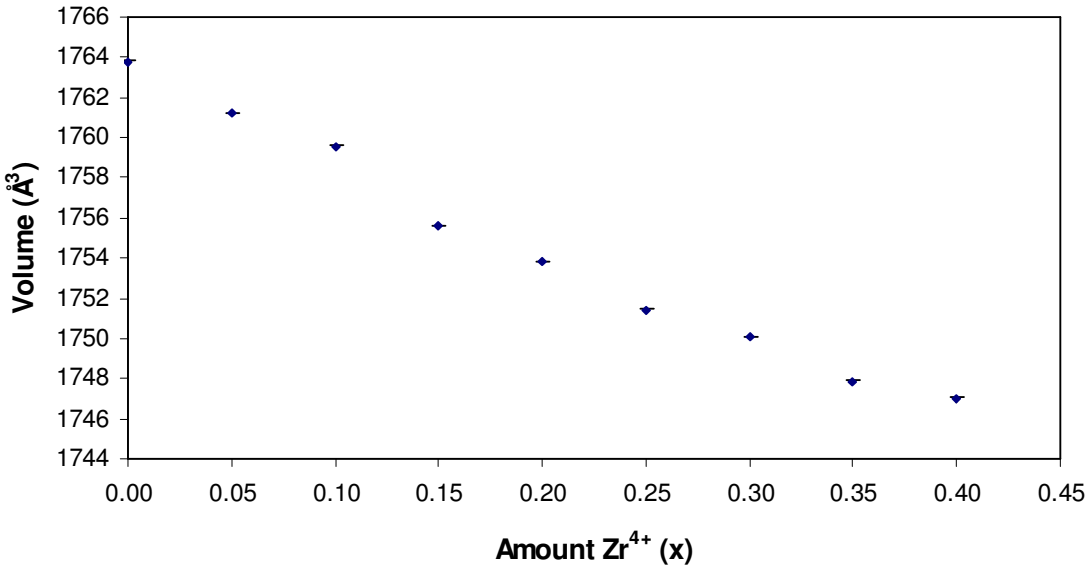

Figure 6.25: Variation of cell volume with Zr^{4+} content in the $Bi_6W_{1-x}Zr_xO_{12-x}$ system.

6.7.3.2 Impedance

At low temperatures, one semi-circle arc and a Warburg-type electrode response were observed in the complex impedance plot of $Bi_6W_{0.95}Zr_{0.05}O_{11.95}$ (Figure 6.26). The semi-circle arc had a capacitance of 6.7 pF cm^{-1} (calculated from the formula $\omega RC = 1$) and was assigned to the bulk response. At lower frequencies, only a spike was observed due to the electrode response, which has a capacitance of approximately 10^{-7} F cm^{-1} at frequencies of 1 Hz or less, indicative of ionic conductivity. At high temperatures, only one arc was observed, due to the electrode response, with a capacitance of 2.214×10^{-6} F cm^{-1}. All densities of the pellets were around 80%. The impedance plots of all other $Bi_6W_{1-x}Zr_xO_{12-x}$ compounds could be described in the same way.

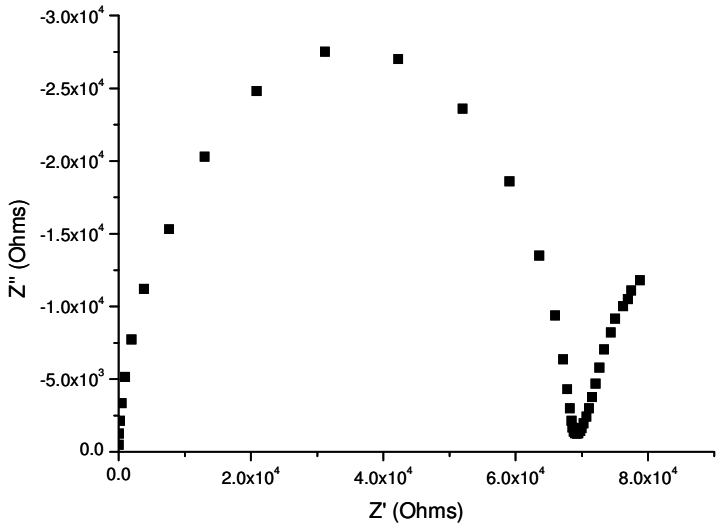

Figure 6.26: Complex impedance plot for $Bi_6W_{0.95}Zr_{0.05}O_{11.95}$ at 192 °C.

Figure 6.27 shows the Arrhenius plot of conductivity for the $Bi_6W_{1-x}Zr_xO_{12-x}$ system. Doping with Zr^{4+} increases the conductivity. An increase in conductivity was observed for $Bi_6W_{0.95}Zr_{0.05}O_{11.95}$ and $Bi_6W_{0.85}Zr_{0.15}O_{11.85}$, of approximately half an order of magnitude, at temperatures below 600 °C.

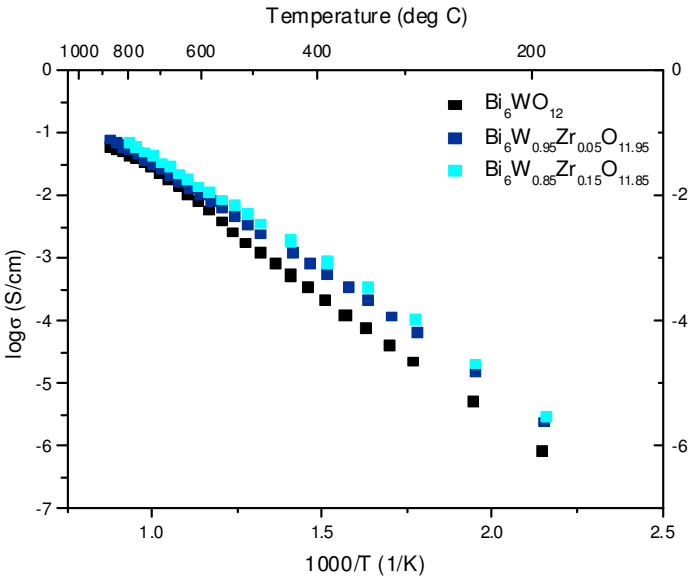

Figure 6.27: Arrhenius plots for the $Bi_6W_{1-x}Zr_xO_{12-x}$ system.

6.7.4 $Bi_{6-x}Er_xWO_{12}$ phases

6.7.4.1 Structural characterisation

Six phases in the $Bi_{6-x}Er_xWO_{12}$ system (where x = 0.05, 0.10, 0.15, 0.20, 0.30 and 0.40) were synthesised. The PXRD pattern of $Bi_{5.6}Er_{0.4}WO_{12}$ showed no impurities. Rietveld refinement was carried out using the parameters described in 6.7. The Rietveld fit for $Bi_{5.6}Er_{0.4}WO_{12}$ is shown in Figure 6.28.

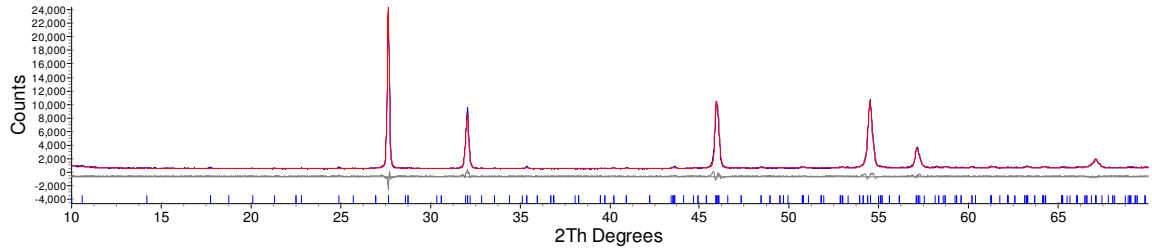

Figure 6.28: d9_03885: Rietveld refinement for $Bi_{5.6}Er_{0.4}WO_{12}$. R_{wp} = 6.006%

The graph shown in Figure 6.29 shows the variation of cell volume with Er^{3+} content. The cell volume decreases with increasing Er^{3+}, as expected, due to the smaller size of Er^{3+} (1.00 Å) compared to Bi^{3+} (1.17Å).[19]

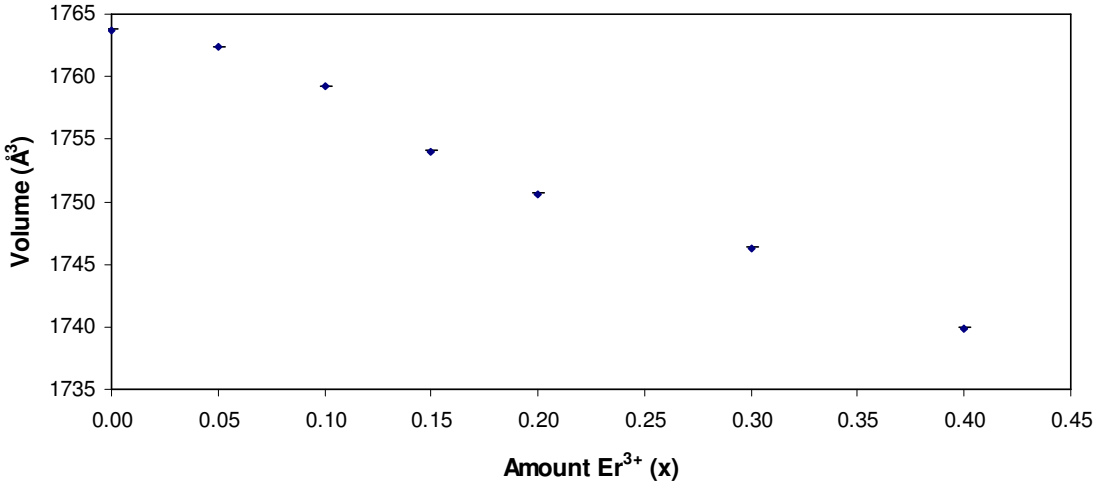

Figure 6.29: Variation of cell parameters with Er^{3+} content in the $Bi_{6-x}Er_xWO_{12}$ system.

6.7.4.2 Impedance

At low temperatures, two semi-circle arcs were seen in the complex impedance plot for $Bi_{5.95}Er_{0.05}WO_{12}$, as shown in Figure 6.30. The high frequency arc capacitance was calculated to be 7.6 pF cm^{-1} using the formula ωRC=1 and therefore represents the bulk contribution. At low frequencies only a partial semi-circle arc was observed and this has been attributed to the electrode response. At frequencies less than 1Hz, the capacitance was 10^{-7} F cm^{-1}, indicative of ionic conductivity.

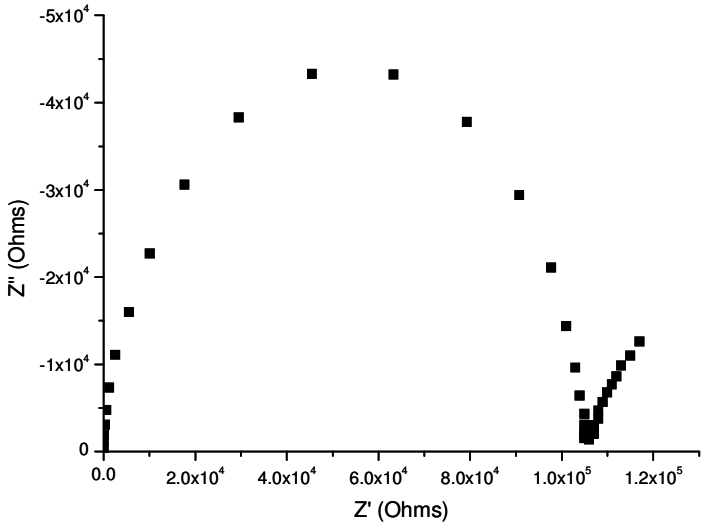

Figure 6.30: Complex impedance plot at 191 °C for $Bi_{5.95}Er_{0.05}WO_{12}$. Response shows one high frequency arc due to the bulk contributions and one low frequency arc due to the electrode response.

At high temperatures, only one semi-circle arc is observed which is due to the collapse of the spike seen at low temperatures due to the electrode response. At 752 °C the capacitance equals 2.776×10^{-7} F cm^{-1} and the resistance was obtained at the high frequency intercept of the arc. The impedance spectra of other $Bi_{6-x}Er_xWO_{12}$ may be described in the same way. All pellet densities were around 90%.

Figure 6.31 shows the Arrhenius plot of conductivity for the $Bi_{6-x}Er_xWO_{12}$ system. An increase in conductivity is observed for $Bi_{5.95}Er_{0.05}WO_{12}$ at low temperatures of approximately half an order of magnitude. However, the conductivity at high temperature is the same as Bi_6WO_{12}. Further doping with Er^{3+} does not increase the conductivity.

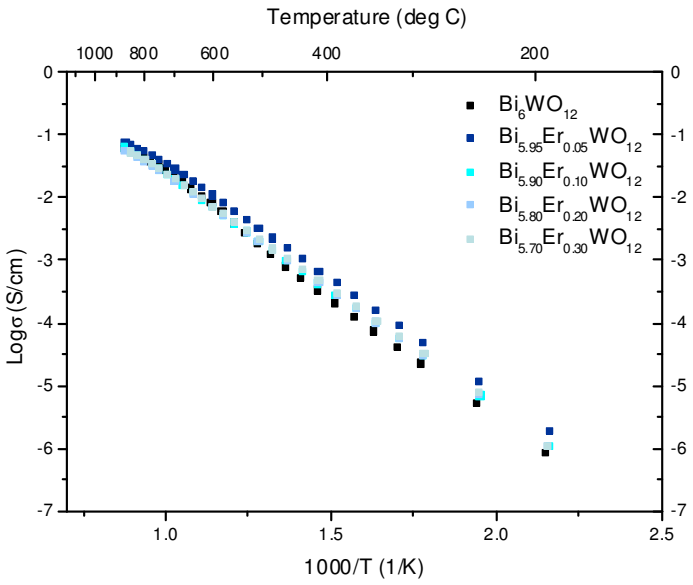

Figure 6.31: Arrhenius curves of conductivity for all samples measured in the $Bi_{6-x}Er_xWO_{12}$ system.

6.7.5 $Bi_{6-x}Er_xW_{1-y}Zr_yO_{12-y}$ phases (where x = y)

6.7.5.1 Structural characterisation

Four samples in the $Bi_{6-x}Er_xW_{1-y}Zr_yO_{12-y}$ system were prepared with $x = y = 0.05$-0.20. Rietveld refinement was carried out using the parameters described in 6.7. Figure 6.32 shows the Rietveld fit for $Bi_{5.95}Er_{0.05}W_{0.95}Zr_{0.05}O_{11.95}$.

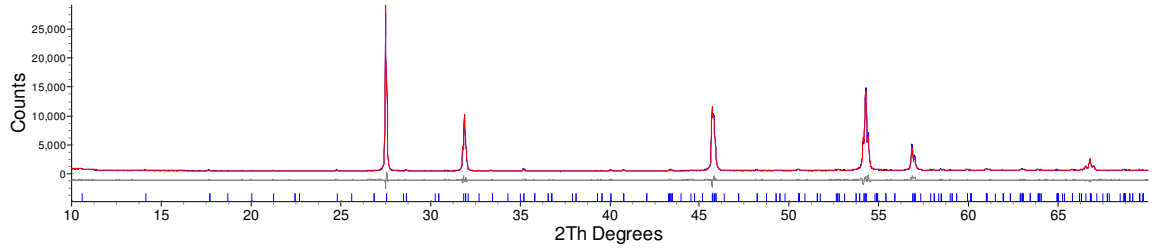

Figure 6.32: d9_04106: Rietveld fit for $Bi_{5.95}Er_{0.05}W_{0.95}Zr_{0.05}O_{11.95}$. R_{wp} 5.869%.

6.7.5.2 Impedance

All pellet densities were around 90%. At 190 °C, the complex impedance plot of $Bi_{5.95}Er_{0.05}W_{0.95}Zr_{0.05}O_{11.95}$ consisted of one full semi-circle arc and a second partial semi-circle arc (Figure 6.33). The capacitance was estimated using the formula $\omega RC = 1$. The large arc, which could be modeled by a resistor and capacitor in parallel, had a capacitance of 1.1×10^{-11} F cm^{-1} and was assigned to the bulk response. The partial semi-circle arc was attributed to the electrode response and had a capacitance of 10^{-7}-10^{-6} F cm^{-1} at low frequencies, which is indicative of ionic conductivity. At high temperatures, only one semi-circle arc (with high capacitance) was observed, due to the collapse of the electrode response, therefore the bulk resistance was taken from the high frequency intercept.

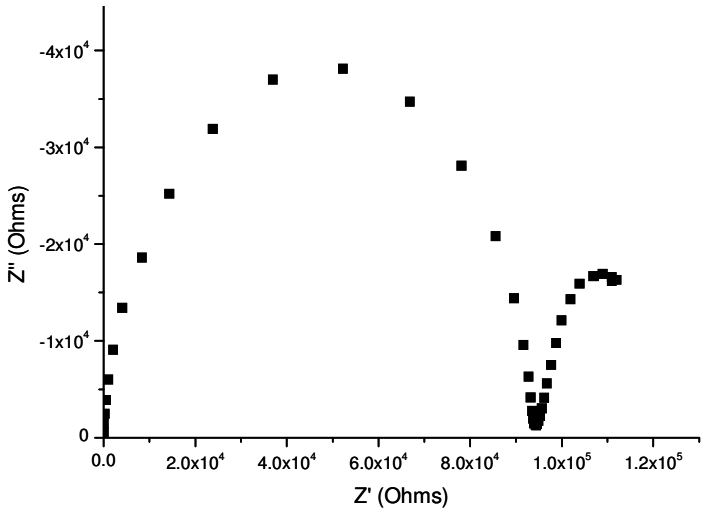

Figure 6.33: Complex impedance plot for $Bi_{5.95}Er_{0.05}W_{0.95}Zr_{0.05}O_{11.95}$ at 190 °C.

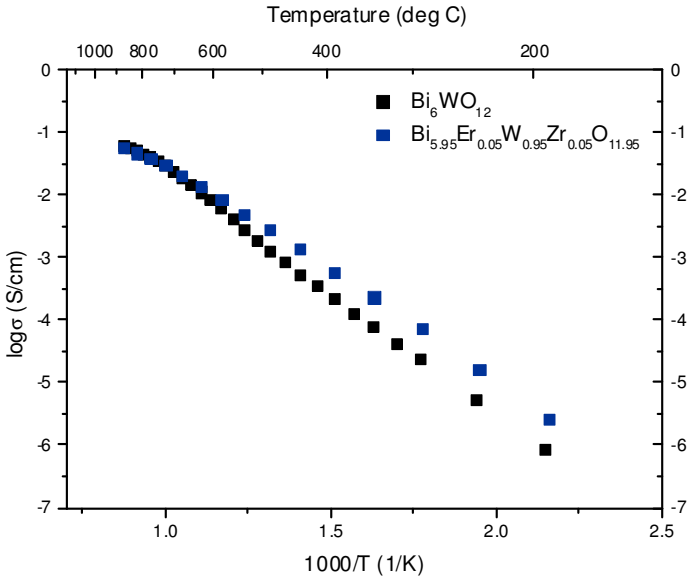

Figure 6.34: Arrhenius plot for members of the $Bi_{6-x}Er_xW_{1-y}Zr_yO_{12-y}$ series.

Figure 6.34 shows the Arrhenius plot for $Bi_{5.95}Er_{0.05}W_{0.95}Zr_{0.05}O_{11.95}$. An increase in conductivity of approximately 0.5 orders of magnitude was achieved below temperatures of 600 °C, which is comparable to the trends seen for $Bi_{5.95}Er_{0.05}WO_{12}$ and $Bi_6W_{0.95}Zr_{0.05}O_{11.95}$.

6.7.6 $Bi_{6-x}Er_xW_{1-y}Zr_yO_{12}$ phases (where x ≠ y)

6.7.6.1 Structural characterisation

Four samples in the $Bi_{6-x}Er_xW_{1-y}Zr_yO_{12-y}$ were prepared with x = 0.05-0.20 and y = 0.05-0.20. Rietveld refinement was carried out using the parameters described in 6.7. A typical Rietveld fit is shown in Figure 6.35.

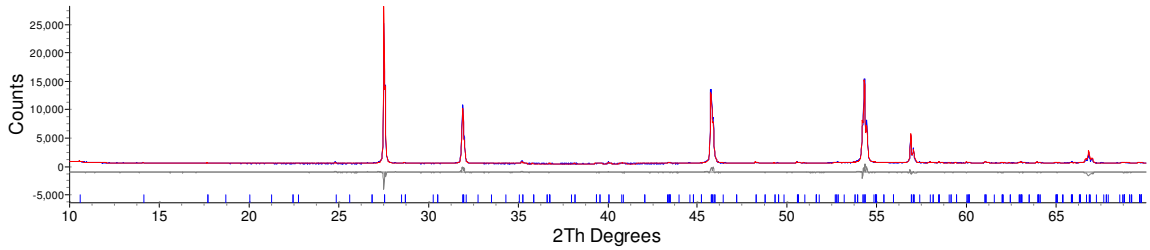

Figure 6.35: d9_04121: Rietveld fit for $Bi_{5.95}Er_{0.05}W_{0.90}Zr_{0.10}O_{11.90}$. R_{wp} = 6.734%.

6.7.6.2 Impedance

The complex impedance plot for $Bi_{5.95}Er_{0.05}W_{0.90}Zr_{0.10}O_{11.90}$ comprised of one large semi-circle arc and one partial semi-circle arc (Figure 6.36). The capacitance of the large semi-circle arc was 1.1×10^{-11} F cm^{-1} and was therefore assigned to the bulk

response. The arc could be modeled by a resistor and capacitor in parallel. The partial arc was assigned to the electrode response and at low frequencies the capacitance was of the order of magnitude 10^{-7}-10^{-6} F cm^{-1}, indicative of ionic conductivity. At high temperatures the arc corresponding to the bulk disappeared, leaving only one arc, due to the collapse of the electrode response. Therefore, at high temperatures the high frequency intercept was taken as the bulk resistance. The impedance plot of $Bi_{5.9}Er_{0.1}W_{0.95}Zr_{0.05}O_{11.95}$ could be described in the same way. Densities of all pellets were around 90%.

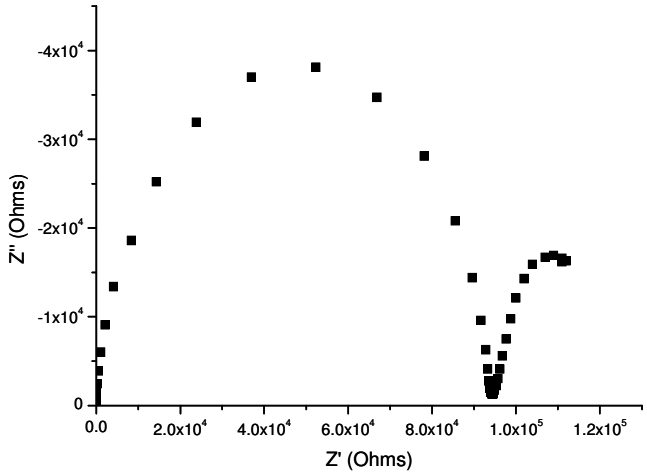

Figure 6.36: Complex impedance plot for $Bi_{5.95}Er_{0.05}W_{0.90}Zr_{0.10}O_{11.90}$.

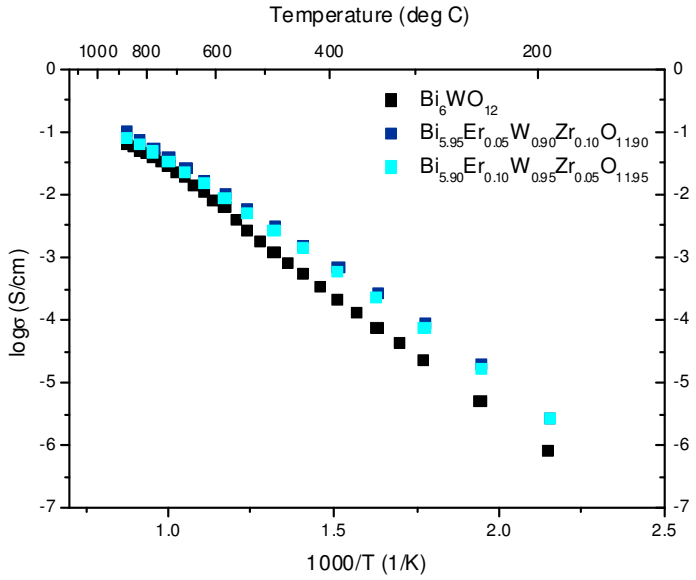

Figure 6.37: Arrhenius plots of conductivity for $Bi_{6-x}Er_xW_{1-y}Zr_yO_{12-y}$ where $x \neq y$

Figure 6.37 shows the Arrhenius plot for $Bi_{6-x}Er_xW_{1-y}Zr_yO_{12-y}$. At temperatures below 600 °C, an increase in conductivity of approximately half an order of magnitude was observed.

6.7.7 Comparison of conductivity of doped analogues

Figure 6.38 shows the increase in conductivity compared to Bi_6WO_{12} achieved when different dopants were used. Improvements were observed for $Bi_{5.95}Er_{0.05}WO_{12}$, $Bi_6W_{0.95}Zr_{0.05}O_{11.95}$, $Bi_{5.95}Er_{0.05}W_{0.95}Zr_{0.05}O_{11.95}$ and $Bi_{5.90}Er_{0.10}W_{0.95}Zr_{0.05}O_{11.95}$. At low temperatures, an increase of 0.5 - 0.75 orders of magnitude was observed. The activation energies and conductivity values at 400 °C, 600 °C and 800 °C are summarised in Table 6.4. This increase in conductivity is smaller than that observed for Nb^{5+} or Ta^{5+} doped Bi_2WO_6, as at 300 °C in $Bi_2W_{0.95}M^{5+}_{0.05}O_{11.95}$ (where $M^{5+} = Ta^{5+}$ or Nb^{5+}) the increase in conductivity was approximately 3 orders of magnitude.[8] At 800 °C, $Bi_2W_{0.95}Ta_{0.05}O_{11.95}$ and $Bi_2W_{0.95}Nb_{0.05}O_{11.95}$ display a conductivity 1.5 orders of magnitude higher than Bi_2WO_6. However, at high temperature the conductivity of the Bi_6WO_{12} doped analogues remains the same as the parent compound Bi_6WO_{12}, regardless of the dopant used.

The difference in the magnitude of the conductivity increase between the Bi_2WO_6 and Bi_6WO_{12} related compounds is probably structurally related. Bi_2WO_6 contains no oxygen vacancies, whilst Bi_6WO_{12} has the fluorite related structure, with 14.3 % anion sites vacant. Therefore aliovalent doping in Bi_2WO_6 creates oxygen vacancies, whereas aliovalent doping in Bi_6WO_{12} increases the number of oxygen vacancies. It is likely that aliovalent doping in Bi_6WO_{12} creates some vacancy clustering, therefore above certain levels of dopant the conductivity may not be increased.[18]

Table 6.4: List of oxide ion conductivities at 400 °C, 600 °C and 800 °C for Bi_6WO_{12} related phases and their activation energies.

	400 °C ($S\ cm^{-1}$)	600 °C ($S\ cm^{-1}$)	800 °C ($S\ cm^{-1}$)	Activation energy (eV)
Bi_6WO_{12}	3.56×10^{-4}	8.59×10^{-3}	4.67×10^{-2}	0.838(9)
$Bi_{5.95}Er_{0.05}WO_{12}$	7.17×10^{-4}	1.16×10^{-2}	5.78×10^{-2}	0.787(3)
$Bi_6W_{0.95}Zr_{0.05}\ O_{11.95}$	8.74×10^{-4}	1.13×10^{-2}	5.65×10^{-2}	0.755(1)
$Bi_{5.95}Er_{0.05}W_{0.95}Zr_{0.05}O_{11.95}$	8.18×10^{-4}	1.18×10^{-2}	5.95×10^{-2}	0.733(6)
$Bi_{5.90}Er_{0.10}W_{0.95}Zr_{0.05}O_{11.95}$	8.23×10^{-4}	1.18×10^{-2}	5.93×10^{-2}	0.754(3)

Our MD simulations have shown that both the OBi_4 and WO_x units are involved in the conduction pathways. This is echoed in the fact that conductivity enhancement occurs when either the bismuth ($Bi_{6-x}Er_xWO_{12}$) or tungsten sites ($Bi_6W_{1-y}Zr_yO_{12-y}$), or both sites ($Bi_{6-x}Er_xW_{1-y}Zr_yO_{12-y}$) are doped.

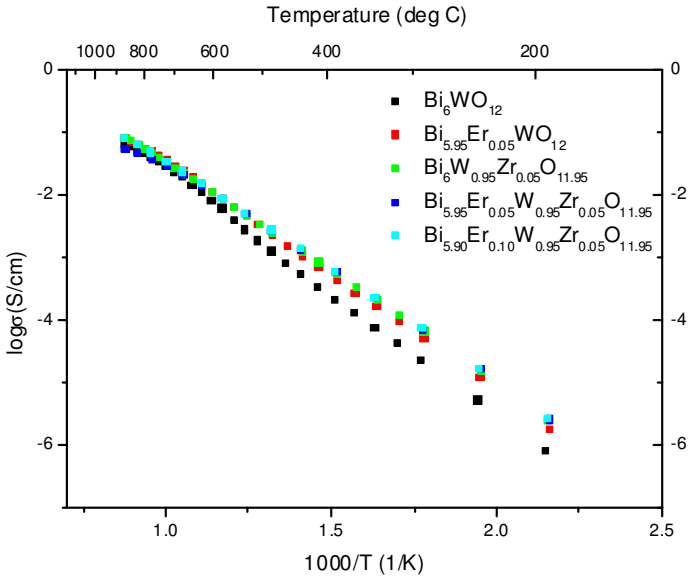

Figure 6.38: Comparison of conductivities achieved with different dopants in Bi_6WO_{12} related phases.

The conductivity of some bismuth erbium tungstates have previously been reported, but in the bismuth rich region, where they possess the fluorite structure.[20] $Bi_{1.47}Er_{0.42}W_{0.055}O_3$ had the highest conductivity, of the order of 0.05 S cm^{-1} at 550 °C, higher than our $Bi_{5.95}Er_{0.05}WO_{12}$ sample.[20] Almost no difference was observed in the conductivity when the Bi:Er ratio was varied from 3.5:1 to 2.9:1.[20]

Unlike Bi_2WO_6, no increase was seen with Nb^{5+} doping in Bi_6WO_{12}.[13] It is likely that there is some contribution from electronic conductivity in the Nb^{5+} system, as Abrahams *et al.* have reported that in the $Bi_{3.5}Nb_{1-x}Y_xO_{7.75}$ system, the niobium rich members show a significant electronic conductivity contribution to the total conductivity, with the lowest ionic transference number being found for $Bi_{3.5}NbO_{7.75}$.[21] In a separate paper, Abrahams *et al.* have also looked at the conductivity for $Bi_{3+x}Nb_{0.8}W_{0.2}O_{7.1+3x/2}$ with a fixed Nb:W ratio of 0.8:0.2 with the bismuth content varying from $x = 0$ to $x = 2.0$. $Bi_5Nb_{0.8}W_{0.2}O_{8.6}$ showed the highest conductivity, of the order 1.76×10^{-1} S cm^{-1} at 800 °C.[22]

In summary, enhancements of conductivity of 0.5-0.75 orders of magnitude have been made when Er^{3+} and Zr^{4+} have been used as dopants. This is supported by the results of MD simulations which show that OBi_4 and WO_x units are involved in the migration pathway.

6.8 Conclusions

Of the three published structural models, Nespolo's model fits the data for Bi_6WO_{12} best. No evidence for superstructure reflections have been found in the diffraction data.

A change in gradient in both the impedance data and variable temperature X-ray daya are indicative of an order-disorder transformation on a local scale, as no long range transformations have been observed in PND or PXRD variable temperature data. MD simulations have shown that both OBi_4 and WO_6 units are involved in the diffusion process. Improvements to the conductivity of Bi_6WO_{12} (of approximately half an order of magnitude) have been made for the following compounds: $Bi_{5.95}Er_{0.05}WO_{12,}$ $Bi_6W_{0.95}Zr_{0.05}O_{11.95}$, $Bi_{5.95}Er_{0.05}W_{0.95}Zr_{0.05}O_{11.95}$ and $Bi_{5.90}Er_{0.10}W_{0.95}Zr_{0.05}O_{11.95}$.

6.9 References

1. T. Takahashi and H. Iwahara, *J. Appl. Electrochem.*, 1973, **3**, 65-72.
2. W. Zhou, *J. Solid State Chem.*, 1994, **108**, 381-394.
3. C. D. Ling, R. L. Withers, S. Schmid and J. G. Thompson, *J. Solid State Chem.*, 1998, **137**, 42-61.
4. A. Watanabe, N. Ishizawa and M. Kato, *J. Solid State Chem.*, 1985, **60**, 252-257.
5. N. Sharma, R. B. Macquart , M. Avdeev, M. Christensen, G. J. McIntyre, Y.-S. Chen and C. D. Ling, *Acta Crystallogr.*, 2010, **B66**, 165-172.
6. C. D. Ling, *J. Solid State Chem.*, 1999, **148**, 380-405.
7. M. Nespolo, A. Watanabe and Y. Suetsugu, *Cryst. Res. Technol.*, 2002, **37**, 414-422.
8. N. Baux, R. N. Vannier, G. Mairesse and G. Nowogrocki, *Solid State Ionics*, 1996, **91**, 243-248.
9. M. S. Islam, S. Lazure, R. N. Vannier, G. Nowogrocki and G. Mairesse, *J. Mater. Chem.*, 1998, **8**, 655-660.
10. J. S. O. Evans, Durham, 1999, p. Fortran 77 routine.
11. V. V. Kharton, F. M. B. Marques and A. Atkinson, *Solid State Ionics*, 2004, **174**, 135-149.
12. J. E. H. Sansom and P. R. Slater, *Solid State Ionics*, 2004, **167**, 23-27.
13. J. C. Boivin and G. Mairesse, *Chem. Mater.*, 1998, **10**, 2870-2888.
14. J. B. Goodenough, *Solid State Ionics*, 1997, **94**, 17-25.
15. LAMP.The Large Array Manipulation Program. http://www.ill.eu/instruments-support/computing-for-science/cs-software/all-software/lamp
16. T. Rog, K. Murzyn, K. Hinsen and G. R. J. Kneller, *J. Comput. Chem*, 2003, **24**, 657-667.
17. I. R. Evans, J. S. O. Evans and J. A. K. Howard, *Chem. Mater.*, 2005, **17**, 4074 - 4077.
18. J. A. Kilner, *Solid State Ionics*, 2000, **129**, 13-23.
19. R. D. Shannon, *Acta Crystallogr. A*, 1976, **32**, 751-767.
20. A. Watanabe and M. Sekita, *Solid State Ionics*, 2005, **176**, 2429-2433.
21. M. Malys, M. Holdynski, F. Krok, W. Wróbel, J. R. Dygas, C. Pirovano, R. N. Vannier, E. Capoen and I. Abrahams, *J. Power Sources*, 2009, **194**, 16-19.
22. A. Borowska-Centkowska, A. Kario, F. Krok, I. Abrahams, S. C. M. Chan, X. Liu, W. Wrobel, M. Malys, S. Hull, J. R. Dygas and E. Suard, *Solid State Ionics*, 2010, **181**, 1750-1756.

7 Simulations, Characterisation and Properties of New Bismuth Vanadate Oxide Ion Conductors

7.1 Background

Bismuth vanadates have received considerable attention, due to the high oxide ion conductivity displayed by $Bi_2VO_{5.5}$, the parent member of the 'BIMEVOX' family of oxide ion conductors, with the Aurivillius structure.[1] Many fluorite superstructures exist in the Bi_2O_3-V_2O_5 system.[2] Using electron diffraction data, Zhou initially classified Bi_9VO_{16} as a 3 × 3 × 3 fluorite related type I superstructure.[2] Kashida later found that this structure could be approximately described using a rhombohedral (R3m) unit cell, with the cell volume being 25% of the volume of the 3 × 3 × 3 fluorite cell.[3] Here, vanadium exists in a tetrahedral coordination, with the tetrahedra being isolated from one another. However, Kashida's model was only an approximate structural model, as certain weak superstructure peaks cannot be fitted using this model and some oxygen positions could not be refined.[3] Compared to the ideal fluorite, $M_{10}O_{20}$, Bi_9VO_{16} can be seen as having 20% of oxygen sites vacant, although these vacant oxygen sites were reported by Kashida *et al.* to cluster around the vanadium, to create tetrahedral VO_4 units.[3] Kashida's model for Bi_9VO_{16} is shown in Figure 7.1.

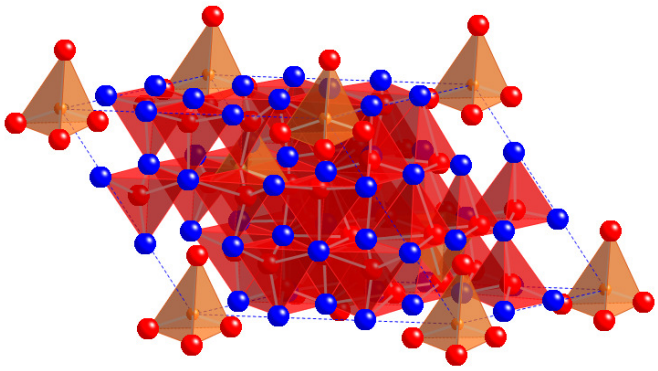

Figure 7.1: Kashida's model of Bi_9VO_{16}. Orange polyhedra are VO_4 tetrahedra, red polyhedra are OBi_4 tetrahedra, blue spheres are bismuth atoms, orange spheres are vanadium atoms and red spheres are oxygen atoms.

Previous work in our group by Xiaojun Kuang has shown that $Bi_{19}V_2O_{33.5}$ has an exceptionally high oxide ion conductivity below 500 °C.[4] In fact, it appears to be the second best fluorite-type oxide ion conductor in the temperature region between 300-400 °C (narrowly beaten by $Bi_{12.5}La_{1.5}ReO_{24.5}$).[5] The aim of this work was firstly to carry out DFT molecular dynamics studies to provide insight into the conduction

pathway, in particular to determine whether the fluorite-like OBi_4 sublattice, the VO_4 tetrahedra or both the VO_4 and OBi_4 sub-units were primarily responsible for conduction and secondly to use this information to guide further synthetic work to tune the conductivity by aliovalent doping of the parent compound.

7.2 Synthetic routes to $Bi_{19-x}M_xV_2O_{33.5-x/2}$ and $Bi_{19}V_{2-x}M'_xO_{33.5-y}$

7.2.1 Conventional solid state synthesis

Table 7.1: Target compositions, synthetic conditions and outcomes for doped $Bi_{19}V_2O_{33.5}$ phases.

Dopant	x	T(°C)	Time (hours)	Product obtained
Ca^{2+}	0.1	700, 750, 800, 825	4 × 12h	$Bi_{19-x/2}Ca_xV_2O_{33.5-x/2}$
	0.2	700, 750, 800, 825	4 × 12h	$Bi_{19-x/2}Ca_xV_2O_{33.5-x/2}$
	0.5	700, 750, 800, 825	4 × 12h	$Bi_{19-x/2}Ca_xV_2O_{33.5-x/2}$
	1.0	700, 750, 800, 825	4 × 12h	$Bi_{19-x/2}Ca_xV_2O_{33.5-x/2}$
	2.0	700, 750, 800, 825	4 × 12h	$Bi_{19-x/2}Ca_xV_2O_{33.5-x/2}$
Sr^{2+}	0.1	700, 750, 800, 825	4 × 12h	$Bi_{19-x/2}Sr_xV_2O_{33.5-x/2}$
	0.2	700, 750, 800, 825	4 × 12h	$Bi_{19-x/2}Sr_xV_2O_{33.5-x/2}$
	0.5	700, 750, 800, 825	4 × 12h	$Bi_{19-x/2}Sr_xV_2O_{33.5-x/2}$
	1.0	700, 750, 800, 825	4 × 12h	$Bi_{19-x/2}Sr_xV_2O_{33.5-x/2}$
	2.0	700, 750, 800, 825	4 × 12h	$Bi_{19-x/2}Sr_xV_2O_{33.5-x/2}$
Si^{4+}	0.1	700, 750, 800, 825	4 × 12h	$Bi_{19}V_{2-x}Si_xO_{33.5-x/2}$ + $Bi_{24}Si_2O_{40}$
	0.1	700, 825, 875	12h, 12h, 24h	$Bi_{19}V_{2-x}Si_xO_{33.5-x/2}$ + $Bi_{24}Si_2O_{40}$
	0.2	700, 750, 800, 825	4 × 12h	$Bi_{19}V_{2-x}Si_xO_{33.5-x/2}$ + $Bi_{24}Si_2O_{40}$
	0.2	700, 825, 875	12h, 12h, 24h	$Bi_{19}V_{2-x}Si_xO_{33.5-x/2}$ + $Bi_{24}Si_2O_{40}$
Ga^{3+}	0.1	700, 750, 800, 825, 875	5 × 12h	$Bi_{19}V_{2-x}Ga_xO_{33.5-x}$ + $Bi_{25}GaO_{40}$
	0.2	700, 750, 800, 825, 875	5 × 12h	$Bi_{19}V_{2-x}Ga_xO_{33.5-x}$ + $Bi_{25}GaO_{40}$

$Bi_{19-x}M_x V_2O_{33.5-x/2}$, where M = Ca^{2+} or Sr^{2+}, were synthesised for x = 0.1, 0.2, 0.5, 1.0, and 2.0. Bi_2O_3, V_2O_5, and either CaO or SrO were ground in an agate pestle and mortar then fired at 700, 750, 800 and 825 °C for 12 hours at each temperature, with intermittent grindings. The same procedure was followed for $Bi_{19}V_{2-x}M'_xO_{33.5-y}$, where x = 0.1 or 0.2 and M' = Si^{4+} or Ga^{3+}, using SiO_2 or Ga_2O_3 as starting materials. These materials were impure and further firing at 875 °C for 12 hours did not yield a pure compound. In the case of $Bi_{19}V_{2-x}M'_xO_{33.5-y}$, a $Bi_{25}GaO_{40}$ impurity phase was observed.

7.2.2 Single Crystal Growth

Single crystals of $Bi_{19}V_2O_{33.5}$, $Bi_{19-x}M_xV_2O_{33-x/2}$ (where M = Ca^{2+} and Sr^{2+}) were grown by heating a sample of the desired composition to its melting point. The sample was then slow cooled, at a rate of 3 °C/hour to 400 °C and then furnace cooled to room temperature. Identification of cell parameters using laboratory single crystal XRD has confirmed that single crystals of the desired product have been grown.

7.3 Molecular dynamics simulations

The rhombohedral structure of $Bi_{19}V_2O_{33.5}$ may be expressed as a pseudo-cubic $3 \times 3 \times 3$ fluorite-type superstructure with P1 symmetry. This consists of a network of edge-sharing, oxygen centred OBi_4 tetrahedra and isolated VO_4 tetrahedra. In this pseudo-cubic $3 \times 3 \times 3$ model, there are 264 oxygen sites, some of which are partially occupied. There are also 12 vanadium sites, some of which are partially occupied by bismuth. As molecular dynamics simulations required all sites to be fully occupied, calculations were carried out on the $Bi_{96}V_{12}O_{174}$ composition. Geometry optimisation was carried out before MD simulations. Molecular dynamics simulations have been carried out at 473 K and 873 K. A MD time step of 2 fs was used and simulations were ran for 10 000 steps, leading to a trajectory of 20 000 fs in duration. The atomic displacements of oxygen atoms have been visualised using LAMP and mean square displacements calculated using nMOLDYN.[6, 7] The aim of this work was to determine whether oxygen diffusion occurs via VO_4 units, OBi_4 units or both.

At 473K, oxygen displacement clouds link VO_4 tetrahedra (which are only separated by approximately 7 Å), as shown in Figure 7.2a, with diffusion mediated by a vacancy in an OBi_4 unit. In Figure 7.2b, diffusion occurs between VO_4-OBi_4-VO_4, giving evidence for the exchange of oxygen between VO_4 and OBi_4 units. The right hand side of this diagram shows diffusion from one VO_4 tetrahedron to two VO_4 units, via diffusion of oxygen through the face of an OBi_4 tetrahedron. Oxygen atoms in OBi_4 tetrahedra are more localised and there are no examples of OBi_4 tetrahedra forming a continuous diffusion pathway through the unit cells at 473 K. This is shown in Figure 7.2c, where it is clear to see that the oxygen displacement clouds are elongated for oxygen atoms in the top left and top middle of the diagram, but are much more localised for the other oxygen atoms in the diagram, indicating vibrational motion. No diffusion pathway was seen between these oxygen atoms. Although no diffusion in the OBi_4 units was observed in the simulations at 473 K, the timescale of the MD simulation is much shorter than the experimental timescale.

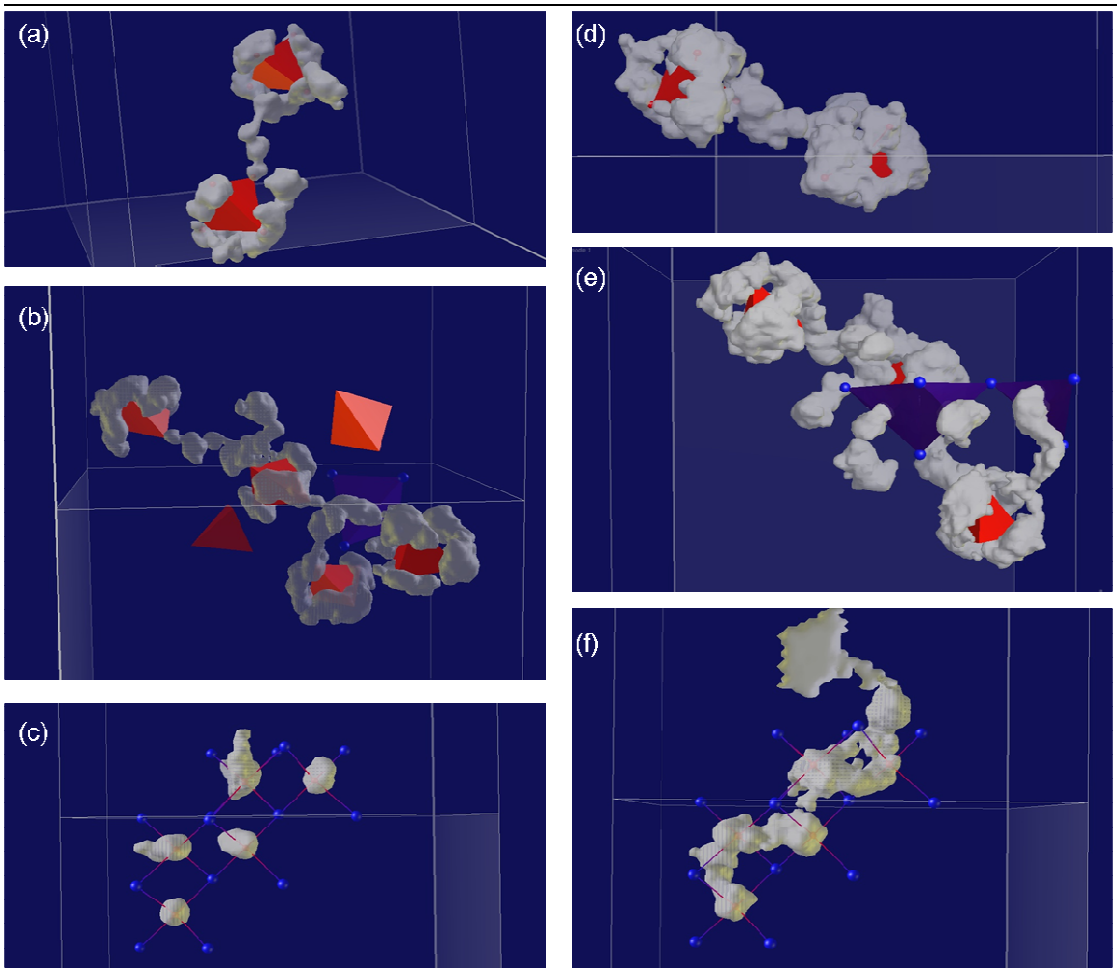

Figure 7.2: Oxygen atom displacement clouds at 473 K (a-c) and 873 K (d-f). (a and d) show two linked VO_4 tetrahedra. (b and e) show migration pathways involving both VO_4 and OBi_4. (c and f) show migration pathways through OBi_4 tetrahedra. In (c) some ellipsoids are more localised than others, however, no displacement clouds are joined together to form a diffusion pathway, but in (f) a diffusion pathway can be seen between the OBi_4 units. Orange polyhedra represent VO_4 tetrahedra, blue polyhedra represent OBi_4 tetrahedra and blue spheres represent bismuth atoms. Due to the constraints of the LAMP program, it may be difficult to visualise blue atoms and polyhedra.

At 873 K, the oxygen displacement clouds of adjacent VO_4 tetrahedra are linked, indicating that there is oxygen diffusion between VO_4 units (Figure 7.2d). Figure 7.2e shows the exchange of oxygen between VO_4 and OBi_4 units. The diffusion pathways between OBi_4 units are shown in Figure 7.2f. Unlike the situation observed at 473 K, at 873 K oxygen displacement clouds from OBi_4 tetrahedra only are much more elongated and show diffusion pathways between OBi_4 units. Figure 7.2c and Figure 7.2f show the OBi_4 sub-units at 473 K and 873 K, respectively. As they show the same bismuth and oxygen atoms, they may be compared. It is clear to see that at 873 K there is a diffusion pathway between OBi_4 units. However, there is still not a continuous migration pathway through the unit cell involving OBi_4 units only.

To determine whether oxygen motion is vibrational or diffusional, mean square displacements (MSDs) were calculated. Figure 7.3 shows the MSDs for all oxygen atoms in VO_4 and OBi_4 units. At both 473 K and 873 K, VO_4 oxygens display a higher MSD than the OBi_4 oxygens. This is consistent with the displacement clouds linking VO_4 units, which is observed at both temperatures. At 873 K, the MSD for OBi_4 oxygens is higher than at 473 K, indicating that there is more diffusion through OBi_4 units, which has been observed in the plots of the oxygen displacement clouds (see Figure 7.2c and f).

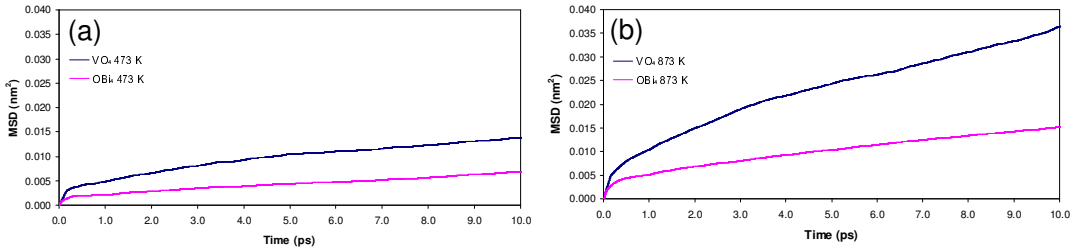

Figure 7.3: MSDs for all oxygens in either VO_4 units or OBi_4 units at (a) 473 K and (b) 873 K.

Figure 7.4 shows that vanadium may exhibit a variable coordination number. In Figure 7.4a, vanadium is four coordinate, but in Figure 7.4b the coordination number of vanadium increases to five, due to exchange of oxygen from the OBi_4 units. Two oxygen atoms leave the VO_4 unit and three oxygen atoms enter the VO_4 unit. When the oxygen displacement clouds are plotted for the oxygen atoms shown in Figure 7.4, it consists of a sphere (due to rotation) and 'branches' due to oxygen exchange between VO_4 and OBi_4 units (Figure 7.5). The VO_4 unit rotates in order to accommodate the change in coordination number and coordination environment.

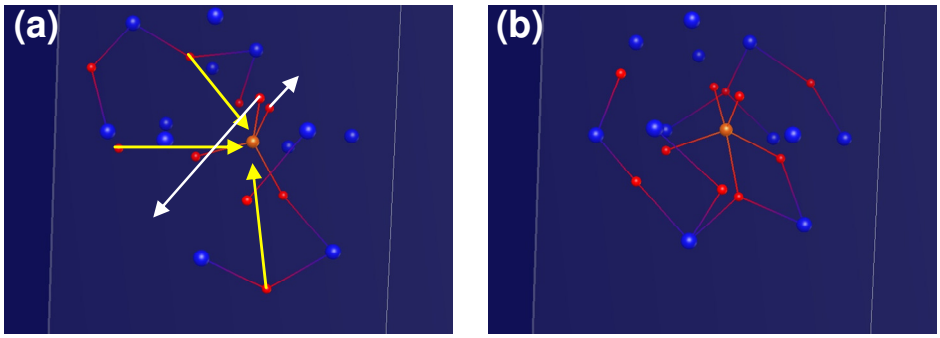

Figure 7.4: Variable coordination number environments for VO_x at 873 K. (a) Four coordinate vanadium and (b) five coordinate vanadium. White arrows show oxygen atoms leaving the coordination sphere of vanadium, whilst yellow arrows show oxygen atoms entering the coordination sphere of vanadium. Red spheres are oxygen atoms, orange spheres are vanadium atoms and blue spheres are bismuth atoms.

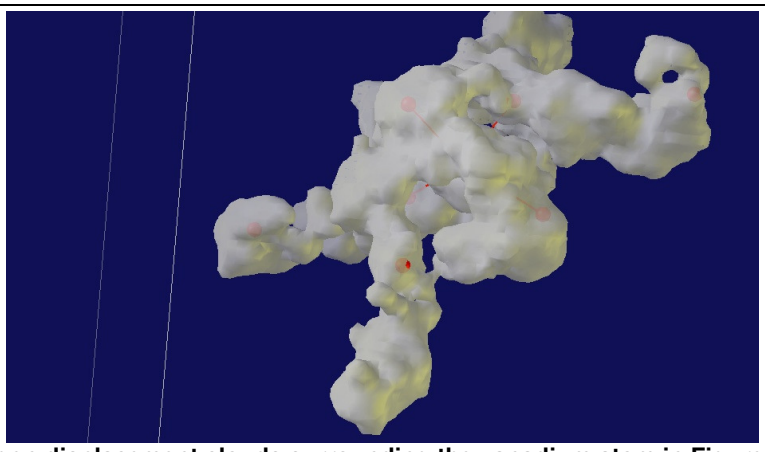

Figure 7.5: Oxygen displacement clouds surrounding the vanadium atom in Figure 7.4.

The importance of exhibiting a variable coordination number has been illustrated in the study of another good oxide ion conductor, $La_2Mo_2O_9$. At room temperature the α-$La_2Mo_2O_9$ structure is present, but above 580 °C the β-$La_2Mo_2O_9$ structure is adopted and it is this form which has a high oxide ion conductivity.[8, 9] Structure solution of α-$La_2Mo_2O_9$ by Evans *et al.* found that molybdenum exists with several different coordination numbers (four, five and six) and environments, and can be viewed as static ordering of the β-$La_2Mo_2O_9$ phase.[9] Therefore, molybdenum may be viewed as having 'virtual' oxide ion vacancies, providing a suitable pathway for oxide ion migration.[9]

In summary, MD simulations have shown that the migration pathway for oxide ion conduction involves VO_4 units and exchange between VO_4 and OBi_4 units. Migration through only OBi_4 units appears to require higher temperatures, as diffusion pathways involving OBi_4 units were only observed at 873 K. Therefore, doping studies on both the bismuth and vanadium sites were carried out in order to try and enhance the ionic conductivity.

7.4 $Bi_{19-x}Ca_xV_2O_{33.5-x/2}$

As MD simulations have shown that the oxygen migration pathways involve both the VO_4 units and OBi_4 units, doping studies have been carried on both the bismuth and vanadium sites. As phase pure samples could not be obtained for the Si^{4+} and Ga^{3+} samples which involved doping the vanadium sites, only substitution on the bismuth site will be discussed.

7.4.1 Structural characterisation of $Bi_{19-x}Ca_xV_2O_{33.5-x/2}$

Samples of $Bi_{19-x}Ca_xV_2O_{33.5-x/2}$ were prepared for $x = 0.1$, 0.2, 0.5, 1.0 and 2.0. Impurity phases were observed in the $x = 0.5$, 1.0 and 2.0 XRD patterns. In a typical

refinement, 18 background terms, peak shape, scale factor, cell parameters and one overall temperature factor were refined. A rhombohedral model was used with occupancies of both cation and anion sites adjusted to take into account the incorporation of Ca^{2+}. A typical Rietveld fit is shown in Figure 7.6.

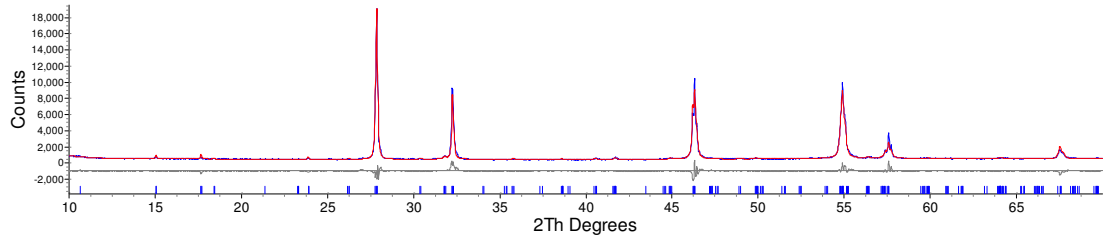

Figure 7.6: d9_04445: Rietveld fit for $Bi_{18.9}Ca_{0.1}V_2O_{33.45}$, R_{wp} = 8.387%.

7.4.2 Laboratory VT-PXRD $Bi_{18.9}Ca_{0.1}V_2O_{33.45}$

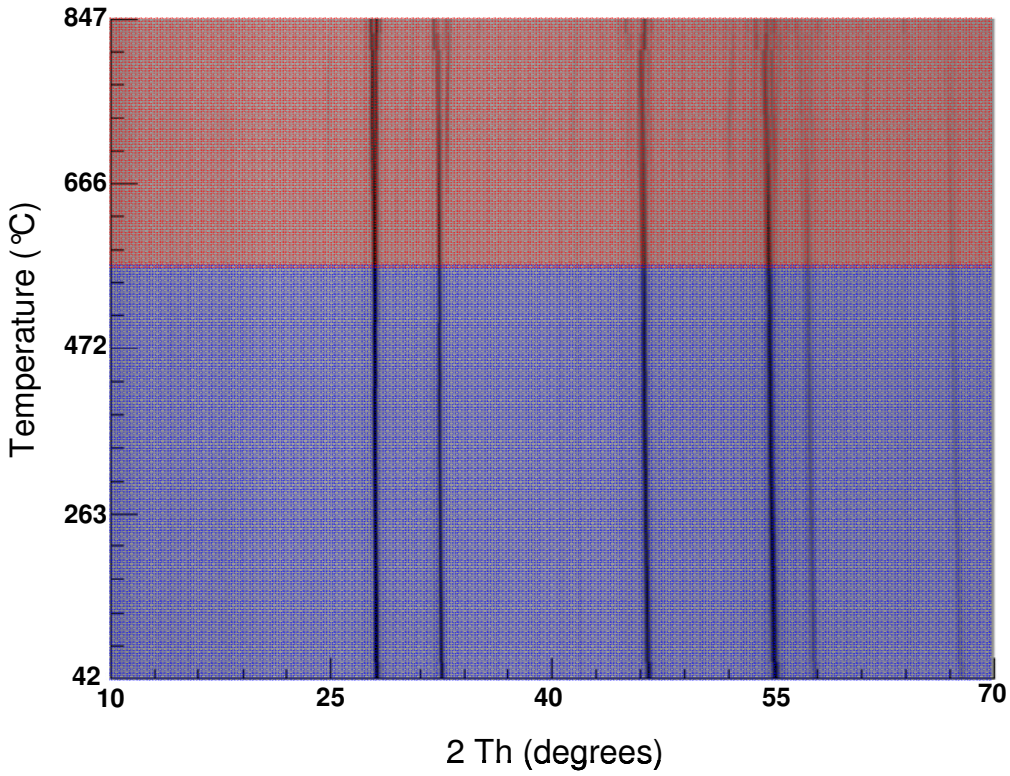

Figure 7.7: d9_04850: VT-PXRD on $Bi_{18.9}Ca_{0.1}V_2O_{33.45}$. No phase transitions were observed over the temperature range studied and partial decomposition occurred at 571 °C and above. Pale blue region represents stability range, whilst light red region represents decomposition ranges.

An *in-situ* VT-PXRD was carried out on $Bi_{18.9}Ca_{0.1}V_2O_{33.45}$ (see Figure 7.7). Decomposition of this phase occurred at 571 °C, which is in line with that observed for the parent phase.[4] At this temperature, PXRD patterns showed the presence of vanadium doped γ-Bi_2O_3 ($Bi_{25}VO_{40}$). Rietveld refinement was carried out for $Bi_{18.9}Ca_{0.1}V_2O_{33.45}$ at each temperature using 'Mulitopas', an in-house local routine for sequential Rietveld refinement.[10] At each temperature, 18 background parameters,

specimen displacement height, scale factor, peak shape, cell parameters and one overall isotropic temperature factor were refined. Figure 7.8 shows the variation of cell volume with temperature, which varies smoothly with temperature.

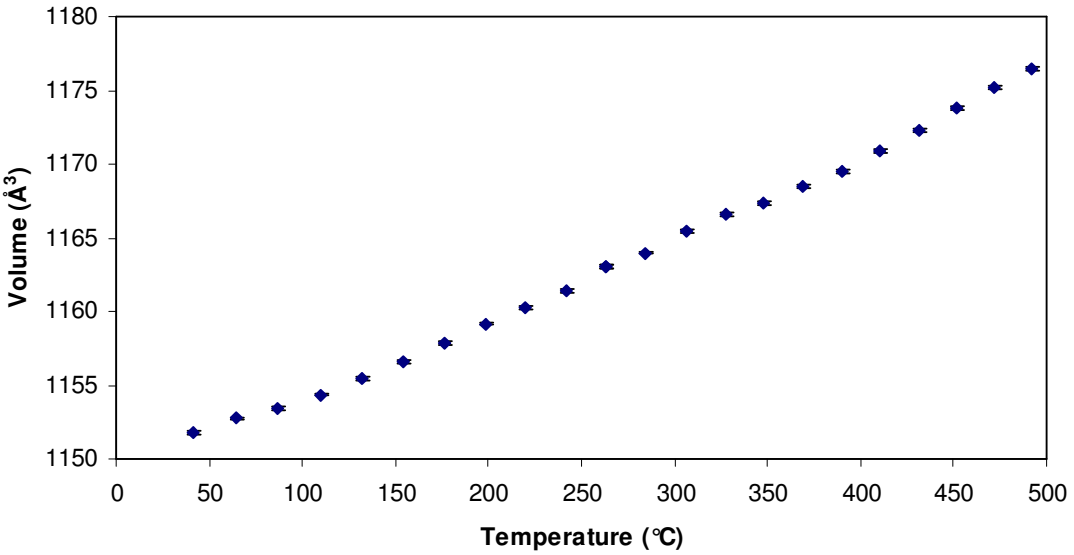

Figure 7.8: Variation of cell volume with temperature for $Bi_{18.9}Ca_{0.1}V_2O_{33.45}$.

7.4.3 Impedance measurements on $Bi_{19-x}Ca_xV_2O_{33.5-x/2}$

An impedance measurement was carried out on $Bi_{18.9}Ca_{0.1}V_2O_{33.45}$. The density of the pellet was 85%. At low temperatures, one semi-circle arc and one Warburg-type electrode spike was observed in the complex impedance plot (Figure 7.9). The capacitance of the semi-circle arc was estimated using the formula $\omega RC = 1$. At 192 °C, the capacitance of the arc was 5.4 pF cm^{-1}, typical of the bulk response. At low frequencies, the capacitance of the spike was 10^{-7} F cm^{-1}, indicative of ionic conduction. With increasing temperature, the bulk response gradually decreased, leaving only the electrode response and hence the resistance was taken from the high frequency intercept.

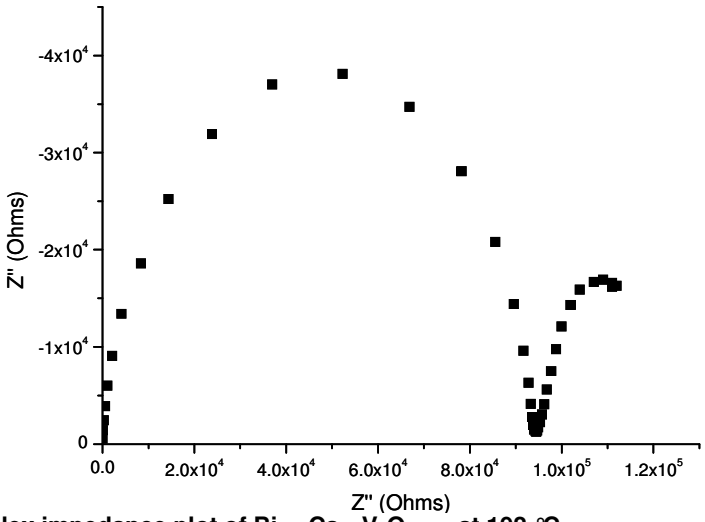

Figure 7.9: Complex impedance plot of $Bi_{18.9}Ca_{0.1}V_2O_{33.45}$ at 192 °C.

Figure 7.10 shows the Arrhenius plot for $Bi_{18.9}Ca_{0.1}V_2O_{33.45}$, compared to the parent material of $Bi_{19}V_2O_{33.5}$ (which was measured by Xiaojun Kuang). $Bi_{18.9}Ca_{0.1}V_2O_{33.45}$ has a conductivity slightly lower than the parent compound $Bi_{19}V_2O_{33.5}$.

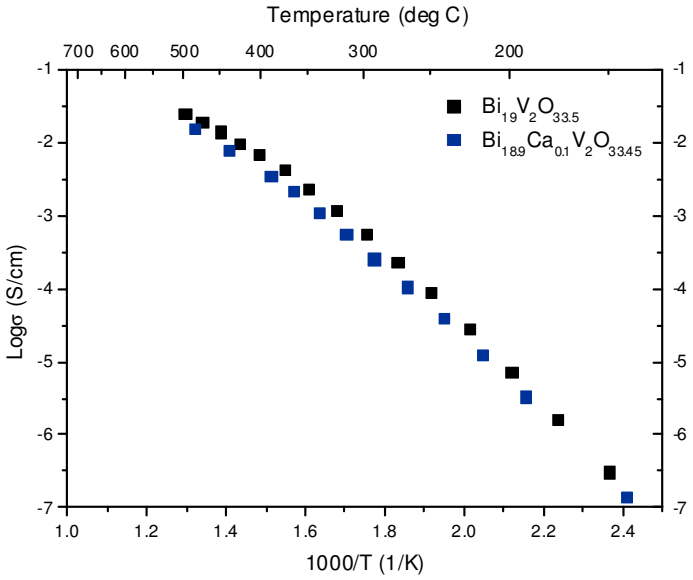

Figure 7.10: Arrhenius plot of conductivity for parent material $Bi_{19}V_2O_{33.5}$ and Ca^{2+} doped $Bi_{18.9}Ca_{0.1}V_2O_{33.45}$.

The conductivity displayed by $Bi_{18.9}Ca_{0.1}V_2O_{33.45}$ reaches 0.016 S cm^{-1} at 486 °C. This is higher than $Ce_{0.9}Gd_{0.1}O_{1.95}$ and $Bi_7WO_{13.5}$, both of which display a conductivity of 0.01 S cm^{-1} at 500 °C and it is also much better than the commercially used yttria stabilised zirconia, which only displays a conductivity of 1.19×10^{-3} S cm^{-1} at 500 °C.[11-13] The conductivity is only slightly lower than $Bi_{0.88}Dy_{0.08}W_{0.04}O_{1.56}$ which has one of the highest conductivities known, displaying a magnitude of 0.043 S cm^{-1} at 500 °C and is comparable to $Bi_{12.5}La_{1.5}ReO_{24.5}$, which has a conductivity of 0.030 S cm^{-1} at 500 °C.[5, 14] The conductivity of $Bi_{18.9}Ca_{0.1}V_2O_{33.45}$ is also comparable to

$Bi_2V_{0.9}Cu_{0.1}O_{5.35}$, which has the highest conductivity in the BIMEVOX series.[1] A comparison of the conductivity of $Bi_{18.9}Ca_{0.1}V_2O_{33.}$ with other leading oxide ion conductors is shown in Figure 7.16.

7.5 $Bi_{19-x}Sr_xV_2O_{33.5-x/2}$

7.5.1 Structural characterisation of $Bi_{19-x}Sr_xV_2O_{33.5-x/2}$

For all samples synthesised (x = 0.1, 0.2, 0.5, 1.0 and 2.0) no impurities were observed in the XRD patterns. In a typical refinement, 18 background terms, peak shape, scale factor, cell parameters and one overall temperature factor were refined. A rhombohedral model was used with occupancies of both cation and anion sites adjusted to take into account the incorporation of Sr^{2+}. A typical Rietveld fit is shown in Figure 7.11.

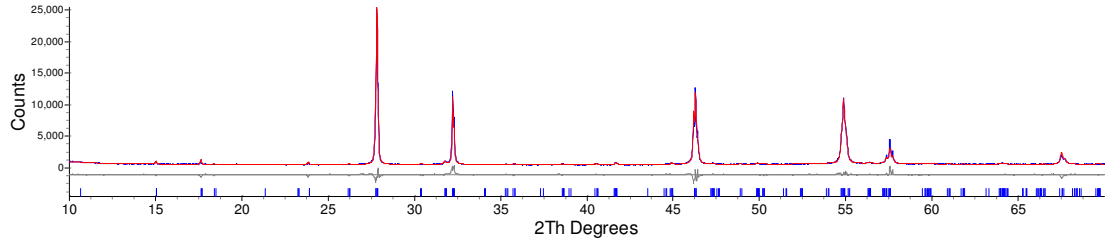

Figure 7.11: d9_04599: Rietveld fit of $Bi_{18.9}Sr_{0.1}V_2O_{33.45}$. R_{wp} = 7.914%.

7.5.2 Laboratory VT-PXRD $Bi_{18}SrV_2O_{33.5}$

Figure 7.12 shows an *in-situ* VT-PXRD carried out on $Bi_{18}SrV_2O_{33}$. Decomposition occurred at 666 °C and at this temperature, PXRD patterns showed the presence of vanadium doped γ-Bi_2O_3 ($Bi_{25}VO_{40}$). The decomposition temperature for $Bi_{18}SrV_2O_{33}$ is 95 °C higher that of $Bi_{18.9}Ca_{0.1}Sr_2O_{33.45}$. This shows that with appropriate substitution the stability may be improved with respect to the parent phase, $Bi_{19}V_2O_{33.5}$. Rietveld refinement was carried out using the 'Multitopas' local routine for sequential refinements.[10] The same parameters were refined for $Bi_{18}SrV_2O_{33}$ as were described for $Bi_{18.9}Ca_{0.1}V_2O_{33.45}$. Figure 7.13 shows the variation of cell volume with temperature, which varies smoothly with temperature.

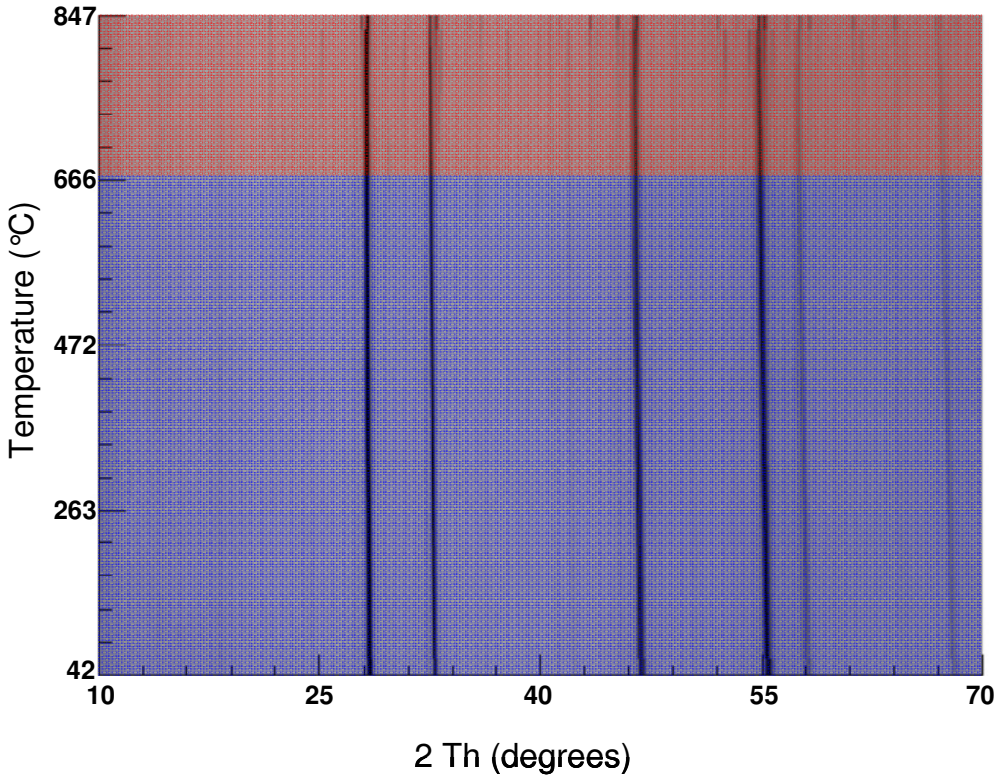

Figure 7.12: d9_04852: *In-situ* VT-PXRD for $Bi_{18}SrV_2O_{33}$. No phase transformations were observed in the laboratory PXRD data and decomposition occurred at 666 °C. Pale blue region represents the stability range, whilst pale red region represents the decomposition range.

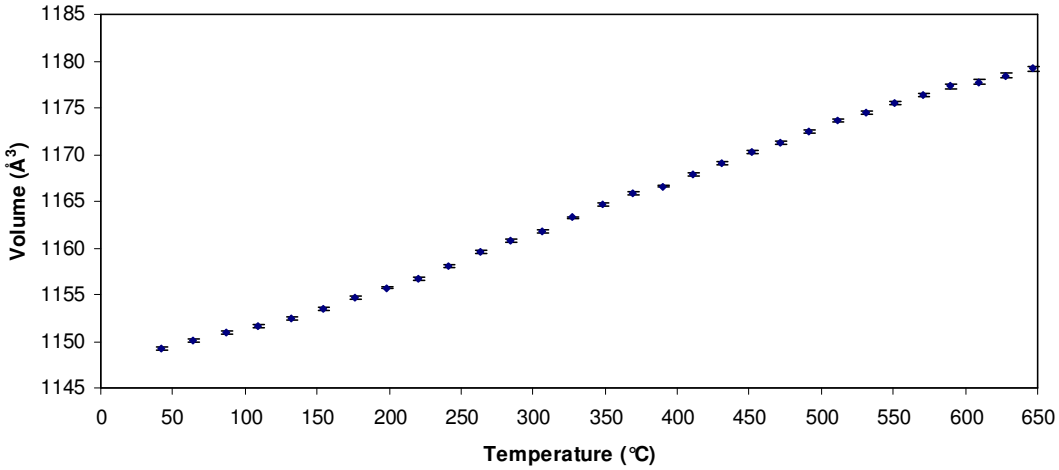

Figure 7.13: Variation of cell volume with temperature for $Bi_{18}SrV_2O_{33}$.

7.5.3 Impedance measurements on $Bi_{19-x}Sr_xV_2O_{33.5-x/2}$

Impedance measurements were carried out in the $Bi_{19-x}Sr_xV_2O_{33.5-x/2}$ system with $x = 0.2$, 1.0 and 2.0. The densities of the pellets were around 85%. A complex impedance plot for $Bi_{18}SrV_2O_{33}$ is shown in Figure 7.14 which is typical for all three compounds at low temperature. It consists of one large semi-circle arc with a

Warburg-type electrode spike. The capacitance of the arc is 7.5 pF cm^{-1}, which is typical of the bulk response. At low frequencies the spike has a capacitance of the order of 10^{-7} F cm^{-1}, signifying ionic conduction. With increasing temperature, the bulk response gradually disappears, leaving only the spike from the electrode response, hence the resistance was taken from the high frequency intercept.

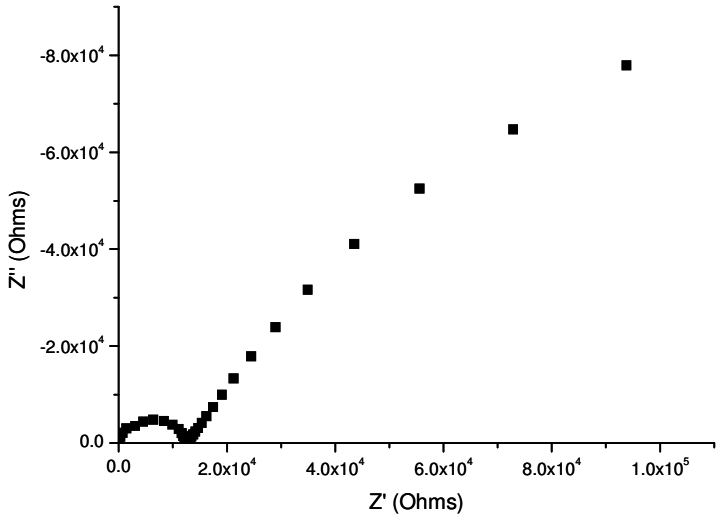

Figure 7.14: Complex impedance plot for $Bi_{18}SrV_2O_{33}$ at 216 °C.

The conductivity of $Bi_{18}SrV_2O_{33}$ is 0.018 S cm^{-1} at 486 °C and $Bi_{17}Sr_2V_2O_{32.5}$ is 0.006 S cm^{-1} at 460 °C. Figure 7.15 shows the Arrhenius plots of conductivity for $Bi_{19-x}Sr_xV_2O_{33.5-x/2}$, where $x = 0.2$, 1.0 and 2.0. No increase in conductivity was observed with Sr^{2+} doping. The conductivities of the $x = 0.2$ and $x = 1.0$ samples are comparable to the parent material, but the $x = 2.0$ sample has a lower conductivity. A similar situation was observed for the Ca^{2+} analogues. The $x = 0.2$ and 1.0 samples still show a high conductivity with respect to other solid electrolytes, as discussed for the $Bi_{18.9}Ca_{0.1}V_2O_{33.45}$ sample in 7.4.3.

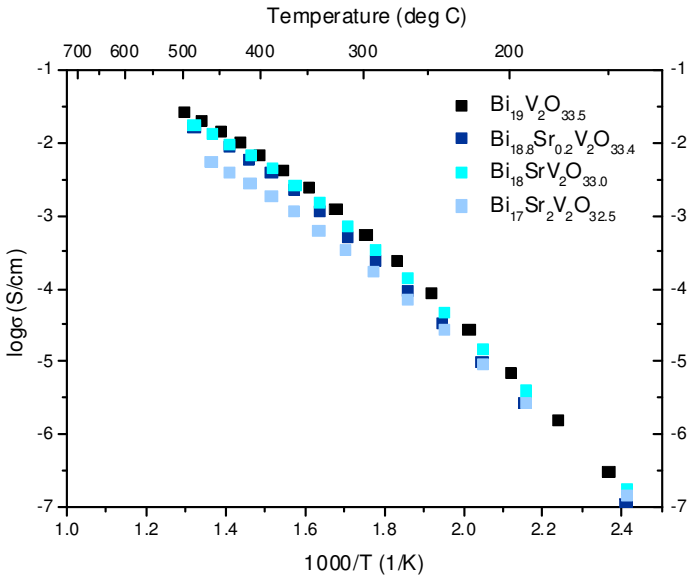

Figure 7.15: Arrhenius plot of conductivity showing $Bi_{19-x}Sr_xV_2O_{33.5-x/2}$ phases.

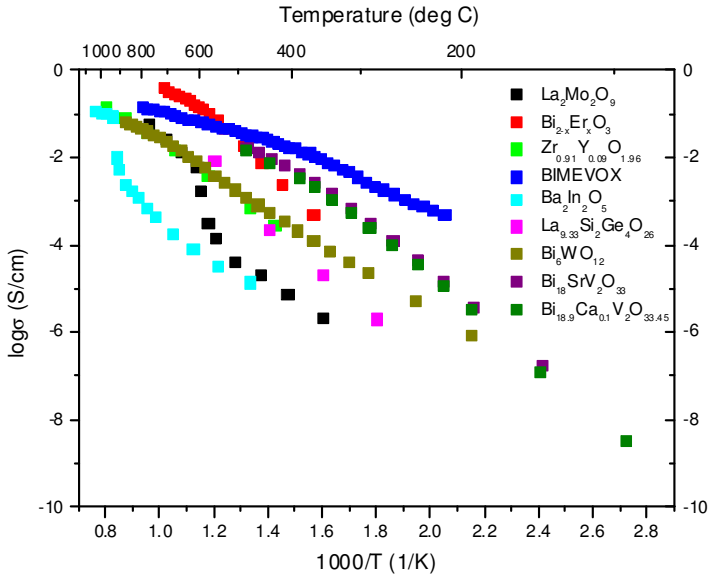

Figure 7.16: Comparsion of conductivity of $Bi_{18.9}Ca_{0.1}V_2O_{33.45}$ and $Bi_{18}SrV_2O_{33}$ with that of other good, well known oxide ion conductors.[4, 10-13]

Figure 7.16 shows the conductivity of $Bi_{18}SrV_2O_{33}$ compared to other good oxide ion conductivities. It shows that at low temperatures, $Bi_{18}SrV_2O_{33}$ has a higher oxide ion conductivity (of more than one order of magnitude) than yttria stabilised zirconia, erbium doped bismuth oxide, $La_2Mo_2O_9$ and $Ba_2In_2O_5$. It also has a higher conductivity than the sample of Bi_6WO_{12} described in Chapter 6. The BIMEVOX sample has a higher conductivity than the $Bi_{19-x}M_xV_2O_{33.5-x/2}$ samples, although as the temperature approaches 500 °C, the conductivity of $Bi_{18}SrV_2O_{33}$ is close to the values achieved by BIMEVOX.

7.6 Conclusions

Good quality single crystals of $Bi_{19}V_2O_{33.5}$ and $Bi_{19-x}M_xV_2O_{33.5-x/2}$ (M = Ca^{2+} and Sr^{2+}) have been grown. The unit cell of the expected $3 \times 3 \times 3$ fluorite superstructure has been confirmed by laboratory single crystal X-ray diffraction, indicating that the crystals are of the desired phase.

MD simulations have shown that the oxygen diffusion mechanisms involve VO_4 units and VO_4-OBi_4-VO_4 units at low temperature. At higher temperature, diffusion also occurs through OBi_4 tetrahedra.

The doping limit of Sr^{2+} is higher than Ca^{2+} and strontium doping has increased the temperature stability range. Substitution of Bi^{3+} with M = Ca^{2+} and Sr^{2+} did not increase ionic conductivity in the $Bi_{19-x}M_xV_2O_{33.5-x/2}$ systems. This may be related to the MD simulations, which have shown that oxide ion conductivity occurs through VO_4 units and exchange between VO_4 and OBi_4 units at low temperatures, rather than only the OBi_4 units. Diffusion pathways were only observed in the OBi_4 sublattice at 873K, therefore doping the bismuth site does not enhance the conductivity in the temperature range studied.

Although the conductivity of the $Bi_{19-x}M_xV_2O_{33.5-x/2}$ systems has not been increased, the conductivities of these samples were still comparable to the parent material, making them some of the best oxide ion conductors known to date.

7.7 References

1. K. R. Kendall, C. Navas, J. K. Thomas and H. C. zurLoye, *Chem. Mater.*, 1996, **8**, 642-649.
2. W. Zhou, *J. Solid State Chem.*, 1988, **76**, 290-300.
3. S. Kashida, T. Hori and K. Nakamura, *J. Phys. Soc. Jpn.*, 1994, **63**, 4422-4426.
4. X. J. Kuang, J. L. Payne and I. R. Evans, *Unpublished results*, 2010.
5. R. Punn, A. M. Feteira, D. C. Sinclair and C. Greaves, *J. Am. Chem. Soc.*, 2006, **128**, 15386-15387.
6. LAMP.The Large Array Manipulation Program. http://www.ill.eu/instruments-support/computing-for-science/cs-software/all-software/lamp
7. T. Rog, K. Murzyn, K. Hinsen and G. R. J. Kneller, *J. Comput. Chem*, 2003, **24**, 657-667.
8. P. Lacorre, F. Goutenoire, O. Bohnke, R. Retoux and Y. Laligant, *Nature*, 2000, **404**, 856-858.
9. I. R. Evans, J. S. O. Evans and J. A. K. Howard, *Chem. Mater.*, 2005, **17**, 4074 - 4077.
10. J. S. O. Evans, Durham, 1999, p. Fortran 77 routine.
11. V. V. Kharton, F. M. B. Marques and A. Atkinson, *Solid State Ionics*, 2004, **174**, 135-149.
12. T. Takahashi and H. Iwahara, *J. Appl. Electrochem.*, 1973, **3**, 65-72.

13. H. Inaba and H. Tagawa, *Solid State Ionics*, 1996, **83**, 1-16.
14. N. X. Jiang, E. D. Wachsman and S. H. Jung, *Solid State Ionics*, 2002, **150**, 347-353.

8 Overall Conclusions and Suggestions for Future Work

We have explored the structural and transport properties in the $Bi_2Zr_{2-x}Ti_xO_7$ system for the first time. Doping Zr^{4+} into $Bi_2Ti_2O_7$ increases the conductivity, with a difference of three orders of magnitude observed between the $Bi_2Ti_2O_7$ and $(BiZr)_2O_7$ parent members. This is consistent with a crystallographic transition from the pyrochlore to fluorite-type structure. Pyrochlore-type $Bi_2Ti_2O_7$, which adopts centrosymmetric space group $Fd\bar{3}m$, has been shown to be SHG active and this is supported by total scattering and RMC simulations which show a range of distortions on a local scale.

$Bi_2Sn_2O_7$ and Bi_2ScNbO_7 have identical radius ratios, and exhibit different pyrochlore related structures. At room temperature, $Bi_2Sn_2O_7$ exhibits a subtle monoclinic distortion of the $\sqrt{2} \times \sqrt{2} \times 2$ pyrochlore superstructure and adopts space group *Pc*. Bi_2ScNbO_7 is cubic, but departs from the ideal pyrochlore structure in that the Bi(III) cations are displaced off the three-fold axis.[1, 2] Bi_2ScNbO_7 displays a higher conductivity than $Bi_2Sn_2O_7$. This demonstrates that the chemical nature of the B-cations affect both the crystal structure and the conductivity. Further work could involve $Bi_2(ScNb)_{1-x}Zr_{2x}O_7$ systems in order to correlate any changes in structure or properties with $Bi_2Sn_{2-x}Zr_xO_7$ and other $M_2Sn_{2-x}Zr_xO_7$ compounds (where M = Gd^{3+} and Y^{3+}).

As the conductivities of several $Bi_2M_2O_7$ compounds have been measured, it is interesting to compare them. Figure 8.1 shows the comparison of conductivities for $Bi_2M_2O_7$ compounds (where M = Ti, Sn, Zr or 0.5 Sc:0.5 Nb). The highest conductivity is observed for $(BiZr)_2O_7$, which has the fluorite structure, whilst the lowest conductivity is observed for $Bi_2Ti_2O_7$ with the pyrochlore structure. As already discussed, the conductivities of Bi_2ScNbO_7 and $Bi_2Sn_2O_7$ may be attributed to differences in the chemical nature of the B-site cation.

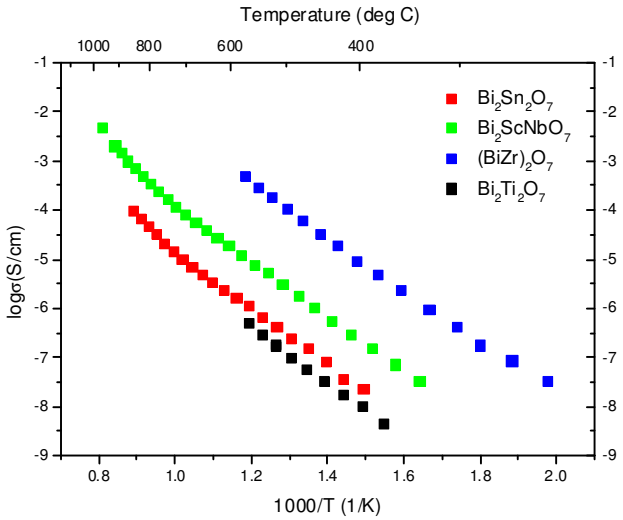

Figure 8.1: Comparison of the conductivity of $Bi_2Ti_2O_7$, $Bi_2Sn_2O_7$, Bi_2ScNbO_7 and $(BiZr)_2O_7$.

The observed trends in the conductivity as a function of composition is comparable to that of other well studied $A_2M_2O_7$ compounds, where A = Gd^{3+} or Y^{3+} and M = Zr^{4+}, Sn^{4+} and Ti^{4+}. In these systems, zirconate pyrochlores always have higher conductivities than the both the titanates and the stannates.[3-6] In the literature, the differences in conductivity between the stannate and the titanate pyrochlores are always smaller than that observed between the zirconates and titanates.[3] For $M_2Sn_{2-x}Ti_xO_7$ (M = Y^{3+} and Gd^{3+}) the difference in the conductivity is approximately 0.75 orders of magnitude, similar to the difference observed here.[3] Our results on the Bi(III) containing pyrochlores with varying B-cations are in excellent agreement with the literature for related materials with different compositions. [3-6]

Future work on the $Bi_2M_2O_7$ compounds could involve carrying out impedance measurements under varying partial pressures of oxygen and determining transference numbers in order to clarify the nature of the carrier.

We have shown for the first time that β-$Bi_2Sn_2O_7$ is not cubic. High-resolution synchrotron X-ray diffraction data clearly show peaks splitting, which can be accounted for only if the metric symmetry is lowered to monoclinic. Structure solution using simulated annealing has shown a small preference for space group *Pc*. However, further cycles of simulated annealing are required to conclusively determine the structure of β-$Bi_2Sn_2O_7$.

$Nd_2Zr_2O_7$ synthesised by a precursor route has been characterised using a variety of local and average structure techniques. They have indicated that $Nd_2Zr_2O_7$ has a fluorite structure when prepared using a wet chemistry, precursor method. Existing

literature on structural characterisation of $Nd_2Zr_2O_7$ has mainly been based on laboratory X-ray diffraction, which has shown broad peaks corresponding to the fluorite structure. In cases such as these, the structure cannot be unambiguously assigned to the fluorite structure as any broad pyrochlore superstructure peaks of low intensity may not be identifiable using laboratory PXRD. Our work offers a significant improvement over existing literature as we have used a variety of techniques which probe the average and local structures in different ways, with each method contributing a different piece of information. Neutron diffraction studies of pyrochlore $Nd_2Zr_2O_7$ have shown that it has a disordered oxygen sublattice, which is comparable to the situation observed for the chemically similar $Nd_2Hf_2O_7$. Further work could involve full structural characterisation of other related materials, which have been prepared either through mechanochemical synthesis or precursor methods, but where it appears to be unclear whether the materials possess the pyrochlore or fluorite structure.[5, 7-9]

Molecular dynamics simulations of the Bi_6WO_{12} oxide ion conductor have shown that the migration pathway proceeds through both the WO_x and OBi_4 units. An enhancement in conductivity was achieved by doping the parent compound for $Bi_{5.95}Er_{0.05}WO_{12}$, $Bi_6W_{0.95}Zr_{0.05}O_{11.95}$ and $Bi_{5.95}Er_{0.05}W_{0.95}Zr_{0.05}O_{11.95}$ and $Bi_{5.90}Er_{0.10}W_{0.95}Zr_{0.05}O_{11.95}$. Despite there being three different crystallographic models for this compound in the literature, it is clear that all of them are (good) approximations. Neutron total scattering studies will be undertaken to elucidate the structure fully, in particular to resolve the issues of the oxygen sublattice disorder and the Bi/W distribution in the cation sublattice.

The synthesis and characterisation of several new doped bismuth vanadates with formula $Bi_{19-x}M_xV_2O_{33.5-x/2}$ ($M = Ca^{2+}$ or Sr^{2+}), have been reported and these display excellent ionic conductivities with magnitudes approaching that of the BIMEVOX family. Molecular dynamics simulations on the parent compound $Bi_{19}V_2O_{33.5}$ have shown that at lower temperatures VO_4 units are involved in the oxide ion migration pathway, with some exchange occurring between VO_4 and OBi_4. Diffusion in the OBi_4 sublattice occurs at higher temperatures.

As molecular dynamics simulations on $Bi_{19}V_2O_{33.5}$ have shown that the VO_4 units play an important role in the oxide ion migration pathway, it is likely that the appropriate doping of the tetrahedral vanadium site could result in the enhancement of the ionic conductivity. However, using conventional solid state routes, single phases

could not be prepared. Therefore, alternative methods for the synthesis of V-site doped bismuth vanadates, including those with formula $Bi_{19}V_{2-y}M'_yO_{33.5-z}$ ($M' = Si^{4+}$ or Ga^{3+}), using soft chemical routes will be explored in our future work.

Good quality single crystals of $Bi_{19}V_2O_{33.5}$ have been successfully grown. As the current structural model for this material is only an approximate one, our further work on this bismuth vanadate (and potentially its derivatives) will focus on structural analysis using single crystal synchrotron XRD data.

8.1 References

1. I. R. Evans, J. A. K. Howard and J. S. O. Evans, *J. Mater. Chem.*, 2003, **13**, 2098-2103.
2. Y. Liu, R. L. Withers, H. B. Nguyen, K. Elliott, Q. J. Ren and Z. H. Chen, *J. Solid State Chem.*, 2009, **182**, 2748-2755.
3. B. J. Wuensch, K. W. Eberman, C. Heremans, E. M. Ku, P. Onnerud, E. M. E. Yeo, S. M. Haile, J. K. Stalick and J. D. Jorgensen, *Solid State Ionics*, 2000, **129**, 111-133.
4. C. Heremans, B. J. Wuensch, J. K. Stalick and E. Prince, *J. Solid State Chem.*, 1995, **117**, 108-121.
5. K. J. Moreno, M. A. Guevara-Liceaga, A. F. Fuentes, J. Garcia-Barriocanal, C. Leon and J. Santamaria, *J. Solid State Chem.*, 2006, **179**, 928-934.
6. T. H. Yu and H. L. Tuller, *Solid State Ionics*, 1996, **86-8**, 177-182.
7. Y. H. Lee, H. S. Sheu, J. P. Deng and H. C. I. Kao, *J. Alloys and Compounds*, 2009, **487**, 595-598.
8. K. J. Moreno, A. F. Fuentes, J. García-Barriocanal, C. León and J. Santamaría, *J. Solid State Chem.*, 2006, **179**, 323-330.
9. K. J. Moreno, A. F. Fuentes, M. Maczka, J. Hanuza and U. Amador, *J. Solid State Chem.*, 2006, **179**, 3805-3813.